Sensorless control of synchronous permanent magnet motors by signal injection

Al Kassem Jebai

ParisTech
INSTITUT DES SCIENCES ET TECHNOLOGIES
PARIS INSTITUTE OF TECHNOLOGY

MINES ParisTech

École doctorale n° 432: Sciences et Métiers de l'Ingénieur

Doctorat ParisTech

T H È S E

pour obtenir le grade de docteur délivré par

l'École Nationale Supérieure des Mines de Paris

Spécialité Mathématique et Automatique

présentée et soutenue publiquement par

Al Kassem JEBAI

le 15 mars 2013

Commande sans capteur des moteurs synchrones à aimants permanents par injection de signaux

Directeurs de thèse: **Pierre Rouchon et Philippe Martin**

Jury

M. François Auger, Professeur, IREENA et CRTT	Président
M. Jan MELKEBEEK, Professeur, Gent University	Rapporteur
M. Alain GLUMINEAU, Professeur, IRCCYN et Ecole Centrale de Nantes	Rapporteur
M. Romeo ORTEGA, Directeur de recherche, CNRS, LSS	Examinateur
M. François MALRAIT, Docteur, Schneider Electric	Examinateur
M. Pierre Rouchon, Professeur, MINES ParisTech	Examinateur
M. Philippe Martin, Maître de Recherche, MINES ParisTech	Examinateur

MINES ParisTech
Centre Automatique et Systèmes
60-62, Boulevard Saint Michel 75272 PARIS cedex 06 France

THÈSE

ParisTech
INSTITUT DES SCIENCES ET TECHNOLOGIES
PARIS INSTITUTE OF TECHNOLOGY

MINES ParisTech

École doctorale 432: Sciences et Métiers de l'Ingénieur

ParisTech Doctorate

T H E S I S

to obtain the

Doctor's degree from the Ecole Nationale Supérieure des Mines de Paris

Speciality "Mathematics and Control"

defended in public by

Al Kassem JEBAI

on March, 15^{th}, 2013

Sensorless control of permanent magnet motors by signal injection

Advisors: **Pierre Rouchon and Philippe Martin**

Jury

M. François Auger, Professeur, IREENA et CRTT	President
M. Jan MELKEBEEK, Professeur, Gent University	Referee
M. Alain GLUMINEAU, Professeur, IRCCYN et Ecole Centrale de Nantes	Referee
M. Romeo ORTEGA, Directeur de recherche, CNRS, LSS	Examiner
M. François MALRAIT, Docteur, Schneider Electric	Examiner
M. Pierre Rouchon, Professeur, MINES ParisTech	Examiner
M. Philippe Martin, Maître de Recherche, MINES ParisTech	Examiner

MINES ParisTech
Centre Automatique et Systèmes
60-62, Boulevard Saint Michel 75272 PARIS cedex 06 France

THÈSE

A mes parents, ma femme et mon fils

Al Kassem JEBAI

Centre Automatique et Systèmes

Unité Mathématiques et Systèmes

MINES ParisTech

60 boulevard St Michel

75272 Paris Cedex

France.

E-mail: al-kassem.jebai@mines-paristech.fr, alkassem.jebai@gmail.com

Science is a way of thinking much more then it is a body of knowledge.

CARL SAGAN

Remerciements

Je tiens à remercier en premier lieu mes directeurs de thèse Pierre Rouchon et Philippe Martin ainsi que mon responsable au sein de Schneider Electric François Malrait qui m'ont guidé tout au long de ma thèse et qui étaient à mes côtés et m'ont toujours aidé par leur suivi et leurs conseils. Je vous remercie pour votre enthousiasme pour le projet et votre sens pratique et de m'avoir toujours poussé à être plus précis et rigoureux.

Je souhaite remercier Jan Melkebeek ainsi qu'Alain Glumineau qui ont accepté d'être les rapporteurs de cette thèse. Je remercie également François Auger et Romeo Ortega qui m'ont fait l'honneur de participer au jury de soutenance.

Je remercie aussi l'ensemble du Centre Automatique et Système pour l'excellent environnement de travail qu'il offre aux chercheurs comme moi. Je remercie les différents chercheurs du Centre, Laurent Praly, Jean Lévine, François Chaplais et le directeur du laboratoire Nicolas Petit. Je remercie mes collègues docteurs et doctorants: Paul, Caroline, Delphine, Eric, Hadis, Nadège, Pierre-Jean, Stéphane, Zaki, Florent, Lionel, Nicolas ...

Je tiens à remercier les nombreuses personnes de Schneider Electric avec qui j'ai pu travailler durant ma thèse, et tout particulièrement Duro Basic, Thomas Devos, Stéphane Capitaneau et Michael Hernandez pour leur soutien. Je souhaite remercier encore les personnes du Techno Centre de Pacy pour leur aide et leurs conseils précieux.

Enfin, je dédie ma thèse à ma famille et particulièrement à mon père et à ma mère pour m'avoir toujours soutenu, encouragé et appris à aimer la science et qui ont beaucoup sacrifié pour que je puisse arriver ici. Je souhaite dire encore mille merci à ma femme qui m'a soutenu et supporté durant ces trois années, et à mon fils qui est né pendant ma thèse.

Résumé

Cette thèse étudie la problématique du fonctionnement sans capteur et à basse vitesse des moteurs synchrones à aimants permanents (MSAP) par l'injection de signaux (nous nous focalisons sur les effets de la saturation magnétique car leur compensation est primordiale pour résoudre cette problématique). Nous proposons une méthode originale pour modéliser la saturation magnétique en utilisant une approche énergétique (les formulations Lagrangienne et Hamiltonienne), où les symétries physiques sont exploitées pour simplifier l'expression de l'énergie magnétique. Les données expérimentales montrent qu'un polynôme de degré 4 est suffisant pour décrire avec précision les effets de la saturation. Ensuite, nous proposons une analyse claire et originale basée sur la moyennisation de second ordre et qui explique comment obtenir l'information de position à partir de l'injection des signaux (en utilisant le modèle proposé). Nous donnons une relation explicite entre les oscillations des courants statoriques et la position du rotor; cette relation est utilisée en temps réel. Ce modèle de saturation magnétique ainsi que la procédure d'estimation de position ont été testés et validés sur deux types de moteurs à aimants permanents: à l'intérieur ou en surface du rotor. Les résultats expérimentaux obtenus sur un banc de test montrent que l'erreur d'estimation de la position du rotor n'excède pas quelques degrés électriques dans la zone d'opération à basse vitesse.

Abstract

This thesis addresses the problematic of sensorless low speed operation of permanent magnet synchronous motors (PMSM) by signal injection (we focus on the effects of magnetic and cross saturations because their compensation is paramount to solve this problematic). We propose an original way of modeling magnetic saturation using an energy approach (Lagrangian and Hamiltonian formulations), where the physical symmetries are exploited to simplify the expression of the magnetic energy. Experimental data show that a simple polynomial of degree 4 is sufficient to describe accurately magnetic saturation effects. Then we propose a clear and original analysis based on second-order averaging of how to recover the position information from signal injection (using the proposed model). We give an explicit relation between stator current ripples and rotor position; this relation is used in real time operation. Such magnetic saturation model and the resulting position estimates were tested and validated on two types of motors: with interior and surface permanent magnets (IPM and SPM). Experimental results obtained on a test bench show that estimation errors of the rotor position do not exceed few electrical degrees in the low speed operating domain.

Symbols and abbreviations

In the sequel, ν can be a, b, c, α, β, 0, d or q.

u_ν **:** Voltage across winding ν.

v_ν **:** Electric potential of the point ν.

$v_{\nu'}$ **:** Electric potential of the point $\nu^{'}$.

v_N **:** Potential of the star point N

Ψ_ν **:** Total flux linkage of winding ν.

t **:** Time.

i_ν **:** Current of winding ν.

R **:** Motor resistance per phase.

J **:** Motor inertia.

n **:** Number of the motor pole pair.

τ_e **:** Electromagnetic torque.

τ_L **:** Load torque.

θ **:** Rotor electric position.

θ_m **:** Rotor mechanical position.

λ^{abc} **:** Magnitude of the magnet flux.

λ **:** Permanent magnet flux amplitude in $dq0$ and $\alpha\beta0$ frame.

L **:** Self inductance per phase in the abc frame.

M **:** mutual inductance in the abc frame.

L_Δ **:** Maximum inductance variation in abc frame.

$\mathbf{L}^{abc}$ **:** Matrix of inductance in abc frame.

$\mathcal{L}$ **:** Lagrangian.

$\mathcal{L}^{abc}$ **:** Lagrangian in abc frame.

$\mathcal{L}^{\alpha\beta0}$ **:** Lagrangian in $\alpha\beta0$ frame.

ϕ_ν^m **:** Permanent flux linkage of winding ν.

$\mathbf{\Phi}_{abc}^m = (\phi_a^m, \phi_b^m, \phi_c^m)^T$ **:** Vector of permanent magnet flux in abc frame.

$\mathbf{\Phi}^m_{\alpha\beta 0} = (\phi^m_\alpha, \phi^m_\beta, \phi^m_0)^T$ **:** Vector of permanent magnet flux in $\alpha\beta 0$ frame.

$\mathbf{\Phi}^m_{\alpha\beta} = (\phi^m_\alpha, \phi^m_\beta)^T$ **:** Vector of permanent magnet flux in $\alpha\beta$ frame.

$\mathbf{\Phi}_m = (\phi^m_d, \phi^m_q)^T$ **:** Vector of permanent magnet flux in dq frame.

ϕ_ν **:** ν- axis flux linkage due to the current excitation.

$\mathbf{\Phi}_{dq} = (\phi_d, \phi_q)^T$ **:** Vector of electric flux linkage due to the current excitation flux in dq frame.

L_d **:** d- axis inductance.

L_q **:** q- axis inductance.

$\mathbf{L}^{\alpha\beta}$ **:** Matrix of inductance in $\alpha\beta$ frame.

$\mathcal{P}_\theta$ **:** Park transformation matrix.

$\widetilde{\mathcal{L}}^{dq0}$ **:** Co-energy in $dq0$ frame.

L_0 **:** 0- axis inductance.

ω **:** Electric motor speed.

p_θ **:** Moment of inertia.

$\mathcal{H}^{abc}$ **:** Hamiltonian in abc frame.

$\mathcal{H}^{\alpha\beta 0}$ **:** Hamiltonian in $\alpha\beta 0$ frame.

$\widetilde{\mathcal{H}}^{dq0}$ **:** Total energy in $dq0$ frame.

$\mathbb{L}^{\alpha\beta}$ **:** Lagrangian in $\alpha\beta$ frame with star connection of stator windings.

$\mathbb{H}^{\alpha\beta}$ **:** Hamiltonian in $\alpha\beta$ frame with star connection of stator windings.

$\widetilde{\mathbb{L}}^{dq}$ **:** Co-energy in dq frame with star connection of stator windings.

$\widetilde{\mathbb{H}}^{dq}$ **:** Energy in dq frame with star connection of stator windings.

$\mathcal{R}_\theta = \begin{pmatrix} \cos\theta & -\sin\theta \\ \sin\theta & \cos\theta \end{pmatrix}$ **:** Unitary rotation matrix of angle θ. We note that $\mathcal{R}_\theta^{-1} = \mathcal{R}_\theta^T = \mathcal{R}_{-\theta}$.

$\mathbf{C} = \begin{pmatrix} 0 & 1 & 0 \\ 0 & 0 & 1 \\ 1 & 0 & 0 \end{pmatrix}$ **:** Circular permutation matrix.

$\mathcal{J} = \begin{pmatrix} 0 & -1 \\ 1 & 0 \end{pmatrix}$ **:** $\mathcal{J}$ verifies $\frac{d\mathcal{R}_\theta}{d\theta} = \mathcal{J}\mathcal{R}_\theta = \mathcal{R}_\theta\mathcal{J}$.

$\mathbf{U} = \begin{pmatrix} \frac{\sqrt{2}}{\sqrt{3}} & -\frac{1}{\sqrt{6}} & -\frac{1}{\sqrt{6}} \\ 0 & \frac{1}{\sqrt{2}} & -\frac{1}{\sqrt{2}} \\ \frac{1}{\sqrt{3}} & \frac{1}{\sqrt{3}} & \frac{1}{\sqrt{3}} \end{pmatrix}$ **:** Clarke transformation matrix.

Notations

We denote by:

- $\mathbf{x}_{ijk} = (x_i, x_j, x_k)^T$ the vector made from the real numbers x_i, x_j, and x_k, where ijk can be $dq0$, $\alpha\beta0$ or abc; $\mathbf{x}$ is bold face.
- $\mathbf{x}_{ij} = (x_i, x_j)^T$ the vector made from the real numbers x_i, x_j, where ij can be dq or $\alpha\beta$; $\mathbf{x}$ is bold face.
- $\frac{\partial X}{\partial \mathbf{x}_{ijk}} = (\frac{\partial X}{\partial x_i}, \frac{\partial X}{\partial x_j}, \frac{\partial X}{\partial x_k})^T$ by the vector made from the partial derivatives $\frac{\partial X}{\partial x_i}$, $\frac{\partial X}{\partial x_j}$, and $\frac{\partial X}{\partial x_k}$, where X is a real function of the real numbers x_i, x_j, and x_k; ijk can be $dq0$, $\alpha\beta0$ or abc.
- $\frac{\partial X}{\partial \mathbf{x}_{ij}} = (\frac{\partial X}{\partial x_i}, \frac{\partial X}{\partial x_j})^T$ by the vector made from the partial derivatives $\frac{\partial X}{\partial x_i}$ and $\frac{\partial X}{\partial x_j}$, where X is a real function of the real numbers x_i and x_j; ij can be dq or $\alpha\beta$.
- All matrices and vectors are **bold face** or *italic*.

Contents

Chapter 1

Introduction (version française)

Contents

1.1 Préambule

Ce travail de thèse a été réalisé en collaboration avec Schneider Electric pour l'entité Drives basé à Pacy-sur-Eure. La mission de cette entité est de devenir le spécialiste mondial des solutions de commande de moteurs pour une utilisation sûre, fiable, productive et efficace de l'énergie grâce à l'innovation, la simplicité et l'excellence opérationnelle. Dans ce contexte, ce travail porte sur la problématique de l'opération à basse vitesse et sans capteur de moteurs synchrones à aimants permanents par injection de signaux.

Les offres industrielles existantes dans le domaine de la variation de vitesse proposent déjà un haut niveau de performance mais ces offres sont limitées à basse vitesse en fonction des paramètres du variateur de vitesse, la connaissance du moteur, l'environnement d'opération et l'application. L'approche traditionnelle pour assurer un haut niveau de performance quelles que soient les conditions de fonctionnement consiste à installer des capteurs mécaniques sur l'application. Mais l'ajout d'un élément supplémentaire dans la solution complète a un impact négatif sur la fiabilité et la robustesse globale

d'une part et augmente le coût de production du système d'autre part. Dans ce travail, nous adressons à la fois les deux problématiques existantes:

- assurer un fonctionnement stable et robuste du moteur dans la région d'opération à basse vitesse sans l'utilisation d'un capteur mécanique;
- atteindre un niveau de performance qui soit comparable pour un fonctionnement avec capteur en particulier à basse vitesse.

Aujourd'hui, l'approche de commande sans capteur par injection de signaux commence à être présente dans les offres industrielles. Cependant, il y a toujours un besoin pour optimiser la consommation d'énergie et pour renforcer la robustesse et la stabilité du fonctionnement du moteur à basse vitesse et sans capteur mécanique. Il est également important de simplifier l'interface homme machine (IHM)au client en simplifiant la configuration du variateur de vitesse. Pour ces raisons, cette approche reste un domaine de recherche très actif dans le cadre industriel ainsi que dans le cadre académique.

Les travaux menant aux résultats présentés ont été financés par Schneider Toshiba Inverter Europe (STIE). Tous les essais et les expériences ont été réalisés dans le laboratoire de recherche et développement de cette entreprise, à Pacy-sur-Eure.

1.2 Le moteur MSAP

Un moteur synchrone à aimants permanents (MSAP) est un système électromécanique qui transforme l'énergie électrique en énergie mécanique par l'intermédiaire des champs magnétiques. Cette énergie mécanique produit un mouvement de rotation et un couple mécanique.

Un MSAP triphasé est composé de deux parties principales. Une partie fixe qui s'appelle stator et qui est composé de trois enroulements (bobines). Une partie tournante qui s'appelle rotor et qui est composé d'un aimant permanent. Le stator et le rotor ont une forme cylindrique où le rotor est recouvert par le stator. Ils sont séparés par un petit entrefer.

Le principe de fonctionnement du MSAP est décrit dans [1, 2]- [3, p.261]. Les bobines (phases) du stator sont reliées à une source triphasée de tensions sinusoïdales. La superposition des trois flux magnétiques créés par les trois bobines du stator produit un flux magnétique sinusoïdal tournant à la fréquence de la source de tension. Ce flux magnétique tournant interagit avec le flux de rotor dans l'entrefer qui sépare le stator du rotor et crée ainsi une force électromagnétique. Cette force se traduit par la rotation du rotor. La vitesse de rotation du rotor est proportionnelle à la fréquence de la source de tension.

Il existe deux grandes catégories de MSAP selon le type du rotor : 1- moteur synchrone avec aimants en surface (MSAS) où les aimants permanents sont fixés à la surface du rotor ; 2- moteur synchrone avec aimants à l'intérieur (MSAI) où les aimants permanents sont montés à l'intérieur du rotor. Un MSAI a une plus forte résistance mécanique qu'un MSAS, car les aimants de MSAS ont besoin d'être fixés sur la surface du rotor. Par rapport au comportement magnétique, le rotor du MSAS est symétrique tandis que le rotor du MSAI est asymétrique. Ainsi, les inductances statoriques du MSAS ne varient pas avec la position du rotor [4]. Par contre, les inductances du MSAI varient en fonction de la position du rotor [5] ce qui crée une saillance géométrique du rotor. Cette saillance est très utile pour le contrôle du moteur à basse vitesse.

1.2.1 Applications

Actuellement, les moteurs électriques sont largement utilisés. Selon [6], plus de 60% de l'énergie électrique est consommée par les moteurs électriques. Le MSAP est l'un des types les plus utilisés des moteurs électriques surtout pendant les dernières années. Le MSAP est caractérisé par une densité élevée de puissance et de couple, une faible consommation d'énergie (facteur de puissance proche de 1) et un très bon comportement dynamique. Ainsi, les MSAPs commencent à remplacer les moteurs asynchrones dans des nombreuses applications. En plus, le développement des composants de l'électronique de puissance et l'augmentation de la vitesse de traitement du signal sont également à l'origine de la hausse de l'utilisation de ce type des moteurs.

Les MSAPs sont utilisés dans plusieurs applications citons par exemple les véhicules électriques et les machines à laver (qui nécessitent une densité élevée de puissance). Ils sont également utilisés dans les appareils de haute précision comme les imprimantes électriques, les outils de fabrication, les équipements médicaux (pompes, ventilateurs et compresseurs) ...

1.2.2 Variateur de vitesse

Un variateur de vitesse électrique est utilisé pour commander les moteurs électriques et en particulier les MSAPs. Il s'agit d'un dispositif d'électronique de puissance qui génère une tension ayant une fréquence et une amplitude variables à partir d'une source de tension à fréquence et amplitude fixes. L'utilisation d'un variateur de vitesse (plutôt que brancher le moteur directement au réseau électrique) présente plusieurs avantages. En effet, un variateur de vitesse permet typiquement (comme son nom l'indique) de varier la vitesse du moteur et de réduire de 50% l'énergie consommée par le moteur.

Plusieurs entreprises industrielles proposent des variateurs de vitesse des MSAPs. Il s'agit d'un marché important où les ventes mondiales atteignent plusieurs milliards d'euros par an. Schneider Electric est un leader mondial dans ce domaine, les autres entreprises les plus importantes sont Toshiba, ABB, Danfoss, Mitsubishi, Yaskawa, Fuji, GE, Siemens, ...

1.3 Contrôle sans capteur à basse vitesse

Il existe plusieurs méthodes de contrôle de la vitesse du MSAP par un variateur. Ils se distinguent par:

- le type de la loi de commande de vitesse: contrôle scalaire [7] ou commande basée sur le modèle du moteur [8];
- le mode de fonctionnement: boucle fermée [9] (avec un capteur d'angle) ou sans capteur [10] (sans capteur de position);
- la plage de vitesse de fonctionnement: basse vitesse [11] ou moyenne à grande vitesse [12].

Aujourd'hui, le fonctionnement du MSAP sans capteur et à basse vitesse représente un enjeu industriel majeur ; il peut faire la différence entre les différentes entreprises concurrentes qui travaillent dans ce domaine. En plus, c'est un sujet de recherche scientifique très intéressant car il existe un problème d'observabilité théorique à zéro de vitesse.

Dans la suite, nous présentons brièvement les différentes lois existantes de contrôle de vitesse du MSAP. Ensuite, nous détaillons le contrôle sans capteur par l'injection de signaux à basse vitesse. Enfin, nous nous focalisons sur l'impact de la saturation magnétique dans ce cas et la compensation de ces effets (qui constitue la partie majeure de notre travail).

1.3.1 Contrôle scalaire

Ce type de contrôle est caractérisé par un rapport constant entre l'amplitude et la fréquence de la tension fournie au moteur (V/f) [7]. Ce rapport est égal à la valeur du flux magnétique de l'aimant permanent. Ce type de contrôle a les avantages de simplicité et de faible coût, ainsi il n'a pas besoin de la position du rotor. Par contre, la loi V/f ne prend pas en compte la dynamique du moteur. Ainsi, cette loi n'est pas adaptée pour les applications qui nécessitent une réponse dynamique rapide. D'autre part, elle ne peut pas être utilisée à basse vitesse. En plus, cette méthode conduit à une grande perte d'énergie.

1.3.2 Commande basée sur le modèle

Pour obtenir de meilleures performances dynamiques avec moins de consommation d'énergie, nous devons prendre en compte le modèle dynamique du moteur composé des équations électriques (tensions) et mécaniques. Ainsi, l'algorithme de commande sera adapté au modèle du moteur. Nous trouvons dans la littérature plusieurs lois de commande de ce type: contrôle direct du couple (DTC) [13]; contrôle en mode glissant [14, 15] et contrôle vectoriel [6, p.230]. Toutes ces méthodes nécessitent l'information de position du rotor pour devenir opérationnelles. La valeur de position du rotor peut être obtenue par l'une des deux méthodes suivantes:

- en utilisant un capteur de position mécanique comme un encodeur incrémental ou un capteur à effet Hall, il s'agit dans ce cas du mode de fonctionnement en boucle fermée;
- en estimant la position à partir des courants mesurés, ce qui est le mode de fonctionnement sans capteur.

1.3.2.1 Contrôle en boucle fermée

La technique de commande en boucle fermée a l'avantage d'une simple mise en œuvre, car l'angle du rotor est directement obtenu à partir du capteur de position sans avoir besoin de calcul supplémentaire pour estimer cet angle. Par contre, pour plusieurs applications, la présence d'un tel capteur de position a beaucoup d'inconvénients:

- le capteur de position est soumis à de fortes sollicitations mécaniques, car il est monté directement sur l'arbre du moteur. En effet, il tourne à la vitesse mécanique du moteur qui peut être très élevée. De plus, il est parfois soumis à des fortes accélérations. D'autre part, les vibrations mécaniques de l'arbre du moteur perturbent le fonctionnement du capteur. Tous ces effets réduisent la durée de vie du capteur et peuvent même causer son endommagement;
- le capteur est situé dans l'environnement hostile du moteur (pour cet élément de mesure) à cause des températures élevées du moteur et d'autres effets indésirables liés à l'application;

- un câble est nécessaire pour connecter le capteur au variateur de vitesse, ce câble génère des bruits de mesure qui se superposent à l'information de position donnée par le capteur, en particulier lorsque le moteur est loin du variateur. En plus, la présence de ce câble nécessite un espace supplémentaire ce qui n'est pas possible pour certaines applications (véhicule électrique). Lorsque ces bruits de perturbation sont importants, l'information de position pourrait être perdue ce qui réduit la fiabilité du système de contrôle;
- le capteur génère un signal numérique à haute fréquence (atteignant quelques KHz), ce signal numérique nécessite un traitement spécial et un matériel de conditionnement (carte codeur) qui doit être intégré au variateur de vitesse;
- le capteur de position et la carte de conditionnement ont un coût très élevé par rapport à des nombreuses applications.

Pour éviter les inconvénients du capteur de position, on privilégie le mode de fonctionnement sans capteur. Dans la suite, l'algorithme de contrôle vectoriel est utilisé. Il consiste à réguler la vitesse du moteur en contrôlant la position instantanée du vecteur de flux statorique [6, p.230].

1.3.2.2 Contrôle vectoriel sans capteur à moyenne et grande vitesse

En commande vectorielle sans capteur, le capteur de position est remplacé par un observateur de position à partir des mesures des courants électriques. L'algorithme de contrôle vectoriel sans capteur le plus simple consiste à estimer la position du rotor à partir de la tension générée par la force contre électromotrice notée tension (FCEM) [10, 16–18]. En effet, la rotation du flux de l'aimant permanent du rotor crée un vecteur de tension FCEM orthogonale à ce vecteur de flux magnétique. Ainsi, la position du rotor est obtenue directement par l'estimation de ce vecteur de tension.

En temps réel, l'estimation de la position à partir de la tension FCEM est faite en utilisant un observateur-contrôleur de la vitesse du moteur. Cette stratégie de contrôle est basée sur les courants fondamentaux (utilisés pour contrôler le moteur) et elle ne nécessite pas l'ajout de signaux supplémentaires. Il existe dans la littérature plusieurs algorithmes de contrôle du MSAP en utilisant cette méthode:

- la méthode standard consiste à contrôler le courant du moteur en utilisant un contrôleur de type proportionnel intégral (PI) où la tension FCEM est estimée à partir de la sortie de l'intégrateur de ce PI. Ensuite, la position est estimée à partir de la tension FCEM à l'aide d'un estimateur de type boucle à verrouillage de phase [10, 17].
- la seconde méthode consiste à utiliser un filtre de Kalman étendu pour estimer la position du rotor à partie de la tension FCEM [16, 18].

Ces méthodes assurent de bonnes performances dans la plage de fonctionnement de moyenne jusqu'à grande vitesse. On trouve dans le marché plusieurs types de variateur de vitesse basés sur ces méthodes et qui assurent un bon fonctionnement des MSAPs.

En revanche, l'amplitude de la tension FCEM est proportionnelle à la vitesse du moteur. Ainsi, à basse vitesse (inférieure à 5% de la vitesse nominale) l'amplitude de tension FCEM est très faible et elle est nulle lorsque la vitesse est nulle. Dans ce cas, cette tension est de même ordre de grandeur que les bruits de mesure et elle est très sensible aux incertitudes paramétriques. Par conséquent, les

signaux fondamentaux deviennent pratiquement inutilisables autour de la vitesse nulle. Ceci peut être expliqué par le problème bien connu d'observabilité à zéro de vitesse lorsque les courants statoriques sont les seules variables mesurées [19–21].

1.3.3 Injection de signaux

Pour résoudre le problème d'observabilité à basse vitesse, il faut ajouter une excitation persistante à la tension fondamentale du moteur. Ceci doit être fait indépendamment de la technique du contrôle de la vitesse: DTC [22]; commande par mode glissant [23] et commande vectorielle [24].

Pendant ces vingt dernières années, le contrôle sans capteur et à basse vitesse des MSAPs par l'injection de signaux est un domaine de recherche actif. Plusieurs techniques ont été proposées. Ces techniques consistent à injecter une tension à haute fréquence (HF) à la tension fondamentale du moteur [8, 11, 24–36]. La position du rotor est ensuite estimée à partir du courant à haute fréquence (HF) grâce à la saillance du rotor. Cette saillance est sous forme géométrique pour les moteurs MSAI, tandis qu'elle est de forme magnétique pour les moteurs MSAS. On trouve une présentation détaillée de l'état de l'art de la méthode de contrôle par injection de signaux dans la section 5.1 du chapitre 5.

Il est important de noter qu'il existe une autre méthode d'estimation de la position en utilisant le courant HF généré par la tension MLI (modulation de largeur d'impulsion) [37]. Cette technique ne nécessite pas l'injection d'une tension supplémentaire. Par contre, elle n'est pas adaptée pour une utilisation industrielle car elle a besoin d'une fréquence d'échantillonnage de courant très élevée (dizaines de KHz).

A basse vitesse et autour de zéro de vitesse, la méthode d'estimation de la position par injection de signaux remplace les méthodes basées sur le modèle fondamental du MSAP. Cette méthode est d'ailleurs considérée comme un bloc de contrôle standard (à basse vitesse) dans les variateurs de vitesse hybrides couvrant la plage complète de fonctionnement de zéro jusqu'à grande vitesse [38–42].

Pour conclure, durant ces dernières années, des variateurs de vitesse des MSAPs qui utilisent l'injection de signaux à basse vitesse pour le contrôle sans capteur ont été proposés par certaines entreprises. Par contre, les applications couvertes par ces variateurs sont limitées. Cette limitation est due aux effets importants de la saturation magnétique. Ainsi, la compensation de ces effets est primordiale pour un bon fonctionnement du MSAP à basse vitesse par l'injection de signaux.

1.3.4 Saturation magnétique

Les effets non linéaires de la saturation magnétique introduisent une grande erreur à la valeur de position estimée à fort couple de charge. Cette erreur cause des pertes énergétiques importantes et réduit la valeur maximale du couple électromagnétique produit par le moteur. En plus, si cette erreur est très élevée, le système du contrôle du moteur peut devenir instable. Ainsi, un algorithme de contrôle sans capteur par injection de signaux n'est ni fiable ni robuste sauf si les effets de la saturation magnétique du MSAP sont modélisés et compensés.

Récemment, la saturation magnétique a été largement étudiée pour les deux principaux types des MSAP (MSAS et MSAI). Plusieurs modèles de saturation ainsi que plusieurs méthodes de compensation de l'erreur de position due à cette saturation ont été proposés dans la littérature [28, 43–63]. Nous proposons une étude bibliographique détaillée de la saturation magnétique du MSAP dans la section 4.3.2 du chapitre 4 et la section 5.1 du chapitre 5.

Les méthodes de compensation de la saturation proposées dans la littérature permettent un bon fonctionnement des MSAPs à basse vitesse. En revanche, ces méthodes nécessitent un processus complexe de calibration et d'implémentation qui n'est pas adapté à une utilisation industrielle. D'autre part, ces méthodes sont heuristiques et ne sont pas toujours basées sur une modélisation physique du moteur. Certaines méthodes ne conviennent que pour un seul type de MSAP, nous n'avons pas trouvé dans la littérature une procédure générale qui peut être utilisé pour tous les types des MSAPs. En plus, ces méthodes ne sont pas basées sur un modèle mathématique général de MSAP; elles sont basées seulement sur des simulations et des tests expérimentaux.

1.4 Contributions

Les contributions de mon travail se résument en ces trois points principaux.

1. Nous proposons une structure originale de modélisation de la saturation magnétique en utilisant une approche énergétique. La formulation d'Euler-Lagrange a été utilisée pour obtenir les équations mathématiques du moteur synchrone à aimants permanents (MSAP) à partir de l'énergie magnétique totale. Nous proposons un modèle paramétrique du MSAP où l'énergie magnétique totale est égale à l'énergie quadratique standard plus des petits termes polynomiaux de troisième et quatrième degré (petites perturbations). Ces termes supplémentaires sont obtenus par développement en série de Taylor de l'énergie du moteur tout en tenant compte des symétries présentes par construction dans le moteur. Ces termes représentent les effets de la saturation magnétique.

   Ce modèle est adapté pour le contrôle car il est assez riche pour représenter la saturation magnétique, et suffisamment simple pour être utilisé en temps réel avec une procédure simple de calibration et d'implémentation pratique. En plus, ce modèle est adapté a tous les types de MSAP (MSAI et MSAS).

2. Nous proposons une analyse claire et originale basée sur la moyennisation de second ordre qui explique comment estimer la position du rotor par l'injection de signaux. Cette analyse est adaptée à toutes les formes de signaux injectés au moteur, et elle convient bien à n'importe quel modèle de saturation magnétique. Cette méthode prend en compte les effets de la saturation magnétique et permet ainsi de réduire les erreurs d'estimation à quelques degrés électriques seulement.

3. Nous démontrons expérimentalement la pertinence de notre approche sur deux types de moteurs: un MSAI et un MSAS qui a un très faible niveau de saillance. Nous montrons la nécessité de considérer la saturation afin d'estimer correctement la position pour bien contrôler ensuite le moteur par injection de signaux.

1.5 Plan de la thèse

Le rapport de thèse est organisé comme suivant.

Chapitre 3 Le but de ce chapitre est de montrer les problèmes d'implémentation pratiques à basse vitesse, et d'expliquer le dispositif expérimental utilisé pour valider le modèle de saturation

magnétique proposé et la procédure d'estimation de la position du rotor. Dans la première section, nous décrivons le fonctionnement du variateur de vitesse du MSAP. Dans les deuxième et troisième sections, nous présentons les problèmes expérimentaux et les contraintes liés au temps réel concernant la génération de la tension du moteur et la mesure du courant. Dans la quatrième section, nous présentons la procédure d'implémentation du banc d'essai.

Chapitre 4 Dans ce chapitre, nous expliquons la formulation énergétique utilisée pour obtenir le modèle de saturation. Dans la première section, nous décrivons la formulation Lagrangienne et Hamiltonienne du MSAP. Ensuite, dans la deuxième section, nous nous concentrons sur le moteur avec connexion en étoile des bobines statoriques et nous considérons les symétries du moteur afin de simplifier l'expression de l'énergie. Dans la troisième section, nous proposons une expression polynomiale paramétrique et simple de l'énergie magnétique du MSAP saturé. Cette énergie est exprimée en terme du flux statorique dans le repère tournant dq. En plus, nous donnons les expressions du courant et du couple électromagnétique. Enfin, dans la quatrième section, nous présentons une analyse de l'observabilité du MSAP à zéro de vitesse.

Chapitre 5 Dans ce chapitre, nous expliquons la procédure proposée d'estimation de la position du MSAP à faible vitesse par l'injection de tensions HF en utilisant le modèle de saturation proposé dans le chapitre 4. Dans la première section, nous résumons l'état de l'art du contrôle de MSAP par injection de signaux où nous nous concentrons sur l'importance de la compensation des effets de la saturation pour bien estimer la position du rotor. Ensuite, dans la deuxième section, nous présentons la séparation des échelles de temps par la moyennisation au second ordre du système du MSAP avec l'injection de signaux. Dans la troisième section, nous proposons une procédure d'estimation de la position du rotor par moindres carrés non linéaires. Finalement, dans la quatrième section, nous proposons un algorithme de commande sans capteur du MSAP basé sur cette méthode d'estimation de position.

Chapitre 6 Dans ce chapitre, nous présentons les résultats de validation expérimentaux. Nous proposons également une méthode simple d'estimation des paramètres de saturation. Cette méthode est basée sur les moindres carrés linéaires. Dans la première section, la procédure d'estimation des paramètres de saturation est détaillée et appliquée à un moteur MSAI et un moteur MSAS. Ensuite, dans la deuxième section, les résultats de tests de validation expérimentaux du modèle proposé du MSAP sont présentés. Dans la troisième section, la procédure d'estimation de la position du rotor est testée et validée sur les deux moteurs MSAI et MSAS. Finalement, dans la quatrième section, la loi de contrôle vectoriel sans capteur proposée au chapitre 5 est appliquée avec succès à ces deux moteurs.

Chapter 2

Introduction

Contents

2.1 Preamble

This thesis work has been done in collaboration with Schneider Electric - Drives entity in Pacy-sur-Eure. The mission statement of this entity is to become the leading global specialist in motor control solutions for a safe, reliable, productive and efficient usage of energy through innovation, simplicity and operational excellence. In this context, this work addresses the problematic of sensorless low speed operation of permanent magnet synchronous motors by signal injection.

The existing industrial offers in the domain of variable speed drive already provide a high level of performance with limitation at low speed depending on drive settings, motor knowledge, operation environment and application. The traditional approach to ensure high performance whatever the operation conditions is to install mechanical sensors on application in particular at low speed. But adding elements in the solution impacts the global robustness and increases the system cost. Herein, we address both existing problematic:

- ensure stable and robust motor operation in the low speed area without a mechanical sensor;

- reach comparable level of performance between operation with sensor and without sensor at low and zero speed.

Today, the challenging approach of sensorless control by signal injection begins to be present in industrial offers. However, there is still a need to optimize the energy consumption and to reinforce the robustness and stability of the motor operation at low speed without a mechanical sensor. It is also important to simplify the customer interface by simplifying the drive configuration. For these reasons, this approach remains a very active field of industrial and academic research area.

The research leading to the presented results has received funding also from Schneider Electric. All the tests and experiences were performed in the research and development laboratory of this company, in Pacy-sur-Eure.

2.2 PMSM motor

A permanent magnet synchronous motor (PMSM) is an electromechanical device which transforms electrical energy into mechanical energy by using electromagnetic fields. This mechanical energy produces a rotational motion and a mechanical torque.

A three phase PMSM is composed of two main parts. A fixed part called stator and composed of three phase windings. A rotating part called rotor and formed by a permanent magnet. The stator and rotor have cylindrical shape where the rotor is covered by the stator. They are separated by a small air gap.

The principle of operation of PMSM is described in [1,2]- [3, p.261]. Briefly, the stator phases are connected to a sinusoidal three phase voltage source. The superposition of the three magnetic fluxes created by the three phase windings of the stator produces a sinusoidal flux rotating at the frequency of the voltage source. This rotating magnetic flux interacts with the rotor flux in the air gap separating the stator from the rotor and creates an electromagnetic force leading to the rotation of the rotor. The value of the motor speed corresponds then to the frequency of the motor voltage.

There are two main types of PMSMs: the surface mounted permanent magnet motor also called SPM which has attached magnets to the surface of the rotor; the interior permanent magnet motor also called IPM which has buried magnets inside the rotor. An IPM motor has stronger mechanical strength than SPM because the magnets of SPM need to be fixed on the surface of the rotor. From magnetic point of view, the SPM rotor is symmetric while the IPM rotor is asymmetric. Hence, the SPM stator inductances do not vary with the rotor position [4]. By contrast, the IPM inductances values change according to the rotor position [5] and create a geometric saliency which is an important feature for low speed control.

2.2.1 Applications

Nowadays, electric motors are widely used. According to [6], more than 60% of the electricity is used to run electric machines. The PMSM is an important type of electric motor which is increasingly used in the recent years. The main features of a PMSM motor are its high power and torque density, low energy consumption (high power factor) and good dynamic behavior. Thus, PMSM are replacing asynchronous motors in many types of applications. Besides, the fast development of power electronics components and the fast increasing of signal processing speed are also behind the increase use of these motors.

PMSMs are used in multiple applications as electric vehicles and washing machines (which need high power density). They are also used for high precision devices as electric printer, manufacture tools, high precision medical equipment (medical pumps, blowers and compressors) and many other domains.

2.2.2 Electric drive

In general, an electric drive is used to control electric motors and in particular PMSMs. It is a power electronic device which generates a variable frequency and variable amplitude voltage using a voltage source with fixed frequency and amplitude. There are many advantages of using an electric drive rather than plugging the motor directly into a fixed frequency and amplitude voltage source. Indeed, an electric drive is used to vary the motor speed and to save the electric energy where 50% of the energy consumed by the motor can be reduced.

Many industrial companies offer variable speed drive to control the PMSM speed. This is an important and very profitable market where the worldwide sales reach up to several billions of euros per year. Schneider Electric is one of the worldwide market leader in this domain, the most important other companies are Toshiba, ABB, Danfoss, Mitsubishi, Yaskawa, Fuji, GE, Siemens, ...

2.3 Sensorless low speed control

There are several methods of PMSM speed control by an electric drive. They are distinguished by:

- the type of the speed control law: scalar control [7] law or model based control law [8];
- the mode of operation: closed loop mode [9] (with an angle sensor) or sensorless mode [10] (without a rotor position sensor);
- the operation speed range: low speed range [11] or medium to high speed range [12].

Nowadays, the challenge is the sensorless PMSM drive operation at low speed. This is an important industrial concern and it can make the difference between industrial competitor companies. In addition, this is an interesting scientific research topic where we have a theoretical problem of observability at low speed.

In the sequel, we present briefly the existing speed control laws. Then, we detail the sensorless low speed control by signal injection. Finally, we focus on magnetic and cross coupling saturation compensation which is the main concern of our work.

2.3.1 Scalar control

This type is also called constant volt per hertz control (V/f) which is a fully open loop [7]. The ratio of the input motor voltage to the input frequency is chosen constant and equal to the value of the magnetic flux. The scalar control has the advantages of simplicity and low cost and it does not require the rotor position information. By contrast, this method does not take into account the motor dynamics. Thus, it is not suitable for applications needing fast dynamic operation and it cannot be used at low speed. In addition, this method leads to high energy losses.

2.3.2 Model based control

To get better performances in dynamic operation and less energy consumption, we must take into account the motor dynamic model which is composed from voltage and speed differential equations. In this case, the motor control algorithm is based on the motor equations (model based control). We find in the literature multiple types of model based control: direct torque control (DTC) [13]; sliding mode control [14, 15]; and vector control [6, p.230]. All these methods require the rotor position information in order to be operational.

The rotor position value can be obtained by one of the following two methods:

- by using a mechanical position sensor as incremental encoder or hall sensor; this is the closed loop operation mode;
- by estimating the rotor angle information from the measured currents; this is the sensorless operation mode.

2.3.2.1 Closed loop control

The closed loop control technique has the advantage of simple implementation because the rotor position is directly obtained from the position sensor without the need of additional computation to estimate the rotor angle. By contrast, for multiple applications, the presence of a position sensor has multiple disadvantages:

- the sensor is subjected to high mechanical solicitations because it is mounted at the shaft of the motor. For example, it turns at the mechanical speed of the motor which can be very high; in addition it must run under high accelerations and torques. Furthermore, the mechanical vibrations of the motor shaft disturb the operation of the sensor. All these effects reduce the lifetime of the sensor and can even cause its damage;
- the position sensor is located in the motor environment which can be hostile to the sensor because of high motor temperature and other undesired effects related to the application;
- a cable is needed to connect the sensor to the motor drive, this cable can introduce noises to the measured position signal in particular when the motor is located far from the drive. In addition, the presence of the cable can require additional space which it is not suitable for some applications. When the cable disturbance noises are important, the position information can be lost which reduces the reliability of the control system;
- the sensor generates high frequency digital signal (with frequency reaching several thousands of the motor speed); this digital signal needs special processing and conditioning hardware (encoder board) which must be connected to the drive;
- the position sensor and the conditioning board are expensive for several applications.

To avoid these drawbacks of position sensors, the sensorless operation mode is used. In the sequel, the vector control algorithm is used. It consists of regulating the motor speed by controlling the instantaneous position of the stator flux vector [6, p.230].

2.3.2.2 Sensorless vector control at medium and high speed

In sensorless vector control, the position sensor is replaced by a position observer using electric variables measurements. The simplest sensorless vector control algorithm is the estimation of the position by estimating the induced back electromotive force voltage denoted BEMF [10, 16–18]. Indeed, the rotation of the permanent magnet flux of the rotor creates an induced BEMF vector orthogonal to this magnet flux vector. Hence, the rotor position can be obtained directly by estimating this BEMF vector.

In real time operation, the estimation of the position from the BEMF is done using a state observer combined with a speed controller. This control strategy is called fundamental excitation method because it does not require any additional signal. We find in the literature several methods of PMSM fundamental excitation control:

- the standard method consists of controlling the motor current using a proportional integral (PI) kind controller where the BEMF voltages are estimated from the outputs of the PI integrators. Then, the position is estimated from the BEMF using a Phase Looked Loop (PLL) estimator [10, 17].

- the second method consists of using Extended Kalman Filer (EKF) to estimate the rotor position from the BEMF [16, 18].

These methods have good performances in medium to high speed range; many industrial inverters based on the fundamental excitation methods give satisfactory results.

However, the magnitude of BEMF voltage is proportional to the rotor speed. Thus, at very low speed operation (below 5% of the rated speed) and near the standstill position (zero speed), the BEMF voltage magnitude is very small and it is zero when the speed is zero. Hence, the fundamental excitation techniques are not suitable for low and zero speed operation. This can be explained to the well known lack of observability at zero speed when the stator currents are the only measured variables [19–21].

2.3.3 Signal injection

To solve the observability problem at low speed, we must add a persistent excitation signal to the motor voltage. This is independent from the type of the speed control method: DTC [22]; sliding mode control [23]; and vector control [24].

During the last two decades, the sensorless PMSM control at low speed by signal injection was an active field of research. Several techniques were proposed. They consist of superposing a persistent excitation to the motor fundamental voltage by injecting a high frequency (HF) signal [8, 11, 24–36]. The rotor position is estimated from the HF current using the rotor saliency, whether geometric for IPM motors or induced by main flux saturation for SPM motors. A more detailed state of the art about signal injection is presented in section 5.1 of chapter 5.

We note that there is an alternative method of position estimation from the HF current generated by the pulse width modulation (PWM) motor voltage [37]. This technique does not require the injection of an additional voltage. But it is not suitable for industrial use because it needs a high current sampling frequency (in order of tenth of KHz).

At low and zero speed, position estimation by signal injection substitutes the fundamental model based strategy for sensorless PMSM control. It is moreover considered as a standard building block in hybrid control schemes for complete drives operating from zero to full speed [38–42].

To conclude, PMSM electric drives with signal injection for low speed sensorless control was proposed by some industrial companies in the last years. But for instance the applications covered by these drives are limited. The reason of this limitation is the important effects of magnetic and cross saturations. The compensation of these effects is paramount for low speed operation by signal injection of PMSM.

2.3.4 Magnetic saturation

Due to magnetic saturation, a position error is added to the estimated rotor position at high load torque. This error causes important energy losses and reduces the maximum electromagnetic torque that can be produced by the motor. Besides, if this error is high then the system may be unstable. Therefore, if we want a reliable and robust sensorless control algorithm with high energy efficiency at low speed, then the magnetic and cross saturation of PMSM must be modeled and compensated.

Recently, magnetic saturation have been widely studied for the two main types of PMSM motors IPM and SPM. Many PMSM saturation models and position error compensation methods based on these models were proposed [28,43–63]. For more information about saturation, a more detailed literature study of the PMSM magnetic saturation is proposed in section 4.3.2 of chapter 4 and section 5.1 of chapter 5.

The compensation strategies of saturation proposed in the literature lead to good motor operation performances when used for sensorless position estimation and low speed control. By contrast, they need a complicated commissioning process which is not suitable for industrial use. Furthermore, these methods are heuristic and they are not always based on a physical modeling of the motor. Some methods are suitable only for one type of PMSM, we do not find in the literature a general procedure which can be used for all PMSM types. In addition, these methods are not based on a general mathematical model of PMSM but they are based only on simulations or experimental tests.

2.4 Contributions

The contributions of this work can be summarized by three main points.

1. We propose an original way of modeling magnetic saturation using an energy approach. The Euler-Lagrange formulation was used to derive the mathematical equations of the PMSM from the total magnetic energy. We propose a parametric perturbation model of PMSM where the total magnetic energy is the sum of the standard quadratic energy and small polynomial perturbation terms of third and fourth degree. These additional terms are obtained by finite expansion of the motor energy and by considering the motor construction symmetries. They represent the magnetic saturation effects.

   This model is adapted to control purposes where it is rich enough to capture magnetic and cross-saturation but also simple enough to be used in real-time and to be easily identified in practice. In addition, this model can be used for any type of PMSM motors (IPM and SPM motors).

2. We propose a clear and original analysis based on second-order averaging of how to recover the position information from signal injection. This analysis can accommodate to any form of injected signals, and blends well with any magnetic saturation model. This method takes into account the effects of magnetic and cross saturations and reduces the estimation errors to few electrical degree only.

3. We demonstrate experimentally the relevance of our approach on two kinds of motors: an IPM motor and a SPM having a very small level of saliency. We show the necessity of considering saturation to correctly estimate the position and to control the motor with signal injection.

2.5 Outline

The thesis report is organized as follows.

Chapter 3: Experimental protocols and issues The goal of this chapter is to show the practical implementation issues at low speed operation, and to explain the experimental setup used to validate the proposed saturation model and the position estimation procedure. In the first section we describe the operation of the PMSM electric drive. In the second and third sections we present experimental issues and real time constraints related to motor voltage generation and stator current measurement mainly at low speed operation. In the fourth section, we present the implementation procedure of the experimental test bench.

Chapter 4: Energy-based modeling of the PMSM In this chapter we explain the energy formulation used to get the saturation model. In the first section we describe Euler-Lagrange and Hamiltonian energy formulation of PMSM. In the second section we focus on PMSM with star connection type and we consider motor symmetries to simplify the energy expression. In the third section we propose a simple parametric polynomial expression of magnetic energy of the saturated PMSM in terms of the stator fluxes in the rotating dq frame. In addition, we derive the expressions of the currents and electromagnetic torque. Finally, in the fourth section we present an observability analysis of the PMSM at zero speed.

Chapter 5: Position estimation by signal injection and averaging In this chapter we explain the proposed position estimation procedure of PMSM at low speed by HF voltage injection using the saturation model proposed in chapter 4. In the first section we give an overview of the state of the art of PMSM control by signal injection where we focus on the importance of the compensation of saturation effects to correctly estimate the rotor position. In the second section we present time scale separation by second order averaging of PMSM with signal injection. In the third section we propose a rotor position estimation procedure of PMSM using nonlinear least square. In the fourth section we propose a sensorless control scheme based on this position estimation method.

Chapter 6: Parameter identification and experimental validation In this chapter we present experimental validation results. We propose also a simple method of saturation parameters estimation based on linear least square. In the first section, the procedure of saturation parameters estimation is detailed and applied to an IPM motor and a SPM motor. In the second section, some experimental validation tests of the proposed PMSM model are presented. In the third

section the position estimation procedure is tested and validated using the IPM and SPM motors. In the fourth section the proposed sensorless control law of chapter 5 is successfully applied to these motors.

2.6 Publications

Part of the work described in this thesis was published:

- A. Jebai, F. Malrait, P. Martin, and P. Rouchon: Estimation of saturation of permanent-magnet synchronous motors through an energy-based model. IEEE International Electric Machines Drives Conference, 2011, Niagara Falls, Canada [64].
- A. Jebai, F. Malrait, P. Martin, and P. Rouchon: Sensorless position estimation of permanent magnet synchronous motors using a nonlinear magnetic saturation model. IEEE International Conference on Electrical Machines ICEM, 2012, Marseille, France [65].
- A. Jebai, F. Malrait, P. Martin, and P. Rouchon: Signal injection and averaging for position estimation of permanent-magnet synchronous motors. IEEE International Conference on Decision and Control CDC,2012, Hawaï, USA [66].
- D. Basic, A. Jebai, F. Malrait, P. Martin, and P. Rouchon: Using Hamiltonians to model saturation in space vector representations of AC electrical machines. Lecture Notes in Control and Information Sciences, vol. 407, pp. 41-48, 2010 [67].
- A. Jebai, F. Malrait, P. Martin, and P. Rouchon: Control method implemented in a power converter and intended for identifying parameters linked to the magnetic saturation of an electric motor. Patent no. WO2012123255.

An experiment is a question which science poses to Nature and a measurement is the recording of Nature's answer.

MAX PLANCK

Chapter 3

Experimental protocols and issues

Contents

Introduction

Dans ce chapitre, nous décrivons en détail le fonctionnement du variateur de vitesse du MSAP ainsi que les procédures utilisées pour implémenter expérimentalement les lois de contrôle de ce moteur. Nous discutons également les problématiques expérimentales de génération de la tension et de mesure du courant ainsi que les contraintes du contrôle en temps réel.

Un variateur de vitesse est composé de deux parties principales: un étage de puissance et un contrôleur qui se compose essentiellement d'un processeur. La fig. 3.1 illustre la composition d'un variateur de vitesse. Le principe de fonctionnement se résume par : en utilisant la vitesse de référence fournie par l'utilisateur et les courants statoriques mesurés, le processeur commande l'étage de puissance afin de produire la tension nécessaire pour contrôler le moteur à la vitesse de référence désirée. Les tensions physiques du moteur sont ensuite générées par l'étage de puissance en utilisant la technique de modulation de largeur d'impulsion (MLI).

Dans la première section, nous expliquons la procédure de génération de la tension en utilisant les signaux MLI. Ensuite, dans la deuxième section, nous discutons les problématiques pratiques de

génération des tensions comme le temps mort et les chutes de pont au niveau des semi-conducteurs. Dans la troisième section, nous expliquons les procédures utilisées pour la mesure et le filtrage du courant. Enfin, dans la quatrième section, nous expliquons l'implémentation pratique du contrôleur numérique et nous décrivons les logiciels et le matériel utilisés pour générer les signaux de commande du moteur.

In this chapter we describe in details the operation of the PMSM drive and the procedures used herein for experimental motor control law implementation. We discuss also experimental issues of voltage generation and current measurement and controller real time constraints.

An electric drive is composed of two main parts: a power stage and a control stage which is composed mainly of a processor. Fig. 3.1 illustrates the composition of a drive. The principle of operation is as follows. Using the reference speed provided by the user and the measured stator currents, the processor commands the power stage to generate the voltage needed to control the PMSM at the desired speed. The motor voltages are generated by the power stage using pulse width modulation technique (PWM).

In the first section we explain the voltage generation procedure using PWM signals. Then, in the second section we discuss practical issues of voltage generation as the inverter dead time and the voltage drop across the semiconductor devices. In the third section we explain the current measurement and filtering procedures. Finally, in the fourth section we discuss the digital implementation of the controller; and we describe the software and hardware used to generate control signals.

3.1 Voltage generation

The motor voltage is the output of the power stage. The power stage is a power electronic device connected to a three phase electric line voltage source. It is an electric power conversion system and it is composed of three distinct sub-systems:

- an AC/DC converter which transforms the AC line voltage to a DC voltage. It is composed

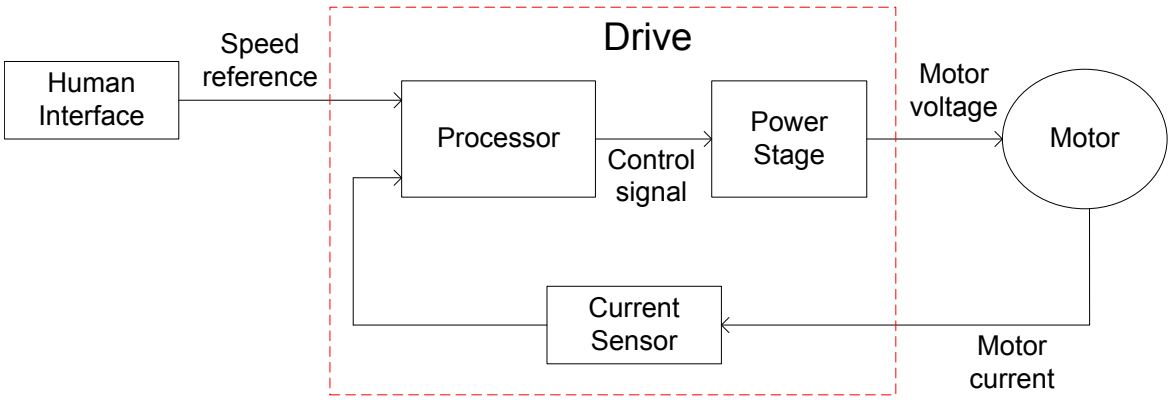

Figure 3.1: Illustration of motor and drive operation.

from passive or active components. The main types of AC/DC converters are diode bridge rectifier (passive); mixed bridge rectifier (passive); bridge inverter (active);

- a DC/DC link which provides the inverter by the DC voltage of the AC/DC converter. The main types of DC/DC are DC capacitor (passive); DC choke (also passive) and electronic smooth inductance (active);

- a DC/AC inverter which transforms the DC voltage into a three phase voltage having variable frequency and variable amplitude.

Fig. 3.2 illustrates the power stage of a drive.

In this work, we focus on the operation of the inverter because it generates the motor voltage. We suppose that the input DC voltage of the inverter is constant.

3.1.1 Inverter operation

The bridge inverter is built of three IGBT transistors legs. Each leg is composed from two transistors with a freewheeling diode each, and drives one of the three phases of the motor. The freewheeling diode is necessary to pass the current in a phase which has been turned off but whose winding still

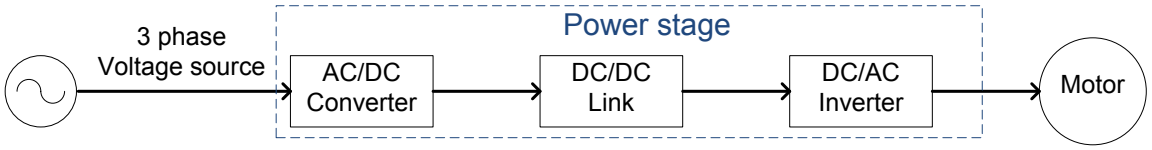

Figure 3.2: Power stage of a drive.

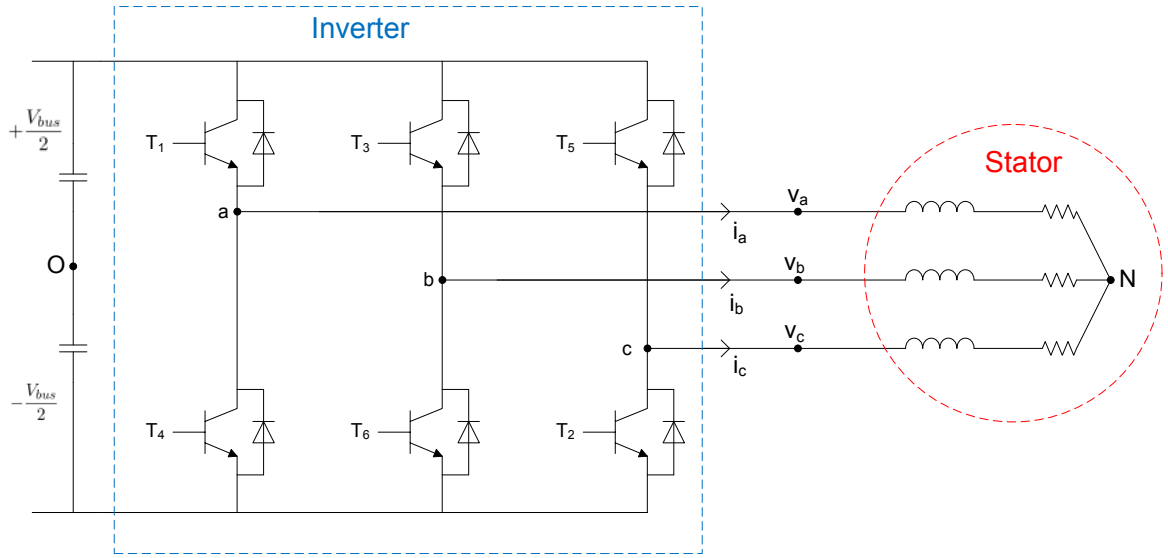

Figure 3.3: A three phase bridge inverter.

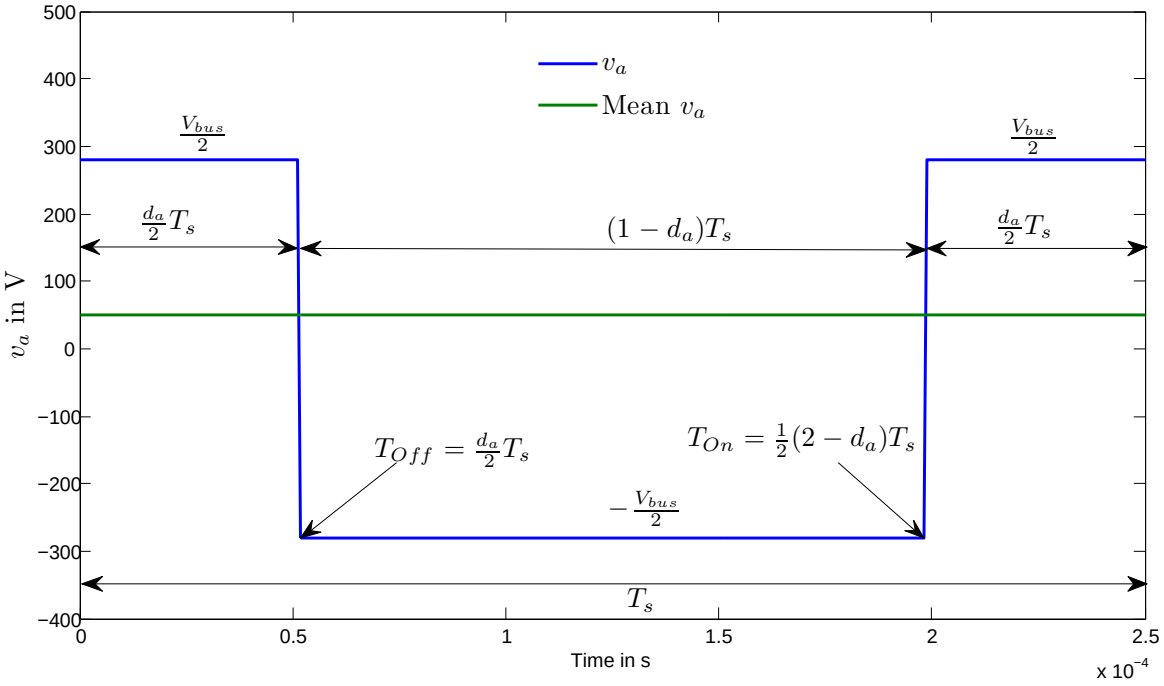

Figure 3.4: A PWM pulse with $T_s = 250\mu s$, $v_a = 50\ V$ and $V_{bus} = 560\ V$.

contains a magnetic field. The diode will conduct as long as there is a current flowing. Fig. 3.3 illustrates a three phase bridge inverter connected to a PMSM stator.

The controller board enables one transistor and blocks the other in each leg of the inverter. The two transistors in one leg cannot be enabled simultaneously in order to prevent short circuit. The controller board modulates the state of the transistors in function of the desired voltage. It is important to note that the motor star point N is not accessible, hence we apply electric potentials to the motor instead of voltages.

The general expressions of the fundamental potentials applied to the motor are

$$\begin{aligned} v_a(t) &= V_m(t)\cos\theta_c(t) \\ v_b(t) &= V_m(t)\cos\left(\theta_c(t) + \frac{2\pi}{3}\right) \\ v_c(t) &= V_m(t)\cos\left(\theta_c(t) + \frac{4\pi}{3}\right) \end{aligned}$$

with

$$\frac{d}{dt}\theta_c(t) = 2\pi f_c(t)$$

where $v_a(t)$, $v_b(t)$ and $v_c(t)$ are the input motor electric potentials; $V_m(t)$ is the instantaneous potential amplitude; $f_c(t)$ is the instantaneous voltage frequency and $\theta_c(t)$ is the instantaneous potential phase. Each electric potential is generated by one inverter leg; see fig. 3.3.

This is a two level inverter where we have only two possible values of electric potentials: $+\frac{V_{bus}}{2}$ when the upper leg transistor is on and $-\frac{V_{bus}}{2}$ when the lower transistor is on (for simplification we

suppose that the potential of the inverter midpoint O is zero $v_O = 0$). The potential of each motor phase is generated using only these two levels. This can be done using a high frequency modulation technique.

3.1.2 Three phase PWM

The PWM signals are used to generate the motor potentials. Each electric potential is modulated by the width of a rectangular pulse. The PWM modulation technique is used because it involves much less power losses than other modulation techniques. In addition, the frequency of the PWM signal is much higher than the instantaneous frequency f_c of the sinusoidal stator potentials. The PWM signal can be used also to generate any type of stator potentials having a frequency smaller than the half of the PWM frequency.

The sampled symmetric low centered PMW modulation type is used here [3, p.494]. The desired potential for each phase is sampled at a constant frequency f_s called PWM frequency. Then, at each time period $T_s = \frac{1}{f_s}$ an electric potential pulse is generated and applied to the motor; the average of this pulse over the time period T_s is equal to the value of the sampled potential in this period. The three pulses corresponding to v_a, v_b and v_c are generated simultaneously.

Fig. 3.4 shows the shape of a pulse corresponding to one period of time T_s of the electric potential v_a where $0 \leq d_a \leq 1$ is called the duty cycle; $T_{Off} = \frac{1}{2} d_a T_s$ is the switching instant when the upper transistor is turned off and $T_{On} = \frac{1}{2}(2 - d_a)T_s$ is the switching instant when the upper transistor is turned on. The duty cycle d_a is the fraction of the period T_s where the upper transistor is on and the output potential is $\frac{V_{bus}}{2}$; during the remaining $1 - d_a$ fraction of T_s the output potential is $-\frac{V_{bus}}{2}$. The value of d_a is set such that the average value of the output potential v_a over one period T_s is equal to the desired potential.

Fig. 3.6 illustrates the principle of operation of one inverter leg which corresponds to the electric potential generated in the figure 3.4. Fig. 3.6 (left) shows the configuration of the first inverter leg when the upper transistor is conducting; in this case the motor voltage is $+\frac{V_{bus}}{2}$ and the motor current flows through the upper branch of this leg. In opposite, fig. 3.6 (right) shows the configuration of the first inverter leg when the lower transistor is conducting; in this case the motor voltage is $-\frac{V_{bus}}{2}$ and the motor current flows through the lower branch of this leg. The variables T_1 and T_4 are boolean complementary variables where $T_4 = \overline{T}_1$; these variables are generated by the digital controller board. The variables T_3, T_4, T_5 and T_6 are also boolean variables generated by the controller board where $T_6 = \overline{T}_3$ and $T_2 = \overline{T}_5$.

The potential expression for one phase during a time $[0, T_s[$ period can be written as follows

$$v_a(t) = \begin{cases} +\dfrac{V_{bus}}{2} & \text{if} \quad 0 \leq t < T_{Off} \\ -\dfrac{V_{bus}}{2} & \text{if} \quad T_{Off} \leq t < T_{On} \\ +\dfrac{V_{bus}}{2} & \text{if} \quad T_{On} \leq t < T_s \end{cases}$$

The electric potential pulse is centered around the middle of the period $\frac{T_s}{2}$. The average value of v_a is

$$\frac{1}{T_s} \int_0^{T_s} v_a(\tau) d\tau = \frac{1}{2}\big(2d_a - 1\big)V_{bus}, \tag{3.1}$$

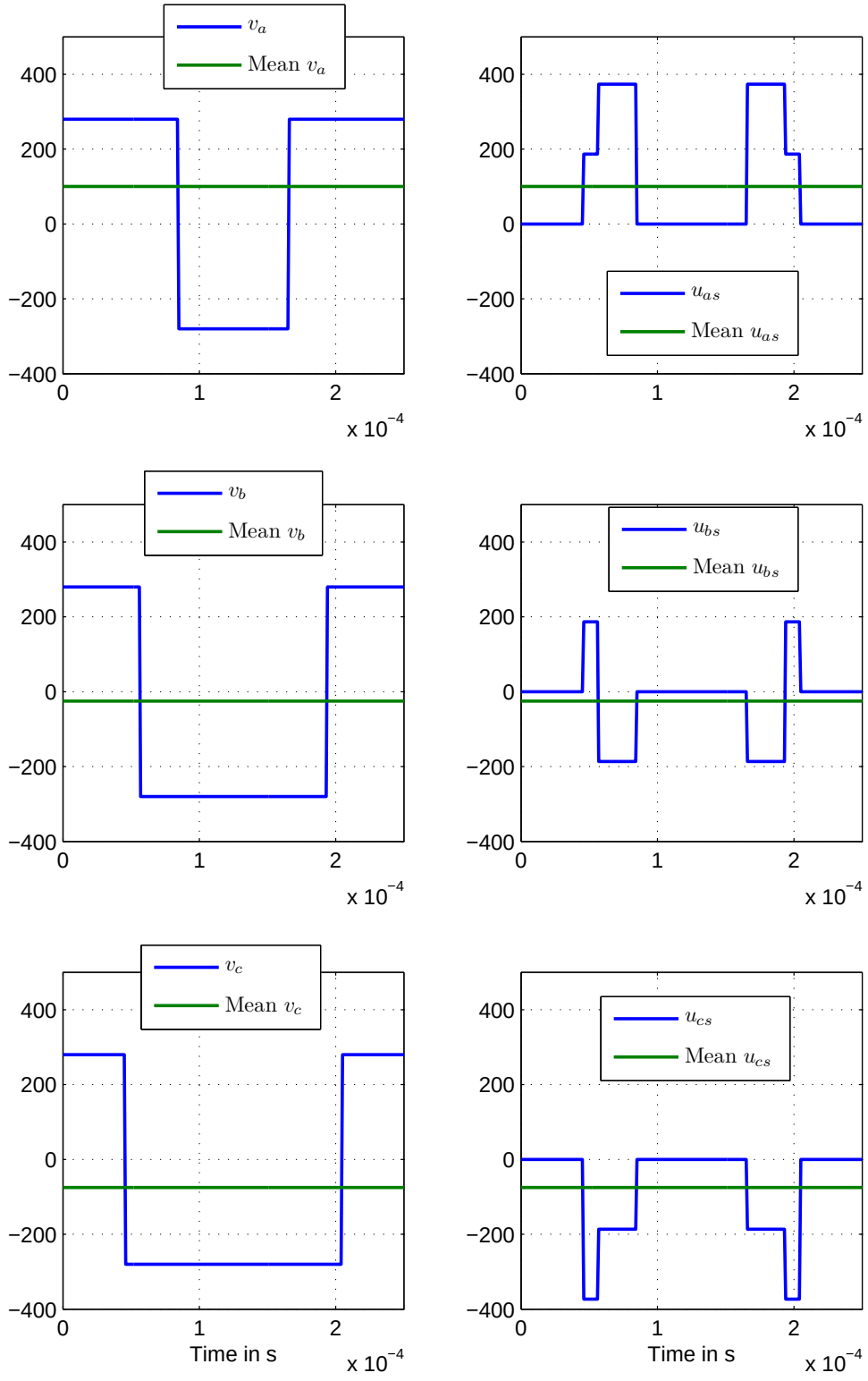

Figure 3.5: Three phase potentials and voltages in V: potentials of the inverter output (left); winding voltages between the inverter output and the motor star point N (right).

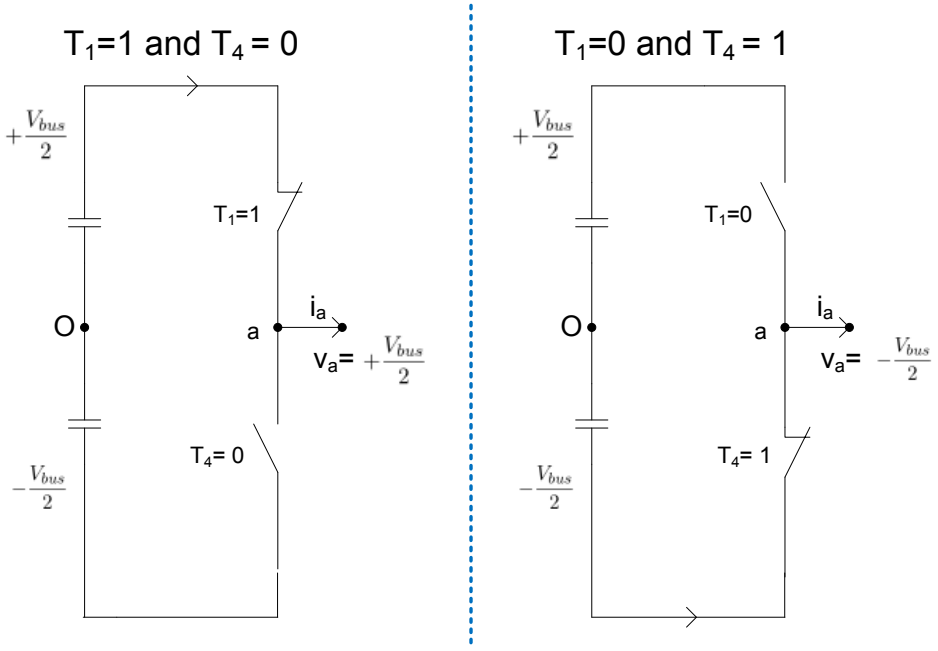

Figure 3.6: Operation of one inverter leg: the upper transistor is conducting (left); the lower transistor is conducting (right).

hence the average of v_a is proportional to the duty cycle d_a. Therefore, by varying d_a from 0 (the upper transistor is turned off during a complete period) to 1 (the upper transistor is turned on during a complete period), the electric potential can be varied from $-\frac{V_{bus}}{2}$ to $+\frac{V_{bus}}{2}$.

The frequency of the PWM signal is much higher than the motor bandwidth. The motor inductances act like a filter, where the high frequency components of the PWM signal are filtered and only the fundamental frequency components which correspond to the modulated signal are seen by the motor. Thus, v_a can be approximated by its average over one period T_s, hence (3.1) leads to

$$v_a = \frac{1}{2}(2d_a - 1)V_{bus}$$

and

$$d_a = \frac{1}{2} + \frac{v_a}{V_{bus}}, \tag{3.2}$$

therefore the duty cycle is obtained from the desired voltage using (3.2). We note that $d_a = \frac{1}{2}$ corresponds to $v_a = 0$ which mean that the electric potential is equal to $+\frac{V_{bus}}{2}$ over one a half period and it is equal to $-\frac{V_{bus}}{2}$ over the other half period. The electric potentials v_b and v_c are generated in the same way as v_a using two duty cycles defined by

$$d_b = \frac{1}{2} + \frac{v_b}{V_{bus}}, \quad d_c = \frac{1}{2} + \frac{v_c}{V_{bus}}.$$

The electric potentials v_a, v_b and v_c are the potentials of the points a, b and c with respect to bus voltage midpoint O. The winding voltages (difference of potentials) across the three motor windings read

$$(u_a = v_a - v_N, u_b = v_b - v_N, u_c = v_c - v_N).$$

For symmetric PMSM with linear magnetics and star connection, the sum of the winding voltages is zero. Thus the star point potential is

$$v_N = \frac{1}{3}(v_a + v_b + v_c),$$

and the motor voltages can be written as

$$\begin{pmatrix} u_a \\ u_b \\ u_c \end{pmatrix} = \frac{1}{3}\begin{pmatrix} 2 & -1 & -1 \\ -1 & 2 & -1 \\ -1 & -1 & 2 \end{pmatrix}\begin{pmatrix} v_a \\ v_b \\ v_c \end{pmatrix}.$$

By contrast, in the case of PMSM with magnetic saturation, the sum of the three winding voltages is not zero due to saturation effects. In section 4.2.1 of chapter 5, we show that the homopolar voltage $(u_a + u_b + u_c)$ does not have an impact on the motor operation. For simplification, we replace the voltages (u_a,u_b,u_c) by (u_{as},u_{bs},u_{cs}) such that $u_{as} + u_{bs} + u_{cs} = 0$. The voltages u_{as}, u_{bs} and u_{cs} are obtained by the projection of the three dimensional vector (u_a,u_b,u_c) on the plane defined by $u_{as} + u_{bs} + u_{cs} = 0$ as follows

$$\begin{pmatrix} u_{as} \\ u_{bs} \\ u_{cs} \end{pmatrix} = \frac{1}{3}\begin{pmatrix} 2 & -1 & -1 \\ -1 & 2 & -1 \\ -1 & -1 & 2 \end{pmatrix}\begin{pmatrix} u_a \\ u_b \\ u_c \end{pmatrix} = \frac{1}{3}\begin{pmatrix} 2 & -1 & -1 \\ -1 & 2 & -1 \\ -1 & -1 & 2 \end{pmatrix}\begin{pmatrix} v_a \\ v_b \\ v_c \end{pmatrix}.$$

Fig. 3.5 shows the potentials (v_a, v_b ,v_c) (left) and the stator voltages (u_{as}, u_{bs}, u_{cs}) (right) corresponding to a three phase PWM modulation.

3.1.2.1 PWM generation

The generation of a PWM signal is not an easy task. Indeed, as explained before the period of a PWM signal is very small with respect to the motor bandwidth; a typical value of T_s is 250 μs. The state of a transistor changes twice during one PWM period T_s. The switching instants are proportional to the desired voltage value which can take any possible value between zero and T_s. To get acceptable performances, the switching time precision must be in the order of 1 μs which mean that the computation frequency must be in the order of one megahertz.

To reach this precision at real time, the desired duty cycle is compared at real time to a triangular signal which increases from zero to one at the first half of the PWM period and decreases from one to zero at the second half of the PWM period. If the duty cycle is greater than the triangular signal then the upper transistor is turned on otherwise it is turned off. This type of signal modulation is called sine-triangle modulation. Fig. 3.7 illustrates the generation procedure of the PWM signal. Fig. 3.8 shows a PWM signal of frequency 500 Hz used to generate a sinusoidal voltage with frequency 50 Hz.

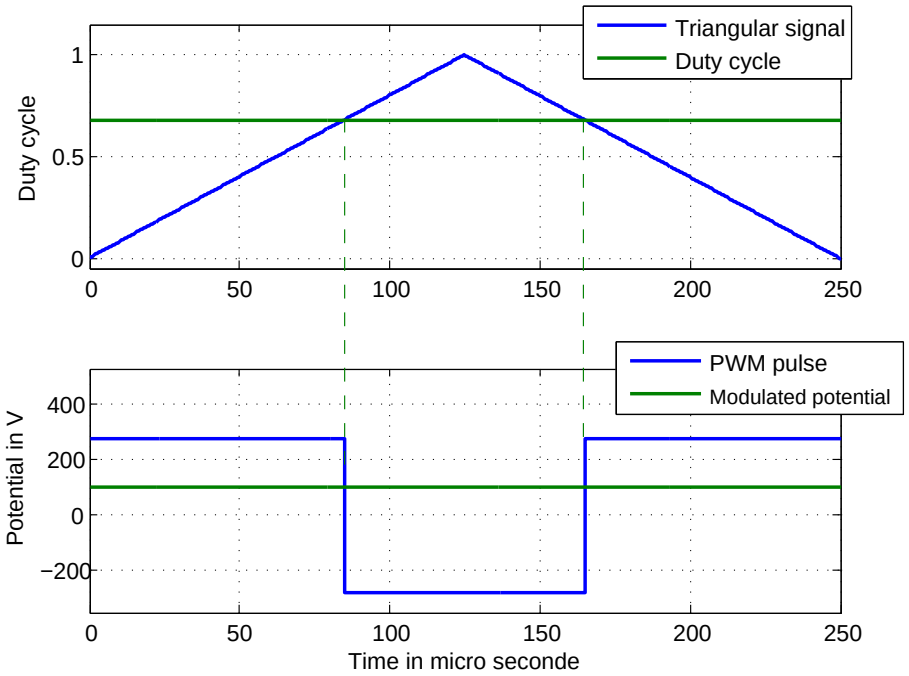

Figure 3.7: Generation of a PWM pulse by comparing the desired electric potential to a triangular signal.

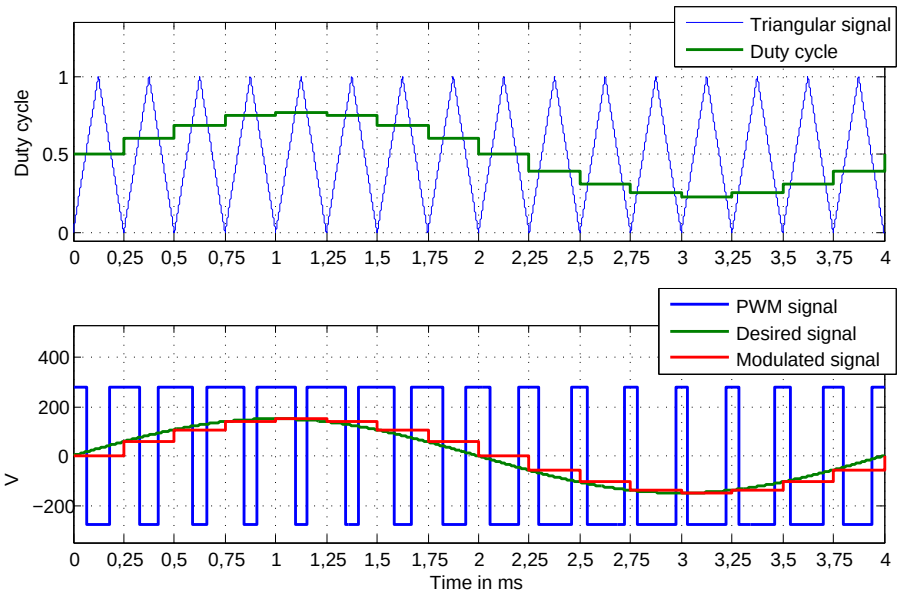

Figure 3.8: Modulation of a $50\ Hz$ sinusoidal signal using PWM signals.

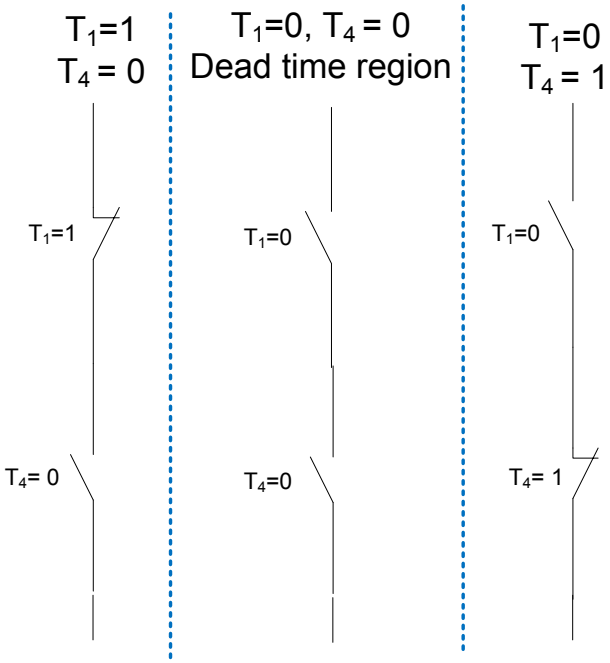

Figure 3.9: Dead time principle.

3.2 Drive nonlinear effects

3.2.1 Dead time

In the previous subsection, we explained the generation of a PWM signal. For each phase, either the upper transistor is conducting or the lower transistor is conducting. We supposed before that the switching between the two states of the transistor is instantaneous. However, in practice there is a small switching time which must be considered. Indeed, the upper and lower transistor must not be conducting at the same time to avoid the short circuit of the DC converter output.

Thus, at every commutation of a transistor, a small switching time (dead time) is added in order to secure the system; during this time the two transistors of one inverter leg are not conducting. This dead time introduces errors on the mean value of the voltage. In addition, after the transistor switching, the output transistor voltage needs a settling time to reach the input voltage (either the bus voltage when the transistor is switched on or zero voltage when the transistor is switched off). This settling time also introduces errors on the average output voltage. These errors caused by the dead time must be compensated [68, 69] to apply the desired voltage to the motor.

Fig.3.9 illustrates the principle of introducing a dead time when the two transistors of one inverter leg are switching simultaneously. Fig. 3.10 shows the transistor command signals T_1 and T_4 of the first inverter leg over a complete PWM period when a dead time is added.

The dead time introduces errors to the motor voltage and it must be compensated to get acceptable performances mainly at low speed operation where the motor voltage are small comparing to the dead time voltage errors. The compensation of these voltage errors is not easy; it can be done by software or hardware ways. In the drive used in the experimental test bench, these errors were compensated

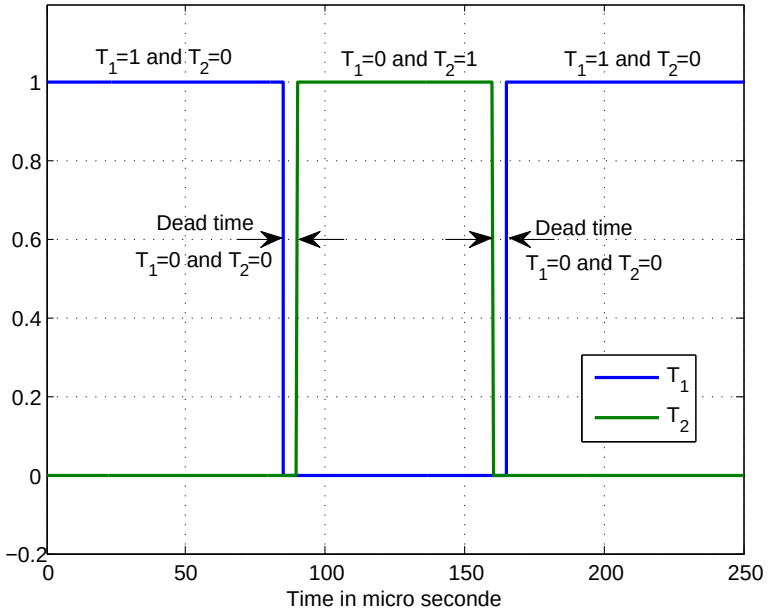

Figure 3.10: Transistor command signals taking into account a small dead time.

using a special hardware compensation procedure of dead time.

3.2.2 Voltage drop

We supposed that the voltage drop across a semiconductor device is zero. But in practice a small voltage drop of the semiconductor device occurs depending on the current. This voltage drop can reach up to 3 V and it has nonlinear characteristics. In practice, this voltage drop is the difference between the instantaneous desired electric potential and the actual applied potential to the motor [70, 71].

To clarify this effect, we consider all possible configurations of voltages and currents of one inverter leg. The upper and lower transistors of one leg are commanded to ON or OFF state. Depending on the current direction, we have four possible configurations as follows:

- the upper transistor is on and the current is positive, in this case the current flows into the upper transistor and the voltage drop is $-v_p$ where v_p is the voltage loss across the transistor. Hence, the output potential is $v_a = v_{as} - v_p$ where v_{as} is the input potential of the semiconductor device; see fig. 3.11-(a).

- the upper transistor is on and the current is negative; in this case the current flows into the upper freewheeling diode and the voltage drop is $+v_p$ where v_p is also the voltage loss across the diode (for simplification reasons we consider that the voltage drop across a transistor and a diode are the same). Hence, the output potential is $v_a = v_{as} + v_p$; see fig. 3.11-(b).

- the lower transistor is on and the current is negative; in this case the current flows into the lower transistor and the voltage drop is $+v_p$. Hence, the output potential is $v_a = v_{as} + v_p$; see

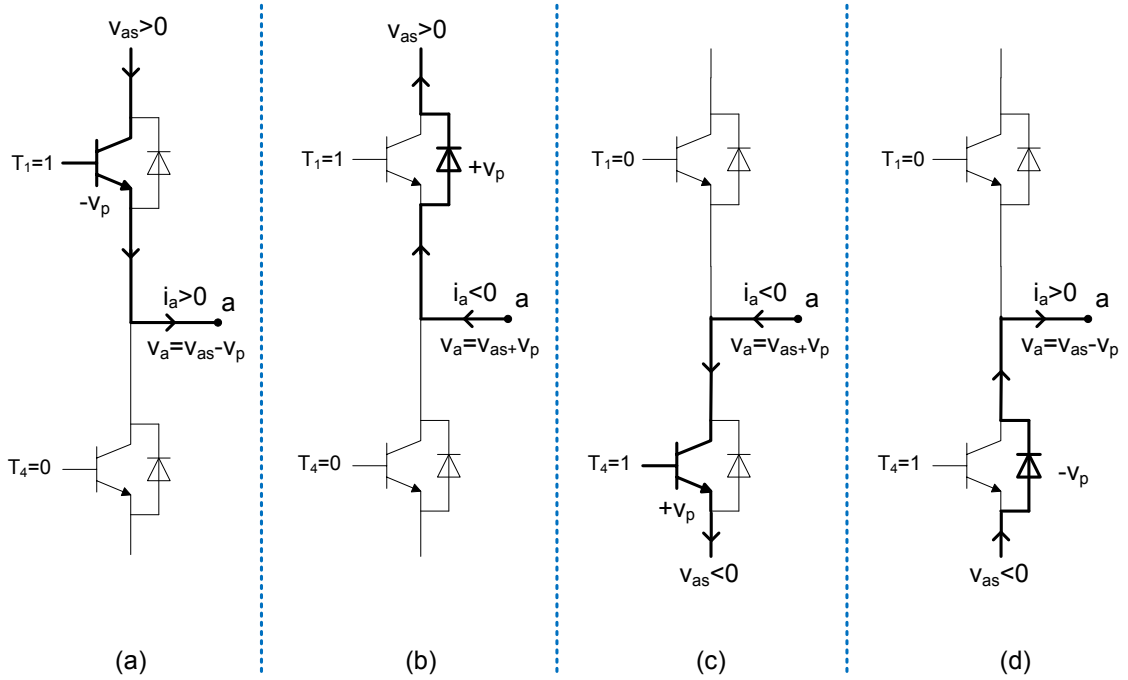

Figure 3.11: Voltage drop across the semiconductor device: (a) $v_{as} > 0$ and $i_a > 0$; (b) $v_{as} > 0$ and $i_a < 0$; (c) $v_{as} < 0$ and $i_a < 0$; (d) $v_{as} < 0$ and $i_a > 0$.

fig. 3.11-(c).

- the lower transistor is on and the current is positive; in this case the current flows into the lower freewheeling diode and the voltage drop is $-v_p$. Hence, the output potential is $v_a = v_{as} - v_p$; see fig. 3.11-(d).

Therefore, the potential v_a can be written as

$$v_a = v_{as} - v_p sign(i_a)$$

where v_{as} is the desired input value and $sign$ is the sign function. The expressions of voltages v_b and v_c are similar to v_a; they can be written as follows

$$v_b = v_{bs} - v_p sign(i_b)$$
$$v_c = v_{cs} - v_p sign(i_c)$$

where v_{bs} and v_{cs} are the desired values of the potentials v_a and v_b respectively.

The voltage v_p is not constant but it varies in terms of the current value and the semiconductor type and temperature. In the most of cases v_p is between $0.7\ V$ and $3\ V$. Thus, this voltage must be compensated in real time to get the desired electric potentials. To compensate this voltage drop, v_p is taken constant such $v_p = 1.8\ V$ and the voltage drop is anticipated by adding to the motor reference

potentials the voltage drop v_p multiplied by the sign of the measured currents as follows

$$\begin{pmatrix} v_{as} \\ v_{bs} \\ v_{cs} \end{pmatrix} = \begin{pmatrix} v_a^{ref} \\ v_b^{ref} \\ v_c^{ref} \end{pmatrix} + v_p \begin{pmatrix} sign(i_a) \\ sign(i_b) \\ sign(i_c) \end{pmatrix}$$

where v_a^{ref}, v_b^{ref} and v_c^{ref} are the desired reference motor potentials; $v_p = 1.8\ V$. If a phase current is small and near zero value, then it is difficult to estimate its sign. In this case, we use the following approximation of the sign function

$$sign(x) = \begin{cases} +1 & \text{if} \quad x > x_t \\ \dfrac{x}{x_t} & \text{if} \quad |x| < x_t \\ -1 & \text{if} \quad x < -x_t \end{cases}$$

where x_t is a small threshold current value; typically $x_t = 100\ mA$.

Finally, even if the semiconductor voltage drops are small, their compensation is crucial at low speed to generate small potentials in the order of some volts where the voltage drop can be up to $3\ V$. For example, consider a motor with a resistance $R = 1.5\ \Omega$ and rated current of $I_n = 4.5\ A$, at zero speed and steady state the current is the ratio of the voltage to the resistance. Thus, a non compensated voltage drop of $v_p = 3\ V$ can generate an undesired current of $2\ A$ which represents 44% of the rated current I_n. Even if the voltage drop is compensated, it difficult to know its real value because it varies according to the working point; this makes the motor control at zero speed a very difficult task.

In this section we discussed the nonlinear behavior of the voltage generated by the motor drive. We focused on dead time and voltage drop, but there are other effects as zero current clamping and semiconductor capacitance which make it difficult to generate the exact desired voltage. These effects can be neglected at high speed where the motor voltage is high; but at low speed they must be considered and sometime they are inevitable. This motivates our work to find a robust control strategy of the PMSM. As we discussed in chapter 2, the controller is based on high frequency voltage injection where the nonlinear inverter effects have a small impact on this type of voltage.

3.3 Current measurement

In this section we describe the measurement procedure of the current generated by the PWM voltage and the extraction of the current fundamental component. The motor current is measured to be used in speed control and position estimation of PMSM. Three sensors are used to measure the PMSM three phase current. These sensors are calibrated offline. Each sensor generates an analog output voltage signal proportional to the measured current value.

Then, the analog current information (the output signal of the current sensor) is converted to a digital signal by an Analog to Digital Converter ADC. After that, the digital current information is sampled and it is used as an input to the digital discrete controller.

The measured current contains high frequency components caused by the PWM modulation and transistor switching current. These HF components must be filtered to get the actual motor current. For this reason, the current sampling frequency is equal to the PWM frequency. In addition, the

sampling time of the current is synchronized with the end of the PWM period. Indeed, at this time the three voltages across the motor phases are zero and the transistors are not in the switching phase; see fig 3.5–3.12. Therefore, the current HF components are not present and hence they are filtered automatically.

Another reason for synchronizing sampling of current is to get the actual current response to the applied voltage. In fact, at the end of the PWM pulse, the mean value of the voltage applied to the motor during this pulse is equal to the desired voltage value.

Fig. 3.12 shows the measured values of the PWM voltages u_{as}, u_{bs} and u_{cs}, and the measured current i_a. The PWM frequency is $f_s = 4\ KHz$ and the PWM period is $T_s = \frac{1}{f_s} = 250\mu s$; the current and voltage are measured using an oscilloscope with a high sampling frequency of $10\ MHz$ (2500 measurement points per PWM period). This figure shows that the motor voltages are zero at the beginning, in the middle and at the end of the PWM pulse where there is no transistor switching. At these moments, the current is stabilized and it does not contain high frequency components. High frequency current components occur only near the switching time of the transistors. The current value increases from $i_a = -6.973\ A$ at $t = 0.1\mu s$ (beginning of the PWM pulse) to $i_a = -6.8\ A$ at $t = 125\ \mu s$ (middle of the PWM pulse) to $i_a = -6.698\ A$ at $t = 250\ \mu s$ (end of the PWM pulse). We note that if the current is not correctly sampled, then we get an aliasing problem and the sampled current will be different from the fundamental motor current.

Fig. 3.13 illustrates an experimental example of the generation of a symmetric sinusoidal three phase voltages using PWM modulation with carrier frequency $f_s = 4\ KHz$. The sinusoidal voltage frequency is $5\ Hz$ and its amplitude is $50\ V$. Fig. 3.13-(c) shows the measured current i_a without synchronized sampling, in this figure the high frequency current components are not filtered. Fig. 3.13-(d) shows the measured current with synchronized sampling; it is clear in this figure that the high frequency components are eliminated thanks to the sampling procedure.

Pulsating high frequency current

As explained in the previous chapter, a high frequency signal must be added to the motor voltage for low speed control. This voltage is generated also using PWM modulation. Fig. 3.14 shows an example of the PWM signal used to generate a sinusoidal voltage of frequency $5\ Hz$ plus a rectangular pulsating voltage of frequency $500\ Hz$ using a PWM carrier of $4\ kHz$. This figure shows the shape of the current which is the sum of a sinusoidal current plus a triangular component of frequency $500\ Hz$.

Fig 3.15 shows one period ($2\ ms$) of the rectangular signal. Fig 3.15-(c) and fig 3.15-(d) illustrate the synchronized current sampling procedure where we clearly see that the PWM high frequency components are filtered by synchronizing the sampling time to the end of the PWM pulse. It is clear in this figure that there is only 8 point per period of the injected signal. Due to the limited number of samples per period, we add a rectangular signal instead of sinusoidal signal because the rectangular signal is constant during the half of its period while the sinusoidal signal varies at each time step and 8 points are insufficient to generate it.

The motor mechanical variables are also measured. The electromagnetic torque is measured by a torquemeter and it is transmitted to the controller by an ADC converter. The position is measured using an incremental encoder which generates 1024 digital pulses per mechanical motor revolution. This digital signal needs a high processing frequency; thus a FPGA unit is used to count these pulses at real time. Then, the FPGA transmits the position information to the controller. The speed is

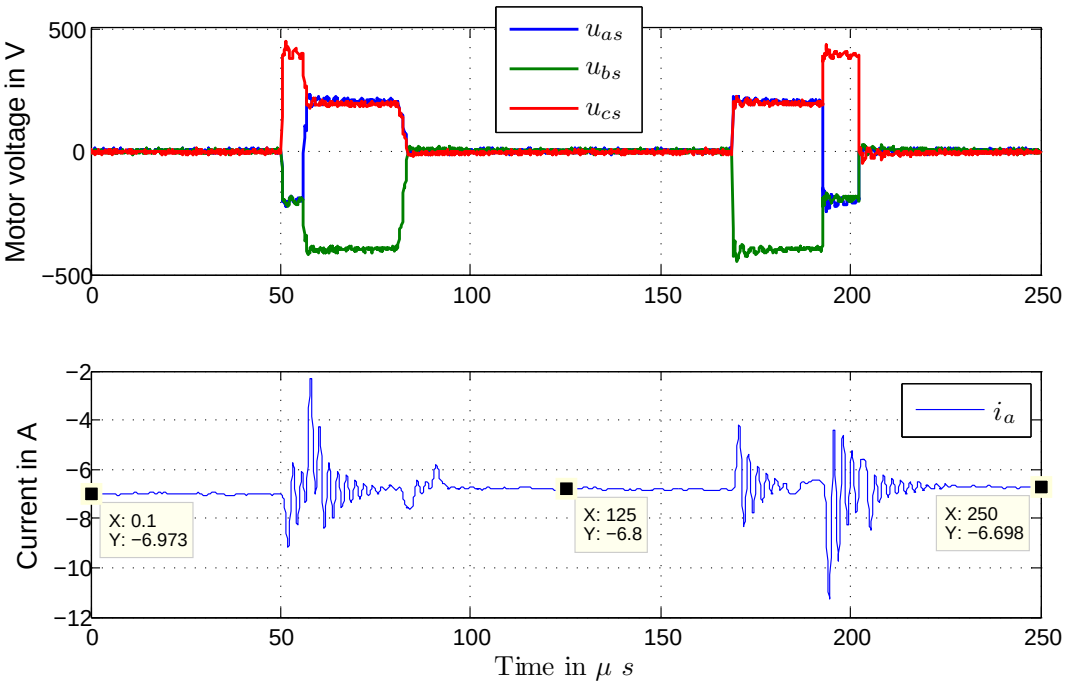

Figure 3.12: Experimental measurements: three phase motor voltages u_{as}, u_{bs} and u_{cs} for one PWM pulse (top); motor current i_a with sampling frequency of 10 MHz (bottom) .

calculated by numerical integration of the measured position.

In sensorless control (without mechanical sensor), only the measured values of the three phase currents are used. The torque, speed and position are measured to monitor the motor operation and to validate the control law by comparing the measured and estimated mechanical variables.

3.4 Practical implementation

In the previous section we explained the motor input voltage generation and the current measurement procedure. In this section we present the software and hardware setup used to concept and implement the motor digital controller. This is not an easy task due to real time requirements and constraints and to the small sampling time.

The inputs of the control system are the measured motor currents and the reference speed. The control system outputs are the PWM switching signals (T_1 to T_6) which commands the inverter to get the desired voltage; see fig. 3.1. In the sequel we describe the controller implementation.

3.4.1 Control hardware

The dSPACE AC Motor Control Solution is used to perform PMSM control. This solution is composed of three boards: a processor board; a FPGA board and an I/O board. They are connected together via a special data connection bus called PHS bus. Fig. 3.16 illustrates the connection of these three boards with a PMSM and a bridge inverter.

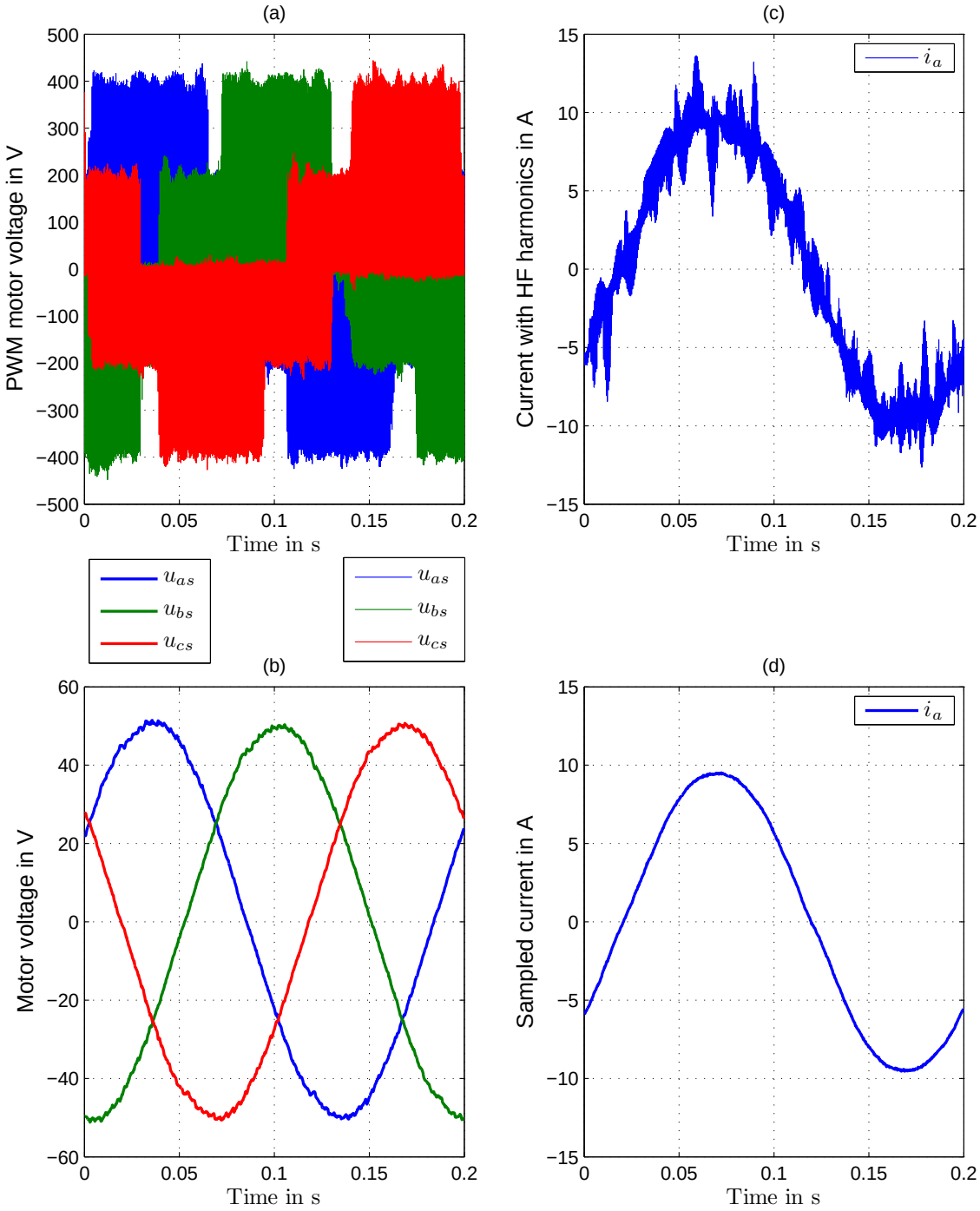

Figure 3.13: Experimental measurements of symmetric sinusoidal three phase PWM voltages; the voltage frequency is $5\ Hz$ and the voltage amplitude is $50\ V$: (a) Three phase PWM voltages u_{as}, u_{bs} and u_{cs} with high frequency components; (b) Fundamental component of u_{as}, u_{bs} and u_{cs}; (c) Phase a current i_a with PWM high frequency components; (d) Fundamental component of i_a obtained by synchronized sampling time with the end of the PWM pulse.

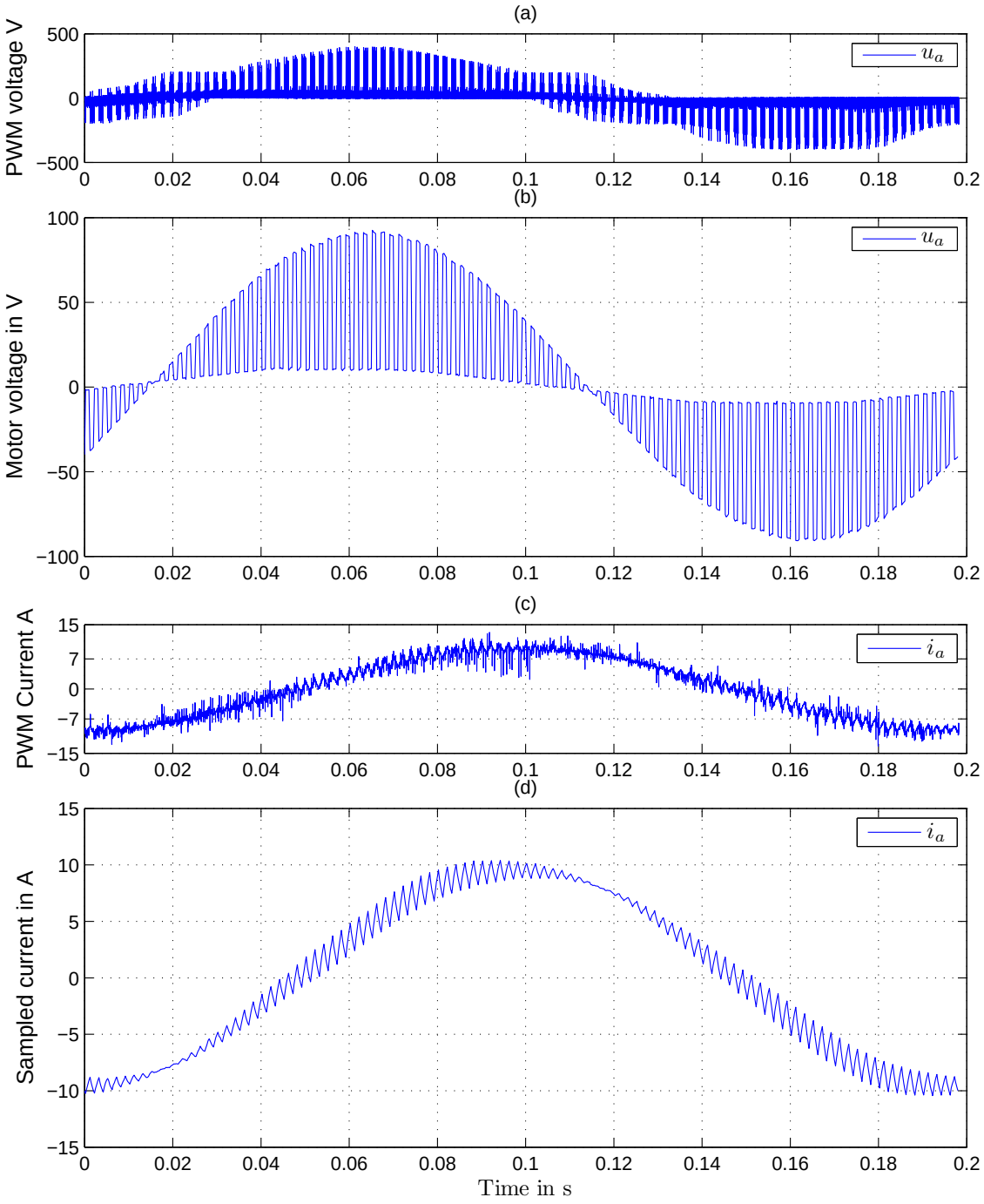

Figure 3.14: Experimental measurements of a rectangular signal of frequency $500\ Hz$ plus a sinusoidal signal of $5\ Hz$ modulated by a PWM signal of frequency $4\ KHz$: (a) PWM voltage u_{as}; (b) Fundamental component of u_{as}; (c) Phase a current i_a with PWM high frequency components; (d) Fundamental component of i_a obtained by synchronized sampling time with the end of the PWM pulse.

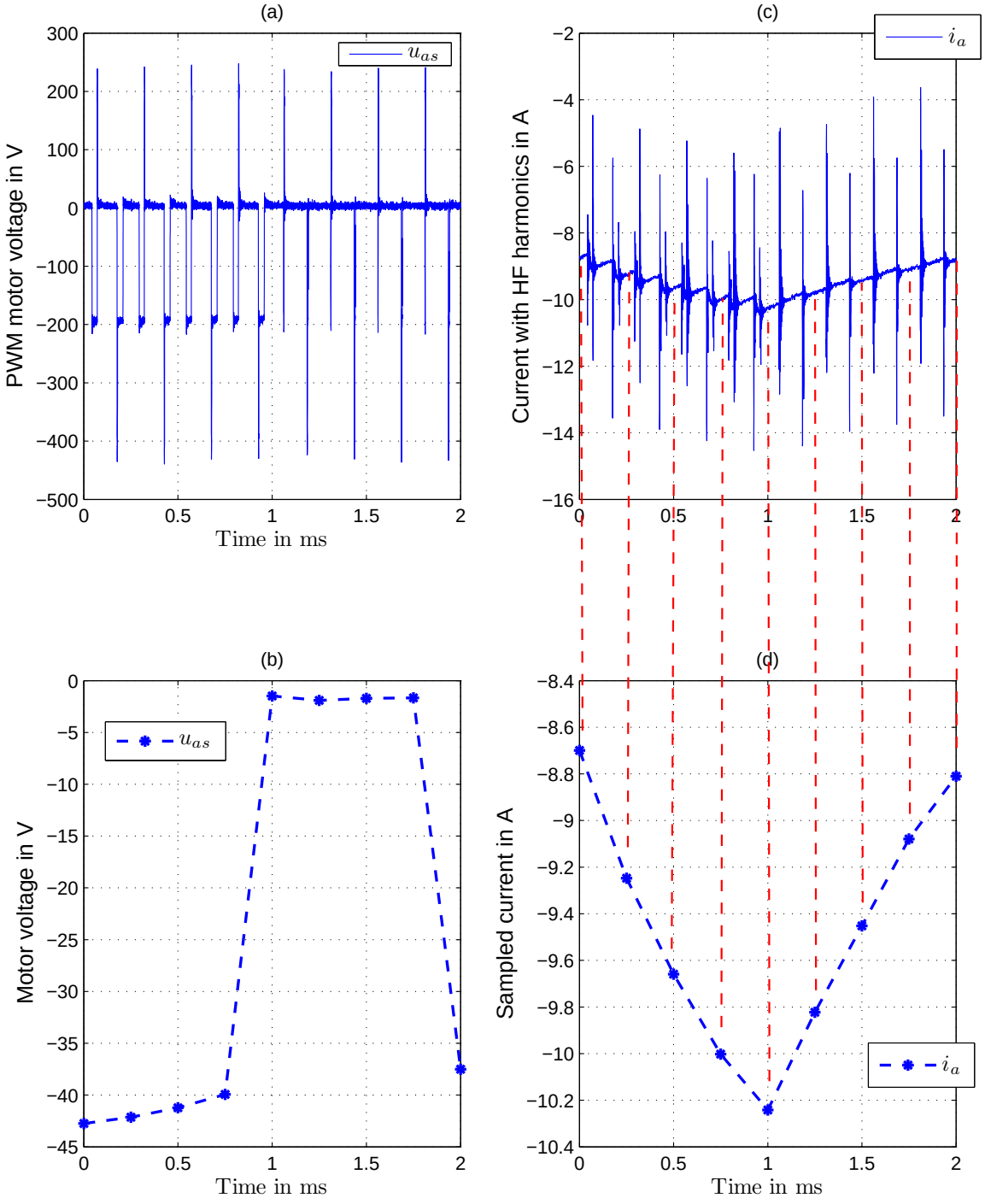

Figure 3.15: Experimental measurements of one period 2 ms of the signal shown in fig. 3.14: (a) PWM voltage u_{as}; (b) Fundamental component of u_{as}; (c) Phase a current i_a with PWM high frequency components; (d) Fundamental component of i_a obtained by synchronized sampling time with the end of the PWM pulse.

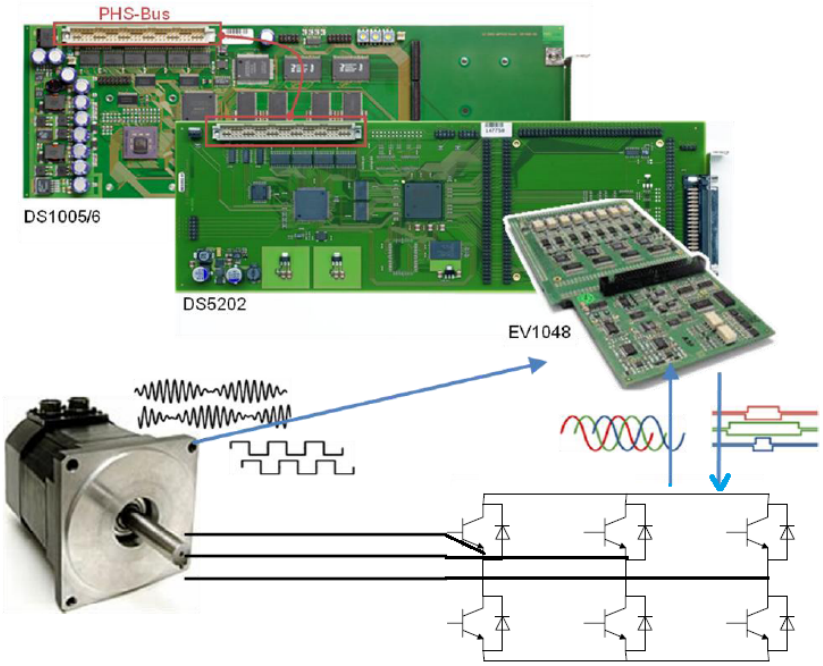

Figure 3.16: Processor, FPGA and input and output boards with a motor and a bridge inverter. This figure is get from dSpace 2011 catalog.

The control program is executed at real time is the processor DS1005 board. This board includes a PowerPC (PPC) 750GX processor running at 1 GHz. The FPGA DS5202 board performs the following tasks

- processing and counting of the incremental encoder pulses used to measure the motor position;
- generation of the three digital PWM command signals (T_1 to T_6) of the transistors gates;
- processing and sampling of the measured currents and torque; this include the synchronization of the current sampling time with the end of the PWM pulse.

The FPGA unit communicates with the processor via the data bus. It transmits to the processor the measured signals and receives from the processor the duty cycles needed to generate the PWM signals. The FPGA unit is a programmable electronic device which allows fast processing and generation of signals with high sampling and PWM frequencies up to 80 kHz. It reduces the processor computations load and allows fast execution of the control program. Furthermore, the digital signal processing and PWM generation in FPGA hardware guarantee an efficient implementation with extremely low latency. It is important to note that the FPGA is independent from the processor and it has its own digital clock.

The I/O EV1048 board is the interface between the FPGA board and the motor and the sensors. All the controller input signals (currents, incremental encoder, torque) and the controller output signals (digital PWM signals) are conditioned by this board. It contains also the ADC converters needed for analog signals measurement.

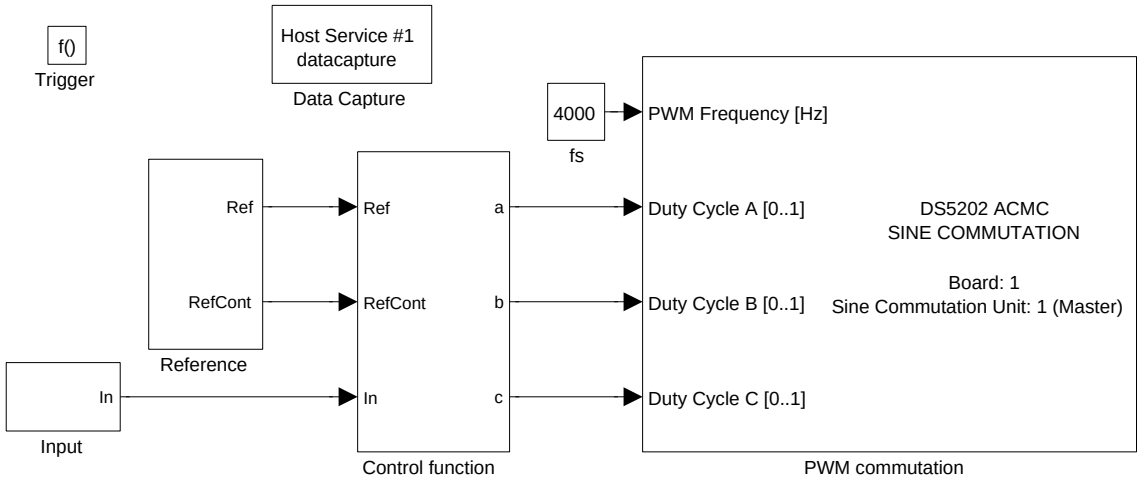

Figure 3.17: Simulink model of the control program.

3.4.2 Control program

The control program is designed using the Simulink software. Control executable code is generated using Matlab Real-Time Workshop (RTW). Then, this code is downloaded to the dSpace processor using the dSpace Real-Time Interface (RTI). The control program is developed using a standard computer with the standard operating system Windows XP. The user computer is connected to the processor via an optical fiber which allows fast data transmission between them. The optical fiber links a PCI card denoted DS817 (plugged into the user computer) to a connection card denoted DS814 (connected to the processor via the data PHS bus).

The control program is designed using standard Simulink blocks and a special library provided by dSpace called ACMC library which contains virtual blocks representing the link between the controller and I/O hardware. Fig. 3.17 shows the general Simulink model of the control program. This model is composed of four main blocks or subsystems:

- input subsystem (**Input**) : it contains all digital values of measured data; at real time program execution, this part of the model transmits these values from the FPGA unit to the processor unit where the program is executed (data acquisition); these data are needed to solve controller equations;

- reference data subsystem (**Reference**): it contains reference data provided by the user via a Human Machine Interface installed on the user computer called dSapce ControlDesk; these data are communicated to the processor during real time operation via the optical fiber connection; the reference data are composed of the desired speed reference and the controller parameters;

- control function (**Control function**): the controller equations are implemented in this subsystem; these equations are discretized using Euler discretization scheme. This subsystem calculates the values of the three PWM duty cycles at real time operation in terms of the input and reference data and internal controller states. This is the main part of the motor control program and it is executed inside the processor;

- PWM generator block (**PWM commutation**): it calculates the three PWM duty cycles from the command voltages.

In addition, the data capture bloc is used to read the motor data at real time and the trigger bloc is used for synchronization sampling.

Fig. 3.18 shows the architecture of the control function implemented in the "**Control function**" block which is the most important part of the control program.

3.4.2.1 HMI interface

The communication between the controller and the user is performed using a Human Machine Interface (HMI) program called dSpace ControlDesk. This program allows the interaction with the processor at real time using the optical fiber link. Using ControlDesk, the control parameters can be modified during real time operation and the evolution of the motor variables can be visualized at real time also. Fig. 3.19 shows a screen shot of this program during motor operation. At the end of each motor test, all data logs recorded during this test are transferred to the user computer using ControlDesk.

3.4.2.2 Test bench

Fig. 3.20 illustrates the test bench used for experimental tests which is composed of the user computer, the dSpace boards, the inverter, the load machine, the PMSM, the current sensors, the torque sensor and the incremental position encoder sensor. Fig. 3.21 shows a zoom on the motor and the $4\ kW$ DC load machine used to generate a mechanical load torque. Fig. 3.22 shows a zoom on the electric inverter used in the experimental tests.

3.4.3 Real time synchronization

The control program runs inside the processor using the processor clock. The PWM signals are generated using the FPGA clock. During the operation time, a small drift between the two clocks (two independent clock are never identical) will be accumulated leading to the loss of synchronism. Though, the duty cycles calculated by the processor must be communicated to the FPGA unit before the end of the PWM pulse. Otherwise, the desired voltage will not be applied to the motor and the controller and the PWM signals will be no more synchronized. This problem can be solved by using a hardware interrupt. A trigger signal is generated at the end of each PWM signal to synchronize the control program and the PWM pulse.

Fig. 3.23 shows the principle of the PWM synchronization. In fact, at the end of a PWM pulse, a trigger signal is generated by the FPGA board to activate the control program which guarantees the synchronization between them. The composition the subsystem "**Speed controller**" are shown in fig 3.17. Another advantage of this hardware trigger signal is that it allows the synchronized current sampling with the PWM interrupt as described in section 3.3.

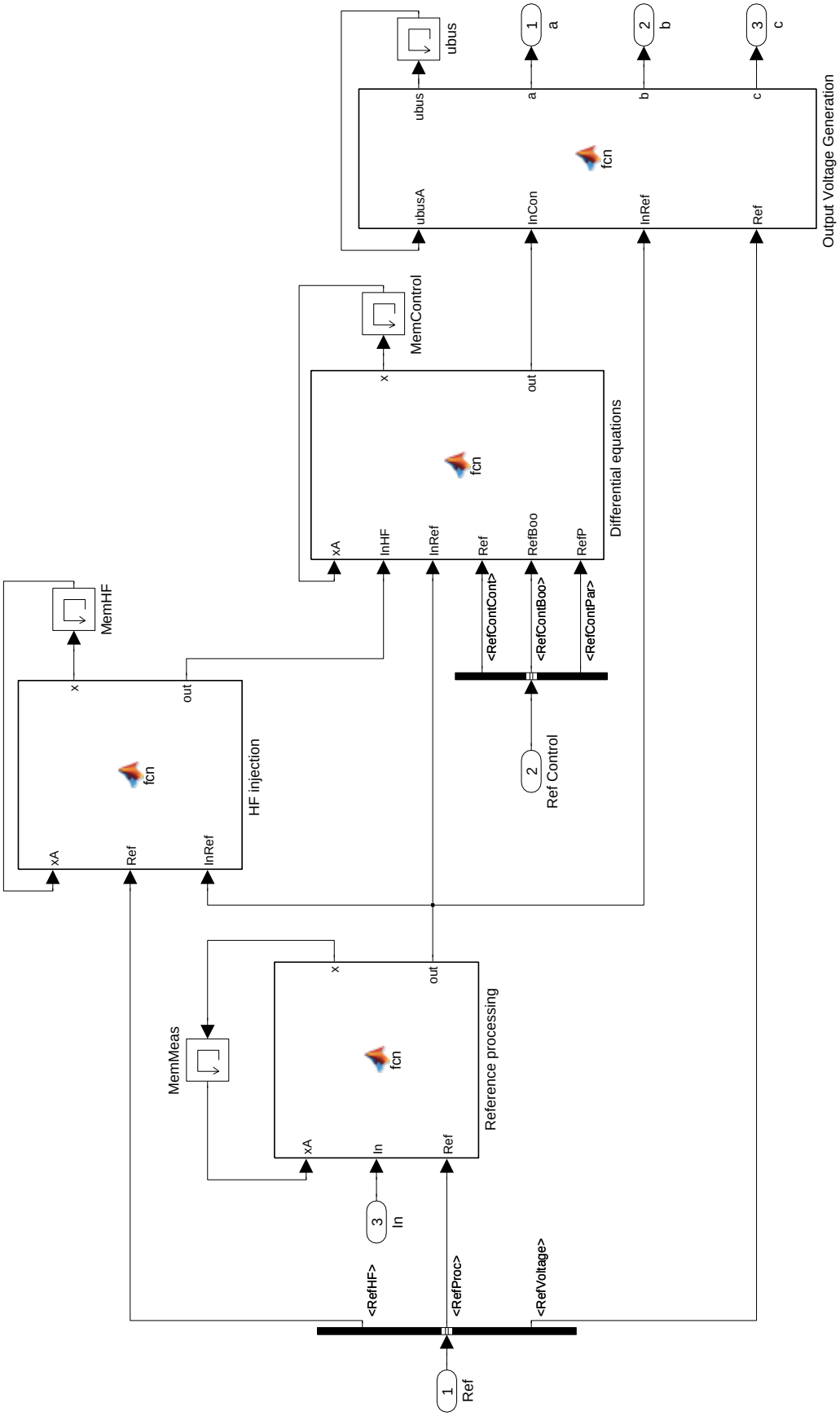

Figure 3.18: Block diagram of the control function.

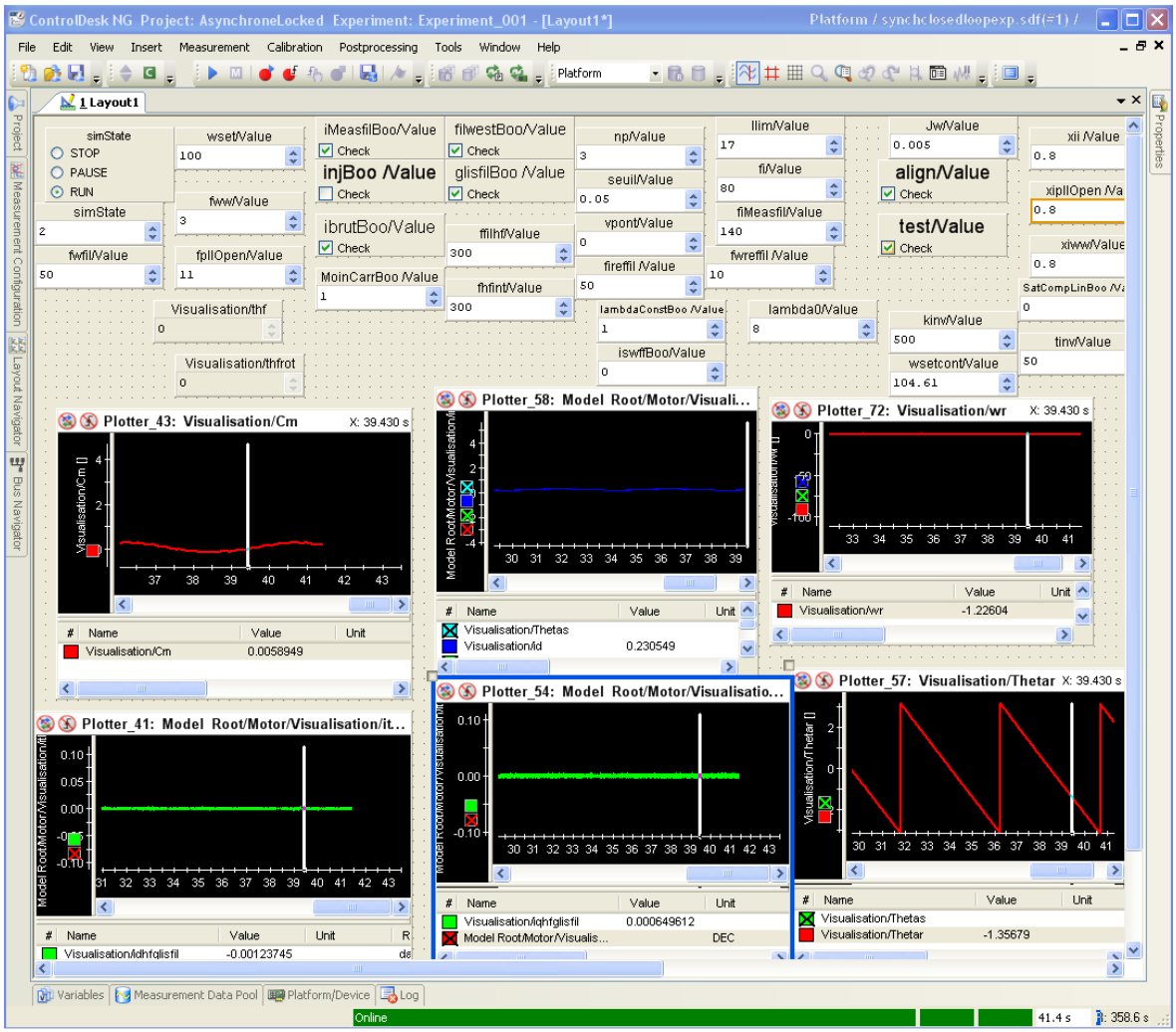

Figure 3.19: IHM Interface between the motor and the user.

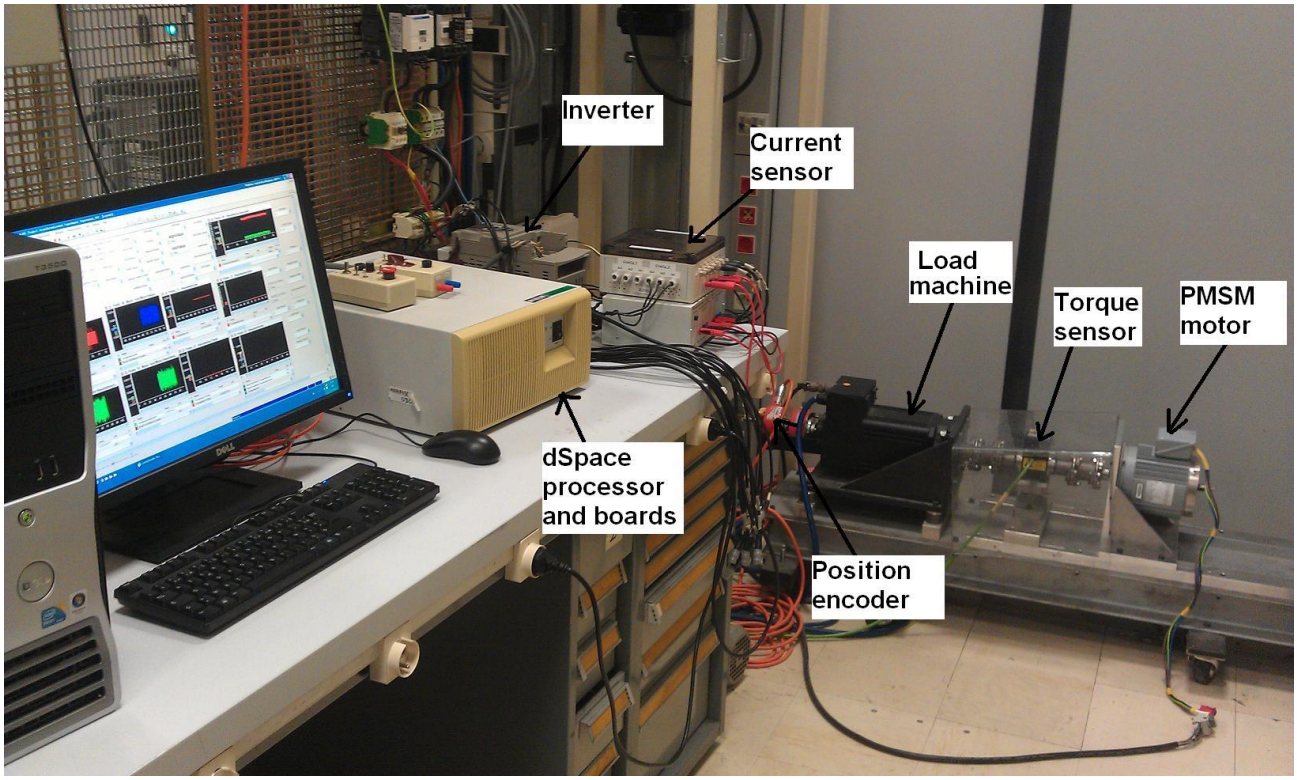

Figure 3.20: Experimental test bench.

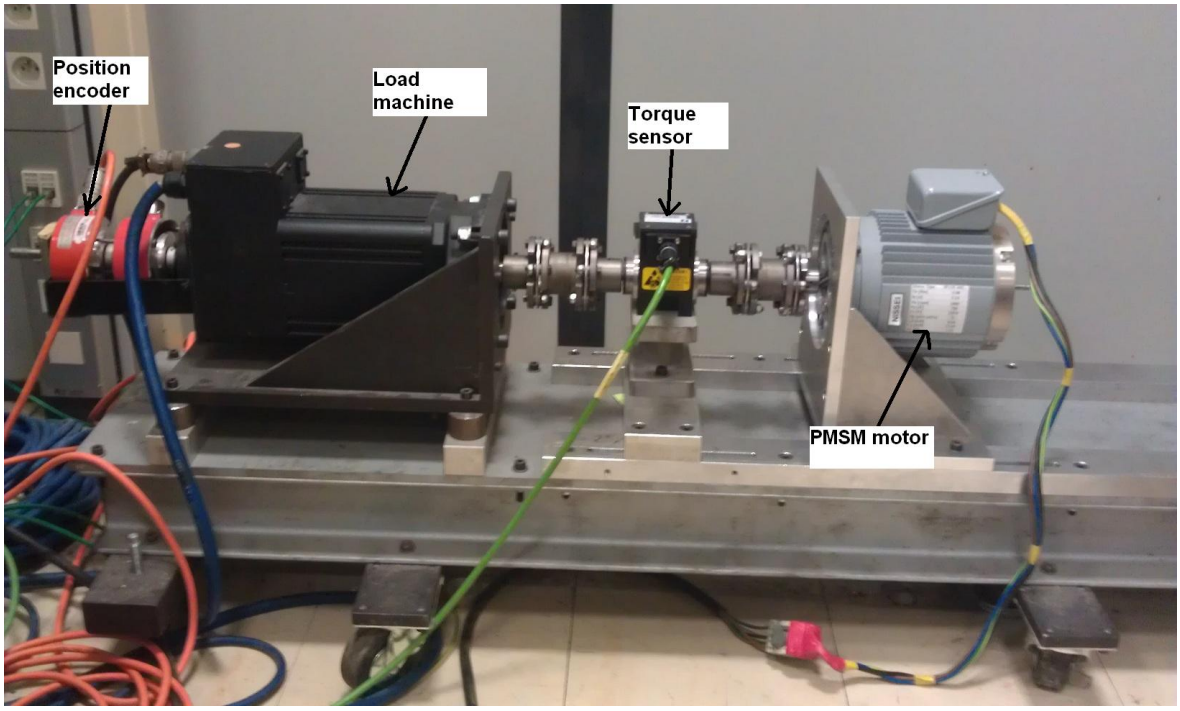

Figure 3.21: PMSM and load machine.

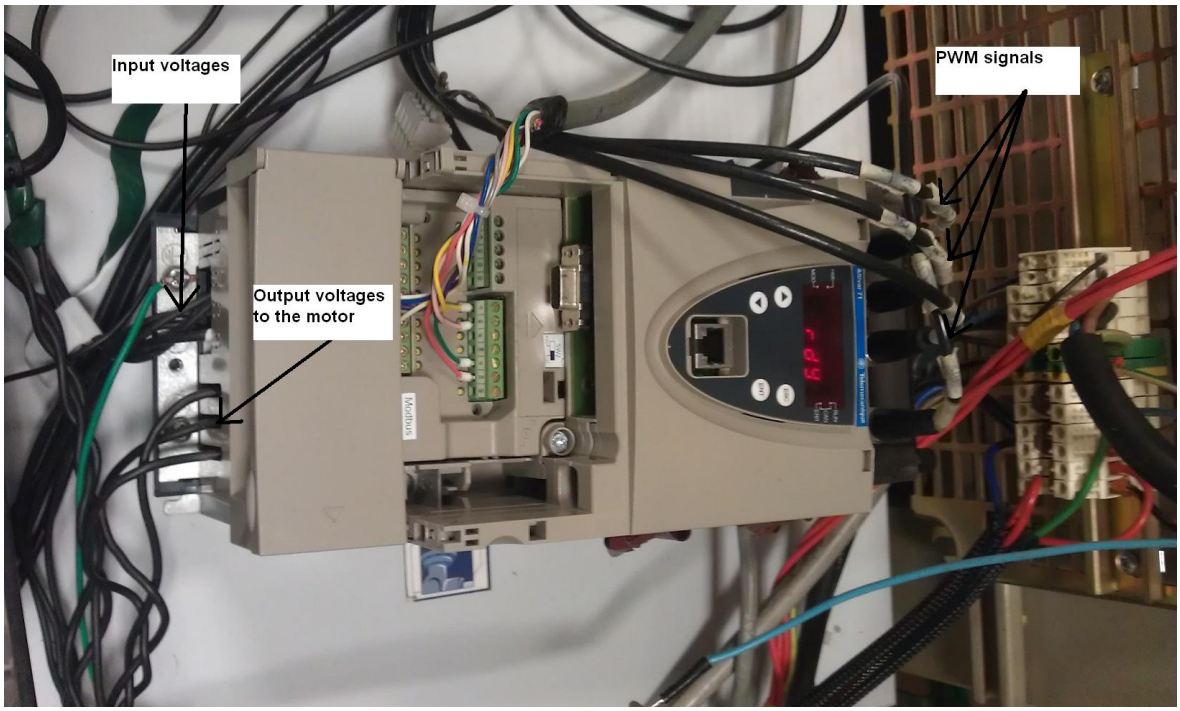

Figure 3.22: Electric inverter.

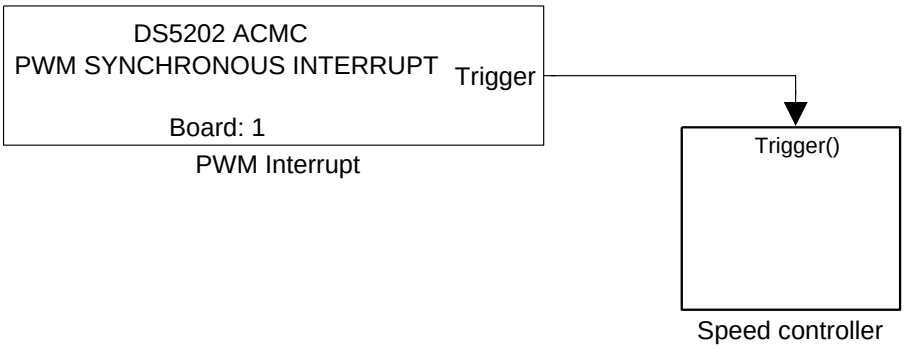

Figure 3.23: PWM synchronization.

Conclusion

We described in this chapter the operation of an electric motor drive. We presented also the experimental procedure which will be used in the next chapters to test the proposed PMSM speed control algorithms. We exposed the main practical implementation issues.

The use of an electric drive add important noises to the command voltage at very low speed. In fact, at low speed the motor voltages are small and the nonlinear inverter effects are important comparing to the motor voltages values. Thus, besides the PMSM observability issue, the inverter nonlinear effects complicate the PMSM control at low speed. This makes the sensorless low speed motor control a challenging problem. In the next chapters, this problem is addressed in details and a robust position observer and speed controller are proposed.

Chapter 4

Energy-based modeling of the PMSM

Contents

Introduction

La modélisation énergétique est omniprésente dans la physique [3, 72–75] puisque la plupart des phénomènes physiques sont modélisés par des échanges d'énergie. L'un des avantages de cette modélisation est d'encoder une grande partie des informations d'un système physique dans une seule fonction d'énergie, ce qui simplifie la formulation théorique.

Dans ce chapitre, nous proposons un modèle du MSAP basé sur une formulation énergétique. Ce modèle tient compte des effets non linéaires dus à la saturation magnétique. Dans la section 4.1, nous proposons un modèle général du MSAP basé sur les principes variationnels et sur la formulation dynamique d'Euler-Lagrange. Les courants électriques, les flux magnétiques ainsi que le couple

électromagnétique du moteur sont d'abord obtenus en utilisant une fonction de co-énergie appelée (Lagrangien), ensuite ils sont obtenus à partir d'une fonction d'énergie (Hamiltonien). Cette formulation est basée sur la conservation de l'énergie totale du moteur. Les expressions explicites de la co-énergie et de l'énergie du MSAP avec un modèle magnétique linéaire sont données dans plusieurs repères.

Ensuite, dans la section 4.2, nous considérons le cas du MSAP avec connexion étoile et nous modifions ainsi le modèle du moteur. Nous réduisons de trois à deux la dimension des variables électriques en utilisant le fait que la somme des courants est nulle dans cette configuration. En plus, nous prenons en compte les symétries géométriques du moteur afin de simplifier l'expression de l'énergie. Nous considérons également le cas d'un moteur non sinusoïdal avec un modèle magnétique linéaire, où nous montrons que le premier terme harmonique par rapport à la position dans les variables du moteur est le sixième harmonique.

Dans la section 4.3, nous présentons d'abord les modèles de saturation existants dans la littérature. Ensuite nous proposons un modèle paramétrique de saturation magnétique du MSAP sinusoïdale, ce modèle est basé sur la formulation énergétique présentée au début de ce chapitre. Dans ce cas, l'expression de l'énergie est obtenue en ajoutant des petits termes d'ordre supérieur à l'énergie du modèle linéaire. Ainsi, ce modèle est basé sur une simple fonction polynomiale dépendant seulement de 5 paramètres de saturation. Ce modèle est utilisé dans les chapitres suivants pour estimer la position du moteur afin de l'utiliser dans un schéma de contrôle sans capteur.

Enfin, dans la section 4.4, nous étudions l'observabilité linéaire et non linéaire du MSAP à vitesse nulle sans capteur de position ou de vitesse et en utilisant uniquement la mesure du courant. Nous démontrons que, indépendamment du modèle utilisé, le système du moteur n'est pas observable à vitesse nulle en considèrant seulement la linéarisation au premier ordre (observabilité linéaire). Par contre, en utilisant l'observabilité non linéaire, nous montrons que le système du moteur devient observable quand on ajoute une excitation persistante périodique à la tension du moteur comme un signal HF. Nous proposons également une condition suffisante d'observabilité non linéaire basée sur le modèle de saturation proposé dans ce chapitre.

Energy-based modeling is ubiquitous in physics [3,72–75] since most physical phenomena consist of energy exchanges. One of its main interests is to encode most of the information in a single energy function, yielding a simple theoretic formulation.

In this chapter we propose a PMSM model based on an energy formulation. This model takes into account nonlinear effects caused by cross coupling and magnetic saturation. In the section 4.1 we propose a general model of the PMSM based on variational principles and Euler-Lagrange formulation of the dynamics. The electric currents and fluxes and the electromagnetic torque are firstly derived from a co-energy function called Lagrangian then from an energy function called Hamiltonian. This formulation is based on the conservation of the total energy of the motor. The explicit expressions of the co-energy and the energy of the PMSM with linear magnetics are given in several reference frames.

Then, in section 4.2 we consider the case of the PMSM with star connection type and we modify the motor model consequently by reducing the electric variable dimensions from three to two using a redundant relation between the currents generated by the star connection. In addition we take into

account the motor symmetries in order to simplify the energy expressions. We also consider the case of non sinusoidal motor (as trapezoidal PMSM) with linear magnetics where we show that the first harmonic term in the motor variables with respect to the rotor position is the sixth harmonic.

In section 4.3 we give an overview of the existing saturation model in the literature, then we propose a parametric model based on the energy formulation of sinusoidal PMSM with magnetic saturation, this model is obtained using a higher order expansion of the linear model. The proposed model is based on simple polynomial functions and uses only 5 saturation parameters. This saturation model will be used in the next chapters to estimate the motor position for sensorless control purpose.

Finally, in section 4.4 we study the linear and nonlinear observability of the PMSM around zero speed without using a position or speed sensor and using the current measurement only. We show that, independently from the motor model, the motor states are not observable at zero speed when we consider only the first order system (linear observability). By contrast, using nonlinear observability, we show that the motor states are observable if we add a periodic persistent excitation to the motor such a HF signal. We propose also a sufficient condition for nonlinear observability based on the saturation model.

4.1 General PMSM model

In this section we propose a general PMSM energy based model independent from the stator windings connection type.

A three-phase PMSM is composed of a fixed part, the stator, and a rotating part, the rotor, fig. 4.1. The stator consists of three identical windings geometrically shifted by $\frac{2\pi}{3}$; the rotor carries permanent magnets which create a constant magnetic field. The electrical vector equation across the stator windings is

$$\frac{d\mathbf{\Psi}_{abc}}{dt} = -R\mathbf{i}_{abc} + \mathbf{u}_{abc}, \tag{4.1}$$

while the mechanical equation is

$$\frac{J}{n}\frac{d^2\theta}{dt^2} = \tau_e - \tau_L, \tag{4.2}$$

with

- $\mathbf{\Psi}_{abc}$ vector of fluxes linked by the windings (due to currents and permanent magnets)
- $\mathbf{i}_{abc}$ vector of currents in the windings
- $\mathbf{u}_{abc} := \mathbf{v}_{abc} - \mathbf{v}_{a'b'c'}$ vector of voltage drop across the windings
- R resistance of a winding
- θ electrical rotor position
- τ_e electromagnetic torque produced by the motor
- τ_L load torque
- J inertia of motor and load

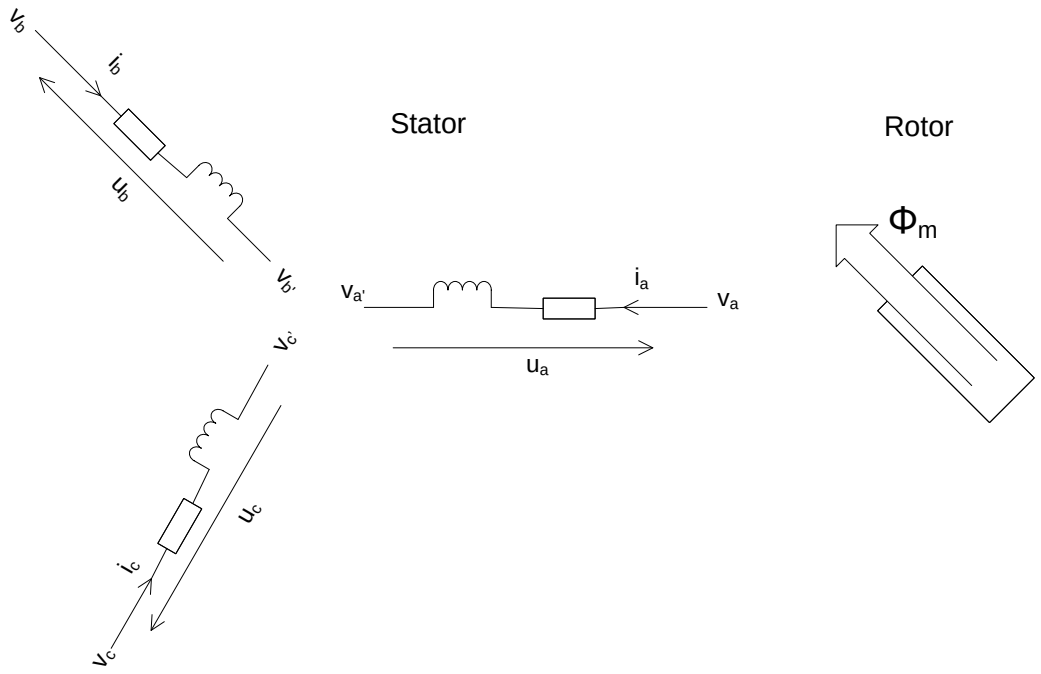

Figure 4.1: Sketch of a PMSM (notice the three windings are not connected yet)

- n number of pole pair.

To complete the model we must express the torque τ_e in function of the flux linkages $\mathbf{\Psi}_{abc}$, the current $\mathbf{i}_{abc}$ and the position θ; we must also write the relations between $\mathbf{\Psi}_{abc}$, $\mathbf{i}_{abc}$ and θ. A convenient way to do that is to use an energy function, which has two main benefits:

- only one energy function encodes the all necessary information. The electromagnetic torque expression and the fluxes-currents relations are obtained from partial derivatives of this energy function. The structural constraints between torque, fluxes and currents are then automatically satisfied.

- the magnetic saturation effects, which conserve energy, can easily be accounted for in the energy function without any modification of the dynamic equations. By contrast nonconservative effects such as hysteresis and iron losses cannot be encoded only in the energy function; since their effects on motor operation and control are limited they will not be considered in the sequel.

The energy formulation is based on the energy conservation principle [3, 75]. The PMSM is an electromechanical system comprised of an electrical subsystem and a mechanical subsystem. The interaction between these two systems takes place through the coupling electromagnetic field. The energy is supplied to the system by an electrical power source and a mechanical power source; the magnetic energy of the coupling field permits the exchange between these two energies. The electromechanical PMSM system is depicted in the fig. 4.2.

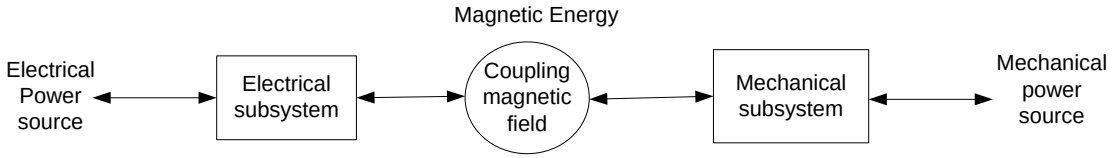

Figure 4.2: Block diagram of the PMSM electromechanical system

4.1.1 Energy and co-energy

The energy is written in function of the states of the PMSM system: the current, the flux and the position. The current and flux are not independent variables, hence we need either the current or the flux to express the system energy. In the literature [3, 48, 75], two types of energy are used to calculate the electromagnetic torque of an AC motor. The first type is the physical energy of the motor when the flux is considered as state variable, this energy represents the actual energy of the motor system. The second type is called co-energy when the current is considered as state variable; this co-energy does not have a physical interpretation but it is used to calculate the physical energy and the electromagnetic torque.

For example, according to [3, p.11] and [75, p.393], the co-energy W_c of a three phase PMSM is defined by the integrand of $(\Psi_a di_a + \Psi_b di_b + \Psi_c di_c)$ as follows

$$W_c(i_a, i_b, i_c, \theta_m) = \int (\Psi_a di_a + \Psi_b di_b + \Psi_c di_c), \tag{4.3}$$

where $\theta_m := \frac{\theta}{n}$ is the mechanical rotor position and $\mathbf{\Psi}_{abc} = \mathbf{\Psi}_{abc}(\mathbf{i}_{abc}, \theta_m)$. The torque is derived from the co-energy as follows

$$\tau_e = \frac{\partial W_c}{\partial \theta_m}. \tag{4.4}$$

The relation between the physical energy and the co-energy is

$$W_f(\Psi_a, \Psi_b, \Psi_c, \theta_m) = i_a \Psi_a + i_b \Psi_b + i_c \Psi_c - W_c(i_a, i_b, i_c, \theta_m) \tag{4.5}$$

where $\mathbf{i}_{abc} = \mathbf{i}_{abc}(\mathbf{\Psi}_{abc}, \theta_m)$. The equation (4.3) is often used to calculate the co-energy and hence the energy and the torque of a PMSM with magnetic saturation [48] where the flux $\mathbf{\Psi}_{abc}$ is a nonlinear function of the currents $\mathbf{i}_{abc}$.

The energy formulation of the PMSM in the literature is not based on a standard mathematical or physical formulation but it is based in general on heuristic considerations. Comparing to existing PMSM models, the contribution of the proposed model is the use of a standard mathematical formulation called Euler-Lagrange formulation which is widely used to model physical systems [72–74]. By using this formulation we have to deal only with one mathematical function to model the motor where we can include all conservative physical effects such as magnetic saturations and spatial harmonics; this can be done by modifying the expression of this function or adding additional terms corresponding to the desired effects. The electric current and flux, and the electromagnetic torque are obtained directly from this mathematical function.

At first, we introduce the Lagrangian formulation of the PMSM which is based on [21]. The Lagrangian is equivalent to the co-energy defined in (4.3) and it is written in terms of the motor

current and position. The motor flux is equal to the partial derivative of the Lagrangian with respect to the current; and the motor electromagnetic torque is equal to the partial derivative of the Lagrangian with respect to the position as in (4.4).

Then, we introduce the Hamiltonian formulation which is based on [67]. The Hamiltonian is the total physical energy of the PMSM written in terms of the flux and the position; it is obtained from the Lagrangian using a mathematical transformation called Legendre transformation which is similar to (4.5). The current is equal to the partial derivative of the Hamiltonian with respect to the flux and the motor electromagnetic torque is equal to the partial derivative of the Hamiltonian with respect to the position.

4.1.2 Lagrangian model

4.1.2.1 abc frame

The equations of the PMSM (4.1)-(4.2) derive from a variational principle and thus can be written as Euler-Lagrange equations with source terms corresponding to the energy exchange with the environment. Consider the additional variable

$$\mathbf{q}_{abc} = (q_a, q_b, q_c)^T, \quad \dot{\mathbf{q}}_{abc} = \frac{d}{dt}\mathbf{q}_{abc} = \mathbf{i}_{abc}$$

where $\mathbf{q}_{abc}$ corresponds to the electrical charges. We take the lagrangian $\mathcal{L}(\mathbf{q}, \dot{\mathbf{q}})$ as a function of the generalized coordinates $\mathbf{q} = (\theta_m, \mathbf{q}_{abc})$ and the generalized velocities $\dot{\mathbf{q}} = (\dot{\theta}_m, \dot{\mathbf{q}}_{abc})$ with $\dot{\theta}_m := \frac{d}{dt}\theta_m$. The Euler-Lagrange differential equation is

$$\frac{d}{dt}\left(\frac{\partial \mathcal{L}}{\partial \dot{\mathbf{q}}}\right) - \frac{\partial \mathcal{L}}{\partial \mathbf{q}} = \mathbf{F_w} \tag{4.6}$$

where

- $\mathbf{F_w} = (-\tau_L, u_a - Ri_a, u_b - Ri_b, u_c - Ri_c)^T$ corresponds to the energy exchange through the mechanical and the electrical system
- $\frac{\partial \mathcal{L}}{\partial \dot{\mathbf{q}}} = (\frac{\partial \mathcal{L}}{\partial \dot{\theta}_m}, \frac{\partial \mathcal{L}}{\partial \dot{q}_a}, \frac{\partial \mathcal{L}}{\partial \dot{q}_b}, \frac{\partial \mathcal{L}}{\partial \dot{q}_c})^T$ and $\frac{\partial \mathcal{L}}{\partial \mathbf{q}} = (\frac{\partial \mathcal{L}}{\partial \theta_m}, \frac{\partial \mathcal{L}}{\partial q_a}, \frac{\partial \mathcal{L}}{\partial q_b}, \frac{\partial \mathcal{L}}{\partial q_c})^T$.

The equation (4.6) can be separated into an electrical equation and a mechanical one. The electrical equation reads

$$\frac{d}{dt}\left(\frac{\partial \mathcal{L}}{\partial \mathbf{i}_{abc}}\right) = \mathbf{u}_{abc} - R\mathbf{i}_{abc} \tag{4.7}$$

where $\mathbf{i}_{abc} = \dot{\mathbf{q}}_{abc}$ and $\frac{\partial \mathcal{L}}{\partial \mathbf{q}_{abc}} = 0$ because the PMSM equations does not depend on the electrical charges $\mathbf{q}_{abc}$ (no capacitor). The energy exchanges in (4.7) are due to the power supply through the voltage $\mathbf{u}_{abc}$ and also to dissipation and irreversible phenomena due to stator resistance represented by the Ohm law $-R\mathbf{i}_{abc}$. The equations (4.7) corresponds to (4.1) where the flux $\mathbf{\Psi}_{abc}$ can be written as

$$\mathbf{\Psi}_{abc} = \frac{\partial \mathcal{L}}{\partial \mathbf{i}_{abc}}. \tag{4.8}$$

The mechanical equation reads

$$\frac{d}{dt}\left(\frac{\partial \mathcal{L}}{\partial \dot{\theta}_m}\right) = \frac{\partial \mathcal{L}}{\partial \theta_m} - \tau_L \tag{4.9}$$

where τ_L corresponds to the energy exchange through the mechanical load torque. The equations (4.9) corresponds to (4.2) where the electromagnetic torque can be written as

$$\tau_e = \frac{\partial \mathcal{L}}{\partial \theta_m}, \tag{4.10}$$

and

$$\frac{d}{dt}\left(\frac{\partial \mathcal{L}}{\partial \dot{\theta}_m}\right) = J\frac{d}{dt}\dot{\theta}_m \tag{4.11}$$

where J is the motor inertia.

We take $\mathcal{L}^{abc}(\theta, \dot{\theta}, \mathbf{i}_{abc})$ the Lagrangian equal to $\mathcal{L}(\mathbf{q}, \dot{\mathbf{q}})$ and written in terms of the electrical rotor position θ and the current $\mathbf{i}_{abc}$. Using the co-energy $\mathcal{L}^{abc}$ and the equations (4.7)–(4.11), hence the motor equations can be written as follows

$$\frac{d}{dt}\left(\frac{\partial \mathcal{L}^{abc}}{\partial \mathbf{i}_{abc}}\right) = -R\mathbf{i}_{abc} + \mathbf{u}_{abc} \tag{4.12}$$

$$\frac{J}{n}\frac{d^2\theta}{dt^2} = n\frac{\partial \mathcal{L}^{abc}}{\partial \theta} - \tau_L \tag{4.13}$$

with

$$\mathbf{\Psi}_{abc}(\theta, \dot{\theta}, \mathbf{i}_{abc}) = \frac{\partial \mathcal{L}^{abc}}{\partial \mathbf{i}_{abc}}(\theta, \dot{\theta}, \mathbf{i}_{abc}) \tag{4.14}$$

$$\tau_e(\theta, \dot{\theta}, \mathbf{i}_{abc}) = n\frac{\partial \mathcal{L}^{abc}}{\partial \theta}(\theta, \dot{\theta}, \mathbf{i}_{abc}). \tag{4.15}$$

The equations (4.12)–(4.15) are the Lagrangian formulation of the PMSM in the abc frame. Thanks to the co-energy function $\mathcal{L}^{abc}$, we get the expression of the motor electromagnetic torque and the flux in terms of the current and the rotor position, see (4.14)-(4.15). Therefore, we get a complete PMSM model using only $\mathcal{L}^{abc}$.

To clarify the idea of the Lagrangian, consider a sinusoidal PMSM with linear magnetic model; its Lagrangian can be written as follows:

$$\mathcal{L}^{abc}(\theta, \dot{\theta}, \mathbf{i}_{abc}) = \frac{J}{2n^2}\dot{\theta}^2 + \frac{1}{2}\mathbf{i}_{abc}^T\mathbf{L}^{abc}(\theta)\mathbf{i}_{abc} + \mathbf{i}_{abc}^T\mathbf{\Phi}_{abc}^m(\theta) \tag{4.16}$$

with

$$\mathbf{\Phi}_{abc}^m(\theta) = \lambda^{abc}\begin{pmatrix} \cos\theta \\ \cos\left(\theta - \frac{2\pi}{3}\right) \\ \cos\left(\theta - \frac{4\pi}{3}\right) \end{pmatrix}$$

and

$$\mathbf{L}^{abc}(\theta) = \frac{1}{2}\begin{pmatrix} 2L & -M & -M \\ -M & 2L & -M \\ -M & -M & 2L \end{pmatrix} + L_\Delta \begin{pmatrix} \cos 2\theta & \cos\left(2\theta - \frac{2\pi}{3}\right) & \cos\left(2\theta - \frac{4\pi}{3}\right) \\ \cos\left(2\theta - \frac{2\pi}{3}\right) & \cos\left(2\theta - \frac{4\pi}{3}\right) & \cos 2\theta \\ \cos\left(2\theta - \frac{4\pi}{3}\right) & \cos 2\theta & \cos\left(2\theta - \frac{2\pi}{3}\right) \end{pmatrix}$$

where $\mathbf{L}^{abc}$ is the matrix of motor inductance in abc frame; $\mathbf{\Phi}_{abc}^m$ is the vector of permanent flux; L is the self inductance per phase; M is the mutual inductance between two phases; L_Δ is the maximum inductance variation due to the geometric saliency; λ^{abc} is the magnitude of the magnet flux.

The expression of the flux can be obtained from (4.16) by using (4.14), hence we get :

$$\mathbf{\Psi}_{abc} = \mathbf{L}^{abc}(\theta)\mathbf{i}_{abc} + \mathbf{\Phi}^{m}_{abc}(\theta). \tag{4.17}$$

Expanding (4.17) leads to

$$\begin{aligned}
\Psi_a &= Li_a - \tfrac{M}{2}i_b - \tfrac{M}{2}i_c + L_\Delta\Big(\cos 2\theta i_a + \cos(2\theta - \tfrac{2\pi}{3})i_b + \cos(2\theta - \tfrac{4\pi}{3})i_c\Big) + \lambda_{abc}\cos\theta \\
\Psi_b &= -\tfrac{M}{2}i_a + Li_b - \tfrac{M}{2}i_c + L_\Delta\Big(\cos(2\theta - \tfrac{2\pi}{3})i_a + \cos(2\theta - \tfrac{4\pi}{3})i_b + \cos 2\theta i_c\Big) + \lambda_{abc}\cos(\theta - \tfrac{2\pi}{3}) \\
\Psi_c &= -\tfrac{M}{2}i_a - \tfrac{M}{2}i_b + Li_c + L_\Delta\Big(\cos(2\theta - \tfrac{4\pi}{3})i_a + \cos 2\theta i_b + \cos(2\theta - \tfrac{2\pi}{3})i_c\Big) + \lambda_{abc}\cos(\theta - \tfrac{4\pi}{3}).
\end{aligned}$$

The expression of the torque can be obtained from (4.16) by using (4.15), hence we get :

$$\begin{aligned}
\tau_e &= \frac{n}{2}\mathbf{i}^T_{abc}\frac{\partial \mathbf{L}^{abc}(\theta)}{\partial\theta}\mathbf{i}_{abc} + n\mathbf{i}^T_{abc}\frac{\partial \mathbf{\Phi}^{m}_{abc}(\theta)}{\partial\theta} \\
&= -nL_\Delta\left(\left(i_a^2 - \tfrac{1}{2}i_b^2 - \tfrac{1}{2}i_c^2 - i_a i_b - i_a i_c + 2i_b i_c\right)\sin 2\theta + \frac{\sqrt{3}}{2}\left(i_b^2 - i_c^2 - 2i_a i_b + 2i_a i_c\right)\cos 2\theta\right) \\
&+ n\lambda^{abc}\left(\frac{\sqrt{3}}{2}(i_b - i_c)\cos\theta - \left(i_a - \tfrac{1}{2}i_b - \tfrac{1}{2}i_c\right)\sin\theta\right).
\end{aligned} \tag{4.18}$$

In (4.17)-(4.18) we recover the standard expressions of fluxes and torque [3, p.263].

4.1.2.2 $\alpha\beta 0$ frame

The Lagrangian expression in abc frame can be simplified by a simple algebraic transformation denoted Clarke transformation. It is a unitary rotation in a three dimensional space, it transforms the abc frame to an orthogonal $\alpha\beta 0$ frame. We use the transformation that conserve the energy (the energy in abc frame and $\alpha\beta 0$ frame is the same), it is defined as follows:

$$\mathbf{x}_{\alpha\beta 0} = \mathbf{U}\mathbf{x}_{abc}, \quad \mathbf{x}_{abc} = \mathbf{U}^T\mathbf{x}_{\alpha\beta 0} \tag{4.19}$$

where $\mathbf{U}$ is a unitary matrix defined by

$$\mathbf{U} = \begin{pmatrix} \frac{\sqrt{2}}{\sqrt{3}} & -\frac{1}{\sqrt{6}} & -\frac{1}{\sqrt{6}} \\ 0 & \frac{1}{\sqrt{2}} & -\frac{1}{\sqrt{2}} \\ \frac{1}{\sqrt{3}} & \frac{1}{\sqrt{3}} & \frac{1}{\sqrt{3}} \end{pmatrix}.$$

Set the Lagrangian expression in $\alpha\beta 0$ as

$$\mathcal{L}^{\alpha\beta 0}(\theta, \dot\theta, \mathbf{i}_{\alpha\beta 0}) = \mathcal{L}^{abc}\left(\theta, \dot\theta, \mathbf{U}^T\mathbf{i}_{\alpha\beta 0}\right).$$

Thus, the Lagrangian formulation (4.12)–(4.15) can be written in $\alpha\beta 0$ frame as follows

$$\frac{d}{dt}\left(\frac{\partial \mathcal{L}^{\alpha\beta 0}}{\partial \mathbf{i}_{\alpha\beta 0}}\right) = -R\mathbf{i}_{\alpha\beta 0} + \mathbf{u}_{\alpha\beta 0} \tag{4.20}$$

$$\frac{J}{n}\frac{d^2\theta}{dt^2} = n\frac{\partial \mathcal{L}^{\alpha\beta 0}}{\partial\theta} - \tau_L, \tag{4.21}$$

with

$$\mathbf{\Psi}_{\alpha\beta 0}(\theta, \dot{\theta}, \mathbf{i}_{\alpha\beta 0}) = \frac{\partial \mathcal{L}^{\alpha\beta 0}}{\partial \mathbf{i}_{\alpha\beta 0}}(\theta, \dot{\theta}, \mathbf{i}_{\alpha\beta 0}) \tag{4.22}$$

$$\tau_e(\theta, \dot{\theta}, \mathbf{i}_{\alpha\beta 0}) = n\frac{\partial \mathcal{L}^{\alpha\beta 0}}{\partial \theta}(\theta, \dot{\theta}, \mathbf{i}_{\alpha\beta 0}), \tag{4.23}$$

we note that the Lagrangian formulation is similar in the abc and $\alpha\beta 0$ frames.

In the case of a sinusoidal PMSM with linear magnetic model, the Lagrangian in the $\alpha\beta 0$ frame can be written as

$$\mathcal{L}^{\alpha\beta 0}(\theta, \dot{\theta}, \mathbf{i}_{\alpha\beta}, i_0) = \tfrac{J}{2n^2}\dot{\theta}^2 + \tfrac{1}{2}\mathbf{i}_{\alpha\beta}^T \mathbf{L}^{\alpha\beta}(\theta)\mathbf{i}_{\alpha\beta} + \tfrac{1}{2}L_0 i_0^2 + \mathbf{i}_{\alpha\beta}^T \mathbf{\Phi}^m_{\alpha\beta}(\theta), \tag{4.24}$$

with

$$\mathbf{L}^{\alpha\beta} = \frac{1}{2}\begin{pmatrix} L_d + L_q + (L_d - L_q)\cos 2\theta & (L_d - L_q)\sin 2\theta \\ (L_d - L_q)\sin 2\theta & L_d + L_q - (L_d - L_q)\cos 2\theta \end{pmatrix}$$

and

$$\mathbf{\Phi}^m_{\alpha\beta} = \lambda \begin{pmatrix} \cos\theta \\ \sin\theta \end{pmatrix}$$

where $L_d = \frac{2}{3}L + \frac{1}{3}M + L_\Delta$; $L_q = \frac{2}{3}L + \frac{1}{3}M - L_\Delta$; $L_0 = \frac{2}{3}(L - M)$; $\lambda = \sqrt{\frac{3}{2}}\lambda_{abc}$. The fluxes can be written in terms of the currents thanks to the equation (4.22) as follows:

$$\begin{aligned} \mathbf{\Psi}_{\alpha\beta} &= \mathbf{L}^{\alpha\beta}\mathbf{i}_{\alpha\beta} + \mathbf{\Phi}^m_{\alpha\beta} \\ \Psi_0 &= L_0 i_0. \end{aligned}$$

Using (4.23), the torque expression reads

$$\tau_e = \frac{n}{2}(L_d - L_q)\Big((-i_\alpha^2 + i_\beta^2)\sin 2\theta + 2i_\alpha i_\beta \cos 2\theta\Big) + n\lambda(-i_\alpha \sin\theta + i_\beta \cos\theta),$$

hence we recover the standard expressions of the flux and the torque [3].

4.1.2.3 $dq0$ frame

To get an energy formulation with less dependence on the rotor position θ, we do a unitary rotation (Park transformation) of an angle θ, it transforms the $\alpha\beta 0$ frame to a rotating $dq0$ frame where the d axis coincides with the magnet flux axis and the 0- axis remains unchanged. The Park transformation can be written as follows

$$\mathbf{x}_{\alpha\beta 0} = \mathcal{P}_\theta \mathbf{x}_{dq0} \tag{4.25}$$

where

$$\mathcal{P}_\theta = \begin{pmatrix} \cos\theta & -\sin\theta & 0 \\ \sin\theta & \cos\theta & 0 \\ 0 & 0 & 1 \end{pmatrix}.$$

In $dq0$ frame we do not have a standard Lagrangian formulation because the Park transformation does not preserve the Lagrangian shape of the dynamic model equations. In fact, this transformation

depends on θ which is a position variable not a speed variable. As the energy is conserved by a unitary rotation, hence we get a co-energy formulation which replaces here the Lagrangian formulation.

Set the co-energy expression in $dq0$ as

$$\widetilde{\mathcal{L}}^{dq0}(\theta, \dot{\theta}, \mathbf{i}_{dq0}) = \mathcal{L}^{\alpha\beta 0}\left(\theta, \dot{\theta}, \mathcal{P}_\theta \mathbf{i}_{dq0}\right). \tag{4.26}$$

Thus, the Lagrangian formulation of the system (4.20)–(4.23) leads to the following co-energy formulation in $dq0$ frame

$$\frac{d}{dt}\left(\frac{\partial \widetilde{\mathcal{L}}^{dq0}}{\partial \mathbf{i}_{dq}}\right) = -R\mathbf{i}_{dq} + \mathbf{u}_{dq} - \dot{\theta}\mathcal{J}\frac{\partial \widetilde{\mathcal{L}}^{dq0}}{\partial \mathbf{i}_{dq}} \tag{4.27}$$

$$\frac{d}{dt}\left(\frac{\partial \widetilde{\mathcal{L}}^{dq0}}{\partial i_0}\right) = -Ri_0 + u_0 \tag{4.28}$$

$$\frac{J}{n}\frac{d^2\theta}{dt^2} = n\frac{\partial \widetilde{\mathcal{L}}^{dq0}}{\partial \theta} + n\mathbf{i}_{dq}^T\mathcal{J}\frac{\partial \widetilde{\mathcal{L}}^{dq0}}{\partial \mathbf{i}_{dq}} - \tau_L, \tag{4.29}$$

with

$$\mathbf{\Psi}_{dq0}(\theta, \dot{\theta}, \mathbf{i}_{dq0}) = \frac{\partial \widetilde{\mathcal{L}}_{dq0}}{\partial \mathbf{i}_{dq0}}(\theta, \dot{\theta}, \mathbf{i}_{dq0}) \tag{4.30}$$

$$\tau_e(\theta, \dot{\theta}, \mathbf{i}_{dq}, i_0) = n\frac{\partial \widetilde{\mathcal{L}}^{dq0}}{\partial \theta} + n\mathbf{i}_{dq}^T\mathcal{J}\frac{\partial \widetilde{\mathcal{L}}^{dq0}}{\partial \mathbf{i}_{dq}} \tag{4.31}$$

where

$$\mathcal{J} = \begin{pmatrix} 0 & -1 \\ 1 & 0 \end{pmatrix}.$$

In the case of a sinusoidal PMSM with linear magnetic model, the co-energy in the $dq0$ frame reads

$$\widetilde{\mathcal{L}}^{dq0}(\theta, \dot{\theta}, i_d, i_q, i_0) = \tfrac{J}{2n^2}\dot{\theta}^2 + \tfrac{1}{2}L_d i_d^2 + \tfrac{1}{2}L_q i_q^2 + \tfrac{1}{2}L_0 i_0^2 + \lambda i_d. \tag{4.32}$$

The fluxes can be written in terms of the currents in the $dq0$ frame using (4.30):

$$\Psi_d = L_d i_d + \lambda, \quad \Psi_q = L_d i_q, \quad \Psi_0 = L_0 i_0. \tag{4.33}$$

Using (4.31), the torque can be expressed as

$$\tau_e = n i_q\Big(\lambda + (L_d - L_q)i_d\Big), \tag{4.34}$$

hence, we obtain the standard expressions of the fluxes and the torque in dq frame [3, p.265].

The complete model of the PMSM in $dq0$ frame is obtained by replacing $\widetilde{\mathcal{L}}^{dq0}$ in (4.27)–(4.31) by its value in (4.32), hence we get:

$$\begin{aligned}
L_d\frac{di_d}{dt} &= -Ri_d + u_d + L_q\dot{\theta}i_q \\
L_q\frac{di_q}{dt} &= -Ri_q + u_q - L_d\dot{\theta}i_d - \lambda\omega \\
L_0\frac{di_0}{dt} &= -Ri_0 + u_0 \\
\frac{J}{n}\frac{d^2\theta}{dt^2} &= n i_q\Big(\lambda + (L_d - L_q)i_d\Big) - \tau_L
\end{aligned}$$

In the sequel we will establish the Hamiltonian formulation. The Hamiltonian is obtained from the Lagrangian by the Legendre transformation. The Hamiltonian formulation is needed for two main reasons:

- the Lagrangian is the co-energy of the PMSM and it does not have a physical meaning but the Hamiltonian energy is the total electromechanical energy of the motor, i.e. the Hamiltonian is the sum of the mechanical energy and the magnetic energy of the motor.

- the Lagrangian is written in terms of the current, but in some cases it is necessary to express the energy in terms of the flux mainly for HF signal calculations as we will see in the next sections.

4.1.3 Hamiltonian model

4.1.3.1 abc frame

The Hamiltonian in abc frame is obtained from the Lagrangian in abc frame by the following Legendre transformation [74, p.490]

$$\mathcal{H}^{abc} = \dot{\theta}\frac{\partial \mathcal{L}^{abc}}{\partial \dot{\theta}} + i_a\frac{\partial \mathcal{L}^{abc}}{\partial i_a} + i_b\frac{\partial \mathcal{L}^{abc}}{\partial i_b} + i_c\frac{\partial \mathcal{L}^{abc}}{\partial i_c} - \mathcal{L}^{abc}. \tag{4.35}$$

This transformation is similar to the relation between the physical energy and the co-energy given by (4.3). Notice that from (4.14) we have $\mathbf{\Psi}_{abc} = \frac{\partial \mathcal{L}^{abc}}{\partial \mathbf{i}_{abc}}$ and from (4.11) we have $\frac{\partial \mathcal{L}^{abc}}{\partial \dot{\theta}} = \frac{J}{n^2}\dot{\theta}$, hence (4.35) leads to

$$\mathcal{H}^{abc}(\theta, p_\theta, \mathbf{\Psi}_{abc}) = \frac{1}{Jn^2}p_\theta^2 + \mathbf{i}_{abc}^T\mathbf{\Psi}_{abc} - \mathcal{L}^{abc} \tag{4.36}$$

where $p_\theta = J\dot{\theta}$ is the moment of inertia of the motor. The Hamiltonian is the energy of the motor expressed in terms of the motor moment of inertia, the motor position and the flux. In this case the current $\mathbf{i}_{abc} = \mathbf{i}_{abc}(\theta, p_\theta, \mathbf{\Psi}_{abc})$ is a function of the flux and the position. In the sequel, all the motor variables will be expressed in terms of the flux and the position.

The total derivative of $\mathcal{H}^{abc}$ with respect to the time is equal to the total power exchange between the motor and the environment. Indeed, $\frac{d}{dt}\mathcal{H}^{abc}$ reads

$$\frac{d}{dt}\mathcal{H}^{abc} = -\frac{\dot{\theta}}{n}\tau_L + \mathbf{u}_{abc}^T\mathbf{i}_{abc} - R\mathbf{i}_{abc}^T\mathbf{i}_{abc} \tag{4.37}$$

where $-\frac{1}{n}\dot{\theta}\tau_L$ is the mechanical power exchange between the motor and the load; $\mathbf{u}_{abc}^T\mathbf{i}_{abc}$ is the electric power supplied by an electrical power source to the motor; $-R\mathbf{i}_{abc}^T\mathbf{i}_{abc}$ is the thermic power loss due to the motor resistance. If the motor is not connected to an electrical power supply nor to a mechanical load and the stator resistance is zero, then the total derivative of the Hamiltonian with respect to the time is zero $\frac{d}{dt}\mathcal{H}^{abc} = 0$ and therefore the total energy $\mathcal{H}^{abc}$ is conserved. The equation (4.37) justifies the designation of the hamiltonian as the total energy of the motor.

The partial derivatives of (4.36) with respect to $\mathbf{\Psi}_{abc}$ leads to

$$\begin{aligned}\frac{\partial \mathcal{H}^{abc}}{\partial \mathbf{\Psi}_{abc}} &= \mathbf{i}_{abc} + \mathbf{\Psi}_{abc}^T \frac{\partial \mathbf{i}_{abc}}{\partial \mathbf{\Psi}_{abc}} - \frac{\partial \mathcal{L}^{abc}}{\partial \mathbf{\Psi}_{abc}} \\ &= \mathbf{i}_{abc} + \mathbf{\Psi}_{abc}^T \frac{\partial \mathbf{i}_{abc}}{\partial \mathbf{\Psi}_{abc}} - \left(\frac{\partial \mathcal{L}^{abc}}{\partial \mathbf{i}_{abc}}\right)^T \frac{\partial \mathbf{i}_{abc}}{\partial \mathbf{\Psi}_{abc}} \\ &= \mathbf{i}_{abc} + \mathbf{\Psi}_{abc}^T \frac{\partial \mathbf{i}_{abc}}{\partial \mathbf{\Psi}_{abc}} - \mathbf{\Psi}_{abc}^T \frac{\partial \mathbf{i}_{abc}}{\partial \mathbf{\Psi}_{abc}} \\ &= \mathbf{i}_{abc}\end{aligned}$$

hence

$$\mathbf{i}_{abc}(\theta, p_\theta, \mathbf{\Psi}_{abc}) = \frac{\partial \mathcal{H}^{abc}}{\partial \mathbf{\Psi}_{abc}}(\theta, p_\theta, \mathbf{\Psi}_{abc}). \tag{4.38}$$

The derivative of (4.36) with respect to θ yields

$$\begin{aligned}\frac{\partial \mathcal{H}^{abc}}{\partial \theta} &= \left(\frac{\partial \mathbf{i}_{abc}}{\partial \theta}\right)^T \mathbf{\Psi}_{abc} - \frac{\partial}{\partial \theta}\mathcal{L}^{abc}\left(\theta, \dot{\theta}, \mathbf{i}_{abc}(\theta, p_\theta, \mathbf{\Psi}_{abc})\right) \\ &= \left(\frac{\partial \mathbf{i}_{abc}}{\partial \theta}\right)^T \mathbf{\Psi}_{abc} - \frac{\partial \mathcal{L}^{abc}}{\partial \theta} - \left(\frac{\partial \mathbf{i}_{abc}}{\partial \theta}\right)^T \frac{\partial \mathcal{L}^{abc}}{\partial \mathbf{i}_{abc}} \\ &= \left(\frac{\partial \mathbf{i}_{abc}}{\partial \theta}\right)^T \mathbf{\Psi}_{abc} - \frac{\partial \mathcal{L}^{abc}}{\partial \theta} - \left(\frac{\partial \mathbf{i}_{abc}}{\partial \theta}\right)^T \mathbf{\Psi}_{abc} \\ &= -\frac{\partial \mathcal{L}^{abc}}{\partial \theta},\end{aligned}$$

hence

$$\tau_e = n\frac{\partial \mathcal{L}^{abc}}{\partial \theta} = -n\frac{\partial \mathcal{H}^{abc}}{\partial \theta},$$

finally we get

$$\tau_e(\theta, p_\theta, \mathbf{\Psi}_{abc}) = -n\frac{\partial \mathcal{H}^{abc}}{\partial \theta}(\theta, p_\theta, \mathbf{\Psi}_{abc}). \tag{4.39}$$

In (4.38)-(4.39) the flux and the torque are expressed in terms of the Hamiltonian and hence in terms of the flux and the position. Replacing $\mathbf{\Psi}_{abc}$ and τ_e in (4.1)-(4.2) by their values in (4.38)-(4.39), hence we get the following Hamiltonian formulation in the abc frame

$$\frac{d}{dt}\mathbf{\Psi}_{abc} = -R\frac{\partial \mathcal{H}^{abc}}{\partial \mathbf{\Psi}_{abc}} + \mathbf{u}_{abc}, \tag{4.40}$$

$$\frac{J}{n}\frac{d^2\theta}{dt^2} = -n\frac{\partial \mathcal{H}^{abc}}{\partial \theta} - \tau_L. \tag{4.41}$$

In the case of a sinusoidal PMSM with linear magnetic model, the Hamiltonian expression in abc frame is

$$\mathcal{H}^{abc}(\theta, p_\theta, \mathbf{\Psi}_{abc}) = \frac{1}{2Jn^2}p_\theta^2 + \frac{1}{2}\Big(\mathbf{\Psi}_{abc} - \mathbf{\Phi}_{abc}^m(\theta)\Big)^T \Big[\mathbf{L}^{abc}(\theta)\Big]^{-1}\Big(\mathbf{\Psi}_{abc} - \mathbf{\Phi}_{abc}^m(\theta)\Big). \tag{4.42}$$

We note that the Hamiltonian energy expression is different from the Lagrangian in the case of a linear magnetic model. Indeed, if we replace the current in (4.16) by its value in terms of the flux, then the obtained Lagrangian (in terms of the flux) is different from the Hamiltonian, we get:

$$\mathcal{L}^{abc} - \mathcal{H}^{abc} = \mathbf{i}_{abc}^T \mathbf{\Phi}_{abc}^m.$$

This difference exists because the Legendre transformation cancels the linear term $\mathbf{i}_{abc}^T \mathbf{\Phi}_{abc}^m$ in the Lagrangian.

4.1.3.2 $\alpha\beta 0$ frame

As for the Lagrangian, we can simplify the Hamiltonian using the Clarke transformation to pass from abc frame to $\alpha\beta 0$ frame. To do that, we apply the Legendre transformation to the Lagrangian $\mathcal{L}^{\alpha\beta 0}$, hence we get

$$\mathcal{H}^{\alpha\beta 0} = \dot{\theta}\frac{\partial \mathcal{L}^{\alpha\beta 0}}{\partial \dot{\theta}} + \mathbf{i}_{\alpha\beta 0}^T \frac{\partial \mathcal{L}^{\alpha\beta 0}}{\partial \mathbf{i}_{\alpha\beta 0}} - \mathcal{L}^{\alpha\beta 0}. \tag{4.43}$$

Using $\mathbf{\Psi}_{\alpha\beta 0} = \frac{\partial \mathcal{L}^{\alpha\beta 0}}{\partial \mathbf{i}_{\alpha\beta 0}}$ and $\frac{\partial \mathcal{L}^{\alpha\beta 0}}{\partial \dot{\theta}} = \frac{J}{n^2}\dot{\theta}$, hence (4.43) leads to

$$\mathcal{H}^{\alpha\beta 0}(\theta, p_\theta, \mathbf{\Psi}_{\alpha\beta 0}) = \frac{1}{Jn^2}p_\theta^2 + \mathbf{i}_{\alpha\beta 0}^T \mathbf{\Psi}_{\alpha\beta 0} - \mathcal{L}^{\alpha\beta 0}. \tag{4.44}$$

The total derivative of $\mathcal{H}^{\alpha\beta 0}$ in (4.44) with respect to the time is equal to the total power exchange between the motor and the environment. Indeed, $\frac{d}{dt}\mathcal{H}^{\alpha\beta 0}$ reads

$$\frac{d}{dt}\mathcal{H}^{\alpha\beta 0} = -\frac{\dot{\theta}}{n}\tau_L + \mathbf{u}_{\alpha\beta 0}^T \mathbf{i}_{\alpha\beta 0} - R\mathbf{i}_{\alpha\beta 0}^T \mathbf{i}_{\alpha\beta 0}. \tag{4.45}$$

The partial derivatives of (4.44) with respect to $\mathbf{\Psi}_{\alpha\beta 0}$ and θ leads to

$$\mathbf{i}_{abc}(\theta, p_\theta, \mathbf{\Psi}_{\alpha\beta 0}) = \frac{\partial \mathcal{H}^{\alpha\beta 0}}{\partial \mathbf{\Psi}_{\alpha\beta 0}}(\theta, p_\theta, \mathbf{\Psi}_{\alpha\beta 0}) \tag{4.46}$$

$$\tau_e(\theta, p_\theta, \mathbf{\Psi}_{\alpha\beta 0}) = n\frac{\partial \mathcal{H}^{\alpha\beta 0}}{\partial \theta}(\theta, p_\theta, \mathbf{\Psi}_{\alpha\beta 0}). \tag{4.47}$$

Finally the equations (4.20)–(4.23) and (4.46)-(4.47) lead to the following Hamiltonian formulation in the $\alpha\beta 0$ frame

$$\frac{d}{dt}\mathbf{\Psi}_{\alpha\beta 0} = -R\frac{\partial \mathcal{H}^{\alpha\beta 0}}{\partial \mathbf{\Psi}_{\alpha\beta 0}} + \mathbf{u}_{\alpha\beta 0}, \tag{4.48}$$

$$\frac{J}{n}\frac{d^2\theta}{dt^2} = -n\frac{\partial \mathcal{H}^{\alpha\beta 0}}{\partial \theta} - \tau_L. \tag{4.49}$$

In the case of a sinusoidal PMSM with linear magnetic model, the Hamiltonian expression in $\alpha\beta 0$ frame is

$$\mathcal{H}^{\alpha\beta 0}(\theta, p_\theta, \mathbf{\Psi}_{\alpha\beta}, \Psi_0) = \frac{1}{2Jn^2}p_\theta^2 + \frac{1}{2}\Big(\mathbf{\Psi}_{\alpha\beta} - \mathbf{\Phi}_{\alpha\beta}^m(\theta)\Big)^T \Big[\mathbf{L}^{\alpha\beta}(\theta)\Big]^{-1} \Big(\mathbf{\Psi}_{\alpha\beta} - \mathbf{\Phi}_{\alpha\beta}^m(\theta)\Big) + \frac{1}{2L_0}\Psi_0^2 \tag{4.50}$$

4.1.3.3 $dq0$ frame

As for the Lagrangian formulation, in $dq0$ frame we do not have a Hamiltonian formulation. We derive an energy formulation using the Hamiltonian in $\alpha\beta0$ frame and the Park transformation from $\alpha\beta0$ frame to $dq0$ frame. Indeed, we define the energy function $\widetilde{\mathcal{H}}^{dq0}$ as follows

$$\widetilde{\mathcal{H}}^{dq0}(\theta, p_\theta, \mathbf{\Psi}_{dq0}) = \mathcal{H}^{\alpha\beta0}(\theta, p_\theta, \mathcal{P}_\theta \mathbf{\Psi}_{dq0}). \tag{4.51}$$

By using (4.26)-(4.43), hence (4.51) leads to

$$\widetilde{\mathcal{H}}^{dq0}(\theta, p_\theta, \mathbf{\Psi}_{dq0}) = \dot{\theta}\frac{\partial \widetilde{\mathcal{L}}^{dq0}}{\partial \dot{\theta}} + \mathbf{i}_{dq0}^T \frac{\partial \widetilde{\mathcal{L}}^{dq0}}{\partial \mathbf{i}_{dq0}} - \widetilde{\mathcal{L}}^{dq0}. \tag{4.52}$$

Thus, in $dq0$ frame the energy $\widetilde{\mathcal{H}}^{dq0}$ can be obtained from the co-energy $\widetilde{\mathcal{L}}^{dq0}$ by the Legendre transformation. Thus, despite the energy and the co-energy in $dq0$ frame are not in the Hamiltonian and the Lagrangian form, the Legendre transformation between them remains valid.

To verify that $\widetilde{\mathcal{H}}^{dq0}$ is an energy function, we calculate its total derivative with respect to the time using (4.27)–(4.31) and (4.52), we get:

$$\frac{d}{dt}\widetilde{\mathcal{H}}^{dq0} = -\frac{\dot{\theta}}{n}\tau_L + \mathbf{u}_{dq0}^T \mathbf{i}_{dq0} - R\mathbf{i}_{dq0}^T \mathbf{i}_{dq0}, \tag{4.53}$$

hence, the total derivative of $\widetilde{\mathcal{H}}^{dq0}$ with respect to the time is equal to the total power exchange between the motor and the environment. Thus, $\widetilde{\mathcal{H}}^{dq0}$ can be considered as an energy function. We can interpret this result by the fact that the energy is conserved by rotation.

Using (4.46)–(4.49) and (4.51), hence the energy formulation in the $dq0$ frame can be written as follows

$$\frac{d\mathbf{\Psi}_{dq}}{dt} = -R\frac{\partial \widetilde{\mathcal{H}}^{dq0}}{\partial \mathbf{\Psi}_{dq}} + \mathbf{u}_{dq} - \dot{\theta}\mathcal{J}\mathbf{\Psi}_{dq} \tag{4.54}$$

$$\frac{d\Psi_0}{dt} = -R\frac{\partial \widetilde{\mathcal{H}}^{dq0}}{\partial \Psi_0} + u_0 \tag{4.55}$$

$$\frac{J}{n}\frac{d^2\theta}{dt^2} = -n\frac{\partial \widetilde{\mathcal{H}}^{dq0}}{\partial \theta} + n\left(\frac{\partial \widetilde{\mathcal{H}}^{dq0}}{\partial \mathbf{\Psi}_{dq}}\right)^T \mathcal{J}\mathbf{\Psi}_{dq} - \tau_L, \tag{4.56}$$

with

$$\mathbf{i}_{dq0}(\theta, p_\theta, \mathbf{\Psi}_{dq0}) = \frac{\partial \widetilde{\mathcal{H}}^{dq0}}{\partial \mathbf{\Psi}_{dq0}}(\theta, p_\theta, \mathbf{\Psi}_{dq0}) \tag{4.57}$$

$$\tau_e(\theta, p_\theta, \mathbf{\Psi}_{dq0}) = -n\frac{\partial \widetilde{\mathcal{H}}^{dq0}}{\partial \theta}(\theta, p_\theta, \mathbf{\Psi}_{dq0}) + n\left(\frac{\partial \widetilde{\mathcal{H}}^{dq0}}{\partial \mathbf{\Psi}_{dq}}(\theta, p_\theta, \mathbf{\Psi}_{dq0})\right)^T \mathcal{J}\mathbf{\Psi}_{dq} \tag{4.58}$$

In the case of a sinusoidal PMSM with linear magnetic model, the energy expression in $dq0$ frame is

$$\widetilde{\mathcal{H}}^{dq0}(\theta, p_\theta, \Psi_d, \Psi_q, \Psi_0) = \frac{1}{2Jn^2}p_\theta^2 + \frac{1}{2L_d}(\Psi_d - \lambda)^2 + \frac{1}{2L_q}\Psi_q^2 + \frac{1}{2L_0}\Psi_0^2 \tag{4.59}$$

In this section, we proposed a PMSM model based on an energy formulation. Lagrangian and co-energy formulations were used when the current is the electrical state variable; Hamiltonian and energy formulations were used when the flux is the electrical state variable. In addition, the dynamic equations of the PMSM were presented in the three reference frames: abc, $\alpha\beta 0$, and $dq0$ where the motor torque, current and flux were expressed in terms of the co-energy and energy functions. The proposed formulation is general and independent of the connection of the stator windings. In the sequel, we consider the case of a PMSM with star connection type.

4.2 Star connection and symmetry considerations

The PMSM models proposed in the previous section are independent of the connection of the stator windings. In this section we apply this formulation to the PMSM with star connection type and we modify the motor equations consequently where we show that only two axis are needed to write the motor equations. In addition, we simplify the motor energy expressions by using the geometric symmetries presented in the motor by construction.

4.2.1 Star connection

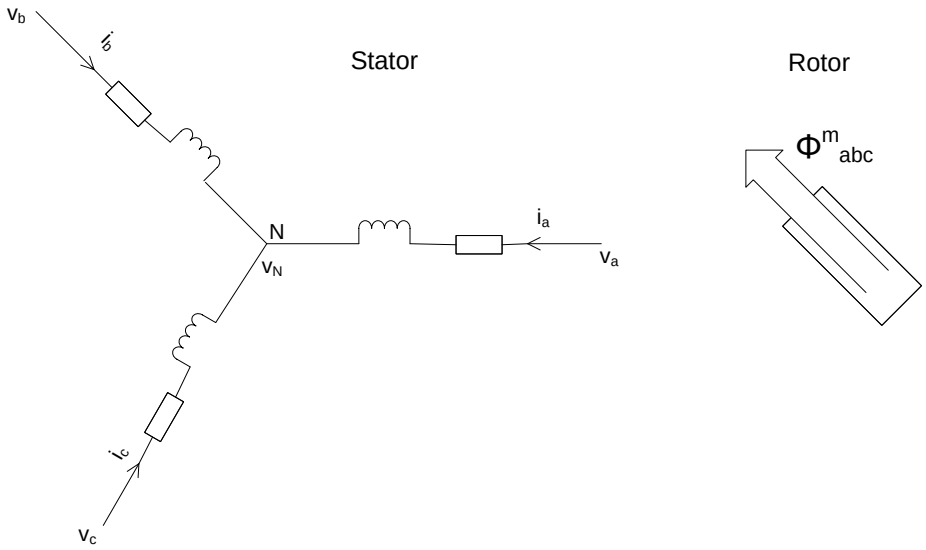

Figure 4.3: Star connection configuration

In the case of the star connection of the stator windings, the points a', b' and c' are connected together and form the star point N having an electrical potential $v_{a'} = v_{b'} = v_{c'} = v_N$ as shown in fig. 4.3. A potential $\mathbf{v}_{abc} = (v_a, v_b, v_c)^T$ is applied to the motor three phases by an external power generator (inverter). For this type of connection the sum of the currents is zero:

$$i_a + i_b + i_c = 0. \tag{4.60}$$

In the sequel, we will simplify the Lagrangian and the Hamiltonian formulation according to (4.60).

4.2.1.1 Modified Lagrangian formulation

The motor equations in $\alpha\beta 0$ frame can be simplified in the case of the star connection. Using the Clarke transformation (4.19), the voltage in $\alpha\beta 0$ can be written as follows

$$\begin{pmatrix} u_\alpha \\ u_\beta \\ u_0 \end{pmatrix} = \begin{pmatrix} \frac{\sqrt{2}}{\sqrt{3}} & -\frac{1}{\sqrt{6}} & -\frac{1}{\sqrt{6}} \\ 0 & \frac{1}{\sqrt{2}} & -\frac{1}{\sqrt{2}} \\ \frac{1}{\sqrt{3}} & \frac{1}{\sqrt{3}} & \frac{1}{\sqrt{3}} \end{pmatrix} \begin{pmatrix} v_a - v_N \\ v_b - v_N \\ v_c - v_N \end{pmatrix} = \begin{pmatrix} v_\alpha \\ v_\beta \\ v_0 - \sqrt{3} v_N \end{pmatrix}$$

where $\mathbf{v}_{\alpha\beta 0} = \mathbf{U}\mathbf{v}_{abc}$, and the current i_0 is

$$i_0 = \frac{1}{\sqrt{3}}(i_a + i_b + i_c) = 0.$$

Thus, in the $\alpha\beta 0$ frame (4.20) leads to

$$\frac{d}{dt}\left(\frac{\partial \mathcal{L}^{\alpha\beta 0}}{\partial \mathbf{i}_{\alpha\beta}}\right) = -R\mathbf{i}_{\alpha\beta} + \mathbf{v}_{\alpha\beta}, \tag{4.61}$$

$$\frac{d}{dt}\left(\frac{\partial \mathcal{L}^{\alpha\beta 0}}{\partial i_0}\right) = v_0 - \sqrt{3} v_N \tag{4.62}$$

$$i_0 = 0$$

Let

$$\mathbb{L}^{\alpha\beta}(\theta, \dot{\theta}, \mathbf{i}_{\alpha\beta}) = \mathcal{L}^{\alpha\beta 0}(\theta, \dot{\theta}, \mathbf{i}_{\alpha\beta}, 0) \tag{4.63}$$

hence (4.61)-(4.62) lead to

$$\frac{d}{dt}\left(\frac{\partial \mathbb{L}^{\alpha\beta}}{\partial \mathbf{i}_{\alpha\beta}}\right) = -R\mathbf{i}_{\alpha\beta} + \mathbf{v}_{\alpha\beta} \tag{4.64}$$

and

$$\frac{d}{dt}\left(\frac{\partial \mathcal{L}^{\alpha\beta 0}}{\partial i_0}(\theta, \dot{\theta}, \mathbf{i}_{\alpha\beta}, i_0)\Big|_{i_0=0}\right) = v_0 - \sqrt{3} v_N. \tag{4.65}$$

This result shows that the electrical system can be separated into two parts. The first part is represented by (4.64) and it is independent of the 0- axis components. The second part is represented by (4.65), it gives the mathematical expression of the star point voltage v_N.

In $dq0$ frame, we take

$$\widetilde{\mathbb{L}}^{dq}(\theta, \dot{\theta}, \mathbf{i}_{dq}) = \mathbb{L}^{\alpha\beta}(\theta, \dot{\theta}, \mathcal{R}_\theta \mathbf{i}_{dq}) \tag{4.66}$$

where

$$\mathcal{R}_\theta = \begin{pmatrix} \cos\theta & -\sin\theta \\ \sin\theta & \cos\theta \end{pmatrix},$$

hence (4.64) leads to the following co-energy formulation

$$\frac{d}{dt}\left(\frac{\partial \widetilde{\mathbb{L}}^{dq}}{\partial \mathbf{i}_{dq}}\right) = -R\mathbf{i}_{dq} + \mathbf{v}_{dq} - \dot{\theta}\mathcal{J}\frac{\partial \widetilde{\mathbb{L}}^{dq}}{\partial \mathbf{i}_{dq}} \tag{4.67}$$

$$\frac{J}{n}\frac{d^2\theta}{dt^2} = n\frac{\partial \widetilde{\mathbb{L}}^{dq}}{\partial \theta} + n\mathbf{i}_{dq}^T\mathcal{J}\frac{\partial \widetilde{\mathbb{L}}^{dq}}{\partial \mathbf{i}_{dq}} - \tau_L \tag{4.68}$$

with

$$\mathbf{\Psi}_{dq}(\theta, \dot{\theta}, \mathbf{i}_{dq}) = \frac{\partial \widetilde{\mathbb{L}}^{dq}}{\partial \mathbf{i}_{dq}}(\theta, \dot{\theta}, \mathbf{i}_{dq}) \tag{4.69}$$

$$\tau_e(\theta, \dot{\theta}, \mathbf{i}_{dq}) = n\frac{\partial \widetilde{\mathbb{L}}^{dq}}{\partial \theta}(\theta, \dot{\theta}, \mathbf{i}_{dq}) + n\mathbf{i}_{dq}^T\mathcal{J}\frac{\partial \widetilde{\mathbb{L}}^{dq}}{\partial \mathbf{i}_{dq}}(\theta, \dot{\theta}, \mathbf{i}_{dq}) \tag{4.70}$$

where $\mathbf{v}_{dq} = \mathcal{R}_\theta \mathbf{v}_{\alpha\beta}$. The star point voltage v_N does not appear explicitly in the motor dynamic equations (4.67)–(4.70). It is obtained directly from the general energy expression in $dq0$ frame (without star connection) as follows

$$\frac{d}{dt}\left(\frac{\partial \mathcal{L}^{dq0}}{\partial i_0}\Big|_{i_0=0}\right) = v_0 - \sqrt{3}v_N. \tag{4.71}$$

4.2.1.2 Modified Hamiltonian formulation

In the case of a star connection (4.60), the Hamiltonian formulation in $\alpha\beta0$ frame can be written as

$$\frac{d}{dt}\mathbf{\Psi}_{\alpha\beta} = -R\frac{\partial \mathcal{H}^{\alpha\beta0}}{\partial \mathbf{\Psi}_{\alpha\beta}} + \mathbf{v}_{\alpha\beta} \tag{4.72}$$

$$\frac{d}{dt}\Psi_0 = -R\frac{\partial \mathcal{H}^{\alpha\beta0}}{\partial \Psi_0} + v_0 - \sqrt{3}v_N. \tag{4.73}$$

The relation $i_0 = 0$ leads to

$$\frac{\partial \mathcal{H}^{\alpha\beta0}}{\partial \Psi_0}(\theta, p_\theta, \mathbf{\Psi}_{\alpha\beta}, \Psi_0) = 0. \tag{4.74}$$

The equation (4.74) represents a mathematical relation between the motor fluxes. Thus, the flux Ψ_0 can be written as a function of $\mathbf{\Psi}_{\alpha\beta}$ and θ in order to satisfy (4.74), hence we get

$$\Psi_0 = \psi_0(\theta, p_\theta, \mathbf{\Psi}_{\alpha\beta}), \tag{4.75}$$

where ψ_0 verifies

$$\frac{\partial \mathcal{H}^{\alpha\beta0}}{\partial \Psi_0}\Big(\theta, p_\theta, \mathbf{\Psi}_{\alpha\beta}, \psi_0(\theta, p_\theta, \mathbf{\Psi}_{\alpha\beta})\Big) = 0. \tag{4.76}$$

We take

$$\mathbb{H}^{\alpha\beta}(\theta, p_\theta, \mathbf{\Psi}_{\alpha\beta}) = \mathcal{H}^{\alpha\beta0}\Big(\theta, p_\theta, \mathbf{\Psi}_{\alpha\beta}, \psi_0(\theta, p_\theta, \mathbf{\Psi}_{\alpha\beta})\Big),$$

hence (4.72)-(4.73) yield

$$\frac{d}{dt}\mathbf{\Psi}_{\alpha\beta} = -R\frac{\partial \mathbb{H}^{\alpha\beta}}{\partial \mathbf{\Psi}_{\alpha\beta}} + \mathbf{v}_{\alpha\beta} \tag{4.77}$$

and

$$\frac{d}{dt}\Big(\psi_0(\theta, p_\theta, \mathbf{\Psi}_{\alpha\beta})\Big) = v_0 - \sqrt{3}v_N. \tag{4.78}$$

The justification of deriving (4.77) from (4.72) is as follows:

$$\begin{aligned}\frac{\partial \mathbb{H}^{\alpha\beta}}{\partial \mathbf{\Psi}_{\alpha\beta}} &= \frac{\partial}{\partial \mathbf{\Psi}_{\alpha\beta}}\left(\mathcal{H}^{\alpha\beta 0}\Big(\theta, p_\theta, \mathbf{\Psi}_{\alpha\beta}, \psi_0(\theta, p_\theta, \mathbf{\Psi}_{\alpha\beta})\Big)\right)\\ &= \frac{\partial \mathcal{H}^{\alpha\beta 0}}{\partial \mathbf{\Psi}_{\alpha\beta}} + \frac{\partial \mathcal{H}^{\alpha\beta 0}}{\partial \Psi_0}\Big(\theta, p_\theta, \mathbf{\Psi}_{\alpha\beta}, \psi_0(\theta, p_\theta, \mathbf{\Psi}_{\alpha\beta})\Big)\frac{\partial \Psi_0}{\partial \mathbf{\Psi}_{\alpha\beta}}\\ &= \frac{\partial \mathcal{H}^{\alpha\beta 0}}{\partial \mathbf{\Psi}_{\alpha\beta}}\end{aligned}$$

where $\frac{\partial \mathcal{H}^{\alpha\beta 0}}{\partial \Psi_0}\Big(\theta, p_\theta, \mathbf{\Psi}_{\alpha\beta}, \psi_0(\theta, p_\theta, \mathbf{\Psi}_{\alpha\beta})\Big) = 0$, see (4.76).

This result shows that the electrical system can be separated into two parts in the case of the star connection. The first part is represented by (4.77) and it is independent from the 0- axis components. The second part is represented by (4.78), it gives the mathematical expression of the star point voltage v_N.

Finally in $dq0$ frame we take

$$\widetilde{\mathbb{H}}^{dq}(\theta, p_\theta, \mathbf{\Psi}_{dq}) = \mathbb{H}^{\alpha\beta}(\theta, p_\theta, \mathcal{R}_\theta \mathbf{\Psi}_{dq}), \tag{4.79}$$

hence the energy formulation in $dq0$ with star connection type reads

$$\frac{d\mathbf{\Psi}_{dq}}{dt} = -R\frac{\partial \widetilde{\mathbb{H}}^{dq}}{\partial \mathbf{\Psi}_{dq}} + \mathbf{v}_{dq} - \dot{\theta}\mathcal{J}\mathbf{\Psi}_{dq} \tag{4.80}$$

$$\frac{J}{n}\frac{d^2\theta}{dt^2} = -n\frac{\partial \widetilde{\mathbb{H}}^{dq}}{\partial \theta} + n\left(\frac{\partial \widetilde{\mathbb{H}}^{dq}}{\partial \mathbf{\Psi}_{dq}}\right)^T \mathcal{J}\mathbf{\Psi}_{dq} - \tau_L \tag{4.81}$$

$$\tag{4.82}$$

with

$$\mathbf{i}_{dq}(\theta, p_\theta, \mathbf{\Psi}_{dq}) = \frac{\partial \widetilde{\mathbb{H}}^{dq}}{\partial \mathbf{\Psi}_{dq}}(\theta, p_\theta, \mathbf{\Psi}_{dq}) \tag{4.83}$$

$$\tau_e(\theta, p_\theta, \mathbf{\Psi}_{dq}) = -n\frac{\partial \widetilde{\mathbb{H}}^{dq}}{\partial \theta}(\theta, p_\theta, \mathbf{\Psi}_{dq}) + n\left(\frac{\partial \widetilde{\mathbb{H}}^{dq}}{\partial \mathbf{\Psi}_{dq}}(\theta, p_\theta, \mathbf{\Psi}_{dq})\right)^T \mathcal{J}\mathbf{\Psi}_{dq} \tag{4.84}$$

Similarly to the co-energy, the star point voltage v_N does not appear explicitly in the motor dynamic equations (4.80)–(4.81). It is obtained directly from the general energy expression in $dq0$ frame (without star connection) as follows

$$\frac{d}{dt}\Big(\psi_0(\theta, p_\theta, \mathcal{R}_\theta \mathbf{\Psi}_{dq})\Big) = v_0 - \sqrt{3}v_N. \tag{4.85}$$

In this section we addressed the PMSM motors with star connection type; this type of motor will be used in the sequel. In addition we will use only the motor model in dq frame because this

frame is more suitable for position estimation and sensorless control which are the main objectives of this work. Thanks to the star connection, the motor dynamical system can be separated into two main parts. The first part is a scalar equation which gives the expression of the star point voltage v_N (4.71)-(4.85). This voltage does not affect the motor operation and does not appear in the motor equations, hence it is not important to be considered unless when it is measured, because in this case it can provide important information about the motor variables, but in the sequel we do not use this voltage for control purpose.

The second part which is more important is a dynamical system having two electrical state variables instead of three. The dynamical system equations are (4.67)–(4.70) when we use the co-energy or (4.80)–(4.84) when we use the energy. These systems are simple to be used because we need only the expression of $\widetilde{\mathbb{L}}^{dq}$ or $\widetilde{\mathbb{H}}^{dq}$ to describe the dynamic behavior of the motor. In the next section, we study the symmetries presented by construction in the motor in order to simplify the expression of the energy functions.

4.2.2 Symmetry considerations

We use geometric symmetries presented by construction in the motor in order to simplify the motor energy expression. A standard symmetric three phase PMSM has three geometric symmetries which are independent from the motor operation and are due only to the motor construction. We denote these symmetries by permutation symmetry; orientation symmetry and reflection symmetry.

Permutation symmetry: a PMSM have three identical phase windings. Each phase winding is shifted by $\frac{2\pi}{3}$ with respect to the other phases. Thus, in abc frame the co-energy and the energy are not modified by a circular permutation of the current variables $\mathbf{i}_{abc} \mapsto \mathbf{C}\mathbf{i}_{abc}$ and the flux variables $\mathbf{\Psi}_{abc} \mapsto \mathbf{C}\mathbf{\Psi}_{abc}$ where

$$\mathbf{C} = \begin{pmatrix} 0 & 1 & 0 \\ 0 & 0 & 1 \\ 1 & 0 & 0 \end{pmatrix},$$

hence we get

$$\mathcal{L}^{abc}(\theta, \dot{\theta}, \mathbf{i}_{abc}) = \mathcal{L}^{abc}(\theta - \tfrac{2\pi}{3}, \dot{\theta}, \mathbf{C}\mathbf{i}_{abc}); \tag{4.86}$$

$$\mathcal{H}^{abc}(\theta, p_\theta, \mathbf{\Psi}_{abc}) = \mathcal{H}^{abc}(\theta - \tfrac{2\pi}{3}, p_\theta, \mathbf{C}\mathbf{\Psi}_{abc}). \tag{4.87}$$

Orientation symmetry: the energy does not vary if we replace the position θ by $-\theta$ and we interchange the phase b and the phase c such that the current variables $\mathbf{i}_{abc} \mapsto \mathbf{O}\mathbf{i}_{abc}$ and the fluxes variables $\mathbf{\Psi}_{abc} \mapsto \mathbf{O}\mathbf{\Psi}_{abc}$ where

$$\mathbf{O} = \begin{pmatrix} 1 & 0 & 0 \\ 0 & 0 & 1 \\ 0 & 1 & 0 \end{pmatrix}.$$

Indeed, the energy does not change when the motor rotates in clockwise direction or counterclockwise direction. Thus, we have

$$\mathcal{L}^{abc}(\theta, \dot{\theta}, \mathbf{i}_{abc}) = \mathcal{L}^{abc}(-\theta, -\dot{\theta}, \mathbf{O}\mathbf{i}_{abc}); \tag{4.88}$$

$$\mathcal{H}^{abc}(\theta, p_\theta, \mathbf{\Psi}_{abc}) = \mathcal{H}^{abc}(-\theta, -p_\theta, \mathbf{O}\mathbf{\Psi}_{abc}). \tag{4.89}$$

In this case we consider that the rotor flux is aligned with the phase a when the electrical position $\theta = 0$.

Reflection symmetry: the energy remains unchanged if we invert the current direction and the flux direction $\mathbf{i}_{abc} \mapsto -\mathbf{i}_{abc}, \quad \mathbf{\Psi}_{abc} \mapsto -\mathbf{\Psi}_{abc}$ and we add a half cycle to the position $\theta \mapsto \pi + \theta$. Indeed, the motor windings have a periodicity of π electrical radian, hence if we invert the direction of the current and the flux and we rotate the rotor magnet by a π electrical radian then we will get the same configuration of the motor and the energy will remain unchanged. Thus we get

$$\mathcal{L}^{abc}(\theta, \dot{\theta}, \mathbf{i}_{abc}) = \mathcal{L}^{abc}(\theta + \pi, \dot{\theta}, -\mathbf{i}_{abc}); \tag{4.90}$$
$$\mathcal{H}^{abc}(\theta, p_\theta, \mathbf{\Psi}_{abc}) = \mathcal{H}^{abc}(\theta + \pi, p_\theta, -\mathbf{\Psi}_{abc}). \tag{4.91}$$

Using the Clarke transformation (4.19), hence in $\alpha\beta 0$ the symmetries (4.86)–(4.91) lead to

$$\mathcal{L}^{\alpha\beta 0}(\theta, \dot{\theta}, \mathbf{i}_{\alpha\beta_0}) = \mathcal{L}^{\alpha\beta 0}(\theta - \tfrac{2\pi}{3}, \dot{\theta}, \mathbf{UCU}^T \mathbf{i}_{\alpha\beta_0}) \tag{4.92}$$
$$\mathcal{L}^{\alpha\beta 0}(\theta, \dot{\theta}, \mathbf{i}_{\alpha\beta_0}) = \mathcal{L}^{\alpha\beta 0}(-\theta, -\dot{\theta}, \mathbf{UOU}^T \mathbf{i}_{\alpha\beta_0}) \tag{4.93}$$
$$\mathcal{L}^{\alpha\beta 0}(\theta, \dot{\theta}, \mathbf{i}_{\alpha\beta_0}) = \mathcal{L}^{\alpha\beta 0}(\theta + \pi, \dot{\theta}, -\mathbf{i}_{\alpha\beta_0}) \tag{4.94}$$

and

$$\mathcal{H}^{\alpha\beta 0}(\theta, p_\theta, \mathbf{\Psi}_{\alpha\beta_0}) = \mathcal{H}^{\alpha\beta 0}(\theta - \tfrac{2\pi}{3}, p_\theta, \mathbf{UCU}^T \mathbf{\Psi}_{\alpha\beta_0}) \tag{4.95}$$
$$\mathcal{H}^{\alpha\beta 0}(\theta, p_\theta, \mathbf{\Psi}_{\alpha\beta_0}) = \mathcal{H}^{\alpha\beta 0}(-\theta, -p_\theta, \mathbf{UOU}^T \mathbf{\Psi}_{\alpha\beta_0}) \tag{4.96}$$
$$\mathcal{H}^{\alpha\beta 0}(\theta, p_\theta, \mathbf{\Psi}_{\alpha\beta_0}) = \mathcal{L}^{\alpha\beta 0}(\theta + \pi, p_\theta, -\mathbf{\Psi}_{\alpha\beta_0}) \tag{4.97}$$

where

$$\mathbf{UCU}^T = \begin{pmatrix} -\frac{1}{2} & \frac{\sqrt{3}}{2} & 0 \\ -\frac{\sqrt{3}}{2} & -\frac{1}{2} & 0 \\ 0 & 0 & 1 \end{pmatrix}$$

and

$$\mathbf{UOU}^T = \begin{pmatrix} 1 & 0 & 0 \\ 0 & -1 & 0 \\ 0 & 0 & 1 \end{pmatrix}.$$

In $dq0$ frame, using the Park transformation (4.25), hence (4.92)–(4.94) lead to

$$\widetilde{\mathcal{L}}^{dq0}(\theta, \dot{\theta}, i_d, i_q, i_0) = \widetilde{\mathcal{L}}^{dq0}(\theta - \tfrac{2\pi}{3}, \dot{\theta}, i_d, i_q, i_0) \tag{4.98}$$
$$\widetilde{\mathcal{L}}^{dq0}(\theta, \dot{\theta}, i_d, i_q, i_0) = \widetilde{\mathcal{L}}^{dq0}(\theta + \pi, \dot{\theta}, i_d, i_q, -i_0) \tag{4.99}$$
$$\widetilde{\mathcal{L}}^{dq0}(\theta, \dot{\theta}, i_d, i_q, i_0) = \widetilde{\mathcal{L}}^{dq0}(-\theta, -\dot{\theta}, i_d, -i_q, i_0). \tag{4.100}$$

and

$$\widetilde{\mathcal{H}}^{dq0}(\theta, p_\theta, \Psi_d, \Psi_q, \Psi_0) = \widetilde{\mathcal{H}}^{dq0}(\theta - \tfrac{2\pi}{3}, p_\theta, \Psi_d, \Psi_q, \Psi_0) \tag{4.101}$$
$$\widetilde{\mathcal{H}}^{dq0}(\theta, p_\theta, \Psi_d, \Psi_q, \Psi_0) = \widetilde{\mathcal{H}}^{dq0}(\theta + \pi, p_\theta, \Psi_d, \Psi_q, -\Psi_0) \tag{4.102}$$
$$\widetilde{\mathcal{H}}^{dq0}(\theta, p_\theta, \Psi_d, \Psi_q, \Psi_0) = \widetilde{\mathcal{H}}^{dq0}(-\theta, -p_\theta, \Psi_d, -\Psi_q, \Psi_0). \tag{4.103}$$

It is obvious that the symmetry relations (4.86)–(4.103) are verified in the case of a sinusoidal PMSM with linear magnetic model.

In the case of a star connection, using (4.63)-(4.66) and (4.92)–(4.94), hence the co-energy $\widetilde{\mathbb{L}}^{dq}$ verifies

$$\widetilde{\mathbb{L}}^{dq}(\theta, \dot{\theta}, i_d, i_q) = \widetilde{\mathbb{L}}^{dq}(\theta + \tfrac{\pi}{3}, \dot{\theta}, i_d, i_q), \tag{4.104}$$

$$\widetilde{\mathbb{L}}^{dq}(\theta, \dot{\theta}, i_d, i_q) = \widetilde{\mathbb{L}}^{dq}(-\theta, -\dot{\theta}, i_d, -i_q). \tag{4.105}$$

and the energy $\widetilde{\mathbb{H}}^{dq}$ verifies

$$\widetilde{\mathbb{H}}^{dq}(\theta, p_\theta, \Psi_d, \Psi_q) = \widetilde{\mathbb{H}}^{dq}(\theta + \tfrac{\pi}{3}, p_\theta, \Psi_d, \Psi_q), \tag{4.106}$$

$$\widetilde{\mathbb{H}}^{dq}(\theta, p_\theta, \Psi_d, \Psi_q) = \widetilde{\mathbb{H}}^{dq}(-\theta, -p_\theta, \Psi_d, -\Psi_q) \tag{4.107}$$

We presented in this section the geometric symmetries of the PMSM and their impact on the energy functions. These symmetry considerations help to simplify the energy and co-energy expressions. For example, the equations (4.104)–(4.107) show that in dq frame, if the energy depends on θ then it must be $\frac{\pi}{3}$-periodic function which simplify consequently the energy expression. In the sequel, we propose an explicit expression of the energy of the non sinusoidal PMSM with star connection type using the geometric symmetries. In addition, we propose an energy expression of sinusoidal PMSM taking into account cross coupling and magnetic saturation effects.

4.2.3 Non sinusoidal motor

In this part, we consider the non sinusoidal PMSM in order to explain the non sinusoidal shape of the back electromotive force voltage (BEMF), and the current harmonics in $dq0$ frame and the torque oscillations (cogging torque). In addition, we give an interpretation of the shape of the star point voltage. The motor equations will be written only in $dq0$ frame.

In general the stator windings of a PMSM are not sinusoidal. For example, in the case of trapezoidal permanent magnet motor, the stator windings are distributed in a trapezoidal shape. In this case, the BEMF voltage is not sinusoidal and the electromagnetic torque is not constant but it depends on the rotor position. This can be explained by the dependence of the energy function in $dq0$ on the rotor position θ.

The relation between the energy and the position must respect the symmetry considerations established in the previous subsection. According to (4.104) and (4.106) $\widetilde{\mathbb{L}}^{dq}$ and $\widetilde{\mathbb{H}}^{dq}$ are $\frac{\pi}{3}$ periodic versus θ. Therefore, the co-energy $\widetilde{\mathbb{L}}^{dq}$ (resp. the energy $\widetilde{\mathbb{H}}^{dq}$) can be decomposed into an independent term of θ : $\widetilde{\mathbb{L}}_0^{dq}$ (resp. $\widetilde{\mathbb{H}}_0^{dq}$) and a dependent term of θ that can be expressed as a $\frac{\pi}{3}$ periodic function of θ: $\widetilde{\mathbb{L}}_6^{dq}$ (resp. $\widetilde{\mathbb{H}}_6^{dq}$) as follows

$$\widetilde{\mathbb{L}}^{dq}(\theta, \dot{\theta}, \mathbf{i}_{dq}) = \widetilde{\mathbb{L}}_0^{dq}(\dot{\theta}, \mathbf{i}_{dq}) + \widetilde{\mathbb{L}}_6^{dq}(6\theta, \dot{\theta}, \mathbf{i}_{dq}) \tag{4.108}$$

$$\widetilde{\mathbb{H}}^{dq}(\theta, p_\theta, \mathbf{\Psi}_{dq}) = \widetilde{\mathbb{H}}_0^{dq}(p_\theta, \mathbf{\Psi}_{dq}) + \widetilde{\mathbb{H}}_6^{dq}(6\theta, p_\theta, \mathbf{\Psi}_{dq}) \tag{4.109}$$

where $\widetilde{\mathbb{L}}_6^{dq}$ and $\widetilde{\mathbb{H}}_6^{dq}$ contain all sinusoidal harmonics of θ of order $6k$ where k in a nonzero positive integer. The independent terms of θ in (4.108) and (4.109) are in general the dominant terms when the motor windings are close to sinusoidal windings, in this case the energy is supposed to be independent

of θ in dq frame. Otherwise, the dependent terms of θ in (4.108) and (4.109) have an important impact on the motor behavior and they cannot be neglected when the motor has strong non sinusoidal windings as trapezoidal motors; it is important to note that in this case the oscillating terms in the energy contain only the harmonics of 6θ.

Using (4.83)–(4.84) and (4.109) hence the motor current and torque in dq frame can be written as

$$\mathbf{i}_{dq}(\theta,\dot{\theta},\mathbf{\Psi}_{dq}) = \frac{\partial\widetilde{\mathbb{H}}_0^{dq}}{\partial\mathbf{\Psi}_{dq}}(\dot{\theta},\mathbf{\Psi}_{dq}) + \frac{\partial\widetilde{\mathbb{H}}_6^{dq}}{\partial\mathbf{\Psi}_{dq}}(\theta,\dot{\theta},\mathbf{\Psi}_{dq})$$
$$\tau_e(\theta,\dot{\theta},\mathbf{\Psi}_{dq}) = n\left(-\frac{\partial\widetilde{\mathbb{H}}_6^{dq}}{\partial\theta}(\theta,\dot{\theta},\mathbf{\Psi}_{dq}) + \mathbf{i}_{dq}^T(\theta,\dot{\theta},\mathbf{\Psi}_{dq})\mathcal{J}\mathbf{\Psi}_{dq}\right)$$

hence the oscillating terms of the current $\mathbf{i}_{dq}$ and the torque τ_e contain only the harmonics of 6θ. The position dependent term of τ_e is called cogging torque. This dependence is well known and observed experimentally [76–78]. Fig. 4.4 shows the experimental shape of the current i_q and the torque τ_e in terms of θ for the IPM and SPM motors whose parameters are listed in table 6.1. We used small values of q- axis current and load torque to highlight the position dependent components. It is clear in this figure that for one period of rotor electrical position θ we have 6 oscillations of τ_e and i_q. These oscillations have small amplitudes (about 6% of rated values), they don't modify the normal behavior of the motor. For these reasons we neglect $\widetilde{\mathbb{H}}_6^{dq}$ for PMSM used in this work and we suppose that the energy does not depend explicitly on the rotor position in dq frame (sinusoidal approximation). The term $\widetilde{\mathbb{H}}_6^{dq}$ can be considered in future work to get a more precise model of PMSM.

It remains to characterize the shape of the star point voltage v_N in the case of a non sinusoidal motor. This voltage does not appear explicitly in the motor dynamic equations, it can be obtained from the energy function using (4.71) and (4.85). As for the current and torque, v_N depends on θ in the case of a non sinusoidal motor. According to (4.92)-(4.95) $\widetilde{\mathcal{L}}^{dq0}$ and $\widetilde{\mathcal{H}}^{dq0}$ and ψ_0 are $\frac{2\pi}{3}$ periodic versus θ (the period is not $\frac{\pi}{3}$ due to the dependence on the 0- axis component). The equations (4.71) and (4.85) lead to

$$\sqrt{3}v_N(\theta) = v_0 - \frac{d}{dt}\Big(\psi_0(\theta,p_\theta,\mathcal{R}_\theta\mathbf{\Psi}_{dq})\Big) = v_0 - \left(\frac{\partial\widetilde{\mathcal{L}}^{dq0}}{\partial i_0}(\theta,\dot{\theta},\mathbf{i}_{dq},0)\right), \tag{4.110}$$

hence v_N is $\frac{2\pi}{3}$ periodic versus θ. Therefore, using Fourier series, we show that v_N contains only the $3k\theta$ harmonics of where k is a positive integer. To verify this result, we measure the voltage v_N experimentally. We used a different PMSM in order to have access to the stator star point because this point is not accessible for the other two motors; the parameter of this motor are listed in table 4.1. Fig. 4.5 shows the shape of v_N in terms of θ. It is clear in this figure that v_N contains exclusively the harmonics components multiple of 3θ and it is $\frac{2\pi}{3}$-periodic function versus θ.

Fig 4.6 shows the voltage across the stator windings $u_a = v_a - v_N$, $u_b = v_b - v_N$ and $u_c = v_c - v_N$ of the motor 4.1 when the stator currents are zero such $i_a = i_b = i_c = 0$. In this case the measured voltages are the the back electromotive voltages (BEMF). This figure shows that the voltages u_a, u_b and u_c are not sinusoidal and the main harmonics components of the voltages are the $3k\theta$ harmonics caused mainly by the star point voltage v_N.

In this section we investigated the dependence of the PMSM energy on on the rotor position in $dq0$ frame. To get an idea of this dependence, we consider the case of a PMSM with linear magnet in the next section.

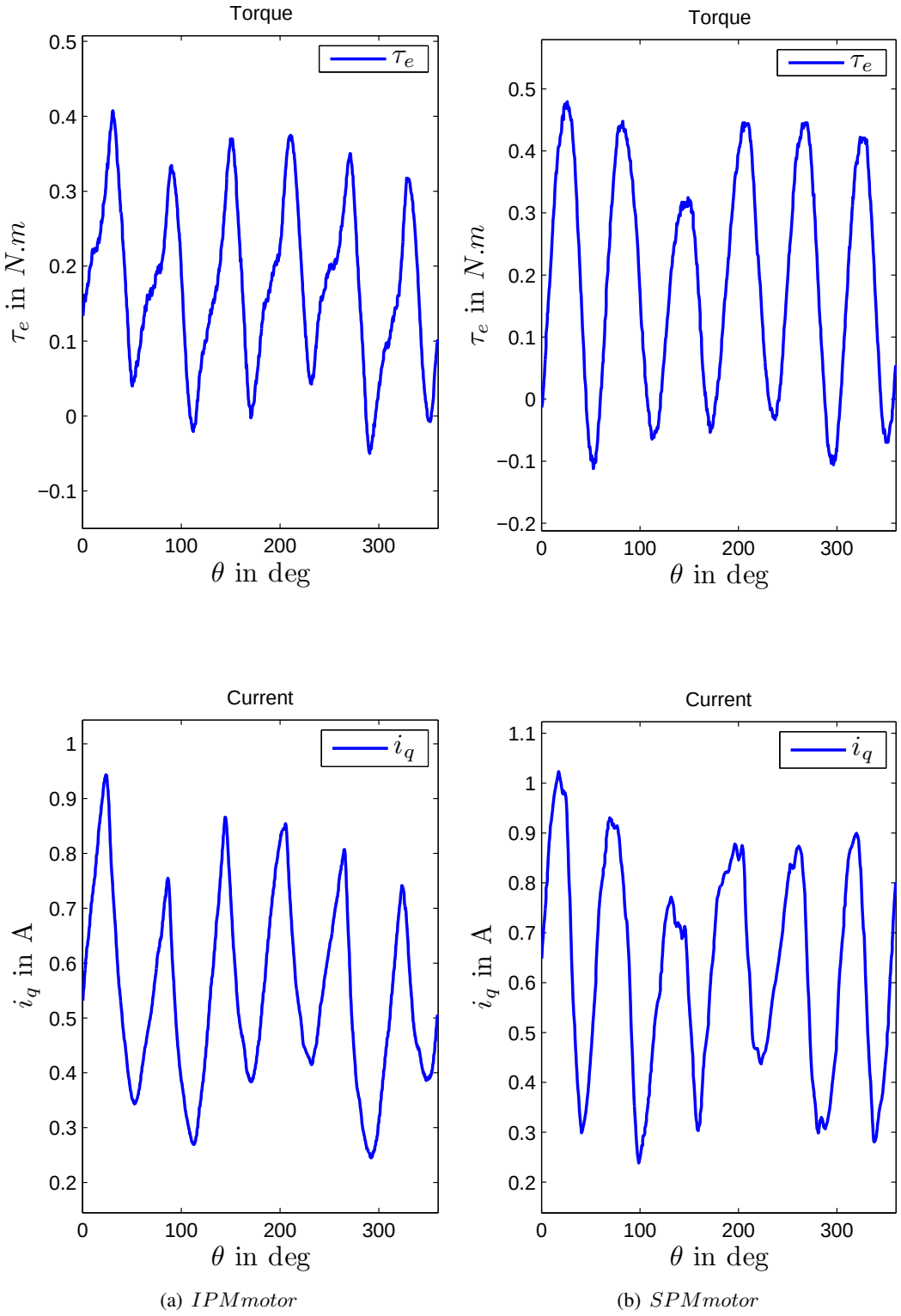

(a) $IPMmotor$ (b) $SPMmotor$

Figure 4.4: Current i_q and electromagnetic torque τ_e in terms of θ

Table 4.1: Rated parameters of the PMSM with star point access

Motor	SPM2	IPM2
Rated power	4 kW	200 W
Rated current I_n (peak)	7 A	1.2 A
Rated voltage (peak per phase)	110 V	136 V
Rated speed	1500 rpm	180 rpm
Rated torque	20 Nm	1.06 N.m
n	2	2
R	1.52 Ω	12.15 Ω
λ (peak)	196 mWb	150 mWb

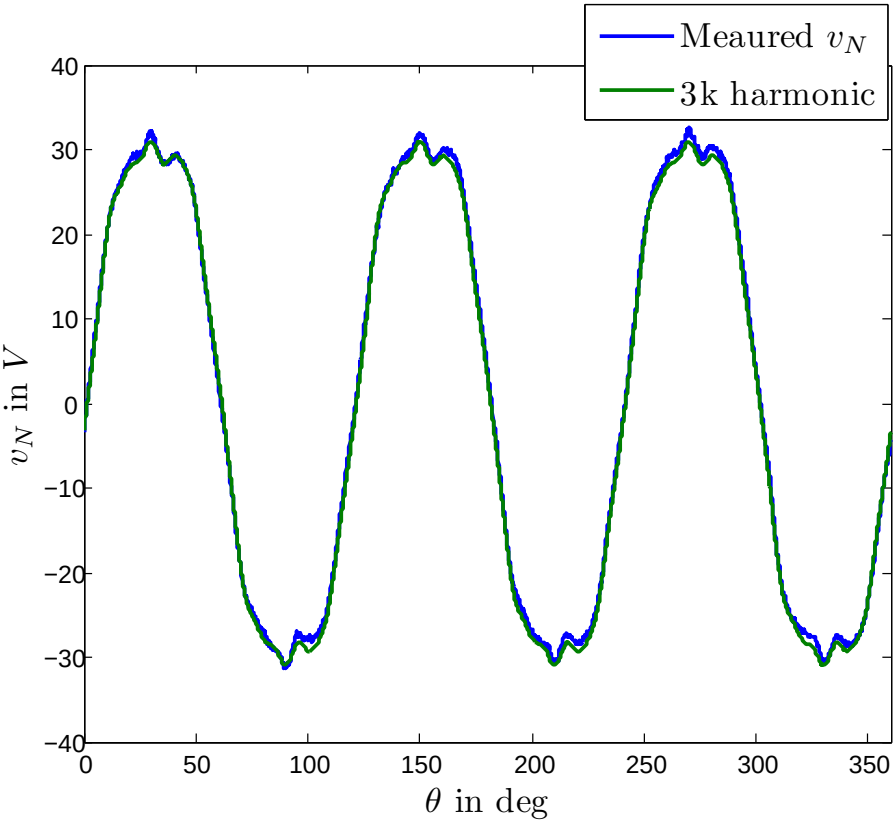

Figure 4.5: Star point voltage v_N in terms of θ

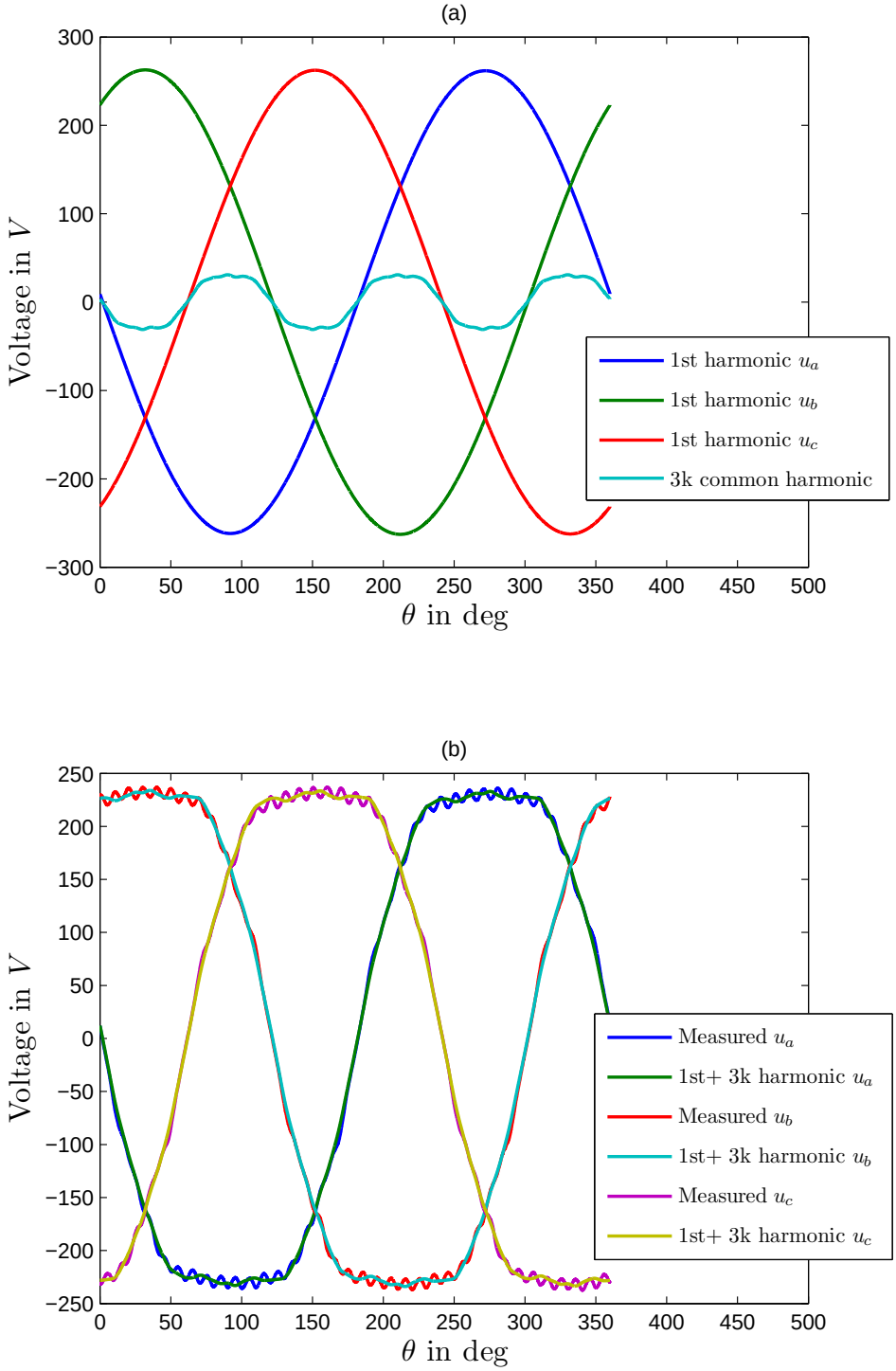

Figure 4.6: BEMF voltages: (a) first harmonics of the voltages u_a, u_b and uc and their common third harmonic versus θ; (b) measured u_a, u_b and uc vs. the sum of their first and third harmonics

4.2.3.1 Linear magnetic model

In this section, we study the case of the star connection configuration considering linear magnetics i.e. when the flux is a linear function of the current. In this case, the relation between the flux and the current in dq frame can be written as follows

$$\mathbf{\Psi}_{dq} = \mathbf{L}^{dq}(\theta)\mathbf{i}_{dq} + \mathbf{\Phi}_m(\theta), \tag{4.111}$$

with

$$\mathbf{L}^{dq}(\theta) = \begin{pmatrix} l^{dd}(\theta) & l^{dq}(\theta) \\ l^{dq}(\theta) & l^{qq}(\theta) \end{pmatrix}$$

and

$$\mathbf{\Phi}_m(\theta) = \begin{pmatrix} \phi_d^m(\theta) \\ \phi_q^m(\theta) \end{pmatrix}$$

where l^{dd} is the d- axis self inductance; l^{qq} is the q- axis self inductance, l^{dq} is the mutual inductance between d- and q- axis; ϕ_d^m is the d- axis permanent magnet component and ϕ_q^m is the q- axis permanent magnet component; $\mathbf{L}^{dq}$ is the symmetric inductance matrix in dq frame; $\mathbf{\Phi}_m$ is the permanent magnet flux vector; for instance we suppose that all these variables depend on θ. We don't consider the 0-axis components and the voltage v_N because in the case of star connection, these components are decoupled from the dq motor components. Using (4.69) and (4.111), hence the expression of the co-energy $\widetilde{\mathbb{L}}^{dq}$ can be written as follows

$$\widetilde{\mathbb{L}}^{dq}(\theta, \dot{\theta}, \mathbf{i}_{dq}) = \frac{J}{2n^2}\dot{\theta}^2 + \frac{1}{2}\mathbf{i}_{dq}^T\mathbf{L}^{dq}(\theta)\mathbf{i}_{dq} + \mathbf{\Phi}_m(\theta)^T\mathbf{i}_{dq}. \tag{4.112}$$

The symmetry conditions (4.104)-(4.105) leads to

$$\begin{aligned}
&l^{dd}(\theta) = l^{dd}(-\theta), \quad l^{dd}(\theta + \tfrac{\pi}{3}) = l^{dd}(\theta) \\
&l^{qq}(\theta) = l^{qq}(-\theta), \quad l^{qq}(\theta + \tfrac{\pi}{3}) = l^{qq}(\theta) \\
&l^{dq}(\theta) = -l^{dq}(-\theta), \quad l^{dq}(\theta + \tfrac{\pi}{3}) = l^{dq}(\theta) \\
&\phi_d^m(\theta) = \phi_d^m(-\theta), \quad \phi_d^m(\theta + \tfrac{\pi}{3}) = \phi_d^m(\theta) \\
&\phi_q^m(\theta) = -\phi_q^m(-\theta), \quad \phi_q^m(\theta + \tfrac{\pi}{3}) = \phi_q^m(\theta).
\end{aligned} \tag{4.113}$$

The fourier expansion with respect to θ of the motor parameter yields

$$
\begin{aligned}
l^{dd}(\theta) &= l_0^{dd} + \sum_{k=1}^{+\infty} l_k^{dd} \cos 6k\theta \\
l^{qq}(\theta) &= l_0^{qq} + \sum_{k=1}^{+\infty} l_k^{qq} \cos 6k\theta \\
l^{dq}(\theta) &= 0 + \sum_{k=1}^{+\infty} l_k^{dq} \sin 6k\theta \\
\phi_d^m(\theta) &= \phi_{d0}^m + \sum_{k=1}^{+\infty} \phi_{dk}^m \cos 6k\theta \\
\phi_q^m(\theta) &= 0 + \sum_{k=1}^{+\infty} \phi_{qk}^m \sin 6k\theta
\end{aligned}
$$

where l_0^{dd} and l_0^{qq} are dominant motor inductances; ϕ_{d0}^m is the dominant permanent magnet flux component. For $k \geq 1$ the parameters l_k^{dd}, l_k^{qq}, l_k^{dq}, ϕ_{dk}^m and, ϕ_{qk}^m are small and they are due to the non sinusoidal windings effects of the motor. In the case of sinusoidal motors, the position dependent terms in the inductances and magnetic flux are zero, hence we recover the standard sinusoidal PMSM model with linear magnet

$$
l^{dd}(\theta) = l_0^{dd} = L_d, \quad l^{qq}(\theta) = l_0^{qq} = L_q, \quad l^{dq}(\theta) = \phi_q^m(\theta) = 0 \quad \phi_d^m(\theta) = \lambda.
$$

In this section we presented the non sinusoidal PMSM model and particularly in the case of PMSM with linear magnets. When the motor windings are close to sinusoidal windings the oscillating terms in the energy and in the motor variables in dq frame are small and can be neglected. In the sequel we consider sinusoidal PMSM such that the energy in dq does not depend on the rotor position θ and we propose an expression of the motor energy taking into account nonlinear effects of magnetic and cross coupling saturation. We will use only the energy formulation in dq with star connection given by (4.80)–(4.84) and we propose an explicit expression of the energy $\widetilde{\mathbb{H}}^{dq}$.

In the next parts, we need from all the previous work only the energy model in dq frame and the orientation symmetry which are as follows

$$
\left.
\begin{aligned}
\frac{d\mathbf{\Psi}_{dq}}{dt} &= -R\mathbf{i}_{dq} + \mathbf{v}_{dq} - \dot{\theta}\mathcal{J}\mathbf{\Psi}_{dq} \\
\frac{J}{n}\frac{d^2\theta}{dt^2} &= \tau_e - \tau_L \\
\mathbf{i}_{dq}(\theta, p_\theta, \mathbf{\Psi}_{dq}) &= \frac{\partial \widetilde{\mathbb{H}}^{dq}}{\partial \mathbf{\Psi}_{dq}}(\theta, p_\theta, \mathbf{\Psi}_{dq}) \\
\tau_e(\theta, p_\theta, \mathbf{\Psi}_{dq}) &= -n\frac{\partial \widetilde{\mathbb{H}}^{dq}}{\partial \theta}(\theta, p_\theta, \mathbf{\Psi}_{dq}) + n\left(\frac{\partial \widetilde{\mathbb{H}}^{dq}}{\partial \mathbf{\Psi}_{dq}}(\theta, p_\theta, \mathbf{\Psi}_{dq})\right)^T \mathcal{J}\mathbf{\Psi}_{dq} \\
\widetilde{\mathbb{H}}^{dq}(\theta, p_\theta, \Psi_d, \Psi_q) &= \widetilde{\mathbb{H}}^{dq}(-\theta, -p_\theta, \Psi_d, -\Psi_q) \\
\widetilde{\mathbb{H}}^{dq}(\theta, p_\theta, \Psi_d, \Psi_q) &= \widetilde{\mathbb{H}}^{dq}(\theta + \tfrac{\pi}{3}, p_\theta, \Psi_d, \Psi_q)
\end{aligned}
\right\} \tag{4.114}
$$

4.3 Proposed model with magnetic saturation

In this section we propose a saturation model of sinusoidal PMSM motors, this model takes into account cross coupling and magnetic saturation effects. It is based on the energy approach developed in the previous sections (4.114). To get the energy expression of the saturated PMSM, we modify the energy of the PMSM with linear magnetics where we add additional higher order terms to the linear energy expression. The added terms have a simple polynomial shape and contain only five additional parameters which can be estimated by simple linear least square. The energy is expressed in terms of fluxes; the expressions of currents in terms of fluxes are equal to the partial derivatives of the energy with respect to the fluxes. The important feature of this model is that we need only one simple polynomial energy function to describe the saturation effects and to get the current and torque expressions.

We consider here only the sinusoidal PMSM where the stator windings are sinusoidal and the energy in dq frame does not depend on θ. We suppose also that the total flux $\mathbf{\Psi}_{dq} = (\Psi_d, \Psi_q)^T$ is the sum of an electric flux $\mathbf{\Phi}_{dq} = (\phi_d, \phi_q)^T$ and a constant flux (permanent magnet flux) $\mathbf{\Phi}_m = (\lambda, 0)^T$ where $\phi_d^m = \lambda$ and $\phi_q^m = 0$ such that

$$\mathbf{\Psi}_{dq} = \mathbf{\Phi}_{dq} + \mathbf{\Phi}_m,$$

hence

$$\begin{aligned} \phi_d &= \Psi_d - \lambda \\ \phi_q &= \Psi_q \end{aligned}$$

where λ is the amplitude of the magnet flux in dq frame. Indeed, for standard sinusoidal PMSM motors, the magnetic flux amplitude is much higher than the electrical flux amplitude, hence we suppose that the variation of the electric fluxes do not impact the constant magnet flux and therefore these two fluxes can be decoupled.

We consider the case of a sinusoidal PMSM with star connection type and we use the motor energy $\widetilde{\mathbb{H}}^{dq}$ defined by (4.79). The PMSM energy $\widetilde{\mathbb{H}}^{dq}$ is the sum of a mechanical energy equal to $\frac{1}{2Jn^2}p_\theta^2$ and a magnetic energy denoted $\mathcal{H}$ which depend only on electric fluxes and is independent from the position θ and the moment p_θ; $\mathcal{H}$ is equal to the difference between the total energy and the mechanical energy as follows

$$\mathcal{H}(\phi_d, \phi_q) = \widetilde{\mathbb{H}}^{dq}(\theta, p_\theta, \phi_d + \lambda, \phi_q) - \frac{1}{2Jn^2}p_\theta^2. \tag{4.115}$$

$\mathcal{H}(\phi_d, \phi_q)$ is the total magnetic energy of the PMSM and it is expressed in terms of the electric fluxes ϕ_d and ϕ_q. In general, this magnetic energy does not depend on the rotor speed $\dot{\theta}$ because the magnetic energy of a motor is the same whatever the level of its speed; only the mechanical energy depends of the rotor speed $\dot{\theta}$. In the sequel we suppose that the magnetic energy of the PMSM depends only on the electric fluxes ϕ_d and ϕ_q and we propose an explicit expression of this energy.

The dynamic PMSM model in (4.114) and (4.115) leads to

$$\frac{d\mathbf{\Phi}_{dq}}{dt} = \mathbf{v}_{dq} - R\mathbf{i}_{dq} - \omega\mathcal{J}(\mathbf{\Phi}_{dq} + \mathbf{\Phi}_m) \tag{4.116}$$

$$\frac{J}{n^2}\frac{d\omega}{dt} = \mathbf{i}_{dq}^T\mathcal{J}(\mathbf{\Phi}_{dq} + \mathbf{\Phi}_m) - \frac{\tau_L}{n} \tag{4.117}$$

$$\frac{d\theta}{dt} = \omega \tag{4.118}$$

with

$$i_d = \frac{\partial\mathcal{H}}{\partial\phi_d}(\phi_d, \phi_q) \tag{4.119}$$

$$i_q = \frac{\partial\mathcal{H}}{\partial\phi_q}(\phi_d, \phi_q) \tag{4.120}$$

and

$$\tau_e = n\mathbf{i}_{dq}^T\mathcal{J}(\mathbf{\Phi}_{dq} + \mathbf{\Phi}_m) \tag{4.121}$$

where $\omega = \dot{\theta} = \frac{d\theta}{dt}$ is the motor speed. The symmetry relation (4.107) leads to

$$\mathcal{H}(\phi_d, -\phi_q) = \mathcal{H}(\phi_d, \phi_q), \tag{4.122}$$

this relation means that the expression for $\mathcal{H}$ should respect the symmetry of the PMSM with respect to the direct axis.

The PMSM dynamic model given by (4.116)–(4.122) is the model which will be used in the sequel and in the next chapters.

4.3.1 The case of standard linear magnetic model

For a PMSM with linear magnetics, the magnetic energy is the sum of the square of the flux divided by twice of the inductance of each axis. Using (4.59), this energy function reads

$$\mathcal{H}_l(\phi_d, \phi_q) = \frac{1}{2L_d}\phi_d^2 + \frac{1}{2L_q}\phi_q^2 \tag{4.123}$$

where L_d and L_q are the motor self-inductances. Using (4.119)–(4.120), we recover the usual linear relations

$$i_d = \frac{\partial\mathcal{H}_l}{\partial\phi_d}(\phi_d, \phi_q) = \frac{\phi_d}{L_d} \tag{4.124}$$

$$i_q = \frac{\partial\mathcal{H}_l}{\partial\phi_q}(\phi_d, \phi_q) = \frac{\phi_q}{L_q}. \tag{4.125}$$

It is obvious that $\mathcal{H}_l$ respects the symmetry relation (4.122). Indeed (4.116)–(4.118) and (4.123) are left unchanged by the transformation

$$(v_d, v_q, \phi_d, \phi_q, i_d, i_q, \omega, \theta, \tau_L) \to (v_d, -v_q, \phi_d, -\phi_q, i_d, -i_q, -\omega, -\theta, -\tau_L).$$

4.3.2 Existing saturation models

In the last fifteen years, the modeling of PMSM with magnetic saturation was widely investigated in the literature [79–92]. Many models of saturated PMSM were proposed for several purposes. Moreover, we find in the literature various saturation models of PMSM dedicated for sensorless position estimation which is the main concern of our work [28, 43–63]. In fact, the saturation compensation is important for sensorless position estimation at low speed; this will be detailed in chapter 5.

In general, the magnetic saturation is represented by two relations between currents and fluxes in dq frame. In this case, the d- axis flux depends on the q- axis current and vice versa [55, 61, 84, 85]. The standard relations (4.124)–(4.125) are substituted by

$$\phi_d = L_d i_d + l_m i_q \tag{4.126}$$

$$\phi_q = l_m i_d + L_q i_q \tag{4.127}$$

where L_d and L_q are the standard d- axis and q- axis inductances; l_m is a mutual inductance between d- axis and q- axis. The inductances L_d, L_q and l_m are no more constant; but they depend on the load torque and the current level i.e. the motor operation point.

Thus, the saturation modeling consists of finding the relations between L_d, L_q, l_m and the currents i_d and i_q. They are obtained form the fluxes ϕ_d and ϕ_q as follows

$$L_d(i_d, i_q) = \frac{\partial \phi_d}{\partial i_d}(i_d, i_q) \tag{4.128}$$

$$L_q(i_d, i_q) = \frac{\partial \phi_q}{\partial i_q}(i_d, i_q) \tag{4.129}$$

$$l_m(i_d, i_q) = \frac{\partial \phi_d}{\partial i_q}(i_d, i_q) = \frac{\partial \phi_q}{\partial i_d}(i_d, i_q). \tag{4.130}$$

These inductances are the incremental motor inductances.

There are multiple ways used to model the relation between the fluxes and currents, they can be summarized as follows:

- by using finite element models [56, 58, 60, 63, 93]. The fluxes and inductances are obtained at each operation point by numerical finite element calculations. This modeling method requires the knowledge of the stator and rotor construction dimensions and parameters and it needs a heavily offline computations;
- by experimental measurement [43, 49, 84, 85] of the fluxes using the integration of the motor voltage equations at locked rotor position ($\omega = 0$):

$$\mathbf{\Phi}_{dq} = \int (\mathbf{u}_{dq} - R\mathbf{i}_{dq})\, dt;$$

- analysis of the equivalent magnetic circuit of PMSM [28, 79, 82, 86];
- modeling of the stator inductances by fourier series expansion [91];
- measurement of the stator inductances by HF voltage injection [94];

- by finding an explicit parametric expressions of inductances in terms of currents using trigonometric, fractional or power functions [80, 81, 83, 88, 92].

The method of saturation modeling listed below provide a good representation of saturation effects in PMSM motors. Although, they have the following drawbacks:

- they require commissioning process, in which the effects of saturation must be measured and stored for each operation point;
- they are based on heuristic considerations without a clear physical and mathematical formulation;
- they need heavy calculations and they are not always suitable for industrial use;
- the inductances are obtained using look up tables or complicated mathematical expressions with a large number of parameters.

For these reasons, we propose in the sequel a simple parametric saturation model based on the energy modeling described in the previous sections. This model is easy to use and it is based only on a fourth order polynomial energy function depending on five linear parameters. All the motor variables are obtained from this function.

4.3.3 Proposed Parametric model

Fig. 4.7 (resp. Fig. 4.8) shows the shape of the current i_d (resp. i_q) in terms of the flux ϕ_d (resp. ϕ_q) for multiple values of i_q (resp. i_d) for two PMSM motors with magnetic saturation. It is clear in these figures that the saturated currents i_d and i_q remain close to the linear currents. In addition, the shape of the current-flux curves is close to a quadratic or cubic polynomial functions of fluxes. Thus, we choose to write the currents as the sum of a linear term plus polynomial quadratic and cubic terms as follows

$$\begin{aligned} i_d &= \frac{\phi_d}{L_d} + \text{higher order quadratic and cubic terms} \\ i_q &= \frac{\phi_q}{L_q} + \text{higher order quadratic and cubic terms.} \end{aligned}$$

It is important to note that the currents i_d and i_q are not independent, hence the added higher order terms cannot be chosen arbitrarily. The best way to find the expressions of i_d and i_q is by using an energy function where the currents are are equal to the partial derivatives of this function with respect to the fluxes ϕ_d and ϕ_q. Thus, magnetic saturation can be accounted for by considering a more complicated magnetic energy function $\mathcal{H}$, having $\mathcal{H}_l$ for quadratic part but including also higher-order terms up to fourth order.

The saturation effects are well captured by considering only third- and fourth-order terms. Indeed, the currents, which are the derivatives of the energy, contain quadratic and cubic terms; therefore the energy must contain cubic and fourth order terms as follows

$$\mathcal{H}(\phi_d, \phi_q) = \mathcal{H}_l(\phi_d, \phi_q) + \sum_{i=0}^{3} \alpha_{3-i,i} \phi_d^{3-i} \phi_q^i + \sum_{i=0}^{4} \alpha_{4-i,i} \phi_d^{4-i} \phi_q^i.$$

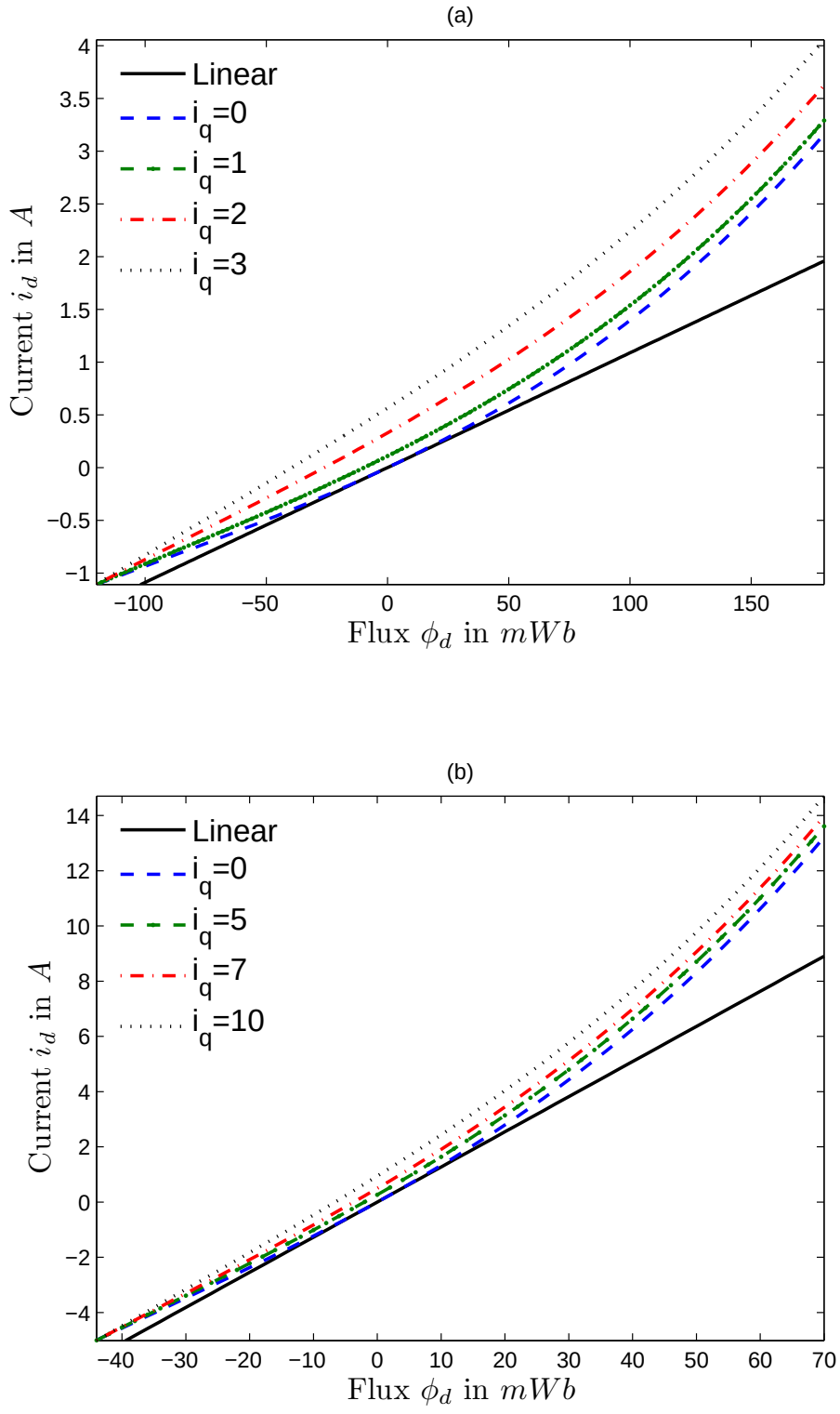

Figure 4.7: d- axis current i_d versus d- axis flux ϕ_d for multiple values of the current i_q: (a) IPM2 motor with rated parameters listed in 4.1; (b) IPM motor with rated parameters listed in 6.1.

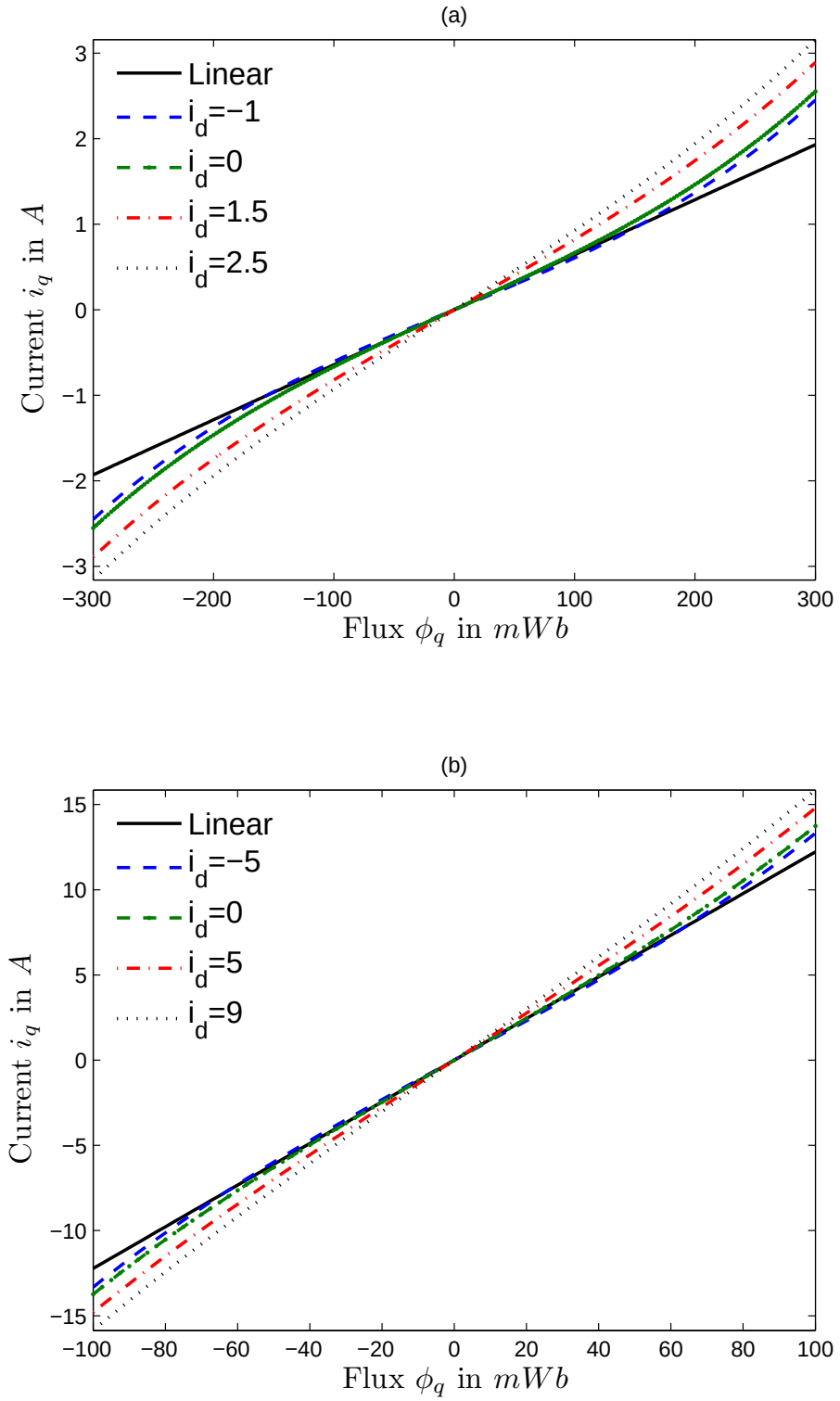

Figure 4.8: q- axis current i_q versus q- axis flux ϕ_q for multiple values of the current i_d: (a) IPM2 motor with rated parameters listed in 4.1; (b) IPM motor with rated parameters listed in 6.1.

This is a perturbative model [64] where the higher-order terms appear as corrections of the dominant term $\mathcal{H}_l$. The higher-order terms are small with respect to the dominant linear terms because the saturated currents are close to the linear currents. These results are also confirmed by experiments as we will see later. The nine coefficients $(\alpha_{3,1}, \alpha_{2,1}, \alpha_{1,2}, \alpha_{0,3}, \alpha_{4,0}, \alpha_{3,1}, \alpha_{2,2}, \alpha_{1,3}, \alpha_{0,4})$, together with L_d, L_q are motor dependent. But the symmetry relation (4.122) implies $\alpha_{2,1} = \alpha_{0,3} = \alpha_{3,1} = \alpha_{1,3} = 0$, so that the energy function eventually reads

$$\mathcal{H}(\phi_d, \phi_q) = \mathcal{H}_l(\phi_d, \phi_q) + \alpha_{3,0}\phi_d^3 + \alpha_{1,2}\phi_d\phi_q^2 + \alpha_{4,0}\phi_d^4 + \alpha_{2,2}\phi_d^2\phi_q^2 + \alpha_{0,4}\phi_q^4. \tag{4.131}$$

From (4.119)-(4.120) and (4.131) the currents are then explicitly given by

$$i_d = \frac{\partial \mathcal{H}}{\partial \phi_d}(\phi_d, \phi_q) = \mathcal{I}_d(\phi_d, \phi_q) = \frac{\phi_d}{L_d} + 3\alpha_{3,0}\phi_d^2 + \alpha_{1,2}\phi_q^2 + 4\alpha_{4,0}\phi_d^3 + 2\alpha_{2,2}\phi_d\phi_q^2 \tag{4.132}$$

$$i_q = \frac{\partial \mathcal{H}}{\partial \phi_d}(\phi_d, \phi_q) = \mathcal{I}_d(\phi_d, \phi_q) = \frac{\phi_q}{L_q} + 2\alpha_{1,2}\phi_d\phi_q + 2\alpha_{2,2}\phi_d^2\phi_q + 4\alpha_{0,4}\phi_q^3, \tag{4.133}$$

which are the so-called flux-current magnetization curves. These expressions correspond to the curves given in 4.7 and 4.8.

4.3.4 Model with i_d, i_q as state variables

The model of the PMSM is usually expressed with currents as state variables. This can be achieved here by time differentiating $\mathbf{i}_{dq} = \mathcal{I}_{dq}(\mathbf{\Phi}_{dq})$,

$$\frac{d\mathbf{i}_{dq}}{dt} = D\mathcal{I}_{dq}(\mathbf{\Phi}_{dq})\frac{d\mathbf{\Phi}_{dq}}{dt},$$

where

$$D\mathcal{I}_{dq} = \begin{pmatrix} \frac{\partial \mathcal{I}_d}{\partial \phi_d} & \frac{\partial \mathcal{I}_d}{\partial \phi_q} \\ \frac{\partial \mathcal{I}_q}{\partial \phi_d} & \frac{\partial \mathcal{I}_q}{\partial \phi_q} \end{pmatrix}$$

is the jacobian of $\mathcal{I}_{dq}$ and $\frac{d\mathbf{\Phi}_{dq}}{dt}$ is given by (4.116). Fluxes are then expressed as $\mathbf{\Phi}_{dq} = \mathcal{I}_{dq}^{-1}(\mathbf{i}_{dq})$ by inverting the nonlinear relations (4.132)-(4.133); rather than performing the exact inversion, we can take advantage of the fact the coefficients $\alpha_{i,j}$ are experimentally small; the interpretation of this hypothesis is given in using experimental data. At first order with respect to the $\alpha_{i,j}$ we have

$$\phi_d = L_d i_d + \mathcal{O}(|\alpha_{i,j}|) \tag{4.134}$$

$$\phi_q = L_q i_q + \mathcal{O}(|\alpha_{i,j}|). \tag{4.135}$$

In addition, (4.132) and (4.133) can be rearranged as follows

$$\phi_d = L_d\left(i_d - 3\alpha_{3,0}\phi_d^2 - \alpha_{1,2}\phi_q^2 - 4\alpha_{4,0}\phi_d^3 - 2\alpha_{2,2}\phi_d\phi_q^2\right) \tag{4.136}$$

$$\phi_q = L_q\left(i_q - 2\alpha_{1,2}\phi_d\phi_q - 2\alpha_{2,2}\phi_d^2\phi_q - 4\alpha_{0,4}\phi_q^3\right). \tag{4.137}$$

Plugging (4.134)-(4.135) into the right side part of (4.136)-(4.137) and neglecting $\mathcal{O}(|\alpha_{i,j}|^2)$ terms, we easily find

$$\phi_d = \mathcal{I}_d^{-1}(i_d, i_q) = L_d\big(i_d - 3\alpha_{3,0}L_d^2 i_d^2 - \alpha_{1,2}L_q^2 i_q^2 - 4\alpha_{4,0}L_d^3 i_d^3 - 2\alpha_{2,2}L_d L_q^2 i_d i_q^2\big) \tag{4.138}$$

$$\phi_q = \mathcal{I}_q^{-1}(i_d, i_q) = L_q\big(i_q - 2\alpha_{1,2}L_d L_q i_d i_q - 2\alpha_{2,2}L_d^2 L_q i_d^2 i_q - 4\alpha_{0,4}L_q^3 i_q^3\big). \tag{4.139}$$

Notice the matrix

$$\mathbf{Y}(\mathbf{i}_{dq}) := \begin{pmatrix} Y^{dd}(\mathbf{i}_{dq}) & Y^{dq}(\mathbf{i}_{dq}) \\ Y^{dq}(\mathbf{i}_{dq}) & Y^{qq}(\mathbf{i}_{dq}) \end{pmatrix} := D\mathcal{I}_{dq}\big(\mathcal{I}_{dq}^{-1}(\mathbf{i}_{dq})\big), \tag{4.140}$$

with coefficients easily found to be

$$Y^{dd}(\mathbf{i}_{dq}) = \frac{1}{L_d} + 6\alpha_{3,0}L_d i_d + 12\alpha_{4,0}L_d^2 i_d^2 + 2\alpha_{2,2}L_q^2 i_q^2 \tag{4.141}$$

$$Y^{dq}(\mathbf{i}_{dq}) = 2\alpha_{1,2}L_q i_q + 4\alpha_{2,2}L_d i_d L_q i_q \tag{4.142}$$

$$Y^{qq}(\mathbf{i}_{dq}) = \frac{1}{L_q} + 2\alpha_{1,2}L_d i_d + 2\alpha_{2,2}L_d^2 i_d^2 + 12\alpha_{0,4}L_q^2 i_q^2, \tag{4.143}$$

is by construction symmetric; indeed

$$D\mathcal{I}_{dq}(\mathbf{\Phi}_{dq}) = \begin{pmatrix} \frac{\partial^2 \mathcal{H}}{\partial \phi_d{}^2}(\mathbf{\Phi}_{dq}) & \frac{\partial^2 \mathcal{H}}{\partial \phi_d \partial \phi_q}(\mathbf{\Phi}_{dq}) \\ \frac{\partial^2 \mathcal{H}}{\partial \phi_q \partial \phi_d}(\mathbf{\Phi}_{dq}) & \frac{\partial^2 \mathcal{H}}{\partial \phi_q{}^2}(\mathbf{\Phi}_{dq}) \end{pmatrix} \tag{4.144}$$

and $\frac{\partial^2 \mathcal{H}}{\partial \phi_d \partial \phi_q} = \frac{\partial^2 \mathcal{H}}{\partial \phi_q \partial \phi_d}$. Therefore the inductance matrix

$$\mathbf{L}_i^{dq} = \begin{pmatrix} l_i^{dd}(\mathbf{i}_{dq}) & l_i^{dq}(\mathbf{i}_{dq}) \\ l_i^{dq}(\mathbf{i}_{dq}) & l_i^{qq}(\mathbf{i}_{dq}) \end{pmatrix} := \begin{pmatrix} Y^{dd}(\mathbf{i}_{dq}) & Y^{dq}(\mathbf{i}_{dq}) \\ Y^{dq}(\mathbf{i}_{dq}) & Y^{qq}(\mathbf{i}_{dq}) \end{pmatrix}^{-1} \tag{4.145}$$

is also symmetric. The explicit expressions of the motor inductances are obtained using the approximation (4.134)-(4.135), hence we get

$$l_i^{dd}(\mathbf{i}_{dq}) = L_d\big(1 - 6\alpha_{3,0}L_d^2 i_d - 12\alpha_{4,0}L_d^3 i_d^2 - 2\alpha_{2,2}L_d L_q^2 i_q^2\big) \tag{4.146}$$

$$l_i^{dq}(\mathbf{i}_{dq}) = L_d L_q\big(-2\alpha_{1,2}L_q i_q - 4\alpha_{2,2}L_d L_q i_d i_q\big) \tag{4.147}$$

$$l_i^{qq}(\mathbf{i}_{dq}) = L_q\big(1 - 2\alpha_{1,2}L_d L_q i_d - 2\alpha_{2,2}L_d^2 L_q i_d^2 - 12\alpha_{0,4}L_q^3 i_q^2\big). \tag{4.148}$$

To conclude, the model of the saturated PMSM is given by (4.116)–(4.118) and (4.132)-(4.133), with $\phi_d, \phi_q, \omega, \theta$ as state variables. The magnetic saturation effects are represented by the five parameters $\alpha_{3,0}, \alpha_{1,2}, \alpha_{4,0}, \alpha_{2,2}, \alpha_{0,4}$ which can be estimated easily by linear least square as we will see in chapter 6. This is a simple and explicit model based on polynomial functions. This model will be used in the sequel to study the observability of the PMSM at zero speed operation. In the next chapters, this model will be used also to find a sensorless rotor position estimation procedure and a sensorless control scheme which take into account cross coupling and magnetic saturation.

4.4 Observability issue

In the previous section, we proposed a PMSM model with magnetic saturation based on an energy approach. In this section, we will study the observability of the PMSM using this saturation model. We show that the PMSM is observable everywhere if $\omega \neq 0$ where the observability rank increases from 2 to 4 and to 5 using the stator current and their first order and second order derivatives. If

$\omega = 0$, we show that the first order linear approximation [66] of the PMSM equations around $\omega = 0$ is not observable, in this case the observability rank increases from 2 to 3 and to 4 and it does not increase even using higher order derivatives of the measured currents. This is a well known property of PMSM, it makes the observability around zero speed of this type of motor a difficult task.

Using the nonlinear observability we show that the PMSM is observable around $\omega = 0$ when a persistent excitation is added to the motor voltage and a saliency condition is satisfied. By contrast, without persistent excitation, the rank of the nonlinear observability matrix at zero speed remains the same as the observability rank of the first order PMSM model whatever the order of the current derivative. We established a sufficient saliency condition to ensure nonlinear observability with persistent excitation. In this case, the observability rank increases from 2 to 4 and to 5 using the stator current and their first order and second order derivatives which is similar to the case when $\omega \neq 0$.

4.4.1 First-order observability

To emphasize that position estimation is not easy at low speed, we study the observability of (4.116)–(4.118), augmented by $\frac{d\tau_L}{dt} = 0$ (unknown constant load):

$$\left.\begin{aligned} \frac{d\mathbf{\Phi}_{dq}}{dt} &= \mathbf{v}_{dq} - R\mathbf{i}_{dq} - \omega\mathcal{J}(\mathbf{\Phi}_{dq} + \mathbf{\Phi}_m) \\ \frac{J}{n^2}\frac{d\omega}{dt} &= \mathbf{i}_{dq}^T\mathcal{J}(\mathbf{\Phi}_{dq} + \mathbf{\Phi}_m) - \frac{\tau_L}{n} \\ \frac{d\theta}{dt} &= \omega \\ \frac{d\tau_L}{dt} &= 0. \end{aligned}\right\} \tag{4.149}$$

This system has 5 state variables. The state variable vector is $(\mathbf{\Phi}_{dq}^T, \omega, \theta, \tau_L)^T$. It is important to note that the physically impressed voltages to the motor are $\mathbf{v}_{\alpha\beta} = \mathcal{R}_\theta\mathbf{v}_{dq}$ while the physically measurable currents are $\mathbf{i}_{\alpha\beta} = \mathcal{R}_\theta\mathbf{i}_{dq}$. Thus, the input variables are $\mathbf{v}_{\alpha\beta}$ and the output variables are $\mathbf{i}_{\alpha\beta}$.

The observability of (4.149) is studied around a permanent trajectory defined by

$$0 = \underline{\mathbf{v}}_{dq} - R\underline{\mathbf{i}}_{dq} - \underline{\omega}\mathcal{J}(\underline{\mathbf{\Phi}}_{dq} + \mathbf{\Phi}_m) \tag{4.150}$$

$$0 = \underline{\mathbf{i}}_{dq}^T\mathcal{J}(\underline{\mathbf{\Phi}}_{dq} + \mathbf{\Phi}_m) - \frac{\underline{\tau}_L}{n} \tag{4.151}$$

$$\frac{d\underline{\theta}}{dt} = \underline{\omega}. \tag{4.152}$$

Notice such a permanent trajectory is not a steady state point unless $\underline{\omega} := 0$ since $\underline{\theta}$ hence $\underline{\mathbf{v}}_{\alpha\beta}$ and $\underline{\mathbf{i}}_{\alpha\beta}$ are time-varying ($\underline{\mathbf{\Phi}}_{dq}, \underline{\mathbf{i}}_{dq}, \underline{\mathbf{v}}_{dq}, \underline{\omega}, \underline{\tau}_L$ are on the other hand constant). Also the reason for augmenting the model with a constant torque is that it is usually also desired to estimate an unknown load torque.

The system (4.149) is linearized around $(\underline{\mathbf{\Phi}}_{dq}, \underline{\omega}, \underline{\theta}, \underline{\tau}_L)$. Set

$$\Delta\mathbf{\Phi}_{dq} = \mathbf{\Phi}_{dq} - \underline{\mathbf{\Phi}}_{dq}, \quad \Delta\theta = \theta - \underline{\theta}, \quad \Delta\omega = \omega - \underline{\omega} \quad \Delta\tau_L = \tau_L - \underline{\tau}_L,$$

a function $X(\mathbf{\Phi}_{dq}, \omega, \theta, \tau_L)$ can be linearized as follows

$$\Delta X = \frac{\partial X}{\partial \mathbf{\Phi}_{dq}}\Delta\mathbf{\Phi}_{dq} + \frac{\partial X}{\partial\theta}\Delta\theta + \frac{\partial X}{\partial\omega}\Delta\omega + \frac{\partial X}{\partial\tau_L}\Delta\tau_L. \tag{4.153}$$

Using (4.153) and $\mathbf{i}_{\alpha\beta} = \mathcal{R}_\theta \mathbf{i}_{dq}$ we then get

$$\begin{aligned}\Delta \mathbf{i}_{\alpha\beta} &= \Delta \mathcal{R}_\theta \underline{\mathbf{i}}_{dq} + \mathcal{R}_{\underline{\theta}} \Delta \mathbf{i}_{dq} \\ &= \mathcal{R}_{\underline{\theta}} \mathcal{J} \underline{\mathbf{i}}_{dq} \Delta\theta + \mathcal{R}_{\underline{\theta}} \Delta \mathbf{i}_{dq} \\ &= \mathcal{R}_{\underline{\theta}} (\mathcal{J} \underline{\mathbf{i}}_{dq} \Delta\theta + \Delta \mathbf{i}_{dq}),\end{aligned} \tag{4.154}$$

and similarly for $\mathbf{v}_{\alpha\beta}$ we have

$$\Delta \mathbf{v}_{\alpha\beta} = \mathcal{R}_{\underline{\theta}} (\mathcal{J} \underline{\mathbf{v}}_{dq} \Delta\theta + \Delta \mathbf{v}_{dq}). \tag{4.155}$$

The linearization of (4.149) around the permanent trajectory (4.150)–(4.152) is then

$$\begin{aligned}\frac{d}{dt}\Delta \mathbf{\Phi}_{dq} &= \mathcal{R}_{\underline{\theta}}^T (\Delta \mathbf{v}_{\alpha\beta} - R \Delta \mathbf{i}_{\alpha\beta}) - \mathcal{J} \left(\underline{\mathbf{\Phi}}_{dq} + \mathbf{\Phi}_m\right) \Delta\omega + \underline{\omega} \Big(\left(\underline{\mathbf{\Phi}}_{dq} + \mathbf{\Phi}_m\right) \Delta\theta - \mathcal{J} \Delta \mathbf{\Phi}_{dq} \Big) \\ \frac{J}{n^2} \frac{d}{dt} \Delta\omega &= \Delta \mathbf{i}_{\alpha\beta}{}^T \mathcal{R}_{\underline{\theta}} \mathcal{J} \left(\underline{\mathbf{\Phi}}_{dq} + \mathbf{\Phi}_m\right) - \underline{\mathbf{i}}_{dq}^T \Big(\left(\underline{\mathbf{\Phi}}_{dq} + \mathbf{\Phi}_m\right) \Delta\theta - \mathcal{J} \Delta \mathbf{\Phi}_{dq} \Big) - \frac{\Delta \tau_L}{n} \\ \frac{d}{dt} \Delta\theta &= \Delta\omega \\ \frac{d}{dt} \Delta\tau_L &= 0,\end{aligned}$$

where we have used $\underline{\mathbf{v}}_{dq} - R \underline{\mathbf{i}}_{dq} = \underline{\omega} \mathcal{J} \left(\underline{\mathbf{\Phi}}_{dq} + \mathbf{\Phi}_m\right)$.

On the other hand time differentiating $\Delta \mathbf{i}_{\alpha\beta}$ yields

$$\begin{aligned}\frac{d}{dt} \Delta \mathbf{i}_{\alpha\beta} &= \frac{d\mathcal{R}_{\underline{\theta}}}{dt} (\mathcal{J} \underline{\mathbf{i}}_{dq} \Delta\theta + \Delta \mathbf{i}_{dq}) + \mathcal{R}_{\underline{\theta}} \Big(\mathcal{J} \underline{\mathbf{i}}_{dq} \frac{d}{dt} \Delta\theta + \frac{d}{dt} \Delta \mathbf{i}_{dq} \Big) \\ &= \underline{\omega} \mathcal{J} \Delta \mathbf{i}_{\alpha\beta} + \mathcal{R}_{\underline{\theta}} \Big(\mathcal{J} \underline{\mathbf{i}}_{dq} \Delta\omega + D\mathcal{I}_{dq} \left(\underline{\mathbf{\Phi}}_{dq}\right) \frac{d}{dt} \Delta \mathbf{\Phi}_{dq} \Big)\end{aligned}$$

where we have used $\Delta \mathbf{i}_{dq} = D\mathcal{I}_{dq} \left(\underline{\mathbf{\Phi}}_{dq}\right) \Delta \mathbf{\Phi}_{dq}$. Therefore

$$\begin{aligned}[D\mathcal{I}_{dq} \left(\underline{\mathbf{\Phi}}_{dq}\right)]^{-1} \mathcal{R}_{\underline{\theta}}^T \frac{d}{dt} \Delta \mathbf{i}_{\alpha\beta} &= [D\mathcal{I}_{dq} \left(\underline{\mathbf{\Phi}}_{dq}\right)]^{-1} \mathcal{J} \underline{\mathbf{i}}_{dq} \Delta\omega + \frac{d}{dt} \Delta \mathbf{\Phi}_{dq} + \mathrm{LC}(\Delta \mathbf{i}_{\alpha\beta}, \Delta \mathbf{v}_{\alpha\beta}) \\ &= \mathcal{J} \mathbf{\Phi} \left(\underline{\mathbf{\Phi}}_{dq}\right) \Delta\omega + \underline{\omega} \mathbf{\Phi} \left(\underline{\mathbf{\Phi}}_{dq}\right) \Delta\theta + \mathrm{LC}(\Delta \mathbf{i}_{\alpha\beta}, \Delta \mathbf{v}_{\alpha\beta})\end{aligned} \tag{4.156}$$

where

$$\mathbf{\Phi} \left(\underline{\mathbf{\Phi}}_{dq}\right) := \mathbf{\Phi}_m + \underline{\mathbf{\Phi}}_{dq} + \mathcal{J} [D\mathcal{I}_{dq} \left(\underline{\mathbf{\Phi}}_{dq}\right)]^{-1} \mathcal{J} \mathcal{I}_{dq} (\underline{\mathbf{\Phi}}_{dq})$$

and $\mathrm{LC}(\Delta \mathbf{i}_{\alpha\beta}, \Delta \mathbf{v}_{\alpha\beta})$ is some matrix linear combination of $\Delta \mathbf{i}_{\alpha\beta}$ and $\Delta \mathbf{v}_{\alpha\beta}$. Similarly

$$\frac{J}{n^2} \frac{d}{dt} \Delta\omega = -\mathbf{\Phi} \left(\underline{\mathbf{\Phi}}_{dq}\right) \Delta\theta - \frac{\Delta \tau_L}{n} + \mathrm{LC}(\Delta \mathbf{i}_{\alpha\beta}, \Delta \mathbf{v}_{\alpha\beta}). \tag{4.157}$$

Now $\mathbf{\Phi} \left(\underline{\mathbf{\Phi}}_{dq}\right)$ is non-zero in any reasonable situation, indeed

$$\mathbf{\Phi} = \begin{pmatrix} \lambda + \phi_d - L^{qq} i_d + L^{dq} i_q \\ \phi_q + L^{dq} i_d - L^{dd} i_q \end{pmatrix}$$

where we have used

$$[D\mathcal{I}_{dq}\left(\underline{\mathbf{\Phi}}_{dq}\right)]^{-1} = \begin{pmatrix} L^{dd} & L^{dq} \\ L^{dq} & L^{qq} \end{pmatrix}.$$

Using the approximation (4.134)-(4.135) leads to

$$\lambda + \phi_d - L^{qq} i_d + L^{dq} i_q = \lambda + (L_d - L_q) i_d + \mathcal{O}(|\alpha_{i,j}|)$$

where $\lambda \gg -(L_d - L_q) i_d + \mathcal{O}(|\alpha_{i,j}|)$, therefore $\mathbf{\Phi}$ is different from zero. Hence $\mathbf{\Phi}$ and $\mathcal{J}\mathbf{\Phi}$ are independent vectors. Indeed

$$\det \begin{pmatrix} \mathbf{\Phi} & \mathcal{J}\mathbf{\Phi} \end{pmatrix} = \|\mathbf{\Phi}\|^2 \neq 0.$$

From (4.156), if $\underline{\omega} \neq 0$ it is thus clear that $\Delta\theta$ and $\Delta\omega$ can be expressed in function of $\mathbf{i}_{\alpha\beta}$, $\frac{d}{dt}\Delta\mathbf{i}_{\alpha\beta}$ and $\mathbf{v}_{\alpha\beta}$; as a consequence $\Delta\tau_L$ is a function of $\mathbf{i}_{\alpha\beta}$, $\frac{d}{dt}\Delta\mathbf{i}_{\alpha\beta}$, $\frac{d^2}{dt^2}\Delta\mathbf{i}_{\alpha\beta}$ and $\mathbf{v}_{\alpha\beta}$, $\frac{d}{dt}\Delta\mathbf{v}_{\alpha\beta}$ by (4.157); finally using

$$\Delta\mathbf{\Phi}_{dq} = [D\mathcal{I}_{dq}(\underline{\mathbf{\Phi}}_{dq})]^{-1}\Delta\mathbf{i}_{dq}$$

hence $\Delta\mathbf{\Phi}_{dq}$ is by (4.154) a function of $\Delta\mathbf{i}_{\alpha\beta}$. In other words the linearized system is observable by $\Delta\mathbf{i}_{\alpha\beta}$.

If $\underline{\omega} = 0$ only $\Delta\omega$ can be recovered from $\mathbf{i}_{\alpha\beta}$, $\frac{d}{dt}\Delta\mathbf{i}_{\alpha\beta}$ and $\mathbf{v}_{\alpha\beta}$; as a consequence only $\mathbf{\Phi}\left(\underline{\mathbf{\Phi}}_{dq}\right)\Delta\theta + \frac{\Delta\tau_L}{n}$ can be recovered from (4.157), and nothing new is gained by further differentiation. In other words the linearized system is not observable as pointed out in [21].

The first order observability can be summarized as follows

- case $\omega \neq 0$: the five motor states are observable. The observability rank is 2 using the measured current $\mathbf{i}_{\alpha\beta}$; it increases to 4 with the first order derivative of the measured current $\frac{d\mathbf{i}_{\alpha\beta}}{dt}$; then it increases to 5 with the second order derivative of the measured current $\frac{d^2\mathbf{i}_{\alpha\beta}}{dt^2}$.
- case $\omega = 0$: the five motor states are not all observable. Indeed, the observability rank is only 4 even if we use the current and all their derivatives. In this case the observability rank increases from 2 to 3 to 4 and remains 4 with higher order derivatives of the current.

Estimating the rotor position at low speed is thus inherently difficult. Yet it is doable when the motor exhibits some saliency, geometric or saturation-induced, with the help of permanent excitation such as signal injection. In the following subsection we study the nonlinear observability [19, 20] where we show that in some cases the PMSM system is observable in the nonlinear sense provide the motor exhibits some saliency.

4.4.2 Nonlinear observability

In this part we give the definition of the nonlinear observability of a nonlinear system. Then, we study the nonlinear observability of the PMSM where the current is the only measured signal.

A nonlinear system can be written as follows

$$\left.\begin{aligned} \dot{\mathbf{x}} &= f_x(\mathbf{x}, \mathbf{u}) \\ \mathbf{y} &= h(\mathbf{x}) \end{aligned}\right\} \tag{4.158}$$

where $\mathbf{x} \in \mathbb{R}^n$ is the state vector, $\mathbf{u} \in \mathbb{R}^m$ is the input vector, and $\mathbf{y} \in \mathbb{R}^p$ is the output vector. f_x and h are smooth functions defined in $\mathbb{R}^{n+m}$ and $\mathbb{R}^p$ respectively.

To define the nonlinear observability, we give firstly the definition of the indistinguishability. All the following definitions are given in [95].

Definition 1 (Indistinguishability)**.** *Two initial states $\mathbf{x}_1$ and $\mathbf{x}_2$ of (4.158) are indistinguishable (denoted $\mathbf{x}_1 I \mathbf{x}_2$) if for every time $t \geq 0$, the outputs $\mathbf{y}_1(t)$ and $\mathbf{y}_2(t)$ are identical for every admissible input $\mathbf{u}(t)$ where $\mathbf{y}_1(t)$ (resp. $\mathbf{y}_2(t)$) is the output of (4.158) that corresponds to the input $\mathbf{u}(t)$ and to the initial state $\mathbf{x}_1$ (resp. $\mathbf{x}_2$). $\mathbf{x}_1$ and $\mathbf{x}_2$ are distinguishable elsewhere.*

The indistinguishability is an equivalence relation. Notice $I(\mathbf{x})$ the equivalence class of $\mathbf{x}$. Hence, the observability is defined as follows

Definition 2 (Global observability)**.** *The system (4.158) is said to be observable at $\mathbf{x}$ if $I(\mathbf{x}) = \{\mathbf{x}\}$ and it is observable if $I(\mathbf{x}) = \{\mathbf{x}\}$ for every $\mathbf{x}$.*

Notice that observability is a global concept; it might be necessary to travel a considerable distance or for a long time to distinguish between two initial states. Therefore we introduce a local concept which is stronger than observability:

Definition 3 (Locally weak observability)**.** *The system (4.158) is locally weakly observable at $\mathbf{x}$ if there exists an open neighborhood U of $\mathbf{x}$ such that for every open neighborhood V of $\mathbf{x}$ contained in U, $I(\mathbf{x}) = \{\mathbf{x}\}$ and (4.158) is locally weakly observable if it is so at every $\mathbf{x}$.*

Intuitively (4.158) is locally weakly observable if one can instantaneously distinguish each point from its neighbors by an appropriate input choice.

Criteria for locally weak observability: The system (4.158) is locally weakly observable if there exists an integer l such that the matrix

$$\mathcal{LA}_l = \begin{pmatrix} \mathcal{L}_0^T & \mathcal{L}_1^T & \dots & \mathcal{L}_l^T \end{pmatrix}^T \tag{4.159}$$

has the same rank of $\mathbf{x}$ i.e. $rank(\mathcal{LA}_l) = n$ with

$$\mathcal{L}_k = D_{\mathbf{x}}[h_k(\mathbf{x}, \mathbf{u})], \quad h_k(\mathbf{x}, \mathbf{u}) = \frac{d^k}{dt^k} h(\mathbf{x})$$

where $D_{\mathbf{x}}[h_k(\mathbf{x}, \mathbf{u})]$ is the jacobian of the vector h_k with respect to the vector $\mathbf{x}$.

We will now investigate the nonlinear observability of the nonlinear system (4.149). For this system, we take:

- the state vector $\mathbf{x} = (\mathbf{i}_{\alpha\beta}^T, \omega, \theta, \tau_L)^T$
- the output vector $\mathbf{y} = h(\mathbf{x}) = \mathbf{i}_{\alpha\beta}$
- the input vector $\mathbf{u} = \mathbf{v}_{\alpha\beta}$.

In the sequel, we calculate the expressions of $\mathcal{LA}_0$, $\mathcal{LA}_1$, and $\mathcal{LA}_2$. To do that, we need the expression of the current and their first and second order derivatives which are as follows

$$\mathbf{i}_{\alpha\beta} = \mathcal{R}_\theta \mathcal{I}_{dq}(\mathbf{\Phi}_{dq}) \tag{4.160}$$

$$\frac{d}{dt}\mathbf{i}_{\alpha\beta} = \omega \mathcal{J}\mathbf{i}_{\alpha\beta} + \mathcal{S}(\theta, \mathbf{i}_{\alpha\beta})\Big(\mathbf{v}_{\alpha\beta} - R\mathbf{i}_{\alpha\beta} - \omega\mathcal{J}(\mathbf{\Phi}_{\alpha\beta} + \mathcal{R}_\theta \mathbf{\Phi}_m)\Big) \tag{4.161}$$

$$\frac{d^2\mathbf{i}_{\alpha\beta}}{dt^2} = -\frac{n_p}{J}\mathcal{S}\mathcal{R}_\theta \mathcal{J}\mathbf{\Phi}(\mathbf{\Phi}_{dq})\tau_L + \text{NF}(\mathbf{i}_{\alpha\beta}, \omega, \theta) \tag{4.162}$$

where

$$\mathcal{S}(\theta, \mathbf{i}_{\alpha\beta}) := \mathcal{R}_\theta D\mathcal{I}_{dq}\Big(\mathcal{I}_{dq}^{-1}(\mathcal{R}_\theta^T \mathbf{i}_{\alpha\beta})\Big)\mathcal{R}_\theta^T; \tag{4.163}$$

and NF is a nonlinear combination of $\mathbf{i}_{\alpha\beta}$, ω and θ.

We will now calculate the expressions of $\mathcal{LA}_0$, $\mathcal{LA}_1$, and $\mathcal{LA}_2$. For $l = 0$ the observability matrix $\mathcal{LA}_0$ reads

$$\mathcal{LA}_0 = \mathcal{L}_0 = \begin{pmatrix} 1 & 0 & 0 & 0 & 0 \\ 0 & 1 & 0 & 0 & 0 \end{pmatrix}.$$

Using (4.161), the expression of $\mathcal{L}_1$ can be written as follows

$$\mathcal{L}_1 = \begin{pmatrix} \frac{\partial}{\partial i_\alpha}(\frac{d}{dt}\mathbf{i}_{\alpha\beta}) & \frac{\partial}{\partial i_\beta}(\frac{d}{dt}\mathbf{i}_{\alpha\beta}) & -\mathcal{S}\mathcal{R}_\theta\mathcal{J}\mathbf{\Phi}(\mathbf{\Phi}_{dq}) & \frac{\partial \mathcal{S}}{\partial\theta}\mathcal{R}_\theta\frac{d\mathbf{\Phi}_{dq}}{dt} + \omega\mathcal{S}\mathcal{R}_\theta\mathbf{\Phi}(\mathbf{\Phi}_{dq}) & 0 \end{pmatrix}$$

where we have used

$$\mathcal{R}_\theta\frac{d\mathbf{\Phi}_{dq}}{dt} = \mathbf{v}_{\alpha\beta} - R\mathbf{i}_{\alpha\beta} - \omega\mathcal{J}(\mathbf{\Phi}_{\alpha\beta} + \mathcal{R}_\theta\mathbf{\Phi}_m).$$

Thus, the matrix $\mathcal{LA}_1$ reads

$$\mathcal{LA}_1 = \begin{pmatrix} 1 & 0 & 0 & 0 & 0 \\ 0 & 1 & 0 & 0 & 0 \\ \frac{\partial}{\partial i_\alpha}\left(\frac{d}{dt}\mathbf{i}_{\alpha\beta}\right) & \frac{\partial}{\partial i_\beta}\left(\frac{d}{dt}\mathbf{i}_{\alpha\beta}\right) & -\mathcal{S}\mathcal{R}_\theta\mathcal{J}\mathbf{\Phi}(\mathbf{\Phi}_{dq}) & \frac{\partial\mathcal{S}}{\partial\theta}\mathcal{R}_\theta\frac{d\mathbf{\Phi}_{dq}}{dt} + \omega\mathcal{S}\mathcal{R}_\theta\mathbf{\Phi}(\mathbf{\Phi}_{dq}) & 0 \end{pmatrix}.$$

Using (4.162), hence the expression of $\mathcal{L}_2$ is

$$\mathcal{L}_2 = \begin{pmatrix} \frac{\partial}{\partial i_\alpha}\left(\frac{d^2\mathbf{i}_{\alpha\beta}}{dt^2}\right) & \frac{\partial}{\partial i_\beta}\left(\frac{d^2\mathbf{i}_{\alpha\beta}}{dt^2}\right) & \frac{\partial}{\partial\omega}\left(\frac{d^2\mathbf{i}_{\alpha\beta}}{dt^2}\right) & \frac{\partial}{\partial\theta}\left(\frac{d^2\mathbf{i}_{\alpha\beta}}{dt^2}\right) & -\frac{n_p}{J}\mathcal{S}\mathcal{R}_\theta\mathcal{J}\mathbf{\Phi}(\mathbf{\Phi}_{dq}) \end{pmatrix}.$$

Thus, the expression of the observability matrix $\mathcal{LA}_2$ reads

$$\mathcal{LA}_2 = \begin{pmatrix} 1 & 0 & 0 & 0 & 0 \\ 0 & 1 & 0 & 0 & 0 \\ \frac{\partial}{\partial i_\alpha}(\frac{d}{dt}\mathbf{i}_{\alpha\beta}) & \frac{\partial}{\partial i_\beta}(\frac{d}{dt}\mathbf{i}_{\alpha\beta}) & -\mathcal{S}\mathcal{R}_\theta\mathcal{J}\mathbf{\Phi}(\mathbf{\Phi}_{dq}) & \frac{\partial\mathcal{S}}{\partial\theta}\mathcal{R}_\theta\frac{d\mathbf{\Phi}_{dq}}{dt} + \omega\mathcal{S}\mathcal{R}_\theta\mathbf{\Phi}(\mathbf{\Phi}_{dq}) & (0,0)^T \\ \frac{\partial}{\partial i_\alpha}\left(\frac{d^2\mathbf{i}_{\alpha\beta}}{dt^2}\right) & \frac{\partial}{\partial i_\beta}\left(\frac{d^2\mathbf{i}_{\alpha\beta}}{dt^2}\right) & \frac{\partial}{\partial\omega}\left(\frac{d^2\mathbf{i}_{\alpha\beta}}{dt^2}\right) & \frac{\partial}{\partial i_\theta}\left(\frac{d^2\mathbf{i}_{\alpha\beta}}{dt^2}\right) & -\frac{n_p}{J}\mathcal{S}\mathcal{R}_\theta\mathcal{J}\mathbf{\Phi}(\mathbf{\Phi}_{dq}) \end{pmatrix}.$$

4.4.2.1 Observability when $\omega \neq 0$ and $\frac{d\mathbf{\Phi}_{dq}}{dt} = 0$ (steady state flux in dq frame)

It is obvious that the rank of $\mathcal{LA}_0$ is equal to two. In addition, the first and second column of the matrix $\mathcal{LA}_1$ are independent for all possible trajectory. The final column is zero, hence the rank of $\mathcal{LA}_1$ is equal to 2 plus the rank of the following square matrix

$$\mathcal{LA}_{s1} = \left(-\mathcal{SR}_\theta \mathcal{J}\mathbf{\Phi}(\mathbf{\Phi}_{dq}) \quad \frac{\partial \mathcal{S}}{\partial \theta}\mathcal{R}_\theta \frac{d\mathbf{\Phi}_{dq}}{dt} + \omega \mathcal{SR}_\theta \mathbf{\Phi}(\mathbf{\Phi}_{dq})\right).$$

As $\omega \neq 0$ then $\det(\mathcal{LA}_{s1}) \neq 0$ for normal operation conditions because the two vectors $-\mathcal{SR}_\theta \mathcal{J}\mathbf{\Phi}(\mathbf{\Phi}_{dq})$ and $\omega \mathcal{SR}_\theta \mathbf{\Phi}(\mathbf{\Phi}_{dq})$ are independent when $\omega \neq 0$ (the matrix $\mathcal{SR}_\theta$ is always different from zero and the two vectors $\mathcal{J}\mathbf{\Phi}(\mathbf{\Phi}_{dq})$ and $\mathbf{\Phi}(\mathbf{\Phi}_{dq})$ are independent as established previously), hence $rank(\mathcal{LA}_1) = 4$.

It is clear that the rank of $\mathcal{LA}_2$ is equal to the rank of $\mathcal{LA}_1$ plus the rank of the last column of $\mathcal{LA}_2$. For normal operation condition, $\mathcal{SR}_\theta \mathcal{J}\mathbf{\Phi}(\mathbf{\Phi}_{dq})$ is different from zero ($\mathbf{\Phi}(\mathbf{\Phi}_{dq}) \neq 0$ and $\mathcal{SR}_\theta \mathcal{J}$ is an invertible non zero matrix), hence the final column of $\mathcal{LA}_2$ has a rank 1. Thus, as the matrix $\mathcal{LA}_1$ has a rank 4, then the observability matrix $\mathcal{LA}_2$ has the full rank 5 and therefore all the system states including speed ω, position θ and torque τ_L are observable when $\omega \neq 0$.

4.4.2.2 Observability when $\omega \equiv 0$

In this case we take $\omega \equiv 0$ which mean that ω and all their derivatives with respect to time are identically equal to zero. The rank of $\mathcal{LA}_{s1}$ is 1 because the vector $\frac{\partial \mathcal{S}}{\partial \theta}\mathcal{R}_\theta \frac{d\mathbf{\Phi}_{dq}}{dt} + \omega \mathcal{SR}_\theta \mathbf{\Phi}(\mathbf{\Phi}_{dq}) = 0$ ($\frac{d\mathbf{\Phi}_{dq}}{dt} = 0$ as $\omega \equiv 0$). Hence the rank of $\mathcal{LA}_1$ is equal to 3 in this case and therefore the rank of $\mathcal{LA}_2$ is equal to 4. If we use higher order derivatives of the current $\mathcal{LA}_l$ with $l > 2$ the rank of $\mathcal{LA}_l$ remains equal to 4. Hence, if the speed is identically equal to zero, then the PMSM system is not observable using nonlinear observability.

4.4.2.3 Observability when $\omega \approx 0$

In this case, a sufficient condition to ensure the observability of the PMSM system is $\frac{d\mathbf{\Phi}_{dq}}{dt} \neq 0$ and $\frac{\partial \mathcal{S}}{\partial \theta} \neq 0$, hence $\det(\mathcal{LA}_{s1}) \neq 0$ and the $rank(\mathcal{LA}_2) = 5$.

To verify the condition $\frac{d\mathbf{\Phi}_{dq}}{dt} \neq 0$, the fluxes in dq frame cannot be constant, but they must oscillate around the constant desired value. Thus $\mathbf{\Phi}_{dq}$ will be the sum of a constant value and a periodic zero mean oscillating function. This is possible by adding a HF voltage to the command voltage. We choose a HF with respect to the motor bandwidth to do not disturb the operation of the motor. Recalling the electrical motor equation

$$\frac{d\mathbf{\Phi}_{dq}}{dt} = \mathbf{v}_{dq} - R\mathbf{i}_{dq} - \omega \mathcal{J}(\mathbf{\Phi}_{dq} + \mathbf{\Phi}_m), \tag{4.164}$$

we apply a HF voltage

$$\mathbf{v}_{dq} = \overline{\mathbf{v}}_{dq} + \widetilde{\mathbf{v}}_{dq} f(\Omega t)$$

where $\overline{\mathbf{v}}_{dq}$ is constant and $\widetilde{\mathbf{v}}_{dq}$ is a low frequency signal and f is a 2π periodic function of amplitude 1 and Ω is a large pulsation. We can show that the corresponding periodic trajectory (see (5.49)–(5.51))

is as follows

$$\mathbf{\Phi}_{dq} = \overline{\mathbf{\Phi}}_{dq} + \frac{\widetilde{\mathbf{v}}_{dq}}{\Omega} F(\Omega t) + \mathcal{O}(\frac{1}{\Omega^2}) \tag{4.165}$$

$$\omega = \overline{\omega} + \mathcal{O}(\frac{1}{\Omega^2}) \tag{4.166}$$

$$\theta = \overline{\theta} + \mathcal{O}(\frac{1}{\Omega^2}) \tag{4.167}$$

where $\overline{\omega} = 0$; $\overline{\theta}$ and $\overline{\mathbf{\Phi}}_{dq}$ are constant; F is the integral of f having zero mean. The speed $\omega = 0 + \mathcal{O}(\frac{1}{\Omega^2})$ oscillates around zero with a very small and negligible amplitude $\mathcal{O}(\frac{1}{\Omega^2})$ and thus it is practically zero. The equation (4.165) yields

$$\frac{d}{dt}\mathbf{\Phi}_{dq} = \widetilde{\mathbf{v}}_{dq} f(\Omega t) + \mathcal{O}(\frac{1}{\Omega}) \tag{4.168}$$

hence $\frac{d}{dt}\mathbf{\Phi}_{dq} \neq 0$ almost everywhere. It remains to verify the saliency condition

$$\frac{\partial \mathcal{S}}{\partial \theta}(\theta, \mathbf{i}_{\alpha\beta}) \neq 0. \tag{4.169}$$

Finally, thanks to the HF signal injection and the motor saliency, the rank of the observability matrix $\mathcal{LA}_2$ is equal to 5 and we recover the nonlinear observability of the PMSM system.

Let's see the case of a PMSM with a linear magnetic model. In this case we have

$$\mathbf{i}_{dq} = \mathcal{I}_{dq}(\mathbf{\Phi}_{dq}) = \begin{pmatrix} \frac{1}{L_d} & 0 \\ 0 & \frac{1}{L_q} \end{pmatrix} \mathbf{\Phi}_{dq} \tag{4.170}$$

where L_d and L_q are the motor inductances. According to (4.163), the saliency matrix can be written as follows

$$\begin{aligned} \mathcal{S}(\theta, \mathbf{i}_{\alpha\beta}) &= \begin{pmatrix} \cos\theta & -\sin\theta \\ \sin\theta & \cos\theta \end{pmatrix} \begin{pmatrix} \frac{1}{L_d} & 0 \\ 0 & \frac{1}{L_q} \end{pmatrix} \begin{pmatrix} \cos\theta & \sin\theta \\ -\sin\theta & \cos\theta \end{pmatrix} \\ &= \frac{L_d + L_q}{2L_dL_q} \begin{pmatrix} 1 + \frac{L_d - L_q}{L_d + L_q}\cos 2\theta & \frac{L_d - L_q}{L_d + L_q}\sin 2\theta \\ \frac{L_d - L_q}{L_d + L_q}\sin 2\theta & 1 - \frac{L_d - L_q}{L_d + L_q}\cos 2\theta \end{pmatrix} \end{aligned}$$

with

$$\frac{\partial \mathcal{S}}{\partial \theta} = \frac{L_d - L_q}{L_dL_q} \begin{pmatrix} -\sin 2\theta & \cos 2\theta \\ \cos 2\theta & \sin 2\theta \end{pmatrix}$$

hence, if $L_d \neq L_q$ (salient) we get $\frac{\partial \mathcal{S}}{\partial \theta} \neq 0$ and then the position is observable. If $L_d = L_q$ (non salient motor) the observability matrix $\mathcal{LA}_1$ is of rank 3 and the position is not observable.

Conclusion

We proposed in this chapter a simple parametric magnetic saturation model for the PMSM motors. This model is based on an energy approach and on Euler-Lagrange formulation. Such formulations

are particularly efficient to preserve the physical insight while maintaining a synthetic view on the physical system i.e. PMSM. Symmetry considerations and the stator connection type were used to simplify the motor energy expression and to reduce the number of parameters needed to model magnetic saturations. At the end; the model depends only on five saturation parameters and is based on simple polynomial functions. Finally, we pointed out the observability problem at low speed using linear and nonlinear observability. Without using persistent excitation, we established that the observability degenerates at zero speed. By contrast, we show that if a persistent excitation is added to the motor voltage then the nonlinear observability is recovered if a saliency condition is verified.

The proposed model is used in the next chapter to solve the observability issue at zero speed. Using this model, we propose in the sequel a rotor position estimation procedure based on HF voltage injection. The position estimation remains possible while the saliency condition is verified.

Chapter 5

Position estimation by signal injection and averaging

Contents

Introduction

Le moteur MSAP a un problème d'observabilité à vitesse nulle lorsque les courants sont les seules grandeurs mesurées, voir section 4.4. Pour résoudre ce problème, un signal de haute fréquence (HF)

est ajouté à la tension du moteur à basse vitesse. Ainsi, la position peut être estimée à partir des oscillations du courant grâce aux saillances géométrique et magnétique du rotor.

Dans ce chapitre, nous proposons une méthode originale pour estimer la position du rotor du MSAP par l'injection de signaux et la moyennisation. D'abord, L'état de l'art de l'estimation de position par injection de tension HF est détaillé dans la section 5.1. A la fin de cette section, nous focalisons sur les effets du couplage et de la saturation magnétique sur l'estimation de position. Ensuite, nous présentons les méthodes existantes de compensation de ces effets et nous discutons leurs limites.

Nous proposons dans la section 5.2 une analyse mathématique claire et originale de la séparation des échelles de temps entre les sous systèmes basse fréquence et haute fréquence du MSAP quand une loi générale de contrôle de vitesse est appliquée au moteur avec l'injection des signaux HF. Cette séparation n'est pas toujours claire dans la littérature. En effet, nous proposons une preuve mathématique que les signaux HF ajoutés à la tension du moteur n'ont pas d'impact visible sur le fonctionnement du moteur. La tension HF ajoutée peut être considérée comme un capteur logiciel de position.

Ensuite, dans la section 5.3, nous proposons une analyse détaillée qui explique comment on peut récupérer les informations de position à partir de l'injection de signaux; cette analyse est adaptée à n'importe quel type ou forme de signaux injectés. Cette procédure d'estimation est basée sur le modèle de saturation magnétique (4.132)–(4.133) proposé dans la section 4.3. La position est estimée à partir des amplitudes du courant HF par moindres carrés non linéaire récursifs. Cette procédure d'estimation est utilisable en temps réel. Enfin, dans la section 5.4, nous proposons une loi de commande du MSAP à basse vitesse et sans capteur de position. Cette loi est basée sur la procédure d'estimation de position proposée dans la section précédente.

The PMSM has an observability problem at zero speed when the currents are the only measured variables, see section 4.4. To overcome this problem, a high frequency (HF) signal is injected to the motor voltage at low speed. Hence, the position can be estimated using the rotor geometric and magnetic saliency.

In this chapter we propose an original way of recovering the PMSM rotor position using signal injection and averging. The state of the art of position estimation by HF voltage injection is detailed in section 5.1. At the end of this section, we focus on the effects of magnetic and cross coupling saturation on the position estimation. Then, we present the existing methods of compensation of these effects and we discuss their limitations.

We propose in section 5.2 a clear and original mathematical analysis of the time scale separation between low frequency and HF motor subsystems when a general speed control law is applied to the motor with HF signal injection. This separation is not always clear in the literature. We propose a mathematical proof that the added HF signal does not have an impact on the motor operation. The injected signal acts as a software sensor to estimate the rotor position.

Then, in section 5.3 we propose an analysis of how to recover the position information from signal injection; this analysis can accommodate to any form of injected signals. This estimation procedure relies on the magnetic saturation model (4.132)–(4.133) proposed in section 4.3. The position is estimated from HF current amplitudes by recursive nonlinear least square which can be done at real

time operation. Finally, in section 5.4 we propose a low speed sensorless control law of PMSM based on the proposed position estimation procedure.

5.1 State of the art

Several methods of signal injection are proposed in the literature [6, 8, 11, 23–27, 29, 30, 32–36, 38, 39, 41, 47, 56, 61, 62, 93, 94, 96–105]. In this section we present these methods and we focus on the impact of magnetic saturation and cross coupling on the rotor position estimation [28, 43, 45–63]. We present also the different methods used to compensate the saturation effects [82, 84–87, 89–91].

5.1.1 Motor model

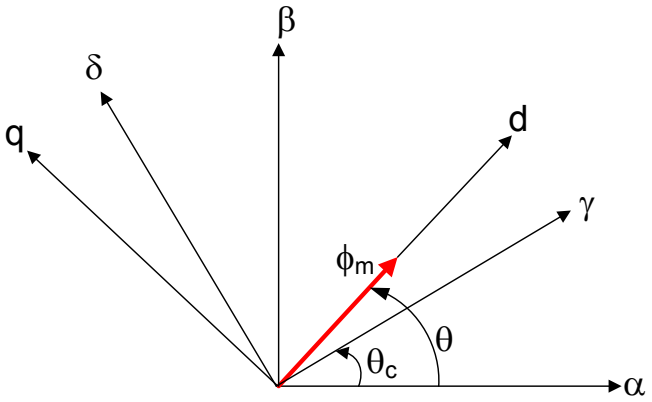

Figure 5.1: $\alpha\beta$, $\gamma\delta$, and dq reference frames

HF voltages are added to the motor voltage in an arbitrary rotating frame denoted $\gamma\delta$ reference frame and defined by

$$\mathbf{x}_{\gamma\delta} := \mathcal{R}_{\theta_c}^T \mathbf{x}_{\alpha\beta} \tag{5.1}$$

where θ_c is chosen by design. Using (5.1), the motor system equations (4.116)–(4.118) can be written in $\gamma\delta$ frame as follows

$$\frac{d\mathbf{\Phi}_{\gamma\delta}}{dt} = \mathbf{v}_{\gamma\delta} - R\mathbf{i}_{\gamma\delta} - \omega_c \mathcal{J}\mathbf{\Phi}_{\gamma\delta} - \omega\mathcal{J}\mathcal{R}_{\theta-\theta_c}\mathbf{\Phi}_m \tag{5.2}$$

$$\frac{J}{n^2}\frac{d\omega}{dt} = \mathbf{i}_{\gamma\delta}^T \mathcal{J}(\mathbf{\Phi}_{\gamma\delta} + \mathcal{R}_{\theta-\theta_c}\mathbf{\Phi}_m) - \frac{\tau_L}{n} \tag{5.3}$$

$$\frac{d\theta}{dt} = \omega. \tag{5.4}$$

The reason for using the $\gamma\delta$ frame instead of dq frame is that the position θ of the rotor is not measured, hence the voltage $\mathbf{v}_{dq} = \mathcal{R}_\theta^T \mathbf{v}_{\alpha\beta}$ and the current $\mathbf{i}_{dq} = \mathcal{R}_\theta^T \mathbf{i}_{\alpha\beta}$ are unknown variables. Indeed, only the physically impressed voltage $\mathbf{v}_{\alpha\beta}$ and the physically measurable current $\mathbf{i}_{\alpha\beta}$ are accessible. Thus, the voltage $\mathbf{v}_{\gamma\delta} = \mathcal{R}_{\theta_c}^T \mathbf{v}_{\alpha\beta}$ and the current $\mathbf{i}_{\gamma\delta} = \mathcal{R}_{\theta_c}^T \mathbf{i}_{\alpha\beta}$ are known since θ_c is a known angle. The $\gamma\delta$ frame is called estimated rotor frame when the position θ_c is the estimated rotor position. In the sequel, the HF signal calculations are performed in $\gamma\delta$ frame.

5.1.2 HF voltages and currents

The principle of HF injection is as follows. A periodic HF signal with zero mean is added to the motor voltage:

$$\begin{pmatrix} v_\gamma \\ v_\delta \end{pmatrix} = \begin{pmatrix} \overline{v}_\gamma + \widetilde{v}_\gamma f(\Omega t) \\ \overline{v}_\delta + \widetilde{v}_\delta g(\Omega t) \end{pmatrix} \tag{5.5}$$

where f and g are zero mean 2π- periodic functions of amplitude 1; Ω is a pulsation higher than the motor bandwidth; $\widetilde{v}_\gamma$ and $\widetilde{v}_\delta$ are the amplitude of the injected signal.

Now, we give the expression of the HF flux as reported in the literature. The equations (5.2) and (5.5) lead to

$$\frac{d\mathbf{\Phi}_{\gamma\delta}}{dt} = \overline{\mathbf{v}}_{\gamma\delta} + \widetilde{\mathcal{V}}_{\gamma\delta} - R\mathbf{i}_{\gamma\delta} - \omega_c \mathcal{J}\mathbf{\Phi}_{\gamma\delta} - \omega\mathcal{J}\mathcal{R}_{\theta-\theta_c}\mathbf{\Phi}_m \tag{5.6}$$

where $\widetilde{\mathcal{V}}_{\gamma\delta} := (\widetilde{v}_\gamma f, \widetilde{v}_\delta g)^T$ is the HF voltage vector in $\gamma\delta$ frame. According to [24, 32], the stator resistive voltage drop $(R\mathbf{i}_{\gamma\delta})$ and the speed dependent voltages $(\omega_c\mathcal{J}\mathbf{\Phi}_{\gamma\delta} + \omega\mathcal{J}\mathcal{R}_{\theta-\theta_c}\mathbf{\Phi}_m)$ are small compared to the induced voltage $\widetilde{\mathcal{V}}_{\gamma\delta}$ at the injected frequency $\frac{\Omega}{2\pi}$. Therefore, the relation between the HF components of (5.6) can be simplified as follows

$$\frac{d\widetilde{\mathbf{\Phi}}_{\gamma\delta}}{dt} = \widetilde{\mathcal{V}}_{\gamma\delta} \tag{5.7}$$

where $\widetilde{\mathbf{\Phi}}_{\gamma\delta}$ is the HF flux component in $\gamma\delta$ frame. The time integration of (5.7) yields

$$\left.\begin{aligned} \widetilde{\phi}_\gamma &= \frac{\widetilde{v}_\gamma}{\Omega} F(\Omega t) \\ \widetilde{\phi}_\delta &= \frac{\widetilde{v}_\delta}{\Omega} G(\Omega t) \end{aligned}\right\} \tag{5.8}$$

where F and G are the primitive with zero mean of f and g respectively.

We will now find the relation between the HF current and the rotor position in the case of a motor with linear relation between fluxes and currents. In this case, we have

$$\mathbf{\Phi}_{dq} = \mathbf{L}^{dq}\mathbf{i}_{dq} \tag{5.9}$$

where $\mathbf{L}^{dq}$ is the matrix of inductance in dq frame. According to [24,32], the flux-current relation (5.9) leads to

$$\widetilde{\mathbf{\Phi}}_{dq} = \mathbf{L}^{dq}\widetilde{\mathcal{I}}_{dq} \tag{5.10}$$

where $\widetilde{\mathcal{I}}_{dq}$ is the HF current component in dq frame. Using (5.9) and (5.10), hence the relation between HF flux and HF current in $\gamma\delta$ frame reads

$$\begin{aligned} \widetilde{\mathbf{\Phi}}_{\gamma\delta} &= \mathcal{R}_{\theta-\theta_c}\widetilde{\mathbf{\Phi}}_{dq} \\ &= \mathcal{R}_{\theta-\theta_c}\mathbf{L}^{dq}\widetilde{\mathcal{I}}_{dq} \\ &= \mathcal{R}_{\theta-\theta_c}\mathbf{L}^{dq}\mathcal{R}^T_{\theta-\theta_c}\widetilde{\mathcal{I}}_{\gamma\delta} \end{aligned}$$

where $\widetilde{\mathbf{\Phi}}_{dq}$ is the HF flux component in dq frame; $\widetilde{\mathcal{I}}_{\gamma\delta}$ is the HF current component in $\gamma\delta$ frame. Thus we get

$$\widetilde{\mathbf{\Phi}}_{\gamma\delta} = \mathbf{L}^{\gamma\delta}(\theta - \theta_c)\widetilde{\mathcal{I}}_{\gamma\delta} \tag{5.11}$$

with

$$\mathbf{L}^{\gamma\delta}(\theta-\theta_c)=\mathcal{R}_{\theta-\theta_c}\mathbf{L}^{dq}\mathcal{R}^{T}_{\theta-\theta_c}. \tag{5.12}$$

From (5.8) and (5.11), it is clear that the HF current can be expressed in terms of the rotor position if the inductance $\mathbf{L}^{\gamma\delta}(\theta-\theta_c)$ depends on the rotor position (saliency condition).

If d- and q- axis fluxes are magnetically decoupled, then the matrix $\mathbf{L}^{dq}$ is diagonal:

$$\mathbf{L}^{dq}=\begin{pmatrix}L_d & 0\\ 0 & L_q\end{pmatrix},$$

hence the inductance $\mathbf{L}^{\gamma\delta}$ in (5.12) can be written as follows

$$\mathbf{L}^{\gamma\delta}(\mu)=\frac{1}{2}\begin{pmatrix}L_d+L_q+(L_d-L_q)\cos 2\mu & (L_d-L_q)\sin 2\mu\\ (L_d-L_q)\sin 2\mu & L_d+L_q-(L_d-L_q)\cos 2\mu\end{pmatrix}. \tag{5.13}$$

where $\mu=\theta-\theta_c$. Therefore, the HF current is

$$\widetilde{\mathcal{I}}_{\gamma\delta}=\frac{1}{\Omega}\left(\mathbf{L}^{\gamma\delta}(\theta-\theta_c)\right)^{-1}\begin{pmatrix}\widetilde{v}_\gamma F(\Omega t)\\ \widetilde{v}_\delta G(\Omega t)\end{pmatrix} \tag{5.14}$$

where

$$\left(\mathbf{L}^{\gamma\delta}(\mu)\right)^{-1}=\frac{1}{2L_dL_q}\begin{pmatrix}L_d+L_q-(L_d-L_q)\cos 2\mu & -(L_d-L_q)\sin 2\mu\\ -(L_d-L_q)\sin 2\mu & L_d+L_q+(L_d-L_q)\cos 2\mu\end{pmatrix}$$

The equation (5.14) gives the expression of the HF current in terms of the rotor angle in the case of a linear and decoupled magnetic model. The result obtained in (5.14) is general and can be used for any HF voltage injection method.

5.1.3 Signal injection types

The types of the HF voltage vary according to the choice of the functions f, g and the voltages $\widetilde{v}_\gamma$ and $\widetilde{v}_\delta$ in (5.5). We find in the literature three main signal injection techniques:

1. **Sinusoidal circular** injection method [8, 11, 25–28, 97, 106, 107]: injection of a sinusoidal rotating carrier where $f(t)=\cos t$ and $g(t)=\sin t$ and $\widetilde{v}_\gamma=\widetilde{v}_\delta$;

2. **Sinusoidal pulsating** injection method [31–34, 94, 103, 105]: injection of a sinusoidal pulsating carrier where $f(t)=g(t)=\cos t$;

3. **Sinusoidal elliptic** injection method [24, 29, 30, 38, 39, 104]: injection of a sinusoidal elliptic carrier where $f(t)=\cos t$ and $g(t)=\sin t$ and $\widetilde{v}_\gamma\neq\widetilde{v}_\delta$.

5.1.3.1 Sinusoidal circular injection-based method

This method was introduced firstly by Jansen and Lorenz in 1995 [8] for sensorless control of AC machines at low and zero speed. It is based on adding a rotating carrier voltage which scan all the anisotropy of the motor in order to estimate the rotor position. This method was successfully tested

on a PMSM by Wang and Lorenz in 2000 [25] and by Consoli et al [11, 97]. In recent years, this method was widely used for sensorless control of PMSM [25–28, 106].

Using this type of signal injection, the expression of the HF voltage is obtained from (5.5) with $f(t) = \cos t$ and $g(t) = \sin t$ and $\widetilde{v}_\gamma = \widetilde{v}_\delta = \widetilde{v}$:

$$\widetilde{\mathcal{V}}_{\gamma\delta} = \widetilde{v} \begin{pmatrix} \cos \Omega t \\ \sin \Omega t \end{pmatrix}$$

where $\widetilde{v}$ is the amplitude of the injected voltage. In this case (5.14) leads to

$$\widetilde{\mathcal{I}}_\gamma = \frac{\widetilde{v}}{2\Omega L_d L_q}\Big((L_d + L_q)\sin(\Omega t) + (L_d - L_q)\sin(2\theta - 2\theta_c - \Omega t)\Big)$$
$$\widetilde{\mathcal{I}}_\delta = -\frac{\widetilde{v}}{2\Omega L_d L_q}\Big((L_d + L_q)\cos(\Omega t) + (L_d - L_q)\cos(2\theta - 2\theta_c - \Omega t)\Big).$$

The computation of the sum of $\widetilde{\mathcal{I}}_\gamma$ and $\jmath\widetilde{\mathcal{I}}_\delta$ yields

$$\widetilde{\mathcal{I}}_\gamma + \jmath\widetilde{\mathcal{I}}_\delta = \widetilde{i}_p e^{\jmath\Omega t} + \widetilde{i}_n e^{-\jmath\Omega t},$$

where $\jmath$ is the complex imaginary number and

$$\widetilde{i}_p = -\jmath\frac{\widetilde{v}(L_d + L_q)}{2\Omega L_d L_q}, \quad \widetilde{i}_n = -\jmath\frac{\widetilde{v}(L_d - L_q)}{2\Omega L_d L_q} e^{\jmath(2\theta - 2\theta_c)}, \tag{5.15}$$

$\widetilde{i}_p$ is the positive rotating component of the current which rotates at speed $+\Omega$ and it is independent from the position information; $\widetilde{i}_n$ is the negative rotating component of the current which rotates at speed $-\Omega$ and it contains the rotor position information. The current $\widetilde{i}_n$ is obtained by multiplying the current by $e^{\jmath\Omega t}$ (heterodyning) and by using a low pass filter as follows:

$$\widetilde{i}_n \approx LPF\Big((\widetilde{\mathcal{I}}_\gamma + \jmath\widetilde{\mathcal{I}}_\delta)e^{\jmath\Omega t}\Big) = LPF\Big(\widetilde{i}_n + \widetilde{i}_p e^{2\jmath\Omega t}\Big)$$

where LPF is the abbreviation of "low pass filter".

The current $\widetilde{i}_n$ can be written as

$$\widetilde{i}_n = \frac{\widetilde{v}(L_d - L_q)}{2\Omega L_d L_q}\Big(\sin(2\theta - 2\theta_c) - \jmath\cos(2\theta - 2\theta_c)\Big).$$

The separation of $\widetilde{i}_n = \widetilde{i}_n^r + \widetilde{i}_n^j$ into a real part $\widetilde{i}_n^r$ and an imaginary part $\widetilde{i}_n^j$ leads to

$$\widetilde{i}_n^r = \frac{\widetilde{v}(L_d - L_q)}{2\Omega L_d L_q}\sin(2\theta - 2\theta_c) \tag{5.16}$$
$$\widetilde{i}_n^j = -\frac{\widetilde{v}(L_d - L_q)}{2\Omega L_d L_q}\cos(2\theta - 2\theta_c). \tag{5.17}$$

It is important to note that if $L_d = L_q$ then the currents $\widetilde{i}_n^r = \widetilde{i}_n^j = 0$ and the position information is lost, hence $L_d \neq L_q$ is a necessary condition to get the position information; this is the saliency condition in the case of a linear and decoupled motor model. Using (5.16)-(5.17) we get

$$\tan(2\theta - 2\theta_c) = -\frac{\widetilde{i}_n^r}{\widetilde{i}_n^j}, \tag{5.18}$$

hence the rotor position can be estimated as follows

$$\theta = \theta_c - \frac{1}{2}\left(\arctan\frac{\widetilde{i}_n^r}{\widetilde{i}_n^j}\right) + k\pi, \tag{5.19}$$

where k is an integer. The position is obtained with a π ambiguity, this can be resolved by the using of an appropriate initial position estimation algorithm.

If we use θ_c as an estimated value of the rotor position, then the current $\widetilde{i}_n$ gives an estimation of the rotor position estimation error $\theta - \theta_c$ between the actual rotor position θ and the estimated position θ_c. Thus $\widetilde{i}_n$ can be used to calculate an error signal for a rotor position tracking observer. In this case, the position error $\theta - \theta_c$ is considered to be small, hence $\widetilde{i}_n^j$ is constant in this case:

$$\widetilde{i}_n^j = -\frac{\widetilde{v}(L_d - L_q)}{2\Omega L_d L_q}\cos\left(2\theta - 2\theta_c\right) \approx -\frac{\widetilde{v}(L_d - L_q)}{2\Omega L_d L_q},$$

and (5.18) yields

$$\theta - \theta_c \approx \frac{\Omega L_d L_q}{\widetilde{v}(L_d - L_q)}\widetilde{i}_n^r. \tag{5.20}$$

In (5.20) we get an error signal proportional to $\widetilde{i}_n^r$. The rotor position error is zero when $\widetilde{i}_n^r$ is zero, hence by controlling $\widetilde{i}_n^r$ to be zero then θ_c will be the good estimation of the rotor position θ.

5.1.3.2 Injection of an pulsating sinusoidal carrier

The injection of an pulsating sinusoidal carrier was introduced by Ha et Sul in 1999 [31]. This method is based on the injection of a pulsating carrier in a fixed direction in the rotating $\gamma\delta$ frame. This direction is selected to locate a specific motor anisotropy which is, for linear model, aligned with the d- axis (minimum inductance L_d) or the q- axis (maximum inductance L_q). This is a standard method of position estimation [31–34, 94, 103, 105] for sensorless PMSM control at low speed including zero speed operation.

In [32, 93, 94] a pulsating HF carrier voltage is injected on the γ- axis of the estimated rotor frame $\gamma\delta$. The HF current on the δ- frame is used to estimate the rotor position. The expression of the injected voltage in $\gamma\delta$ frame is obtained from (5.5) with $f(t) = g(t) = \cos t$ and $\widetilde{v}_\gamma = \widetilde{v}$ and $\widetilde{v}_\delta = 0$:

$$\widetilde{\mathcal{V}}_{\gamma\delta} = \begin{pmatrix} \widetilde{v}\cos\Omega t \\ 0 \end{pmatrix} \tag{5.21}$$

where $\widetilde{v}$ is constant. In this case $F(t) = \sin t$. Thus (5.14) leads to

$$\widetilde{\mathcal{I}}_\gamma = \frac{\widetilde{v}}{2\Omega L_d L_q}\Big((L_d + L_q) - (L_d - L_q)\cos\left(2\theta - 2\theta_c\right)\Big)\sin\left(\Omega t\right) \tag{5.22}$$

$$\widetilde{\mathcal{I}}_\delta = -\frac{\widetilde{v}(L_d - L_q)}{2\Omega L_d L_q}\sin\left(2\theta - 2\theta_c\right)\sin\left(\Omega t\right). \tag{5.23}$$

The δ-axis component $\widetilde{\mathcal{I}}_\delta$ of the HF current is a sinusoidal signal with respect to the time. It can be written in the form:

$$\widetilde{\mathcal{I}}_\delta = \widetilde{i}_\delta \sin\left(\Omega t\right),$$

where

$$\widetilde{i}_\delta = -\frac{\widetilde{v}(L_d - L_q)}{2\Omega L_d L_q} \sin(2\theta - 2\theta_c), \tag{5.24}$$

therefore the HF current amplitude $\widetilde{i}_\delta$ is a function of the rotor position error $\theta - \theta_c$. It is important to note that if $L_d = L_q$ in (5.22)-(5.23) then the position information is lost, hence $L_d \neq L_q$ is also a necessary condition to have the position information, this is the saliency condition in the case of a linear and decoupled motor model. Using (5.24) we get

$$\theta = \theta_c - \frac{1}{2} \arcsin\left(\frac{2\Omega L_d L_q}{\widetilde{v}(L_d - L_q)} \widetilde{i}_\delta\right) + k\pi \tag{5.25}$$

where k is an integer. The position is obtained with a π ambiguity, this can be resolved by the using of an appropriate initial position estimation algorithm.

If we use θ_c as an estimated value of the rotor position, then the current $\widetilde{i}_\delta$ gives an estimation of the rotor position error $\theta - \theta_c$ between the actual rotor position θ and the estimated position θ_c. Thus $\widetilde{i}_\delta$ can be used to calculate an error signal for a rotor position tracking observer. In this case, the position error $\theta - \theta_c$ is considered to be small, hence (5.24) yields

$$\theta - \theta_c \approx -\frac{\Omega L_d L_q}{\widetilde{v}(L_d - L_q)} \widetilde{i}_\delta \tag{5.26}$$

In (5.26) we get an error signal proportional to $\widetilde{i}_\delta$. Thus, the rotor position error is zero when $\widetilde{i}_\delta$ is zero, hence by controlling $\widetilde{i}_\delta$ to be zero then θ_c will be the good estimation of the rotor position θ.

Recently, Yoon et al proposed an new signal injection method based on pulsating rectangular carrier injection [35, 36, 108]. In this case, the sinusoidal signal is replaced by a rectangular signal i.e. the function f is a periodic rectangular function with zero mean and the function F is a triangular function. This method is similar to the sinusoidal pulsating injection-based method, the only difference is that $\cos \Omega t$ is replaced by $f(\Omega t)$ and $\sin \Omega t$ is replaced by $F(\Omega t)$. The motivation of this type of signal injection is that it is easier to implement a rectangular function than a sinusoidal function using an industrial electric drive.

5.1.3.3 Sinusoidal elliptical injection-based method

This method was introduced by Corley et Lorenz in 1998 [24]. It is based on adding an elliptic HF carrier voltage. The major axis carrier voltage is used to track a fixed anisotropy of the rotor while the minor axis voltage is used to compensate the effect of the motor speed. This method can be used up to the nominal speed of the motor. It is also widely used in the literature [29, 30, 38, 39, 104] for sensorless rotor position estimation.

In this case, an elliptical HF sinusoidal voltage rotating at a speed Ω is added to the motor voltage in the estimated $\gamma\delta$ frame as follows

$$\widetilde{\mathcal{V}}_{\gamma\delta} = \widetilde{v} \begin{pmatrix} \cos \Omega t \\ \frac{\omega_c}{\Omega} \sin \Omega t \end{pmatrix}$$

where $\omega_c = \frac{d\theta_c}{dt}$. The position θ_c is considered here as the estimated rotor position and the speed ω_c is considered as the estimated rotor speed. The induced HF voltage by the electrical fluxes and the

motor speed is not neglected here [24], hence (5.6) yields

$$\frac{d\widetilde{\mathbf{\Phi}}_{\gamma\delta}}{dt} = \widetilde{\mathcal{V}}_{\gamma\delta} - \omega_c \mathcal{J} \widetilde{\mathbf{\Phi}}_{\gamma\delta}, \tag{5.27}$$

at steady state, according to [24] the equation (5.27) leads to

$$\left.\begin{aligned} \widetilde{\phi}_\gamma &= \frac{\widetilde{v}}{\Omega}\sin\Omega t \\ \widetilde{\phi}_\delta &= 0 \end{aligned}\right\} \tag{5.28}$$

Using (5.11), (5.13) and (5.28) hence we get

$$\begin{aligned} \widetilde{\mathcal{I}}_\gamma &= \frac{\widetilde{v}}{2\Omega L_d L_q}\Big(L_d + L_q - (L_d - L_q)\cos\left(2\theta - 2\theta_c\right)\Big)\sin\left(\Omega t\right) \\ \widetilde{\mathcal{I}}_\delta &= -\frac{\widetilde{v}(L_d - L_q)}{2\Omega L_d L_q}\sin\left(2\theta - 2\theta_c\right)\sin\left(\Omega t\right), \end{aligned}$$

the expressions of $\widetilde{\mathcal{I}}_\gamma$ and $\widetilde{\mathcal{I}}_\delta$ in this case are the same as their expressions in (5.22) and (5.23). Therefore the rotor position can be estimated by the same way as when a pulsating sinusoidal voltage is injected (5.24)–(5.26).

To conclude, we note that the signal injection techniques presented below are similar because in all cases the position is estimated by demodulating the HF current. These techniques are distinguished by the shape of the added voltage and by the demodulation procedure of the HF current. In the sequel, the pulsating HF signal injection method is only used.

5.1.4 Impact of cross coupling and saturation

The decoupled linear model of PMSM was used previously. But it is well known that this model is not sufficient to get good estimation of rotor position due to cross coupling and to the nonlinear effects of magnetic saturation. These effects introduce an error to the estimated position depending on the load torque and on the current level. Thus, the modeling of cross coupling is important to correctly estimate the rotor position and guarantee the stability of the position observer.

The effects of cross coupling on sensorless position estimation of PMSM have been widely studied in the past 10 years [28, 43–63]. According to chapter 4 section 4.3.2, the saturation effects are represented in the literature by a mutual inductance between the d- and q- axis in the rotor dq frame. Thus, the inductance matrix $\mathbf{L}^{dq}$ defined in (5.9) is no more diagonal and it contains non diagonal terms as follows

$$\mathbf{L}^{dq} = \begin{pmatrix} L_d & l_m \\ l_m & L_q \end{pmatrix}. \tag{5.29}$$

In the case of HF voltage injection, the presence of this cross inductance l_m modifies the HF current expression and leads to position estimation errors. Indeed using (5.29) and (5.12), the expression of the inductance $\mathbf{L}^{\gamma\delta}$ with cross coupling reads

$$\mathbf{L}^{\gamma\delta}(\mu) = \tfrac{1}{2}\begin{pmatrix} L_d + L_q + 2L_e\cos\left(2\mu + \theta_e\right) & 2L_e\sin\left(2\mu + \theta_e\right) \\ 2L_e\sin\left(2\mu + \theta_e\right) & L_d + L_q - 2L_e\cos\left(2\mu + \theta_e\right) \end{pmatrix} \tag{5.30}$$

with

$$\theta_e = \arctan\left(\frac{2l_m}{L_d - L_q}\right) \tag{5.31}$$

where $L_e = \frac{1}{2}\sqrt{(L_d - L_q)^2 + 4l_m^2}$.

We consider here the case of pulsating carrier injection (the impact of cross saturation is similar for the other types of signal injection). Using (5.14) with $F = G$ (pulsating signal) and $\widetilde{v}_\gamma = \widetilde{v}$ and $\widetilde{v}_\delta = 0$, hence the expression of the HF current reads

$$\widetilde{\mathcal{I}}_{\gamma\delta} = \frac{\widetilde{v}}{\Omega}\left(\mathbf{L}^{\gamma\delta}(\theta - \theta_c)\right)^{-1}\begin{pmatrix} F \\ 0 \end{pmatrix}$$

where

$$\left(\mathbf{L}^{\gamma\delta}\right)^{-1}(\mu) = \frac{1}{2(L_dL_q - l_m^2)}\begin{pmatrix} L_d + L_q - 2L_e\cos(2\mu + \theta_e) & -2L_e\sin(2\mu + \theta_e) \\ -2L_e\sin(2\mu + \theta_e) & L_d + L_q + 2L_e\cos(2\mu + \theta_e) \end{pmatrix}.$$

Finally we get

$$\widetilde{\mathcal{I}}_\gamma = \frac{\widetilde{v}}{2\Omega(L_dL_q - l_m^2)}\Big((L_d + L_q) - (L_d - L_q)\cos(2\theta - 2\theta_c + \theta_e)\Big)F(\Omega t) \tag{5.32}$$

$$\widetilde{\mathcal{I}}_\delta = -\frac{\widetilde{v}(L_d - L_q)}{2\Omega(L_dL_q - l_m^2)}\sin(2\theta - 2\theta_c + \theta_e)F(\Omega t). \tag{5.33}$$

The HF current (5.33) can be written as

$$\widetilde{\mathcal{I}}_\delta = \widetilde{i}_\delta F(\Omega t)$$

where $\widetilde{i}_\delta = -\frac{\widetilde{v}(L_d - L_q)}{2\Omega(L_dL_q - l_m^2)}\sin(2\theta - 2\theta_c + \theta_e)$. Thus, the rotor position can be written as follows:

$$\theta = \theta_c - \frac{\theta_e}{2} - \frac{1}{2}\arcsin\left(\frac{2\Omega(L_dL_q - l_m^2)}{\widetilde{v}(L_d - L_q)}\widetilde{i}_\delta\right) + k\pi. \tag{5.34}$$

In the case of small angle approximation we get:

$$\theta - \theta_c \approx -\frac{\Omega(L_dL_q - l_m^2)}{\widetilde{v}(L_d - L_q)}\widetilde{i}_\delta - \frac{\theta_e}{2}. \tag{5.35}$$

The position expressions obtained in (5.34)-(5.35) by considering the mutual inductance contain the additional term $-\frac{\theta_e}{2}$. This term does not appear in the position expressions (5.25)-(5.26) when the cross coupling is not considered. This term leads to a position estimation error and must be compensated to get an acceptable estimation accuracy and to guarantee the stability of the motor when the estimated position is used in a sensorless control scheme. The position error $-\frac{\theta_e}{2}$ caused by the cross coupling is a function of the mutual inductance l_m and the difference between d- and q-axis inductances $L_d - L_q$ (see (5.31)).

We used here a linear model of PMSM where all the inductances are considered constant. However, according to (4.128)–(4.130), (L_d,L_q,l_m) depend on the currents. Thus, the position error introduced by the cross coupling effects is no more constant but it depends on the currents also. Hence,

the compensation procedure must depend on the operation point i.e. in the γ- axis and δ- axis currents which are the measured currents.

We find in the literature several methods to compensate the error caused by the cross coupling. Most of these methods are based on finding relations between the three inductances (L_d, L_q, l_m) and the currents i_d and i_q or by finding directly a relation between θ_e and these currents. This compensation is done during the real time operation of the motor where the saturation information is obtained in function of the operation point by one of the following methods:

- using look up table where the saturation information is stored in a look up table [50]
- using explicit parametric relation between position error and current measurements [56]
- using neural network where the saturation information is stored in a set of neural networks [55].

The existing modeling methods of cross saturation present in the literature permit the compensation of the rotor position error at high load torque and lead to good motor operation performances when used in sensorless position estimation. By contrast, each method presented above is suitable only for one type of PMSM; there is no general procedure which can be used for all PMSM types. In addition, These methods are not based on a clear mathematical interpretation of the separation between the fundamental frequency model and the HF model of PMSM. Finally, we do not have an explicit condition for the feasibility of the sensorless position estimation by HF injection at low speed, they give only some conditions obtained experimentally.

In the sequel, we propose an analysis based on second order averaging of how to recover the position information from signal injection. A clear mathematical condition for sensorless position estimation is given also, this condition is an extension of the saliency condition $L_d \neq L_q$ when the linear PMSM model is used. This method is based on the simple parametric saturation model proposed in the previous chapter (4.132)-(4.133). In this case, we need only 5 saturation parameters which are simple to be estimated as we will see in the next chapter. It can be applied to any type of PMSM i.e. interior magnet and surface mounted PMSM. The cross saturation is well compensated even at 200% of the rated torque.

The saturation model explains the variation of the motor inductances according to the different operation points, in particular, the high dependence of the mutual inductance l_m on the load torque and current levels. Thanks to second order averaging, we give a mathematical interpretation of the separation between the HF motor model and the fundamental frequency motor model where we show that the rotor speed and position are not affected by the voltage injection.

5.2 Signal injection and averaging

In this section we propose an original way for time scale separation between HF signals and low frequency signals of PMSM when voltage injection is used [64–66]. This separation is based on second order periodic averaging. It consists on solving a perturbation problem where the HF voltage is considered as a periodic perturbation of the motor fundamental voltage. This method will be used in the next section to find a relation between the HF current and the rotor position.

5.2.1 General system equations

In this part, we will show that the injection of a HF voltage with a general speed control law (closed loop or sensorless) does not have an impact on the operation of the motor.

We use here the motor dynamic equations (5.2)-(5.4) in $\gamma\delta$ frame. Using the saturation model (4.132)-(4.133), the current in $\gamma\delta$ frame can be written in terms of flux and position as follows

$$\begin{aligned}\mathbf{i}_{\gamma\delta} &= \mathcal{R}_{\theta-\theta_c}\mathbf{i}_{dq} \\ &= \mathcal{R}_{\theta-\theta_c}\mathcal{I}_{dq}(\mathbf{\Phi}_{dq}) \\ &= \mathcal{R}_{\theta-\theta_c}\mathcal{I}_{dq}(\mathcal{R}^T_{\theta-\theta_c}\mathbf{\Phi}_{\gamma\delta}),\end{aligned} \tag{5.36}$$

where $\mathcal{I}_{dq} = (\mathcal{I}_d, \mathcal{I}_q)^T$.

In (5.2)–(5.4) and (5.36) we get a nonlinear dynamic model of PMSM with magnetic saturation in $\gamma\delta$ frame where $\mathbf{\Phi}_{\gamma\delta}$, ω and θ are the state variables; the impressed voltage $\mathbf{v}_{\alpha\beta} = \mathcal{R}_{\theta_c}\mathbf{v}_{\gamma\delta}$ is the input variable; the measured current $\mathbf{i}_{\alpha\beta} = \mathcal{R}_{\theta_c}\mathbf{i}_{\gamma\delta}$ is the output variable. Using this model, a general control law can be expressed in $\gamma\delta$ frame as follows

$$\mathbf{v}_{\alpha\beta} = \mathcal{R}_{\theta_c}\mathbf{v}_{\gamma\delta} \tag{5.37}$$

$$\mathbf{i}_{\gamma\delta} = \mathcal{R}^T_{\theta_c}\mathbf{i}_{\alpha\beta} \tag{5.38}$$

$$\frac{d\theta_c}{dt} = \omega_c \tag{5.39}$$

$$\frac{d\eta}{dt} = \mathbf{a}\big(\mathbf{i}_{\gamma\delta}, \theta, \theta_c, \eta, t\big) \tag{5.40}$$

$$\omega_c = \Omega_c\big(\mathbf{i}_{\gamma\delta}, \theta, \theta_c, \eta, t\big) \tag{5.41}$$

$$\mathbf{v}_{\gamma\delta} = \mathcal{V}_{\gamma\delta}\big(\mathbf{i}_{\gamma\delta}, \theta, \theta_c, \eta, t\big) \tag{5.42}$$

where η is the internal (vector) variable of the controller. The three functions $\mathbf{a}$, Ω_c and $\mathcal{V}_{\gamma\delta}$ define the evolution of the controller in terms of the measured current $\mathbf{i}_{\alpha\beta}$; the internal variables η; the rotor position θ and the time t. These functions are chosen in a way to guarantee the stability of the control law and to define the motor operation at steady state.

A fast-varying pulsating voltage is superimposed to the desirable control voltage (5.42) as follows

$$\mathbf{v}_{\gamma\delta} = \mathcal{V}_{\gamma\delta}\big(\mathbf{i}_{\gamma\delta}, \theta, \theta_c, \eta, t\big) + \widetilde{\mathbf{v}}_{\gamma\delta} f(\Omega t) \tag{5.43}$$

where

- $\mathcal{V}_{\gamma\delta}$ is the fundamental voltage applied to the motor in $\gamma\delta$ frame, this voltage is used to control and stabilize the motor.
- $\widetilde{\mathbf{v}}_{\gamma\delta} f(\Omega t)$ is a HF voltage;
- f is here a 2π-periodic function with zero mean and $\widetilde{\mathbf{v}}_{\gamma\delta}$ could like $\overline{\mathcal{V}}_{\gamma\delta}$ depend on $\mathbf{i}_{\gamma\delta}, \theta_c, \eta, t$ (though it is always taken constant in the sequel);
- The constant pulsation Ω is chosen "large", so that $f(\Omega t)$ can be seen as a "fast" oscillation; typically $\Omega := 2\pi \times 500$ rad/s.

Using the motor model (5.2)–(5.4) and (5.36) with the modified control law (5.37)–(5.41) and (5.43), hence the closed loop motor system equations read

$$\frac{d\mathbf{\Phi}_{\gamma\delta}}{dt} = \widetilde{\mathbf{v}}_{\gamma\delta} f(\Omega t) + \mathcal{V}_{\gamma\delta} - R\mathbf{i}_{\gamma\delta} - \Omega_c \mathcal{J}\mathbf{\Phi}_{\gamma\delta} - \omega\mathcal{J}\mathcal{R}_{\theta-\theta_c}\mathbf{\Phi}_m \tag{5.44}$$

$$\frac{J}{n^2}\frac{d\omega}{dt} = \mathbf{i}_{\gamma\delta}^T \mathcal{J}(\mathbf{\Phi}_{\gamma\delta} + \mathcal{R}_{\theta-\theta_c}\mathbf{\Phi}_m) - \frac{\tau_L}{n} \tag{5.45}$$

$$\frac{d\theta}{dt} = \omega \tag{5.46}$$

$$\frac{d\theta_c}{dt} = \Omega_c\big(\mathbf{i}_{\gamma\delta}, \theta, \theta_c, \eta, t\big) \tag{5.47}$$

$$\frac{d\eta}{dt} = \mathbf{a}\big(\mathbf{i}_{\gamma\delta}, \theta, \theta_c, \eta, t\big) \tag{5.48}$$

with

$$\mathbf{i}_{\gamma\delta} = \mathcal{R}_{\theta-\theta_c}\mathcal{I}_{dq}(\mathcal{R}_{\theta-\theta_c}^T \mathbf{\Phi}_{\gamma\delta}).$$

The motor system (5.44)–(5.48) has two time scales. It has a slow time scale (low or fundamental frequency) which corresponds to the variation of the motor electrical and mechanical variables, the time constant in this case is the electrical time constant of the motor. In addition, this system has a fast time scale introduced by the periodic function $f(\Omega t)$ which has a small period $\frac{2\pi}{\Omega}$ and a high pulsation Ω compared to the motor bandwidth.

5.2.2 Time scale separation by second order averaging

Applying the periodic second order averaging to (5.44)–(5.48), each state variable x can be written as the sum of a low frequency (slow varying) component $\overline{x}$ and a HF component $\widetilde{x}$ (fast varying) as follows

$$x = \overline{x} + \widetilde{x} + \mathcal{O}(\frac{1}{\Omega^2})$$

where x can be ϕ_γ, ϕ_δ, ω, θ, θ_c, η. A fast varying component $\widetilde{x} = \mathcal{O}(\frac{1}{\Omega})$ is periodic with the same period as f and it is small (on order of $\frac{1}{\Omega}$). The order term $\mathcal{O}(\frac{1}{\Omega^2})$ is very small, this term is neglected in the sequel. It can be shown (the proof is given later see section 5.2.3.2) that

$$\widetilde{\mathbf{\Phi}}_{\gamma\delta} = \frac{\widetilde{\mathbf{v}}_{\gamma\delta}}{\Omega} F(\Omega t)$$
$$\widetilde{\omega} = \widetilde{\theta} = \widetilde{\theta}_c = \widetilde{\eta} = 0$$

with

$$F(t) = \int_0^t f(\tau)d\tau - \frac{1}{2\pi}\int_0^{2\pi}\int_0^t f(\tau)d\tau dt$$

where F is the integral of f; it is clear that F is 2π- periodic zero mean function; τ is an integration variable.

Thus, the solution of the closed loop system (5.44)–(5.48) is

$$\mathbf{\Phi}_{\gamma\delta} = \overline{\mathbf{\Phi}}_{\gamma\delta} + \frac{\widetilde{\mathbf{v}}_{\gamma\delta}}{\Omega} F(\Omega t) + \mathcal{O}(\frac{1}{\Omega^2}) \tag{5.49}$$

$$\omega = \overline{\omega} + \mathcal{O}(\frac{1}{\Omega^2}) \tag{5.50}$$

$$\theta = \overline{\theta} + \mathcal{O}(\frac{1}{\Omega^2}) \tag{5.51}$$

$$\theta_c = \overline{\theta}_c + \mathcal{O}(\frac{1}{\Omega^2}) \tag{5.52}$$

$$\eta = \overline{\eta} + \mathcal{O}(\frac{1}{\Omega^2}), \tag{5.53}$$

$(\overline{\mathbf{\Phi}}_{\gamma\delta}, \overline{\omega}, \overline{\theta}, \overline{\theta}_c, \overline{\eta})$ is the "slowly-varying" component of $(\mathbf{\Phi}_{\gamma\delta}, \omega, \theta, \theta_c, \eta)$, i.e. satisfies

$$\frac{d\overline{\mathbf{\Phi}}_{\gamma\delta}}{dt} = \overline{\mathbf{v}}_{\gamma\delta} - R\bar{\mathbf{i}}_{\gamma\delta} - \overline{\omega}_c \mathcal{J} \overline{\mathbf{\Phi}}_{\gamma\delta} - \omega \mathcal{J} \mathcal{R}_{\overline{\theta}-\overline{\theta}_c} \mathbf{\Phi}_m \tag{5.54}$$

$$\frac{J}{n^2}\frac{d\overline{\omega}}{dt} = \bar{\mathbf{i}}_{\gamma\delta}^T \mathcal{J}(\overline{\mathbf{\Phi}}_{\gamma\delta} + \mathcal{R}_{\overline{\theta}-\overline{\theta}_c}\mathbf{\Phi}_m) - \frac{\tau_L}{n} \tag{5.55}$$

$$\frac{d\overline{\theta}}{dt} = \overline{\omega} \tag{5.56}$$

$$\frac{d\overline{\theta}_c}{dt} = \overline{\omega}_c \tag{5.57}$$

$$\frac{d\overline{\eta}}{dt} = \mathbf{a}\big(\bar{\mathbf{i}}_{\gamma\delta}, \overline{\theta}, \overline{\theta}_c, \overline{\eta}, t\big), \tag{5.58}$$

where

$$\begin{aligned} \bar{\mathbf{i}}_{\gamma\delta} &= \mathcal{R}_{\overline{\theta}-\overline{\theta}_c} \mathcal{I}_{dq}(\mathcal{R}^T_{\overline{\theta}-\overline{\theta}_c} \overline{\mathbf{\Phi}}_{\gamma\delta}) \\ \overline{\omega}_c &= \Omega_c\big(\bar{\mathbf{i}}_{\gamma\delta}, \overline{\theta}, \overline{\theta}_c, \overline{\eta}, t\big) \\ \overline{\mathbf{v}}_{\gamma\delta} &= \mathcal{V}_{\gamma\delta}\big(\bar{\mathbf{i}}_{\gamma\delta}, \overline{\theta}, \overline{\theta}_c, \overline{\eta}, t\big). \end{aligned} \tag{5.59}$$

This system represents the fundamental operation of the motor and is used to design the motor controller. The motor is stable only if this system is stable.

Notice this slowly-varying system defined below is exactly the same as (5.2)–(5.2) and (5.36) acted upon by the unmodified control law (5.37)–(5.42). In other words adding signal injection:

- has a very small effect of order $\mathcal{O}(\frac{1}{\Omega^2})$ on the mechanical variables θ, ω and the controller variables θ_c, η;
- has a small effect of order $\mathcal{O}(\frac{1}{\Omega})$ on the flux $\mathbf{\Phi}_{\gamma\delta}$; this effect will be used in the next section to extract the position information from the measured currents.

5.2.3 Mathematical interpretation

In this part we provides the proof of (5.49)–(5.53) using periodic second order averaging. At first, we present the second order averaging. Then, we apply averaging to the motor control system (5.44)–(5.48).

5.2.3.1 Periodic second order averaging

This part relies on the reference [109] section 2.9.1 and section 3.3. Periodic second order averaging with slow-time dependence consists of solving a perturbation problem in the standard form

$$\frac{d\mathbf{x}}{d\sigma} = \varepsilon \mathbf{f}_1(\mathbf{x}, \varepsilon\sigma, \sigma) \tag{5.60}$$

where

- $\mathbf{x} \in \mathbb{R}^n$;
- σ is a time variable;
- ε is a small constant parameter;
- $\mathbf{f}_1$ is a function from $\mathbb{R}^{n+2}$ to $\mathbb{R}^n$;
- $\mathbf{f}_1$ is periodic with respect to its third variable such

$$\mathbf{f}_1(\mathbf{x}, \varepsilon\sigma, \sigma + T_\sigma) = \mathbf{f}_1(\mathbf{x}, \varepsilon\sigma, \sigma)$$

  where T_σ is a constant period.

The solution of (5.60) can be approximated as

$$\mathbf{x}(\sigma) = \mathbf{z}(\sigma) + \varepsilon \mathbf{u}_1\Big(\mathbf{z}(\sigma), \varepsilon\sigma, \sigma\Big) + \mathcal{O}(\varepsilon^2), \tag{5.61}$$

The function $\mathbf{z}(\sigma)$ is the solution of

$$\frac{d\mathbf{z}}{d\sigma} = \varepsilon \mathbf{g}_1(\mathbf{z}, \varepsilon\sigma) + \varepsilon^2 \mathbf{g}_2(\mathbf{z}, \varepsilon\sigma). \tag{5.62}$$

with

$$\mathbf{g}_1(\mathbf{z}, \varepsilon\sigma) := \frac{1}{T_\sigma} \int_0^{T_\sigma} \mathbf{f}_1(\mathbf{z}, \varepsilon\sigma, s) ds \tag{5.63}$$

and

$$\mathbf{g}_2(\mathbf{z}, \varepsilon\sigma) := \frac{1}{T_\sigma} \int_0^{T_\sigma} \mathbf{K}_2(\mathbf{z}, \varepsilon\sigma, s) ds \tag{5.64}$$

where

$$\mathbf{K}_2(\mathbf{z}, \varepsilon\sigma, \sigma) := \frac{\partial \mathbf{f}_1}{\partial \mathbf{z}}(\mathbf{z}, \varepsilon\sigma, \sigma)\mathbf{u}_1(\mathbf{z}, \varepsilon\sigma, \sigma) - \frac{\partial \mathbf{u}_1}{\partial \mathbf{z}}(\mathbf{z}, \varepsilon\sigma, \sigma)\mathbf{g}_1(\mathbf{z}, \varepsilon\sigma); \tag{5.65}$$

$$\mathbf{u}_1(\mathbf{z}, \varepsilon\sigma, \sigma) := \mathbf{v}_1(\mathbf{z}, \varepsilon\sigma, \sigma) - \frac{1}{T_\sigma} \int_0^{T_\sigma} \mathbf{v}_1(\mathbf{z}, \varepsilon\sigma, s) ds; \tag{5.66}$$

and

$$\mathbf{v}_1(\mathbf{z}, \varepsilon\sigma, \sigma) := \int_0^{\sigma} \big(\mathbf{f}_1(\mathbf{z}, \varepsilon\sigma, s) - \mathbf{g}_1(\mathbf{z}, \varepsilon\sigma)\big) ds. \tag{5.67}$$

5.2.3.2 Proof of (5.49)–(5.53)

The proof relies on a direct application of periodic second-order averaging of differential equations presented in 5.2.3.1. We must write the system equations with the modified control law (5.44)–(5.48) in the so-called standard form for averaging (with slow-time dependence); see (5.60). This can be done by setting

$$\varepsilon := \frac{1}{\Omega}, \quad \mathbf{x} := (\mathbf{\Phi}_{\gamma\delta}^T, \omega, \theta, \theta_c, \eta^T)^T, \quad \sigma := \frac{t}{\varepsilon} = \Omega t. \tag{5.68}$$

Thus the system (5.44)–(5.48) leads to

$$\frac{d\mathbf{x}}{d\sigma} = \varepsilon \mathbf{f}_1(\mathbf{x}, \varepsilon\sigma, \sigma) := \varepsilon\Big(\bar{\mathbf{f}}_1(\mathbf{x}, \varepsilon\sigma) + \widetilde{\mathbf{f}}_1(\mathbf{x}, \varepsilon\sigma) f(\sigma)\Big). \tag{5.69}$$

From (5.44)–(5.48) and the variable change (5.68) we get

$$\mathbf{f_1}(\mathbf{x}, \varepsilon\sigma, \sigma) = \begin{pmatrix} \widetilde{\mathbf{v}}_{\gamma\delta} f(\sigma) + \mathcal{V}_{\gamma\delta}\big(\mathbf{i}_{\gamma\delta}, \theta, \theta_c, \eta, \varepsilon\sigma\big) - R\mathbf{i}_{\gamma\delta} - \Omega_c\big(\mathbf{i}_{\gamma\delta}, \theta, \theta_c, \eta, \varepsilon\sigma\big)\mathcal{J}\mathbf{\Phi}_{\gamma\delta} - \omega\mathcal{J}\mathcal{R}_{\theta-\theta_c}\mathbf{\Phi}_m \\ \mathbf{i}_{\gamma\delta}^T\mathcal{J}(\mathbf{\Phi}_{\gamma\delta} + \mathcal{R}_{\theta-\theta_c}\mathbf{\Phi}_m) - \frac{\tau_L}{n} \\ \omega \\ \Omega_c\big(\mathbf{i}_{\gamma\delta}, \theta, \theta_c, \eta, \varepsilon\sigma\big) \\ \mathbf{a}\big(\mathbf{i}_{\gamma\delta}, \theta, \theta_c, \eta, \varepsilon\sigma\big) \end{pmatrix}$$

with

$$\bar{\mathbf{f}}_1(\mathbf{x}, \varepsilon\sigma) = \begin{pmatrix} \mathcal{V}_{\gamma\delta}\big(\mathbf{i}_{\gamma\delta}, \theta, \theta_c, \eta, \varepsilon\sigma\big) - R\mathbf{i}_{\gamma\delta} - \Omega_c\big(\mathbf{i}_{\gamma\delta}, \theta, \theta_c, \eta, \varepsilon\sigma\big)\mathcal{J}\mathbf{\Phi}_{\gamma\delta} - \omega\mathcal{J}\mathcal{R}_{\theta-\theta_c}\mathbf{\Phi}_m \\ \mathbf{i}_{\gamma\delta}^T\mathcal{J}(\mathbf{\Phi}_{\gamma\delta} + \mathcal{R}_{\theta-\theta_c}\mathbf{\Phi}_m) - \frac{\tau_L}{n} \\ \omega \\ \Omega_c\big(\mathbf{i}_{\gamma\delta}, \theta, \theta_c, \eta, \varepsilon\sigma\big) \\ \mathbf{a}\big(\mathbf{i}_{\gamma\delta}, \theta, \theta_c, \eta, \varepsilon\sigma\big) \end{pmatrix}$$

and

$$\widetilde{\mathbf{f}}_1(\mathbf{x}, \varepsilon\sigma) = \begin{pmatrix} \widetilde{\mathbf{v}}_{\gamma\delta}^T & 0 & 0 & 0 & 0 \end{pmatrix}^T.$$

It is clear that $\mathbf{f}_1$ is 2π-periodic with respect to its third variable because f is 2π-periodic, hence

$$\mathbf{f}_1(\mathbf{x}, \varepsilon\sigma, \sigma + 2\pi) = \mathbf{f}_1(\mathbf{x}, \varepsilon\sigma, \sigma),$$

and ε is a small parameter because Ω is supposed to be large.

Therefore, according to (5.61) the solution of (5.69) can be approximated as

$$\mathbf{x}(\sigma) = \mathbf{z}(\sigma) + \varepsilon\mathbf{u}_1\Big(\mathbf{z}(\sigma), \varepsilon\sigma, \sigma\Big) + \mathcal{O}(\varepsilon^2),$$

where $\mathbf{z}(\sigma)$ is the solution of

$$\frac{d\mathbf{z}}{d\sigma} = \varepsilon\mathbf{g}_1(\mathbf{z}, \varepsilon\sigma) + \varepsilon^2\mathbf{g}_2(\mathbf{z}, \varepsilon\sigma).$$

The expressions of $\mathbf{x}$ and $\mathbf{z}$ depend on the three functions $\mathbf{u}_1$, $\mathbf{g}_1$ and $\mathbf{g}_2$ as explained in 5.2.3.1.

The function $\mathbf{g}_1$ represents the low frequency part of the system (5.44)–(5.48) (first order averaging). It is equal to the average of the function $\mathbf{f}_1$ over one period 2π. According to (5.63), $\mathbf{g}_1$ can be written as follows

$$\begin{aligned}\mathbf{g}_1(\mathbf{z},\varepsilon\sigma) :&= \frac{1}{2\pi}\int_0^{2\pi}\mathbf{f}_1(\mathbf{z},\varepsilon\sigma,s)ds\\ &= \frac{1}{2\pi}\bar{\mathbf{f}}_1(\mathbf{z},\varepsilon\sigma)\int_0^{2\pi}ds + \frac{1}{2\pi}\widetilde{\mathbf{f}}_1(\mathbf{z},\varepsilon\sigma)\int_0^{2\pi}f(s)ds\\ &= \bar{\mathbf{f}}_1(\mathbf{z},\varepsilon\sigma)\end{aligned} \tag{5.70}$$

where we have used $\int_0^{2\pi} f(s)ds = 0$ because f has a zero mean over one period 2π. We note that $\mathbf{g}_1(\mathbf{z},\varepsilon\sigma) = \bar{\mathbf{f}}_1$ does not contain HF components.

The function $\mathbf{u}_1$ represents the HF part of the system (5.44)–(5.48) (second order averaging). It is obtained from the difference between the function $\mathbf{f}_1$ and the average function $\mathbf{g}_1$. To find the expression of $\mathbf{u}_1$ we need a function denoted $\mathbf{v}_1$ given by (5.67):

$$\begin{aligned}\mathbf{v}_1(\mathbf{z},\varepsilon\sigma,\sigma) :&= \int_0^{\sigma}\big(\mathbf{f}_1(\mathbf{z},\varepsilon\sigma,s) - \mathbf{g}_1(\mathbf{z},\varepsilon\sigma)\big)ds\\ &= \int_0^{\sigma}\Big(\mathbf{f}_1(\mathbf{z},\varepsilon\sigma,s) - \bar{\mathbf{f}}_1(\mathbf{z},\varepsilon\sigma)\Big)ds\\ &= \widetilde{\mathbf{f}}_1(\mathbf{z},\varepsilon\sigma)\int_0^{\sigma}f(s)ds.\end{aligned}$$

The value of $\mathbf{u}_1$ is equal to $\mathbf{v}_1$ minus the average value of $\mathbf{v}_1$ over one period 2π. According to (5.66) the expression of $\mathbf{u}_1$ reads

$$\begin{aligned}\mathbf{u}_1(\mathbf{z},\varepsilon\sigma,\sigma) &:= \mathbf{v}_1(\mathbf{z},\varepsilon\sigma,\sigma) - \frac{1}{2\pi}\int_0^{2\pi}\mathbf{v}_1(\mathbf{z},\varepsilon\sigma,s)ds\\ &= \widetilde{\mathbf{f}}_1(\mathbf{z},\varepsilon\sigma)F(\sigma)\end{aligned} \tag{5.71}$$

where

$$F(\sigma) := \int_0^{\sigma}f(s)ds - \frac{1}{2\pi}\int_0^{2\pi}\int_0^{\sigma}f(s)dsd\sigma, \tag{5.72}$$

i.e. F is the (of course 2π-periodic) primitive of f with zero mean.

Finally, to find the expression of $\mathbf{g}_2$ we need a function denoted $\mathbf{K}_2$ given by (5.65):

$$\begin{aligned}\mathbf{K}_2(\mathbf{z},\varepsilon\sigma,\sigma) &:= \frac{\partial\mathbf{f}_1}{\partial\mathbf{z}}(\mathbf{z},\varepsilon\sigma,\sigma)\mathbf{u}_1(\mathbf{z},\varepsilon\sigma,\sigma) - \frac{\partial\mathbf{u}_1}{\partial\mathbf{z}}(\mathbf{z},\varepsilon\sigma,\sigma)\mathbf{g}_1(\mathbf{z},\varepsilon\sigma)\\ &= [\bar{\mathbf{f}}_1,\widetilde{\mathbf{f}}_1](\mathbf{z},\varepsilon\sigma)F(\sigma) + \frac{1}{2}\frac{\partial\widetilde{\mathbf{f}}_1}{\partial\mathbf{z}}(\mathbf{z},\varepsilon\sigma)\widetilde{\mathbf{f}}_1(\mathbf{z},\varepsilon\sigma)\frac{dF^2(\sigma)}{d\sigma}\end{aligned}$$

where

$$[\bar{\mathbf{f}}_1,\widetilde{\mathbf{f}}_1](\mathbf{z},\varepsilon\sigma) := \frac{\partial\bar{\mathbf{f}}_1}{\partial\mathbf{z}}(\mathbf{z},\varepsilon\sigma)\widetilde{\mathbf{f}}_1(\mathbf{z},\varepsilon\sigma) - \frac{\partial\widetilde{\mathbf{f}}_1}{\partial\mathbf{z}}(\mathbf{z},\varepsilon\sigma)\bar{\mathbf{f}}_1(\mathbf{z},\varepsilon\sigma).$$

According to (5.64), the expression of $\mathbf{g}_2$ reads

$$\begin{aligned}\mathbf{g}_2(\mathbf{z},\varepsilon\sigma) &:= \frac{1}{2\pi}\int_0^{2\pi}\mathbf{K}_2(\mathbf{z},\varepsilon\sigma,s)ds \\ &= \frac{1}{2\pi}[\bar{\mathbf{f}}_1,\widetilde{\mathbf{f}}_1](\mathbf{z},\varepsilon\sigma)\int_0^{2\pi}F(s)ds + \frac{1}{22\pi}\frac{\partial\widetilde{\mathbf{f}}_1}{\partial\mathbf{z}}(\mathbf{z},\varepsilon\sigma)\widetilde{\mathbf{f}}_1(\mathbf{z},\varepsilon\sigma)\int_0^{2\pi}\frac{dF^2(s)}{ds}ds \\ &= 0,\end{aligned}$$

where $\int_0^{2\pi}F(s)ds = 0$ because F has a zero mean and $\int_0^{2\pi}\frac{dF^2(s)}{ds}ds = F^2(2\pi) - F^2(0) = 0$ because F is 2π-periodic and continuous.

Replacing in (5.61) and (5.62) $\mathbf{g}_1$ and $\mathbf{u}_1$ by their values respectively in (5.70) and (5.71), we get

$$\mathbf{x}(\sigma) = \mathbf{z}(\sigma) + \varepsilon\widetilde{\mathbf{f}}_1(\mathbf{z},\varepsilon\sigma)F(\sigma) + \mathcal{O}(\varepsilon^2), \tag{5.73}$$

and

$$\frac{d\mathbf{z}}{d\sigma} = \varepsilon\bar{\mathbf{f}}_1(\mathbf{z},\varepsilon\sigma). \tag{5.74}$$

Translating back to the original variables using (5.68), hence (5.73) yields the desired result (5.49)–(5.53) and (5.74) leads to the average system (5.54)–(5.58) where $\mathbf{z}$ is the slow varying variable and it is replaced by

$$\mathbf{z} = (\overline{\mathbf{\Phi}}_{\gamma\delta}^T, \overline{\omega}, \overline{\theta}, \overline{\theta}_c, \overline{\eta}^T)^T.$$

5.2.3.3 Simulation example

To clarify the separation between slow and fast varying signals, we will show a simulation example of HF voltage injection using the SPM motor parameters 6.1. The control parameters used in this simulation are as follows:

- the reference speed is constant: $\omega_c = \Omega_c = 10\pi\ rad.s^{-1}$;
- the simulation is done with open loop operation such that $\eta = a = 0$;
- the fundamental reference voltage is constant: $\mathcal{V}_{\gamma\delta} = (15.3, 0)^T\ V$;
- the HF voltage amplitude is constant: $\widetilde{\mathbf{v}}_{\gamma\delta} = (8, 8)^T\ V$;
- the pulsation is high: $\Omega = 1000\pi\ rad.s^{-1}$;
- the HF function f is a 2π- periodic rectangular function; see fig. 5.2; it is defined on $[0, 2\pi[$ by

$$f(\sigma) = \begin{cases} 1 & \text{if} \quad 0 \le \sigma < \pi \\ -1 & \text{if} \quad \pi \le \sigma < 2\pi \end{cases} \tag{5.75}$$

- the HF function F is a 2π- periodic triangular function; see fig. 5.2; it is defined on $[0, 2\pi[$ by

$$F(\sigma) = \begin{cases} \sigma - \dfrac{\pi}{2} & \text{if} \quad 0 \le \sigma < \pi \\ -\sigma + \dfrac{3\pi}{2} & \text{if} \quad \pi \le \sigma < 2\pi \end{cases} \tag{5.76}$$

- the load torque is constant: $\tau_L = 3Nm$.

Fig. 5.3 shows the shape of the HF motor voltage applied to the motor. The simulation results are presented in fig. 5.4. It is clear in this figure that the fluxes ϕ_γ and ϕ_δ contain periodic triangular HF components with the same shape as F. These triangular components have zero mean over one period of the injected signal and they do not perturb (in mean) the fundamental fluxes. In addition, the speed and the position are not affected by the injected voltage, where we see that the speed ω and the position θ do not contain HF components and we have $\omega \approx \overline{\omega}$ and $\theta \approx \overline{\theta}$. This simulation result confirms the theoretical result of the second order averaging given in (5.49)–(5.53).

Fig. 5.5 shows the difference between the simulated speed ω and the low frequency speed $\overline{\omega}$ which corresponds to the term $\mathcal{O}(\frac{1}{\Omega^2})$ in (5.49)–(5.53): $\omega - \overline{\omega} = \mathcal{O}(\frac{1}{\Omega^2})$. It is clear in this figure that the HF component is very small and has an amplitude of $0.2\ rad.s^{-1}$ comparing to $\overline{\omega}$ which is about $25\ rad.s^{-1}$. In addition, this figure shows the difference between the simulated position θ and the low frequency speed $\overline{\theta}$ which corresponds to the term $\mathcal{O}(\frac{1}{\Omega^2})$ in (5.49)–(5.53): $\theta - \overline{\theta} = \mathcal{O}(\frac{1}{\Omega^2})$. In this case the difference is also very small and it is around $0.2\ deg$ comparing to the position which is comprised between -180 and $180\ deg$.

Finally, fig. 5.6 compare the position and the speed obtained with signal injection and the position and the speed obtained without signal injection using the same simulation parameters. This figure shows clearly that the injection of a HF signal does not modify the rotor position and has a very small effect (0.8%) on the speed.

These simulation results are confirmed in the sequel by experimental tests. They validate the separation between HF components and low frequency components of the motor states. In addition, these results validate the approximation used in (5.49)–(5.53). In the sequel, this separation is used to find a relation between HF currents and the rotor position.

5.3 Rotor position and speed estimation

5.3.1 HF current expression

The rotor position is estimated from the HF current. We now express the effect of signal injection on the currents: plugging (5.49) into (5.36) we have

$$\mathbf{i}_{\gamma\delta} = \mathcal{R}_{\overline{\theta}-\overline{\theta}_c+\mathcal{O}(\frac{1}{\Omega^2})}\mathcal{I}_{dq}\Big(\mathcal{R}^T_{\overline{\theta}-\overline{\theta}_c+\mathcal{O}(\frac{1}{\Omega^2})}\big(\overline{\mathbf{\Phi}}_{\gamma\delta} + \frac{\widetilde{\mathbf{v}}_{\gamma\delta}}{\Omega}F(\Omega t) + \mathcal{O}(\tfrac{1}{\Omega^2})\big)\Big). \tag{5.77}$$

We perform a first order Taylor expansion of the current expression in (5.77) according to the powers of $\frac{1}{\Omega}$. In this case we have

$$\begin{aligned}
&\mathcal{I}_{dq}\Big(\mathcal{R}^T_{\overline{\theta}-\overline{\theta}_c+\mathcal{O}(\frac{1}{\Omega^2})}\big(\overline{\mathbf{\Phi}}_{\gamma\delta} + \frac{\widetilde{\mathbf{v}}_{\gamma\delta}}{\Omega}F(\Omega t) + \mathcal{O}(\tfrac{1}{\Omega^2})\big)\Big)\\
=&\mathcal{I}_{dq}\left(\mathcal{R}^T_{\overline{\theta}-\overline{\theta}_c+\mathcal{O}(\frac{1}{\Omega^2})}\overline{\mathbf{\Phi}}_{\gamma\delta} + \frac{1}{\Omega}\mathcal{R}^T_{\overline{\theta}-\overline{\theta}_c+\mathcal{O}(\frac{1}{\Omega^2})}\widetilde{\mathbf{v}}_{\gamma\delta}F(\Omega t) + \mathcal{O}(\tfrac{1}{\Omega^2})\right)\\
=&\mathcal{I}_{dq}\left(\mathcal{R}^T_{\overline{\theta}-\overline{\theta}_c}\overline{\mathbf{\Phi}}_{\gamma\delta}\right) + D\mathcal{I}_{dq}\left(\mathcal{R}^T_{\overline{\theta}-\overline{\theta}_c}\overline{\mathbf{\Phi}}_{\gamma\delta}\right)\mathcal{R}^T_{\overline{\theta}-\overline{\theta}_c}\frac{\widetilde{\mathbf{v}}_{\gamma\delta}}{\Omega}F(\Omega t) + \mathcal{O}(\tfrac{1}{\Omega^2}).
\end{aligned}$$

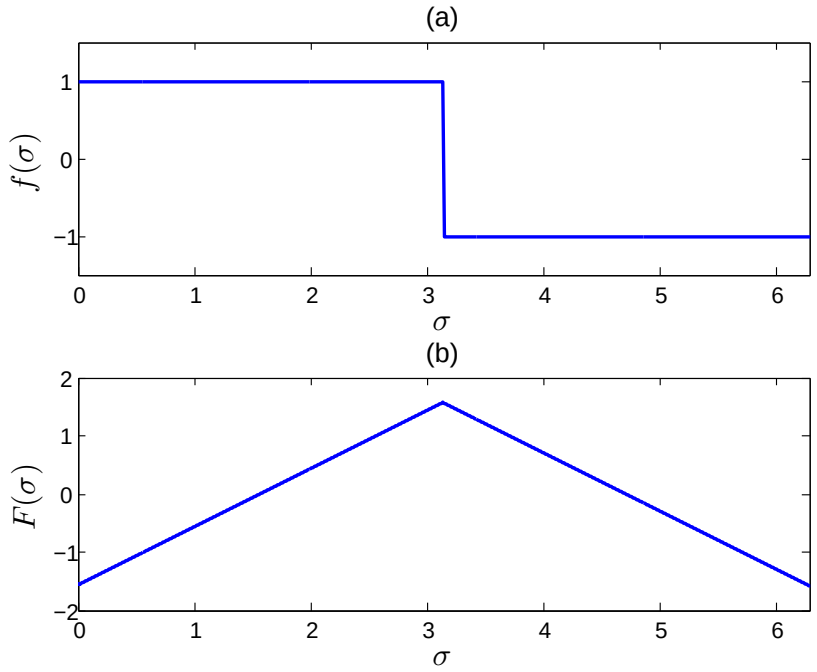

Figure 5.2: HF functions: (a) rectangular function $f(\sigma)$; (b) triangular function $F(\sigma)$.

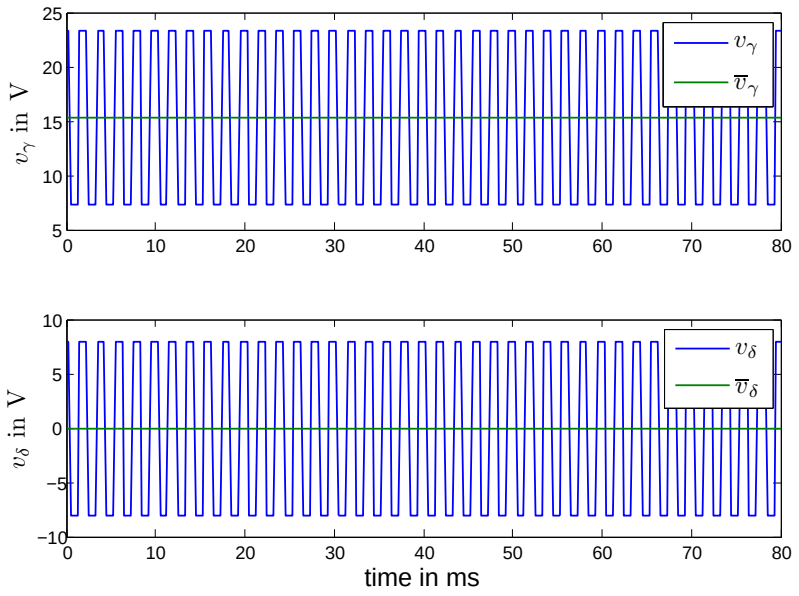

Figure 5.3: Motor voltage: low frequency voltages $\overline{v}_\gamma$ and $\overline{v}_\delta$ (green) and total HF voltages v_γ and v_δ (blue).

where $D\mathcal{I}_{dq}\left(\mathcal{R}^T_{\overline{\theta}-\overline{\theta}_c}\overline{\mathbf{\Phi}}_{\gamma\delta}\right)$ is the Jacobian of $\mathcal{I}_{dq}$ calculated at $\mathcal{R}^T_{\overline{\theta}-\overline{\theta}_c}\overline{\mathbf{\Phi}}_{\gamma\delta}$. Hence, the current expres-

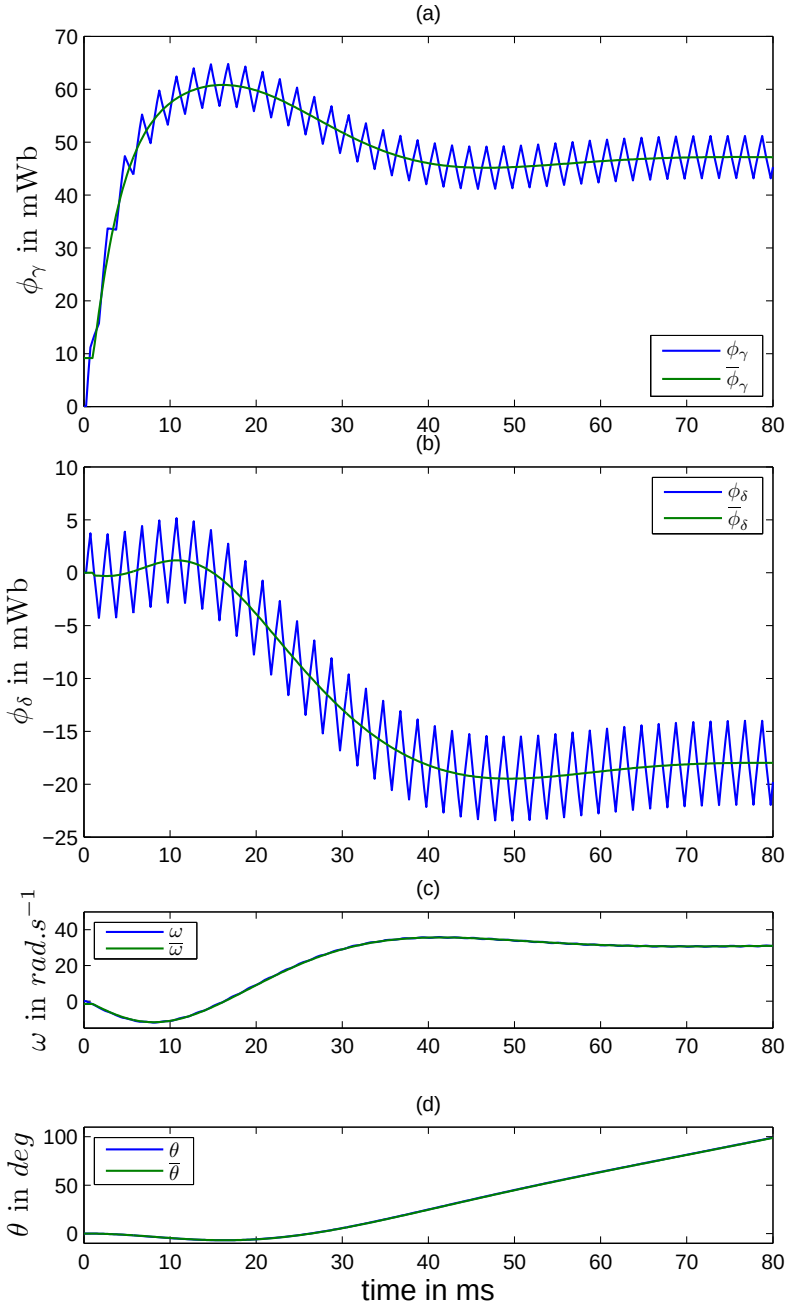

Figure 5.4: Simulation results with signal injection: (a) γ- axis flux ϕ_γ, γ- axis low frequency flux $\overline{\phi}_\gamma$; (b) δ- axis flux ϕ_δ, δ- axis low frequency flux $\overline{\phi}_\delta$; (c) motor speed ω, low frequency motor speed $\overline{\omega}$; (d) rotor position θ, low frequency rotor position $\overline{\theta}$.

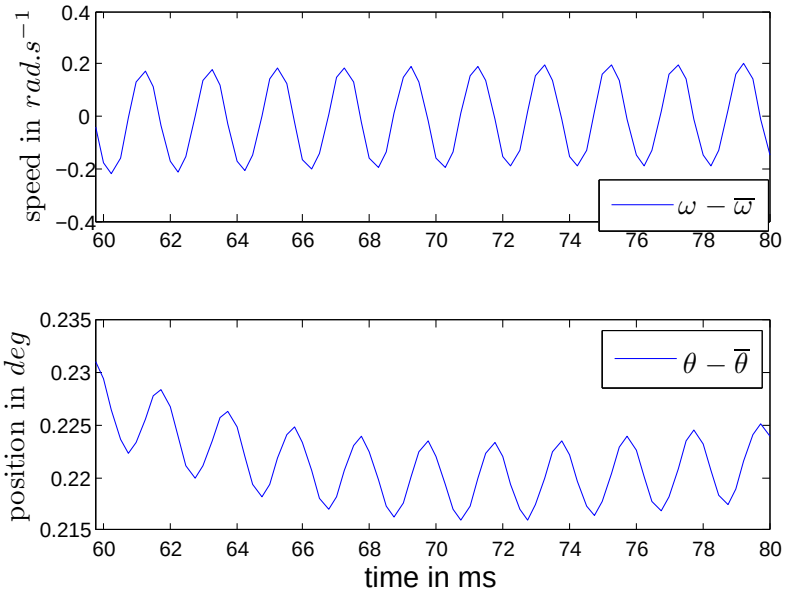

Figure 5.5: Simulation results with signal injection: HF components of speed $\omega - \overline{\omega}$ and position $\theta - \overline{\theta}$.

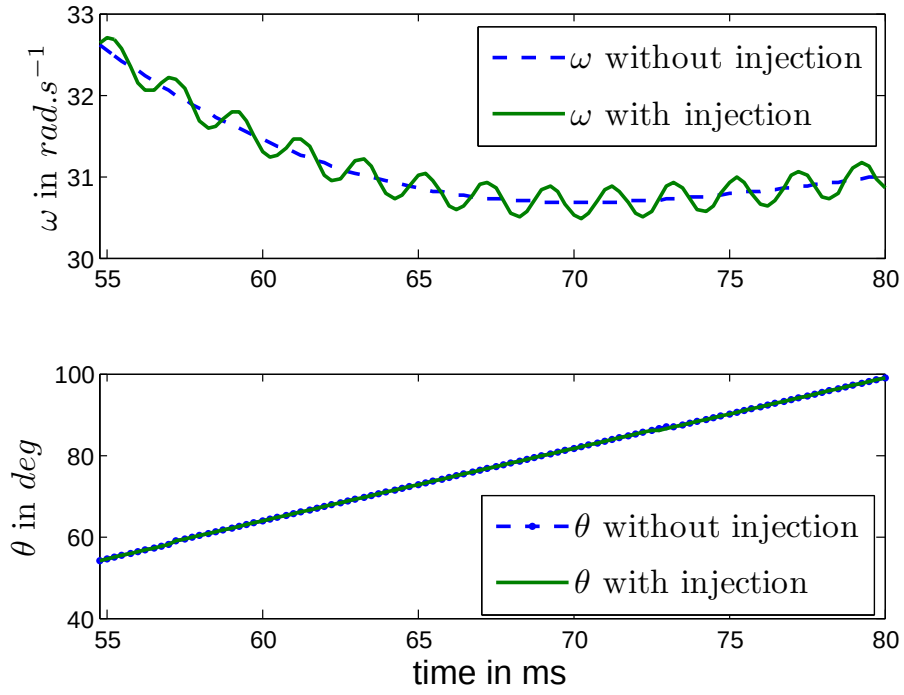

Figure 5.6: Comparison between simulation results with and without signal injection: motor speed ω and rotor position θ.

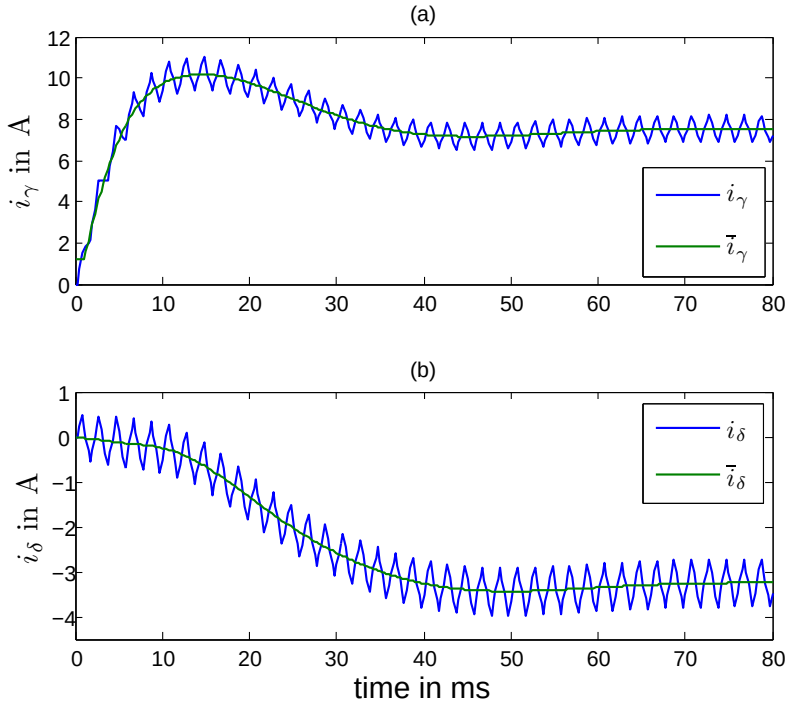

Figure 5.7: Simulation results with signal injection: (a) γ- axis current i_γ, γ- axis low frequency current $\bar{i}_\gamma$; (b) δ- axis current i_δ, δ- axis low frequency current $\bar{i}_\delta$.

sion (5.77) can be written as follows

$$\begin{aligned}\mathbf{i}_{\gamma\delta} &= \mathcal{R}_{\overline{\theta}-\overline{\theta}_c}\mathcal{I}_{dq}\left(\mathcal{R}^T_{\overline{\theta}-\overline{\theta}_c}\overline{\mathbf{\Phi}}_{\gamma\delta}\right) + \mathcal{R}_{\overline{\theta}-\overline{\theta}_c}D\mathcal{I}_{dq}\left(\mathcal{R}^T_{\overline{\theta}-\overline{\theta}_c}\overline{\mathbf{\Phi}}_{\gamma\delta}\right)\mathcal{R}^T_{\overline{\theta}-\overline{\theta}_c}\frac{\widetilde{\mathbf{v}}_{\gamma\delta}}{\Omega}F(\Omega t) + \mathcal{O}(\tfrac{1}{\Omega^2}) \\ &= \bar{\mathbf{i}}_{\gamma\delta} + \widetilde{\mathbf{i}}_{\gamma\delta}F(\Omega t) + \mathcal{O}(\tfrac{1}{\Omega^2}) \end{aligned} \tag{5.78}$$

where

$$\widetilde{\mathbf{i}}_{\gamma\delta} = \mathcal{R}_{\overline{\theta}-\overline{\theta}_c}D\mathcal{I}_{dq}\left(\mathcal{R}^T_{\overline{\theta}-\overline{\theta}_c}\overline{\mathbf{\Phi}}_{\gamma\delta}\right)\mathcal{R}^T_{\overline{\theta}-\overline{\theta}_c}\frac{\widetilde{\mathbf{v}}_{\gamma\delta}}{\Omega}; \tag{5.79}$$

and $\bar{\mathbf{i}}_{\gamma\delta}$ is given by (5.59).

In addition, inverting the expression (5.59) yields

$$\overline{\mathbf{\Phi}}_{\gamma\delta} = \mathcal{R}_{\overline{\theta}-\overline{\theta}_c}\mathcal{I}^{-1}_{dq}\left(\mathcal{R}^T_{\overline{\theta}-\overline{\theta}_c}\bar{\mathbf{i}}_{\gamma\delta}\right).$$

Thus (5.79) leads to

$$\widetilde{\mathbf{i}}_{\gamma\delta} = \mathcal{R}_{\overline{\theta}-\overline{\theta}_c}D\mathcal{I}_{dq}\left(\mathcal{I}^{-1}_{dq}\left(\mathcal{R}^T_{\overline{\theta}-\overline{\theta}_c}\bar{\mathbf{i}}_{\gamma\delta}\right)\right)\mathcal{R}^T_{\overline{\theta}-\overline{\theta}_c}\frac{\widetilde{\mathbf{v}}_{\gamma\delta}}{\Omega}. \tag{5.80}$$

Fig 5.7 shows the shape of the currents i_γ and i_δ obtained in the previous simulation example. It is clear in this figure that the current is the sum of a fundamental low frequency part and a HF part having the same triangular shape of the HF flux.

We will see in the next subsection how to recover $\widetilde{\mathbf{i}}_{\gamma\delta}$ and $\bar{\mathbf{i}}_{\gamma\delta}$ from the measured currents $\mathbf{i}_{\gamma\delta}$. The equation (5.80) can be written as

$$\widetilde{\mathbf{i}}_{\gamma\delta} = \mathcal{S}(\overline{\theta}-\overline{\theta}_c, \bar{\mathbf{i}}_{\gamma\delta})\frac{\widetilde{\mathbf{v}}_{\gamma\delta}}{\Omega} \tag{5.81}$$

where

$$\mathcal{S}(\mu, \bar{\mathbf{i}}_{\gamma\delta}) = \mathcal{R}_\mu D\mathcal{I}_{dq}\Big(\mathcal{I}^{-1}_{dq}\big(\mathcal{R}^T_\mu\bar{\mathbf{i}}_{\gamma\delta}\big)\Big)\mathcal{R}^T_\mu.$$

We note that the matrix $\mathcal{S}$ is the same saliency matrix defined in (4.163). The equation (5.81) gives two (redundant) relations relating the unknown angle $\overline{\theta}$ to the known variables $\overline{\theta}_c, \widetilde{\mathbf{i}}_{\gamma\delta}, \bar{\mathbf{i}}_{\gamma\delta}, \widetilde{\mathbf{v}}_{dq}$, provided the matrix $\mathcal{S}(\mu, \bar{\mathbf{i}}_{\gamma\delta})$ effectively depends on its first argument μ such that

$$\frac{\partial\mathcal{S}}{\partial\mu}(\mu, \bar{\mathbf{i}}_{\gamma\delta}) \neq 0.$$

This "saliency condition" is identical to the observability condition derived in the previous chapter in (4.169) to ensure nonlinear observability. This results shows that if the sufficient observability condition (4.169) is verified, then the rotor position can be recovered using HF voltage injection.

The explicit expression for $\mathcal{S}(\mu, \bar{\mathbf{i}}_{\gamma\delta})$ is obtained thanks to (4.140) and (4.145). Indeed, $\mathcal{S}$ can be written in terms of the matrix $\mathbf{Y}$ and $\mathbf{L}^{dq}_i$ as follows

$$\begin{aligned}\mathcal{S}(\mu, \bar{\mathbf{i}}_{\gamma\delta}) &= \mathcal{R}_\mu\mathbf{Y}\Big(\mathcal{R}^T_\mu\bar{\mathbf{i}}_{\gamma\delta}\Big)\mathcal{R}^T_\mu \\ &= \mathcal{R}_\mu\left[\mathbf{L}^{dq}_i\right]^{-1}\mathcal{R}^T_\mu,\end{aligned}$$

hence the matrix $\mathcal{S}$ reads

$$\mathcal{S} = \frac{1}{2}\begin{pmatrix} l_i^{dd} + l_i^{qq} + 2l_i^e \cos\left(2\mu + \theta_i^e\right) & 2l_i^e \sin\left(2\mu + \theta_i^e\right) \\ 2l_i^e \sin\left(2\mu + \theta_i^e\right) & l_i^{dd} + l_i^{qq} - 2l_i^e \cos\left(2\mu + \theta_i^e\right) \end{pmatrix} \tag{5.82}$$

with

$$\theta_i^e(\mu, \bar{\mathbf{i}}_{\gamma\delta}) = \arctan\left(\frac{2l_i^{dq}\left(\mathcal{R}_\mu^T \bar{\mathbf{i}}_{\gamma\delta}\right)}{l_i^{dd}\left(\mathcal{R}_\mu^T \bar{\mathbf{i}}_{\gamma\delta}\right) - l_i^{qq}\left(\mathcal{R}_\mu^T \bar{\mathbf{i}}_{\gamma\delta}\right)}\right) \tag{5.83}$$

and

$$l_i^e(\mu, \bar{\mathbf{i}}_{\gamma\delta}) = \frac{1}{2}\sqrt{\left(l_i^{dd}\left(\mathcal{R}_\mu^T \bar{\mathbf{i}}_{\gamma\delta}\right) - l_i^{qq}\left(\mathcal{R}_\mu^T \bar{\mathbf{i}}_{\gamma\delta}\right)\right)^2 + 4\left(l_i^{dq}\left(\mathcal{R}_\mu^T \bar{\mathbf{i}}_{\gamma\delta}\right)\right)^2}.$$

The expressions of l_i^{dd} and l_i^{dq} and l_i^{qq} are given in (4.146)–(4.148).

We note that the expression of the saliency matrix $\mathcal{S}$ in (5.82) is similar to the expression of the $\gamma\delta$- inductance $\mathbf{L}^{\gamma\delta}$ in (5.30) which is used in the literature. The major point here, is that we give an expression of the saliency matrix in terms of the currents and saturation parameters. We also give an expression of the rotor position estimation error used in the literature $\theta_i^e(\mu, \bar{\mathbf{i}}_{\gamma\delta})$ which is equivalent to the error introduced by cross saturation in (5.31). The inductance l_i^{dq} is equivalent to the inductance l_m used in (5.31).

In general the values of θ_e and l_m in (5.31) are based on measurements and finite elements analysis in the literature. We propose in (5.82) and (5.83) a mathematical modeling of these important parameters used to compensate the error due to magnetic saturation and cross coupling:

$$\begin{aligned} \theta_e &= \theta_i^e(\mu, \bar{\mathbf{i}}_{\gamma\delta}) \\ l_m &= l_i^{dq}\left(\mathcal{R}_\mu^T \bar{\mathbf{i}}_{\gamma\delta}\right). \end{aligned}$$

In the case of an unsaturated magnetic circuit i.e. $\alpha_{i,j} = 0$ we have according to (4.146)–(4.148) $l_i^{dd} = L_d$, $l_i^{qq} = L_q$ and $l_i^{dq} = 0$. Hence (5.82) yields

$$\mathcal{S}(\mu, \bar{\mathbf{i}}_{\gamma\delta}) = \frac{L_d + L_q}{2L_d L_q}\begin{pmatrix} 1 + \frac{L_d - L_q}{L_d + L_q}\cos 2\mu & \frac{L_d - L_q}{L_d + L_q}\sin 2\mu \\ \frac{L_d - L_q}{L_d + L_q}\sin 2\mu & 1 - \frac{L_d - L_q}{L_d + L_q}\cos 2\mu \end{pmatrix}$$

and does not depend on $\bar{\mathbf{i}}_{\gamma\delta}$; notice this matrix does not depend on μ for an unsaturated machine with no geometric saliency i.e. $L_d = L_q$. Notice also (5.81) defines in that case two solutions on $]-\pi, \pi]$ for the angle $\overline{\theta}$ since $\mathcal{S}(\mu, \bar{\mathbf{i}}_{\gamma\delta})$ is actually a function of 2μ; in the saturated case there is generically only one solution, except for some particular values of $\bar{\mathbf{i}}_{\gamma\delta}$. In the sequel we take $\overline{\theta} \approx \theta$ and $\overline{\theta}_c \approx \theta_c$ because the HF position component is very small and it is hence neglected.

In the next subsection we propose a rotor position estimation procedure which takes into account magnetic and cross coupling saturations.

5.3.2 Nonlinear least square estimation

There are several ways to extract the rotor angle information from (5.81), especially for real-time use inside a feedback law. Firstly, we just want to demonstrate the validity of (5.81) and we will be content with directly solving it through a nonlinear least square problem. Let

$$\mathcal{M}(\mu, \bar{\mathbf{i}}_{\gamma\delta}, \widetilde{\mathbf{i}}_{\gamma\delta}) = \left\| \widetilde{\mathbf{i}}_{\gamma\delta} - \mathcal{S}(\mu, \bar{\mathbf{i}}_{\gamma\delta}) \frac{\widetilde{\mathbf{v}}_{\gamma\delta}}{\Omega} \right\|^2,$$

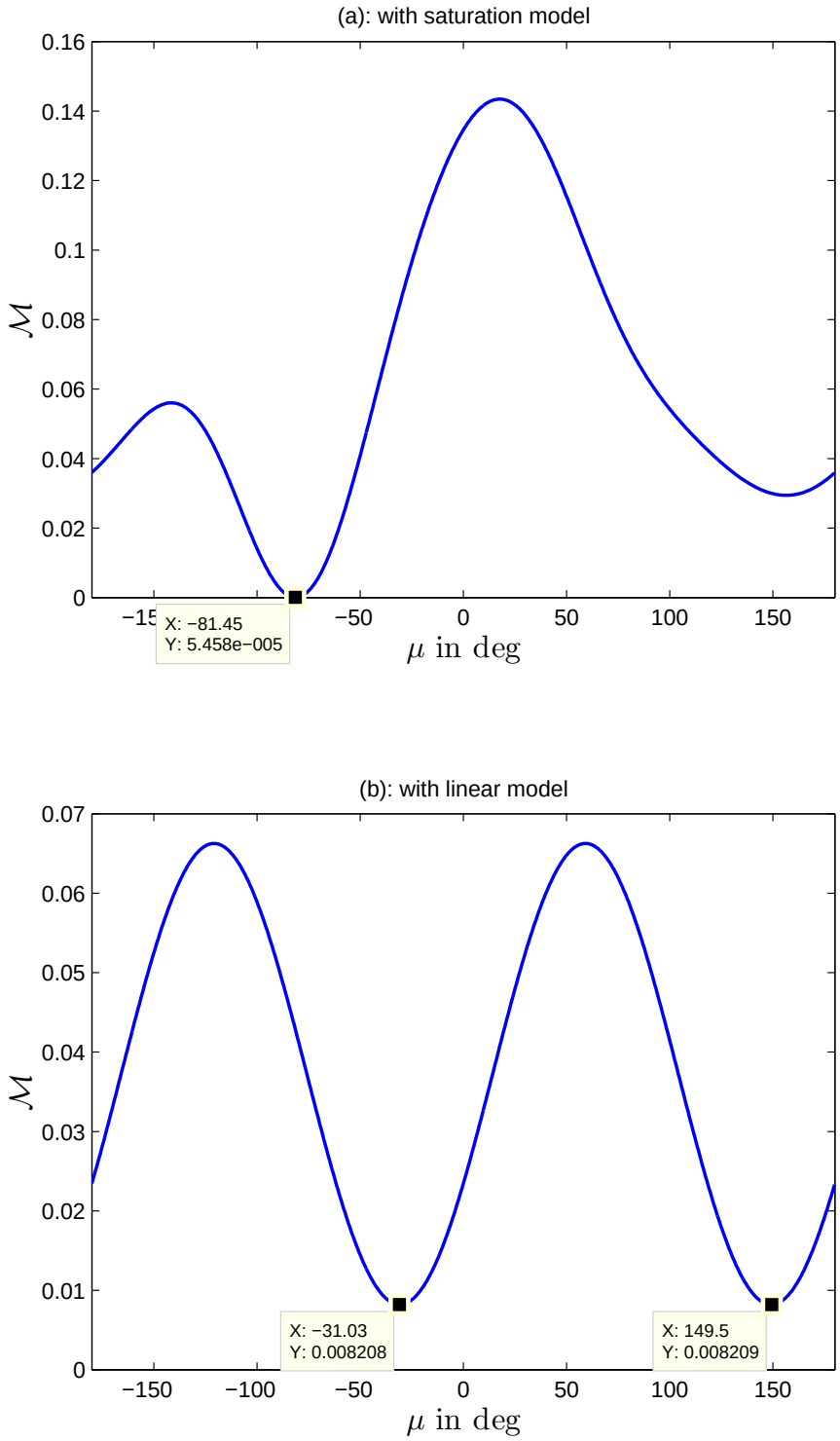

Figure 5.8: $\mathcal{M}$ versus μ: (a) with magnetic saturation; (b) without magnetic saturation.

by using (5.81) it is clear that $\mathcal{M} = 0$ when $\mu = \theta - \theta_c$. Thus, the estimation of the rotor position can be done by minimizing the function $\mathcal{M}$ as follows

$$\widehat{\theta} = \theta_c + \arg \min_{\mu \in]-\pi,\pi]} \left[\mathcal{M}(\mu, \bar{\mathbf{i}}_{\gamma\delta}, \widetilde{\mathbf{i}}_{\gamma\delta}) \right] \tag{5.84}$$

where $\widehat{\theta}$ is the estimated rotor position.

5.3.2.1 Example

To clarify this method, we give an example with experimental data. We take the case when the values of the electrical and mechanical variables are: $\widetilde{i}_\gamma = 510$ mA, $\widetilde{i}_\delta = -153$ mA, $\bar{i}_\gamma = 8.72$ A, $\bar{i}_\delta = -2.3$ A, $\tau_L = 5.53$ N.m, $\omega = 30.73\ rad.s^{-1}$, $\theta = -39$ deg, $\theta_c = 38.5$ deg. These data are obtained using IPM motor with rated parameters listed in 6.1 and saturation parameters listed in 6.2 (the estimation procedure of saturation parameters will be detailed in chapter 6).

Fig. 5.8(a) shows $\mathcal{M}(\mu, \bar{\mathbf{i}}_{\gamma\delta}, \widetilde{\mathbf{i}}_{\gamma\delta})$ versus μ when magnetic saturation is considered, in this case $\mathcal{M}$ has two local minima and one global minimum at -81.45 deg, this gives $\widehat{\theta} = -42.95$ deg. The estimation error is $\left|\theta - \widehat{\theta}\right| = 3.95$ deg only. It is important to note that the function $\mathcal{M}(\mu)$ has two local minima, hence the nonlinear least square method must be well initialized to converge to the correct position value.

Fig. 5.8(b) shows $\mathcal{M}(\mu, \bar{\mathbf{i}}_{\gamma\delta}, \widetilde{\mathbf{i}}_{\gamma\delta})$ versus μ when magnetic saturation is not considered i.e. $\alpha_{i,j} = 0$. In this case, there is no global minimum but we have two local minima at -31.03 deg and 149.5 deg which are far from the actual value of $\mu = -77.5$ deg. Thus, taking into account the saturation model leads to only one global minimum of $\mathcal{M}$ and permits to estimate the rotor position without the 180 deg redundancy. But, this is not a general case, because for small values of $\bar{i}_{\gamma\delta}$ (the saturation is small) we still have two local minima of $\mathcal{M}$.

5.3.3 Nonlinear recursive estimation

In the previous subsection, we proposed a method for position estimation by nonlinear least square. This method gives good estimation of rotor position for validation purpose, but it must be done offline and it needs a large computation time because the nonlinear optimization problem is solved at each time step. We propose here a recursive algorithm for nonlinear least squares which reduce significantly the computation time.

To solve (5.84) we need to find the value of $\mu \in]-\pi, \pi]$ which minimizes $\mathcal{M}(\mu, \bar{\mathbf{i}}_{\gamma\delta}, \widetilde{\mathbf{i}}_{\gamma\delta})$ where $\widetilde{\mathbf{i}}_{\gamma\delta}$ and $\bar{\mathbf{i}}_{\gamma\delta}$ are slowly varying functions of time; $\widetilde{\mathbf{v}}_{\gamma\delta}$ and Ω are constant. The value of

$$\arg \min_{\mu \in]-\pi,\pi]} \mathcal{M}(\mu, \bar{\mathbf{i}}_{\gamma\delta}, \widetilde{\mathbf{i}}_{\gamma\delta})$$

can be approximated by $\widehat{\mu}$ which verifies

$$\frac{d\widehat{\mu}}{dt} = -\Lambda \frac{\partial \mathcal{M}}{\partial \mu}(\widehat{\mu}, \bar{\mathbf{i}}_{\gamma\delta}, \widetilde{\mathbf{i}}_{\gamma\delta}) \tag{5.85}$$

with

$$\Lambda = \rho \frac{\frac{\partial^2 \mathcal{M}}{\partial \mu^2}}{\left(\frac{\partial^2 \mathcal{M}}{\partial \mu^2}\right)^2 + \epsilon} \tag{5.86}$$

where ρ and ϵ are two positive real numbers.

The computation time is considerably reduced because we need only to solve (5.85) in terms of time, which can be done at real time by simple recursive Euler integration; rather than solving the optimization problem (5.84) at each time t which requires a huge amount of computations and must be done offline. In practice, the time $t = nT_s$ is discrete where n is a positive integer and T_s is a constant sampling period. The value of $\arg\min_{\mu\in]-\pi,\pi]} \mathcal{M}(\mu, \bar{\mathbf{i}}_{\gamma\delta}, \widetilde{\mathbf{i}}_{\gamma\delta})$ can be approximated at time nT_s by $\widehat{\mu}_n = \widehat{\mu}(nT_s)$ using (5.85) as follows

$$\widehat{\mu}_n = \widehat{\mu}_{n-1} - \Lambda T_s \frac{\partial \mathcal{M}}{\partial \mu}(\widehat{\mu}_{n-1}, \bar{\mathbf{i}}_{\gamma\delta}, \widetilde{\mathbf{i}}_{\gamma\delta}). \tag{5.87}$$

The equation (5.87) represents a gradient descent algorithm which is usually used to solve minimization problem. The solution of this problem is time dependent but it varies slowly with time because the currents $\bar{\mathbf{i}}_{\gamma\delta}, \widetilde{\mathbf{i}}_{\gamma\delta}$ vary slowly with time. The period T_s is chosen small enough such that the variation of the position is very small between two time steps. Hence, at each time step we need only one iteration to estimate the new position as we see in (5.87). The computation time is then reduced because only one iteration is used rather than solving the optimization problem at each time step which require a large number of iterations.

In (5.86), the parameter ϵ is very small, it is used to avoid the division by zero. If we neglect ϵ, hence Λ is proportional to $\left(\frac{\partial^2 \mathcal{M}}{\partial \mu^2}\right)^{-1}$ which is the Newton optimization coefficient, it is used to enhance the convergence of the optimization problem. The first and second derivative of $\mathcal{M}$ according to μ are needed to solve (5.85), they are as follows

$$\begin{aligned}
\frac{\partial \mathcal{M}}{\partial \mu} &= -2\left(\widetilde{\mathbf{i}}_{\gamma\delta} - \mathcal{S}(\mu, \bar{\mathbf{i}}_{\gamma\delta})\frac{\widetilde{\mathbf{v}}_{\gamma\delta}}{\Omega}\right)^T \frac{\partial \mathcal{S}(\mu, \bar{\mathbf{i}}_{\gamma\delta})}{\partial \mu}\frac{\widetilde{\mathbf{v}}_{\gamma\delta}}{\Omega} \\
\frac{\partial^2 \mathcal{M}}{\partial \mu^2} &= 2\left\|\frac{\partial \mathcal{S}(\mu, \bar{\mathbf{i}}_{\gamma\delta})}{\partial \mu}\frac{\widetilde{\mathbf{v}}_{\gamma\delta}}{\Omega}\right\|^2 - 2\left(\widetilde{\mathbf{i}}_{\gamma\delta} - \mathcal{S}(\mu, \bar{\mathbf{i}}_{\gamma\delta})\frac{\widetilde{\mathbf{v}}_{\gamma\delta}}{\Omega}\right)^T \frac{\partial^2 \mathcal{S}(\mu, \bar{\mathbf{i}}_{\gamma\delta})}{\partial \mu^2}\frac{\widetilde{\mathbf{v}}_{\gamma\delta}}{\Omega}
\end{aligned}$$

with

$$\begin{aligned}
\mathcal{S}(\mu, \bar{\mathbf{i}}_{\gamma\delta}) &= \mathcal{R}_\mu \mathbf{Y}(\mathcal{R}_\mu^T \bar{\mathbf{i}}_{\gamma\delta})\mathcal{R}_\mu^T \\
\frac{\partial \mathcal{S}(\mu, \bar{\mathbf{i}}_{\gamma\delta})}{\partial \mu} &= \mathcal{R}_\mu \left(\mathcal{J}\mathbf{Y}(\mathcal{R}_\mu^T \bar{\mathbf{i}}_{\gamma\delta}) - \mathbf{Y}(\mathcal{R}_\mu^T \bar{\mathbf{i}}_{\gamma\delta})\mathcal{J} + \frac{\partial}{\partial \mu}\Big(\mathbf{Y}(\mathcal{R}_\mu^T \bar{\mathbf{i}}_{\gamma\delta})\Big)\right)\mathcal{R}_\mu^T \\
\frac{\partial^2 \mathcal{S}(\mu, \bar{\mathbf{i}}_{\gamma\delta})}{\partial \mu^2} &= \mathcal{R}_\mu \Big[-2\mathbf{Y}(\mathcal{R}_\mu^T \bar{\mathbf{i}}_{\gamma\delta}) - 2\mathcal{J}\mathbf{Y}(\mathcal{R}_\mu^T \bar{\mathbf{i}}_{\gamma\delta})\mathcal{J} + 2\mathcal{J}\frac{\partial}{\partial \mu}\Big(\mathbf{Y}(\mathcal{R}_\mu^T \bar{\mathbf{i}}_{\gamma\delta})\Big) \\
&\qquad - 2\frac{\partial}{\partial \mu}\Big(\mathbf{Y}(\mathcal{R}_\mu^T \bar{\mathbf{i}}_{\gamma\delta})\Big)\mathcal{J} + \frac{\partial^2}{\partial \mu^2}\Big(\mathbf{Y}(\mathcal{R}_\mu^T \bar{\mathbf{i}}_{\gamma\delta})\Big)\Big]\mathcal{R}_\mu^T,
\end{aligned}$$

the explicit expression of $\mathbf{Y}$ is given by (4.140) and (4.141)–(4.143).

5.3.4 Small angle case

In general, the difference between θ and θ_c is supposed to be small when θ_c is considered as the estimated rotor position. In this case $\theta - \theta_c$ is small, hence we consider that the angle μ in $\mathcal{S}(\mu, \bar{i}_{\gamma\delta})$

is small. Therefore, at first order position approximation, the matrix $\mathcal{S}$ can be written as

$$\mathcal{S}(\mu, \bar{\mathbf{i}}_{\gamma\delta}) = \begin{pmatrix} Y^{\gamma\gamma}(\bar{\mathbf{i}}_{\gamma\delta}) + \mu Y_\mu^{\gamma\gamma}(\bar{\mathbf{i}}_{\gamma\delta}) & Y^{\gamma\delta}(\bar{\mathbf{i}}_{\gamma\delta}) + \mu Y_\mu^{\gamma\delta}(\bar{\mathbf{i}}_{\gamma\delta}) \\ Y^{\gamma\delta}(\bar{\mathbf{i}}_{\gamma\delta}) + \mu Y_\mu^{\gamma\delta}(\bar{\mathbf{i}}_{\gamma\delta}) & Y^{\delta\delta}(\bar{\mathbf{i}}_{\gamma\delta}) + \mu Y_\mu^{\delta\delta}(\bar{\mathbf{i}}_{\gamma\delta}) \end{pmatrix} + \mathcal{O}(\mu^2) \tag{5.88}$$

with

$$\begin{aligned}
Y^{\gamma\gamma}(\bar{i}_\gamma, \bar{i}_\delta) &= \frac{1}{L_d} + 6\alpha_{3,0} L_d \bar{i}_\gamma + 12\alpha_{4,0} L_d^2 \bar{i}_\gamma^2 + 2\alpha_{2,2} L_q^2 \bar{i}_\delta^2 \\
Y_\mu^{\gamma\gamma}(\bar{i}_\gamma, \bar{i}_\delta) &= 6\alpha_{3,0} L_d \bar{i}_\delta + 24\alpha_{4,0} L_d^2 \bar{i}_\gamma \bar{i}_\delta - 4\alpha_{1,2} L_q \bar{i}_\delta - 4\alpha_{2,2} L_q (2L_d + L_q) \bar{i}_\gamma \bar{i}_\delta \\
Y^{\gamma\delta}(\bar{i}_\gamma, \bar{i}_\delta) &= 2\alpha_{1,2} L_q \bar{i}_\delta + 4\alpha_{2,2} L_d L_q \bar{i}_\gamma \bar{i}_\delta \\
Y_\mu^{\gamma\delta}(\bar{i}_\gamma, \bar{i}_\delta) &= \frac{1}{L_d} - \frac{1}{L_q} + 6\alpha_{3,0} L_d \bar{i}_\gamma + 12\alpha_{4,0} L_d^2 \bar{i}_\gamma^2 - 12\alpha_{0,4} L_q^2 \bar{i}_\delta^2 \\
&\quad + 2\alpha_{2,2} \left(L_q^2 \bar{i}_\delta^2 - L_d^2 \bar{i}_\gamma^2 - 2L_d L_q (\bar{i}_\gamma^2 - \bar{i}_\delta^2) \right) - 2\alpha_{1,2} (L_d + L_q) \bar{i}_\gamma \\
Y^{\delta\delta}(\bar{i}_\gamma, \bar{i}_\delta) &= \frac{1}{L_q} + 2\alpha_{1,2} L_d \bar{i}_\gamma + 2\alpha_{2,2} L_d^2 \bar{i}_\gamma^2 + 12\alpha_{0,4} L_q^2 \bar{i}_\delta^2 \\
Y_\mu^{\delta\delta}(\bar{i}_\gamma, \bar{i}_\delta) &= 2\alpha_{1,2} (L_d + 2L_q) \bar{i}_\delta + 4\alpha_{2,2} L_d (L_d + 2L_q) \bar{i}_\gamma \bar{i}_\delta - 24\alpha_{0,4} L_d^2 \bar{i}_\gamma \bar{i}_\delta
\end{aligned}$$

Using (5.79), the relation between $\widetilde{\mathbf{i}}_{\gamma\delta}$ and the position reads

$$\begin{aligned}
\widetilde{\mathbf{i}}_{\gamma\delta} &= \mathcal{S}(\theta - \theta_c, \bar{\mathbf{i}}_{\gamma\delta}) \frac{\widetilde{\mathbf{v}}_{\gamma\delta}}{\Omega} \\
&= \frac{1}{\Omega} \begin{pmatrix} Y^{\gamma\gamma}(\bar{\mathbf{i}}_{\gamma\delta}) \widetilde{v}_\gamma + Y^{\gamma\delta}(\bar{\mathbf{i}}_{\gamma\delta}) \widetilde{v}_\delta + \left(Y_\mu^{\gamma\gamma}(\bar{\mathbf{i}}_{\gamma\delta}) \widetilde{v}_\gamma + Y_\mu^{\gamma\delta}(\bar{\mathbf{i}}_{\gamma\delta}) \widetilde{v}_\delta \right) (\theta - \theta_c) \\ Y^{\gamma\delta}(\bar{\mathbf{i}}_{\gamma\delta}) \widetilde{v}_\gamma + Y^{\delta\delta}(\bar{\mathbf{i}}_{\gamma\delta}) \widetilde{v}_\delta + \left(Y_\mu^{\gamma\delta}(\bar{\mathbf{i}}_{\gamma\delta}) \widetilde{v}_\gamma + Y_\mu^{\delta\delta}(\bar{\mathbf{i}}_{\gamma\delta}) \widetilde{v}_\delta \right) (\theta - \theta_c) \end{pmatrix}.
\end{aligned} \tag{5.89}$$

The equation (5.89) gives two explicit and redundant linear relations between the amplitudes of the HF currents and the rotor position when $\theta - \theta_c$ is small. These relations can be used to estimate the rotor position error when θ_c is the estimated position. This error can be used as an input of a phase locked loop (PLL) kind position estimator.

For example, it is common to add a HF voltage on the γ axis and to estimate the position from the current δ- axis component. In this case, the equation (5.89) leads to

$$\begin{aligned}
\widetilde{i}_\delta = 2\alpha_{1,2} L_q \bar{i}_\delta + 4\alpha_{2,2} L_d L_q \bar{i}_\gamma \bar{i}_\delta + \Big(&\frac{1}{L_d} - \frac{1}{L_q} + 6\alpha_{3,0} L_d \bar{i}_\gamma + 12\alpha_{4,0} L_d^2 \bar{i}_\gamma^2 - 12\alpha_{0,4} L_q^2 \bar{i}_\delta^2 \\
&+ 2\alpha_{2,2} \big(L_q^2 \bar{i}_\delta^2 - L_d^2 \bar{i}_\gamma^2 - 2L_d L_q (\bar{i}_\gamma^2 - \bar{i}_\delta^2) \big) - 2\alpha_{1,2} (L_d + L_q) \bar{i}_\gamma \Big) (\theta - \theta_c).
\end{aligned} \tag{5.90}$$

If the magnetic saturation is neglected i.e. $\alpha_{i,j} = 0$ then (5.90) yields

$$\widetilde{i}_\delta = \left(\frac{1}{L_d} - \frac{1}{L_q} \right) (\theta - \theta_c). \tag{5.91}$$

In (5.90) the current $\widetilde{i}_\delta$ is proportional to the position error $\theta - \theta_c$ if $L_d \neq L_q$. By contrast, in (5.90) an offset value independent of μ is added to the expression of $\widetilde{i}_\delta$ due to the cross coupling and magnetic saturation. This offset term $(2\alpha_{1,2} L_q \bar{i}_\delta + 4\alpha_{2,2} L_d L_q \bar{i}_\gamma \bar{i}_\delta)$ is added to the position information,

This term causes a position estimation error if the saturation is not compensated. Furthermore, the condition to estimate the position in this case is

$$\frac{1}{L_d}-\frac{1}{L_q}+\left[6\alpha_{3,0}L_d-2\alpha_{1,2}(L_d+L_q)+\left(12\alpha_{4,0}L_d^2-2\alpha_{2,2}L_d^2-4\alpha_{2,2}L_dL_q\right)\bar{i}_\gamma\right]\bar{i}_\gamma + \left[2\alpha_{2,2}L_q^2-12\alpha_{0,4}L_q^2+4\alpha_{2,2}L_dL_q\right]\bar{i}_\delta>0 \quad (5.92)$$

because when this expression changes sign, the controller becomes instable. For some values of $\bar{i}_\gamma$ and $\bar{i}_\delta$ the observability can be lost mainly when $\frac{1}{L_d}-\frac{1}{L_q}$ is small. But, in other cases the choice of $\bar{i}_\gamma$ and $\bar{i}_\delta$ can enhance the observability. For example, for must motor type, adding a positive $\bar{i}_\gamma$ current (boost current) increases the value of the expression (5.92) and reinforce the motor stability. This can be explained by the positive term $6\alpha_{3,0}L_d$ ($\alpha_{3,0}$ is always positive) which is multiplied by $\bar{i}_\gamma$.

5.3.5 Current demodulation

To estimate the position information using e.g. (5.84) it is necessary to extract the low- and HF components $\bar{\mathbf{i}}_{\gamma\delta}$ and $\widetilde{\mathbf{i}}_{\gamma\delta}$ from the measured current $\mathbf{i}_{\gamma\delta}$. Using (5.78) we have

$$\mathbf{i}_{\gamma\delta}(t)\approx\bar{\mathbf{i}}_{\gamma\delta}(t)+\widetilde{\mathbf{i}}_{\gamma\delta}(t)F(\Omega t)$$

where $\bar{\mathbf{i}}_{\gamma\delta}$ and $\widetilde{\mathbf{i}}_{\gamma\delta}$ are by construction nearly constant in one period $T:=\frac{2\pi}{\Omega}$ of F. Under this hypothesis, the low frequency current $\bar{\mathbf{i}}_{\gamma\delta}$ can be approximated at time t by moving average which is the average of the measured current $\mathbf{i}_{\gamma\delta}$ over the last period of the HF signal $[t-T,t]$. Indeed, the HF signal has a zero mean over one period T, hence by taking its average over one period we eliminate HF components. Thus, we may write

$$\bar{\mathbf{i}}_{\gamma\delta}(t)\approx\frac{1}{T}\int_{t-T}^{t}\mathbf{i}_{\gamma\delta}(s)ds. \quad (5.93)$$

The mathematical interpretation of (5.93) is as follows

$$\int_{t-T}^{t}\mathbf{i}_{\gamma\delta}(s)ds\approx\bar{\mathbf{i}}_{\gamma\delta}(t)\int_{t-T}^{t}ds = T\bar{\mathbf{i}}_{\gamma\delta}(t)$$

where we have used $\int_{t-T}^{t}F(\Omega s)ds=0$ because F has a zero mean over a period T.

The HF current amplitude $\widetilde{\mathbf{i}}_{\gamma\delta}$ is obtained by heterodyning. The current $\mathbf{i}_{\gamma\delta}(t)$ is multiplied by $F(\Omega t)$ such that

$$\mathbf{i}_{\gamma\delta}(t)F(\Omega t)\approx \underbrace{\bar{\mathbf{i}}_{\gamma\delta}(t)F(\Omega t)}_{\text{zero mean on } [t-T,t]} + \underbrace{\widetilde{\mathbf{i}}_{\gamma\delta}(t)F^2(\Omega t)}_{\text{constant mean on } [t-T,t]},$$

hence integrating the previous relation over the time interval $[t-T, t]$ leads to

$$\begin{aligned}\int_{t-T}^{t} \mathbf{i}_{\gamma\delta}(s)F(\Omega s)ds &\approx \bar{\mathbf{i}}_{\gamma\delta}(t)\int_{t-T}^{t} F(\Omega s)ds \\ &\quad + \widetilde{\mathbf{i}}_{\gamma\delta}(t)\int_{t-T}^{t} F^2(\Omega s)ds \\ &= \widetilde{\mathbf{i}}_{\gamma\delta}(t)\int_{0}^{T} F^2(\Omega s)ds \\ &= \widetilde{\mathbf{i}}_{\gamma\delta}(t)\|F\|^2.\end{aligned}$$

where $\|F\|^2 = \int_0^T F^2(\Omega s)ds$. Finally we get

$$\widetilde{\mathbf{i}}_{\gamma\delta}(t) \approx \frac{1}{\|F\|^2}\int_{t-T}^{t} \mathbf{i}_{\gamma\delta}(s)F(\Omega s)ds. \tag{5.94}$$

Differentiating (5.93) with respect to time, hence the derivative of the low frequency current can be approximated as

$$\frac{d\bar{\mathbf{i}}_{\gamma\delta}(t)}{dt} = \frac{1}{T}\Big(\mathbf{i}_{\gamma\delta}(t) - \mathbf{i}_{\gamma\delta}(t-T)\Big), \tag{5.95}$$

and differentiating (5.94) with respect to time, hence the derivative of the HF current amplitude can be approximated as

$$\frac{d\widetilde{\mathbf{i}}_{\gamma\delta}(t)}{dt} = \frac{1}{\|F\|^2}\Big(\mathbf{i}_{\gamma\delta}(t)F(\Omega t) - \mathbf{i}_{\gamma\delta}(t-T)F\big(\Omega t - 2\pi\big)\Big). \tag{5.96}$$

The two equations (5.95) and (5.96) are used in the sequel to estimate the low and HF currents at real time operation.

5.4 Low speed control

In the previous section, we proposed a rotor position estimation method at low speed for PMSM motors using HF voltage injection. In this section, we propose a low speed sensorless control scheme based on this estimation procedure. The sensorless controller is obtained from a closed loop speed controller where the position sensor is replaced by a position estimator based on signal injection.

At first, we present the closed loop controller where the rotor position is measured using a position sensor. Then, in a second time we propose a real time position estimation procedure using a recursive nonlinear least square estimator based on (5.85). Finally, we incorporate this position estimator into the closed loop controller.

5.4.1 Closed loop controller

The proposed closed loop speed controller is composed of a current proportional integral (PI) controller in cascade with a speed PI controller. The motor speed is estimated from the measured position using a phase looked loop estimator. Fig 5.9 shows a bloc diagram of this controller where ω^{ref} is the speed reference and i_δ^r is the δ- axis current reference. The three main parts of this controller are: the speed controller; the speed estimator and the current controller. They are described in the sequel.

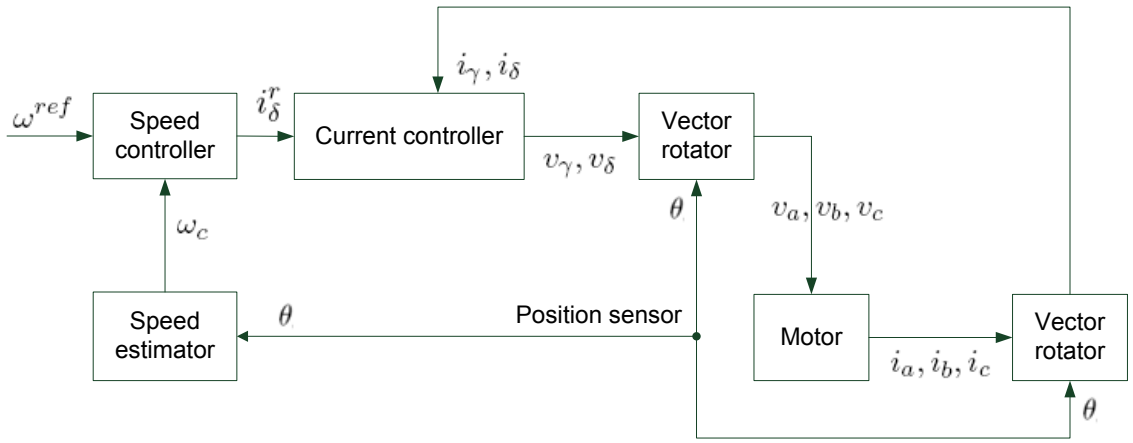

Figure 5.9: Bloc diagram of the closed loop controller.

5.4.1.1 Current controller

The current controller commands the electrical system of the motor and generates the voltage commands. It has the fastest dynamics and converges rapidly. It is composed of a PI regulator. The command voltage expression is

$$\mathbf{v}_{\gamma\delta} = R\mathbf{i}^r_{\gamma\delta} + k^i_p(\mathbf{i}^r_{\gamma\delta} - \mathbf{i}^f_{\gamma\delta}) + \mathbf{e}_{\gamma\delta} \tag{5.97}$$

with the integrator equation

$$\frac{d\mathbf{e}_{\gamma\delta}}{dt} = k^i_I(\mathbf{i}^r_{\gamma\delta} - \mathbf{i}^f_{\gamma\delta}) \tag{5.98}$$

and the measured current filter

$$\frac{d\mathbf{i}^f_{\gamma\delta}}{dt} = k^f_i(\mathbf{i}_{\gamma\delta} - \mathbf{i}^f_{\gamma\delta}) \tag{5.99}$$

where

- $\mathbf{i}^r_{\gamma\delta} = (i^r_\gamma, i^r_\delta)$ is the reference current;
- $\mathbf{i}^f_{\gamma\delta} = (i^f_\gamma, i^f_\delta)$ is the filtered value of the measured currents $\mathbf{i}_{\gamma\delta}$;
- $\mathbf{e}_{\gamma\delta} = (e_\gamma, e_\delta)$ is the integrator state of the current PI controller;
- $k^i_p = 2\xi_i L_d \omega_i$ and $k^i_I = L_d\omega^2_i$ are the proportional and integral gains of the current PI controller; with $\omega_i = 2\pi f_i$ where f_i is the current controller bandwidth and ξ_i is its damping factor;
- $k^f_i = 2\pi f^f_i$ where f^f_i is the current filter cutoff frequency.

In (5.97) the voltage $R\mathbf{i}^r_{\gamma\delta}$ is used to compensate for the voltage drop at the resistance of the motor. This controller requires the values of the reference currents i^r_γ and i^r_δ. The value of i^r_γ is constant, it is in general set to zero. The δ- axis current reference i^r_δ is the output of the speed controller which is described in the following. Fig. 5.10 shows the bloc diagram of the current controller.

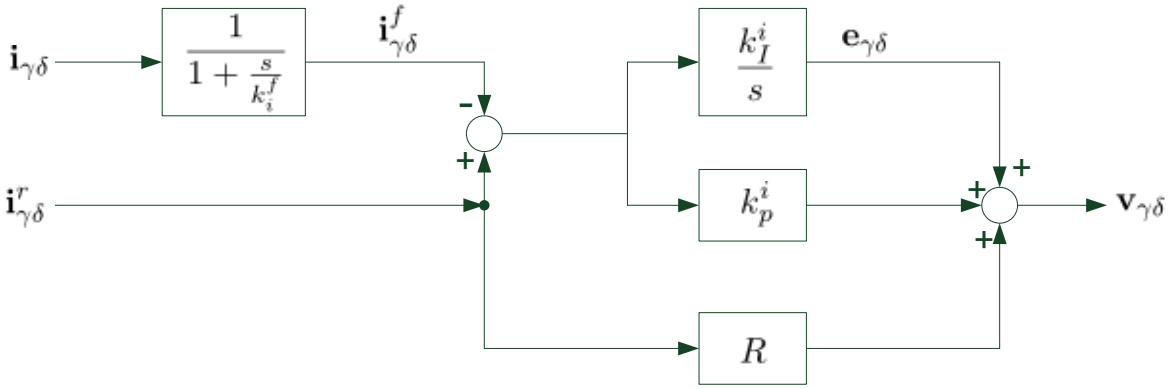

Figure 5.10: Bloc diagram of the current controller.

5.4.1.2 Speed estimator

The motor speed is estimated from the position. Instead of using the time derivative of the measured position which may be noisy, we use a PLL to estimate the frequency of the position. The mathematical equations of this PI speed estimator can be written as follows

$$\omega_c = k_p^\theta(\theta - \theta_c) + \omega_I^\theta \tag{5.100}$$

$$\frac{d\omega_I^\theta}{dt} = k_I^\theta(\theta - \theta_c) \tag{5.101}$$

$$\frac{d\theta_c}{dt} = \omega_c \tag{5.102}$$

where

- ω_c is the estimated speed; and θ_c is the estimated position (the integral of the estimated speed);
- ω_I^θ is the PLL integrator state;
- $k_p^\theta = 2\xi_\theta\omega_\theta$ and $k_I^\theta = \omega_\theta^2$ are the proportional and integral gains of the position estimator; with $\omega_\theta = 2\pi f_\theta$ and f_θ is the position estimator bandwidth and ξ_θ is its damping factor.

Fig. 5.11 shows the bloc diagram of the speed estimator.

5.4.1.3 Speed controller

The motor speed is commanded by a PI controller. This controller generates δ- axis current reference i_δ^r. The inputs of this controller are the speed reference ω^{ref} and the estimated speed ω_c. The speed controller has the slowest dynamics, but this is sufficient because the mechanical bandwidth the motor is small comparing to the electrical one. The estimated speed ω_c is filtered as follows

$$\frac{d\omega_c^f}{dt} = k_\omega^f(\omega_c - \omega_c^f), \tag{5.103}$$

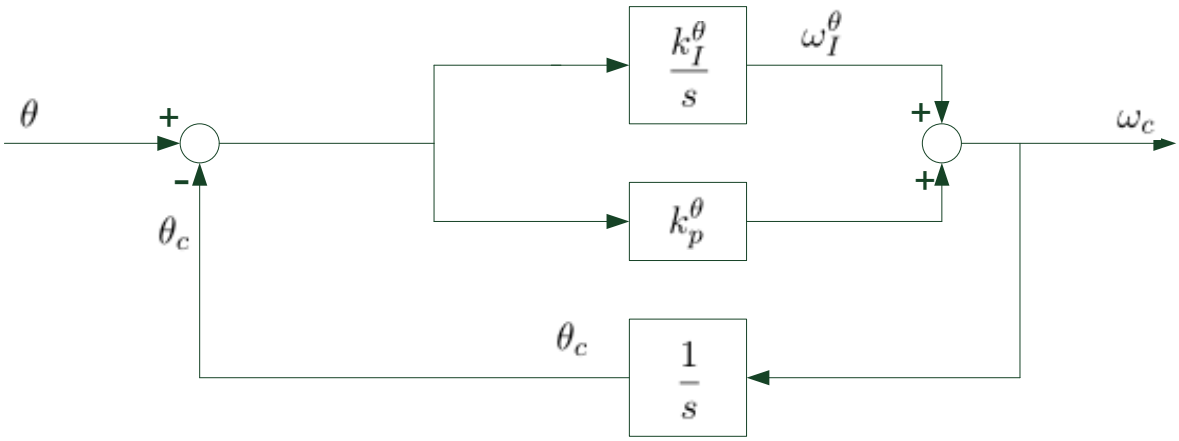

Figure 5.11: Bloc diagram of the speed estimator.

where ω_c^f is the filtered estimated speed; $k_\omega^f = 2\pi f_\omega^f$ is the filter gain and f_ω^f is the speed filter cut off frequency. The equations of the speed controller read

$$\tau_r = k_p^\omega(\omega^{ref} - \omega_c^f) + \tau_I \tag{5.104}$$

$$\frac{d\tau_I}{dt} = k_I^\omega(\omega^{ref} - \omega_c^f) \tag{5.105}$$

where

- ω^{ref} is the speed reference;
- τ_r is the electromagnetic torque reference;
- τ_I is the speed loop integrator state;
- $k_p^\omega = \frac{2J}{n}\xi_\omega\omega_\omega$ and $k_I^\omega = \frac{2J}{n}\omega_\omega^2$ are the proportional and integral gains of the PI speed controller; with $\omega_\omega = 2\pi f_\omega$ and f_ω is the speed loop bandwidth and ξ_ω is its damping factor.

The current reference is

$$i_\delta^{set} = \frac{\tau_r}{\lambda n}, \tag{5.106}$$

this current is filtered as follows

$$\frac{di_\delta^r}{dt} = k_i^r(i_\delta^{set} - i_\delta^r) \tag{5.107}$$

where i_δ^r is the filtered δ- axis current reference and $k_i^r = 2\pi f_i^r$ with f_i^r is the filter cut off frequency. Fig. 5.12 shows the bloc diagram of the speed controller.

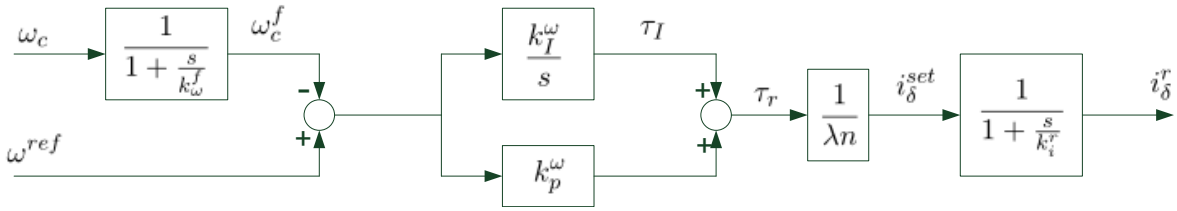

Figure 5.12: Bloc diagram of the speed controller.

5.4.1.4 Closed loop controller equations

The controller equations can be written in the general form given by (5.37)–(5.42). Indeed, using (5.97)–(5.107) the controller equation (5.40) reads

$$\frac{d\eta}{dt} = \frac{d}{dt}\begin{pmatrix} \mathbf{i}_{\gamma\delta}^f \\ \mathbf{e}_{\gamma\delta} \\ i_\delta^r \\ \omega_I^\theta \\ \omega_c^f \\ \tau_I \end{pmatrix} = \mathbf{a}\big(\mathbf{i}_{\gamma\delta}, \theta, \theta_c, \eta, t\big) = \begin{pmatrix} k_i^f(\mathbf{i}_{\gamma\delta} - \mathbf{i}_{\gamma\delta}^f) \\ k_I^i(\mathbf{i}_{\gamma\delta}^r - \mathbf{i}_{\gamma\delta}^f) \\ k_i^r\left(\frac{k_p^\omega(\omega^{ref}-\omega_c^f)+\tau_I}{\lambda n} - i_\delta^r\right) \\ k_I^\theta(\theta - \theta_c) \\ k_\omega^f\left(k_p^\theta(\theta-\theta_c) + \omega_I^\theta - \omega_c^f\right) \\ k_I^\omega(\omega^{ref} - \omega_c^f) \end{pmatrix} \tag{5.108}$$

where ω^{ref} and i_γ^r are input signals; in general i_γ^r is set to zero. The estimated speed is

$$\omega_c = \Omega_c\big(\mathbf{i}_{\gamma\delta}, \theta, \theta_c, \eta, t\big) = k_p^\theta(\theta - \theta_c) + \omega_I^\theta, \tag{5.109}$$

the command voltage is

$$\mathcal{V}_{\gamma\delta}\big(\mathbf{i}_{\gamma\delta}, \theta, \theta_c, \eta, t\big) = R\mathbf{i}_{\gamma\delta}^r + k_p^i(\mathbf{i}_{\gamma\delta}^r - \mathbf{i}_{\gamma\delta}^f) + \mathbf{e}_{\gamma\delta}. \tag{5.110}$$

To simplify the comprehension of this control law, we summarize the description of the controller state variables and the controller parameters in tables 5.1 and 5.2 respectively.

It is important to note that a relation between current and speed controller bandwidths must be respected to ensure the controller stability, this condition reads

$$f_i \gg f_\omega. \tag{5.111}$$

5.4.2 Sensorless controller

We propose here a sensorless speed controller. It has the same structure as the closed loop speed controller (5.108)–(5.110) where the measured position θ is substituted by the estimated position θ_c. The value of θ_c is obtained by signal injection.

Table 5.1: States of the speed controller

Parameter	Description
i_γ^f	filtered value of measured γ- axis current
i_δ^f	filtered value of measured δ- axis current
e_γ	integral state of γ- axis current PI controller
e_δ	integral state of δ- axis current PI controller
i_δ^r	reference δ- axis current
ω_c^f	filtered estimated speed
τ_I	integral state of the speed PI controller

Table 5.2: Parameters of the speed controller

Parameter	Description	Dependent parameters
f_i, ξ_i	bandwidth and damping factor of the current controller	$\omega_i = 2\pi f_i$, $k_p^i = 2\xi_i L_d \omega_i$, $k_I^i = L_d \omega_i^2$
f_θ, ξ_θ	bandwidth and damping factor of the position estimator	$\omega_\theta = 2\pi f_\theta$, $k_p^\theta = 2\xi_\theta \omega_\theta$, $k_I^\theta = \omega_\theta^2$
f_ω, ξ_ω	bandwidth and damping factor of the speed controller	$\omega_\omega = 2\pi f_\omega$, $k_p^\omega = \frac{2J}{n}\xi_\omega \omega_\omega$, $k_i^\omega = \frac{2J}{n}\omega_\omega^2$
f_i^f	cutoff frequency of the current filter	$k_i^f = 2\pi f_i^f$
f_ω^f	cutoff frequency of the speed filter	$k_\omega^f = 2\pi f_\omega^f$
f_i^r	cutoff frequency of the reference current filter	$k_i^r = 2\pi f_i^r$

A HF signal is added to the motor voltage (5.110) as described in (5.43) with

$$\widetilde{v}_{\gamma\delta} = \begin{pmatrix} \widetilde{v} \\ 0 \end{pmatrix}$$

where $\widetilde{v}$ is constant. Thus, we can use the result of second order averaging of section 5.3 where the rotor position is estimated from the low frequency and HF current components $\bar{\mathbf{i}}_{\gamma\delta}$ and $\widetilde{\mathbf{i}}_{\gamma\delta}$. Fig. 5.13 shows the bloc diagram of the proposed sensorless controller.

5.4.2.1 Sensorless position estimator

The solution of (5.84) provides an estimation of the error between the actual position θ and the estimated position θ_c. The estimator proposed here is based on the PLL equations (5.100)–(5.102) where the value of $\theta - \theta_c$ is replaced by the estimated position error obtained from $\bar{\mathbf{i}}_{\gamma\delta}$ and $\widetilde{\mathbf{i}}_{\gamma\delta}$. This PLL regulates ω_c such that the estimated position error converges to zero.

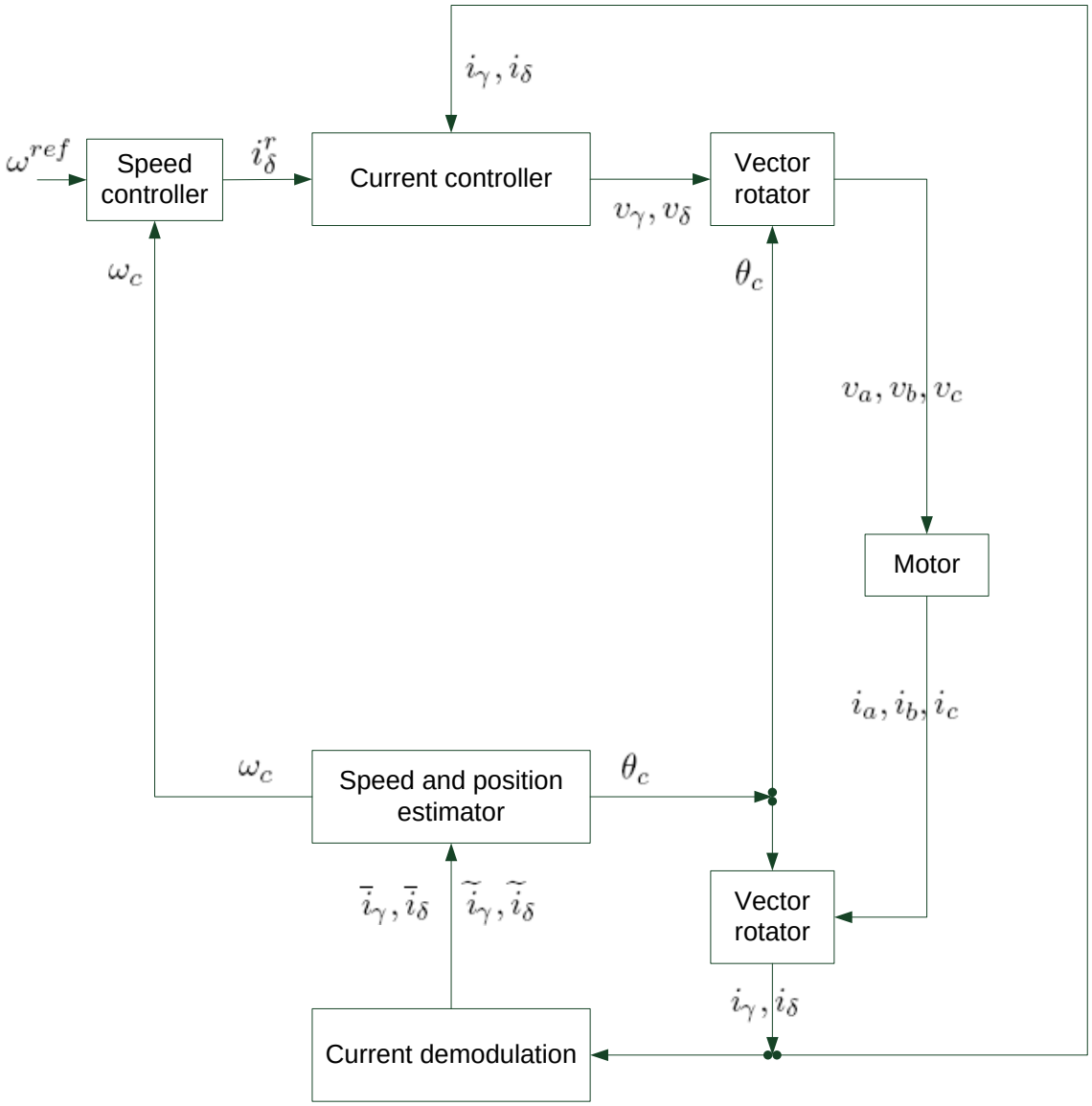

Figure 5.13: Bloc diagram of the sensorless controller.

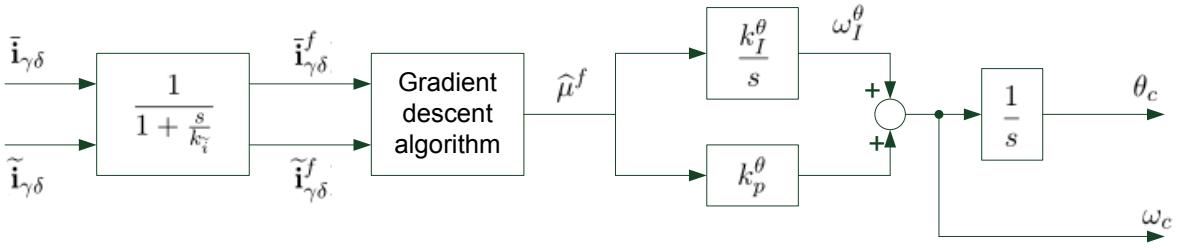

Figure 5.14: Bloc diagram of the sensorless position and speed estimator.

The rotor position estimation is composed of two phases. At a first time, the position error is estimated by recursive nonlinear least square using (5.85) as follows

$$\frac{d\widehat{\mu}^f}{dt} = -\Lambda \frac{\partial \mathcal{M}}{\partial \mu}(\widehat{\mu}^f, \bar{\mathbf{i}}^f_{\gamma\delta}, \widetilde{\mathbf{i}}^f_{\gamma\delta}) \tag{5.112}$$

$$\frac{d\bar{\mathbf{i}}^f_{\gamma\delta}}{dt} = k_{\widetilde{i}}(\bar{\mathbf{i}}_{\gamma\delta} - \bar{\mathbf{i}}^f_{\gamma\delta}) \tag{5.113}$$

$$\frac{d\widetilde{\mathbf{i}}^f_{\gamma\delta}}{dt} = k_{\widetilde{i}}(\widetilde{\mathbf{i}}_{\gamma\delta} - \widetilde{\mathbf{i}}^f_{\gamma\delta}), \tag{5.114}$$

where

- $\widehat{\mu}^f$ is an estimation of the position error;
- $\bar{\mathbf{i}}^f_{\gamma\delta}$ and $\widetilde{\mathbf{i}}^f_{\gamma\delta}$ are the filtered values of $\bar{\mathbf{i}}_{\gamma\delta}$ and $\widetilde{\mathbf{i}}_{\gamma\delta}$ respectively; the filtered values are used to reduce noises and oscillation caused by the HF voltage and measurement noises;
- $k_{\widetilde{i}} = 2\pi f_{\widetilde{i}}$ where $f_{\widetilde{i}}$ is a cutoff frequency;
- Λ is taken constant here because $\frac{\partial^2 \mathcal{M}}{\partial \mu^2}$ is almost constant in practice when μ is near zero;
- the expression of $\frac{\partial \mathcal{M}}{\partial \mu}$ is as follows

$$\frac{\partial \mathcal{M}}{\partial \mu}(\widehat{\mu}^f, \bar{\mathbf{i}}^f_{\gamma\delta}, \widetilde{\mathbf{i}}^f_{\gamma\delta}) = -2\left(\widetilde{\mathbf{i}}^f_{\gamma\delta} - \mathcal{S}(\widehat{\mu}^f, \bar{\mathbf{i}}^f_{\gamma\delta})\frac{\widetilde{\mathbf{v}}_{\gamma\delta}}{\Omega}\right)^T \frac{\partial \mathcal{S}(\widehat{\mu}^f, \bar{\mathbf{i}}^f_{\gamma\delta})}{\partial \mu}\frac{\widetilde{\mathbf{v}}_{\gamma\delta}}{\Omega}. \tag{5.115}$$

In (5.112), we propose a simple gradient descent algorithm to find the position error such that

$$\widehat{\mu}^f \approx \arg\min_{\mu\in]-\pi,\pi]}\left[\mathcal{M}(\mu, \bar{\mathbf{i}}^f_{\gamma\delta}, \widetilde{\mathbf{i}}^f_{\gamma\delta})\right] \approx \arg\min_{\mu\in]-\pi,\pi]}\left[\mathcal{M}(\mu, \bar{\mathbf{i}}_{\gamma\delta}, \widetilde{\mathbf{i}}_{\gamma\delta})\right] = \theta - \theta_c$$

at real time operation. At $t = 0$, $\widehat{\mu}^f$ is initialized by zero because the initial position is obtained using an algorithm of initial rotor position detection.

Then, we replace the term $\theta - \theta_c$ in (5.100)–(5.102) by $\widehat{\mu}^f$. Hence we get

$$\omega_c = k_p^\theta \widehat{\mu}^f + \omega_I^\theta \tag{5.116}$$

$$\frac{d\omega_I^\theta}{dt} = k_I^\theta \widehat{\mu}^f \tag{5.117}$$

$$\frac{d\theta_c}{dt} = \omega_c. \tag{5.118}$$

The equations (5.116)–(5.118) are used to estimate the rotor position at real time operation. Fig. 5.14 shows the bloc diagram of the sensorless position and speed estimator.

Table 5.3: States of the sensorless position observer

State	Description
$\bar{\mathbf{i}}_{\gamma\delta}$	low frequency current
$\widetilde{\mathbf{i}}_{\gamma\delta}$	high frequency current amplitude
$\bar{\mathbf{i}}^f_{\gamma\delta}$	filtered value of low frequency current
$\widetilde{\mathbf{i}}^f_{\gamma\delta}$	filtered value of high frequency current amplitude
$\widehat{\mu}^f$	estimated rotor position error

Finally, the dynamic equations of the sensorless position observer can be written as follows

$$\frac{d}{dt}\begin{pmatrix} \bar{\mathbf{i}}_{\gamma\delta} \\ \widetilde{\mathbf{i}}_{\gamma\delta} \\ \bar{\mathbf{i}}^f_{\gamma\delta} \\ \widetilde{\mathbf{i}}^f_{\gamma\delta} \\ \widehat{\mu}^f \\ \omega^\theta_I \\ \theta_c \end{pmatrix} = \begin{pmatrix} \frac{1}{T}\Big(\mathbf{i}_{\gamma\delta}(t) - \mathbf{i}_{\gamma\delta}(t-T)\Big) \\ \frac{1}{\|F\|^2}\Big(\mathbf{i}_{\gamma\delta}(t)F(\Omega t) - \mathbf{i}_{\gamma\delta}(t-T)F\big(\Omega t - 2\pi\big)\Big) \\ k_{\bar{i}}(\bar{\mathbf{i}}_{\gamma\delta} - \bar{\mathbf{i}}^f_{\gamma\delta}) \\ k_{\widetilde{i}}(\widetilde{\mathbf{i}}_{\gamma\delta} - \widetilde{\mathbf{i}}^f_{\gamma\delta}) \\ 2\Lambda\left(\widetilde{\mathbf{i}}^f_{\gamma\delta} - \mathcal{S}(\widehat{\mu}^f, \bar{\mathbf{i}}^f_{\gamma\delta})\frac{\widetilde{\mathbf{v}}_{\gamma\delta}}{\Omega}\right)^T \frac{\partial \mathcal{S}(\widehat{\mu}^f, \bar{\mathbf{i}}^f_{\gamma\delta})}{\partial \mu}\frac{\widetilde{\mathbf{v}}_{\gamma\delta}}{\Omega} \\ k^\theta_I \widehat{\mu}^f \\ k^\theta_p \widehat{\mu}^f + \omega^\theta_I. \end{pmatrix}$$

And the estimated speed is

$$\omega_c = k^\theta_p \widehat{\mu}^f + \omega^\theta_I.$$

Table. 5.3 provides the description of the observer states.

5.4.2.2 Sensorless controller equations

The equations of the sensorless controller can be written as follows

$$\frac{d}{dt}\begin{pmatrix} \mathbf{i}^f_{\gamma\delta} \\ \mathbf{e}_{\gamma\delta} \\ i^r_\delta \\ \omega^f_c \\ \tau_I \end{pmatrix} = \begin{pmatrix} k^f_i(\mathbf{i}_{\gamma\delta} - \mathbf{i}^f_{\gamma\delta}) \\ k^i_I(\mathbf{i}^r_{\gamma\delta} - \mathbf{i}^f_{\gamma\delta}) \\ k^r_i\left(\frac{k^\omega_p(\omega^{ref}-\omega^f_c)+\tau_I}{\lambda n} - i^r_\delta\right) \\ k^f_\omega\left(k^\theta_p\widehat{\mu}^f + \omega^\theta_I - \omega^f_c\right) \\ k^\omega_I(\omega^{ref} - \omega^f_c) \end{pmatrix}$$

The command voltage is

$$\mathbf{v}_{\gamma\delta} = R\mathbf{i}^r_{\gamma\delta} + k^i_p(\mathbf{i}^r_{\gamma\delta} - \mathbf{i}^f_{\gamma\delta}) + \mathbf{e}_{\gamma\delta} + (\widetilde{v}, 0)^T f(\Omega t).$$

The stability of this sensorless observer-controller is verified and validated by experimental tests in the chapter 6.

Conclusion

We proposed in this chapter a rotor position estimation procedure based on the saturation model (4.132)–(4.133). This method takes into account magnetic and cross coupling saturation to compensate the offset errors caused by load torque and magnetizing current. This method is general in the sense it can accommodate virtually any PMSM type, control law, saturation model, and form of injected signal. Experimental validation results of this position estimation method and the sensorless control law are presented in chapter 6 where we see that the estimation error is less than 5 electrical degree even at high load torque. The saturation parameters needed for this method can be estimated by a simple linear least square; this procedure is detailed in chapter 6 and it is easy to use for industrial purpose.

Chapter 6

Parameter identification and experimental validation

Contents

Introduction

Dans le chapitre 4, nous avons proposé un modèle de saturation paramétrique du MSAP basé sur cinq paramètres de saturation ($\alpha_{3,0}$, $\alpha_{1,2}$, $\alpha_{4,0}$, $\alpha_{2,2}$, $\alpha_{0,4}$) en plus des paramètres magnétiques standards L_d et L_q. Ce modèle a été utilisé dans le chapitre 4 pour trouver une méthode d'estimation de la position du rotor du MSAP et pour élaborer une loi de commande sans capteur et à basse vitesse du MSAP.

Dans ce chapitre, nous proposons une validation expérimentale du modèle de saturation du MSAP ainsi qu'une procédure d'identification des paramètres de ce modèle. Cette procédure est basée encore sur l'injection de signaux et la moyennisation de second ordre où les paramètres de saturation sont estimés simplement par moindres carrés linéaires. Les courants HF obtenus expérimentalement sont comparés aux courants HF obtenus par moyennisation à partir du modèle de saturation dans le but de valider le modèle et d'estimer les paramètres de saturation. En plus, nous utilisons une rampe

de tension pour valider le modèle. Ensuite, en utilisant ces paramètres, la procédure d'estimation de position et la loi de commande sans capteur sont validées expérimentalement sur deux moteurs MSAP.

Les résultats expérimentaux montrent que, grâce au modèle de saturation, l'erreur d'estimation de position est réduite à moins de 5 *degrés électriques pour le moteur MSAI et que cette erreur est réduite à moins de* 10 *degrés pour le moteur MSAS qui a un niveau de saillance très faible. En plus, nous constatons que, grâce au modèle de saturation, la commande sans capteur du moteur MSAS à basse vitesse et à un couple de charge élevé est maintenant possible, ce qui n'était pas le cas si on considère le modèle linéaire seulement.*

Dans la section 6.1, nous proposons une méthode simple d'estimation des paramètres de saturation par moindres carrés linéaires, cette méthode est appliquée et validée expérimentalement sur les moteurs MSAI et MSAS. Dans la section 6.2, nous présentons plusieurs méthodes de validation expérimentale du modèle de saturation à rotor bloqué. Ensuite, dans la section 6.3, nous démontrons expérimentalement sur les deux moteurs MSAI et MSAS la pertinence de la méthode d'estimation de position proposée dans le chapitre 5, où nous montrons la nécessité de considérer la saturation afin d'estimer correctement la position. Enfin, dans la section 6.4, nous présentons la validation expérimentale de la loi de commande du MSAP à basse vitesse et sans capteur proposée dans le chapitre 5.

In chapter 4 we proposed a parametric saturation model based on five saturation parameters ($\alpha_{3,0}$, $\alpha_{1,2}$, $\alpha_{4,0}$, $\alpha_{2,2}$, $\alpha_{0,4}$) in addition to the standard magnetic parameters L_d and L_q. This model was used in chapter 5 to find a rotor position estimation method of the PMSM and to design a sensorless control law of PMSM at low speed.

In this chapter, we propose an experimental validation of the PMSM saturation model and an identification procedure of the saturation parameters for this model. This procedure is also relying on signal injection and averaging where simple linear least square method is used to estimate the saturation parameters. Experimental high frequency currents are compared to high frequency currents obtained by averaging from the saturation model in order to validate the model and to estimate the saturation parameters. In addition, we use step voltage excitation to validate the model. Then, using these parameters, the position estimation procedure and the sensorless control law are applied on two PMSM motors and validated by experimental tests. Experimental results show that, thanks to the saturation model, the position estimation error is reduced to less than 5 electrical degree for IPM motor and this error is reduced to less than 10 electrical degree for the SPM motor with a very low saliency level. In addition, we see that thanks to the saturation model, the sensorless control of the SPM motor at low speed and high load torque is now possible which was not the case with the linear magnetic model.

In section 6.1, we propose a simple method for the saturation parameter estimation by linear least squares; this method is applied and validated experimentally on the IPM and SPM motors. In section 6.2, we present multiple ways of experimental validation of the saturation model at locked rotor position. In section 6.3, we experimentally demonstrate on the two motors IPM and SPM the relevance of the position estimation approach proposed in chapter 5 where we show the necessity of considering saturation to correctly estimate the position. Finally, in section 6.4 we present experi-

mental validation results of the low speed sensorless control law proposed in chapter 5.

6.1 Parameter identification

It is necessary to estimate the saturation parameters to make this saturation model (4.132)–(4.133) useful. The estimation method of these parameters must be simple of use and applicable to all motor types. In this section we propose a procedure for estimating the magnetic parameters presented in the PMSM model (4.132)-(4.133):

$$\begin{pmatrix} L_d & L_q & \alpha_{3,0} & \alpha_{1,2} & \alpha_{4,0} & \alpha_{2,2} & \alpha_{0,4} \end{pmatrix}.$$

The estimation procedure is done by simple linear least squares and using high frequency voltage injection at locked rotor position.

6.1.1 Principle

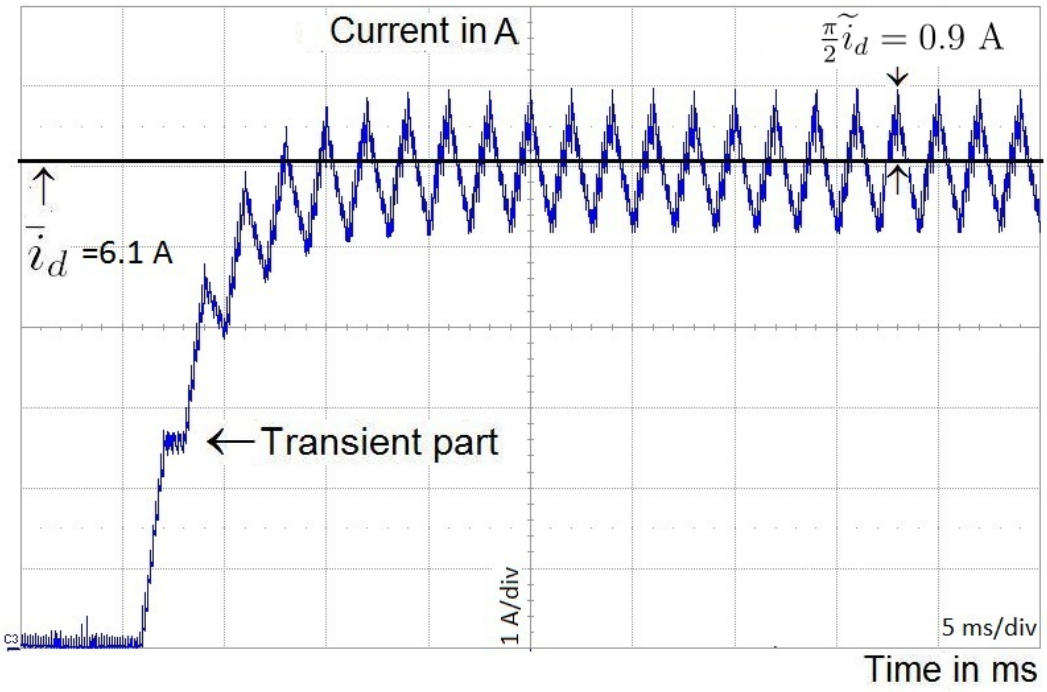

Figure 6.1: Experimental time response of i_d in (6.1)-(6.2)

A high frequency voltage is added to the motor fundamental voltage; the parameters are estimated by comparing the high frequency current obtained experimentally and from the PMSM model. The actual dq frame is used here and the motor is locked at the position $\theta = 0$ and $\omega = 0$ which mean that the dq frame and the $\alpha\beta$ frame are confounded. Therefore, the physically measured currents are $\mathbf{i}_{dq}$ and the physically impressed voltages are $\mathbf{v}_{dq}$. Thanks to this configuration, the motor variables

in the rotor dq frame are accessible and the rotor will not move because the motor is locked at zero position using an external mechanical brake. In the sequel, all the variables are expressed in dq frame.

At locked rotor position, the motor electrical equations (4.116) and (4.132)-(4.133) can be written as

$$\frac{d\mathbf{\Phi}_{dq}}{dt} = \mathbf{v}_{dq} - R\mathbf{i}_{dq}. \tag{6.1}$$

with $\mathbf{i}_{dq} = \mathcal{I}_{dq}(\mathbf{\Phi}_{dq})$. The equation (6.1) describes the PMSM at a fixed position where it is similar to a series RL (resistance-inductance) circuit.

As in section 5.2, but now working directly in the dq frame, we inject a fast-varying pulsating voltage

$$\mathbf{v}_{dq} = \overline{\mathbf{v}}_{dq} + \widetilde{\mathbf{v}}_{dq} f(\Omega t) \tag{6.2}$$

where $\overline{\mathbf{v}}_{dq}$ is a low frequency voltage in dq frame and $\widetilde{\mathbf{v}}_{dq}$ is the amplitude of the added high frequency voltage in dq frame. $\overline{\mathbf{v}}_{dq}$ and $\widetilde{\mathbf{v}}_{dq}$ are taken constant. From (6.1)-(6.2), the electrical system equation reads

$$\frac{d\mathbf{\Phi}_{dq}}{dt} = \overline{\mathbf{v}}_{dq} + \widetilde{\mathbf{v}}_{dq} f(\Omega t) - R\mathbf{i}_{dq}, \tag{6.3}$$

this equation is a particular case of (5.44) where $\omega = \Omega_c = \theta = \theta_c = 0$; $d \equiv \gamma$ and $q \equiv \delta$ and $\mathcal{V}_{\gamma\delta} = \overline{\mathbf{v}}_{dq}$. The solution of (6.3) is obtained from (5.49), hence the flux reads

$$\mathbf{\Phi}_{dq} = \overline{\mathbf{\Phi}}_{dq} + \frac{\widetilde{\mathbf{v}}_{dq}}{\Omega} F(\Omega t) + \mathcal{O}(\frac{1}{\Omega^2})$$

where $\overline{\mathbf{\Phi}}_{dq}$ is the low frequency "slowly-varying" component of $\mathbf{\Phi}_{dq}$, using (5.54) hence $\overline{\mathbf{\Phi}}_{dq}$ satisfies

$$\frac{d\overline{\mathbf{\Phi}}_{dq}}{dt} = \overline{\mathbf{v}}_{dq} - R\bar{\mathbf{i}}_{dq}, \tag{6.4}$$

with $\bar{\mathbf{i}}_{dq} = \mathcal{I}_{dq}(\overline{\mathbf{\Phi}}_{dq})$.

Using (5.78) the current in dq frame can be written as

$$\mathbf{i}_{dq} = \bar{\mathbf{i}}_{dq} + \widetilde{\mathbf{i}}_{dq} F(\Omega t) + \mathcal{O}(\tfrac{1}{\Omega^2})$$

where $\widetilde{\mathbf{i}}_{dq}$ is obtained using (5.80):

$$\widetilde{\mathbf{i}}_{dq} = D\mathcal{I}_{dq}\big(\mathcal{I}_{dq}^{-1}(\bar{\mathbf{i}}_{dq})\big)\frac{\widetilde{\mathbf{v}}_{dq}}{\Omega}. \tag{6.5}$$

Since $\overline{\mathbf{v}}_{dq}$ is constant (6.4) implies $R\bar{\mathbf{i}}_{dq}$ tends to $\overline{\mathbf{v}}_{dq}$, hence after an initial transient $\bar{\mathbf{i}}_{dq}$ is constant such that:

$$\bar{\mathbf{i}}_{dq} \to \frac{\overline{\mathbf{v}}_{dq}}{R}. \tag{6.6}$$

As a consequence $\widetilde{\mathbf{i}}_{dq}$ is by (6.5) also constant. Fig. 6.1 shows for instance the time response of i_d for the SPM motor of 6.1 starting from $i_d(0) = 0$ and using a square function f; notice the current ripples seen on the scope are $\max_{\tau\in[0,2\pi]} F(\tau) = \frac{\pi}{2}$ (since f is square with period 2π) smaller than $\widetilde{\mathbf{i}}_{dq}$. The magnetic parameters can then be estimated repeatedly using (6.5) with various values of $\overline{\mathbf{v}}_{dq}$ and $\widetilde{\mathbf{v}}_{dq}$.

Using (4.140) we get

$$D\mathcal{I}_{dq}\big(\mathcal{I}_{dq}^{-1}(i_d,i_q)\big) = \begin{pmatrix} \frac{1}{L_d}+6\alpha_{3,0}L_d i_d+12\alpha_{4,0}L_d^2 i_d^2+2\alpha_{2,2}L_q^2 i_q^2 & 2\alpha_{1,2}L_q i_q+4\alpha_{2,2}L_d i_d L_q i_q \\ 2\alpha_{1,2}L_q i_q+4\alpha_{2,2}L_d i_d L_q i_q & \frac{1}{L_q}+2\alpha_{1,2}L_d i_d+2\alpha_{2,2}L_d^2 i_d^2+12\alpha_{0,4}L_q^2 i_q^2 \end{pmatrix}.$$

Thus, from (6.5) we get the explicit expressions of the amplitudes of the high frequency currents as follows

$$\widetilde{i}_d = \tfrac{1}{\Omega}\Big(\frac{\widetilde{v}_d}{L_d}+6\alpha_{3,0}L_d\bar{i}_d\widetilde{v}_d+2\alpha_{1,2}L_q\bar{i}_q\widetilde{v}_q+12\alpha_{4,0}L_d^2\bar{i}_d^2\widetilde{v}_d+2\alpha_{2,2}L_q\bar{i}_q(2L_d\bar{i}_d\widetilde{v}_q+L_q\bar{i}_q\widetilde{v}_d)\Big) \tag{6.7}$$

$$\widetilde{i}_q = \tfrac{1}{\Omega}\Big(\frac{\widetilde{v}_q}{L_q}+2\alpha_{1,2}(L_d\bar{i}_d\widetilde{v}_q+L_q\bar{i}_q\widetilde{v}_d)+2\alpha_{2,2}L_d\bar{i}_d(2L_q\bar{i}_q\widetilde{v}_d+L_d\bar{i}_d\widetilde{v}_q)+12\alpha_{0,4}L_q^2\bar{i}_q^2\widetilde{v}_q\Big). \tag{6.8}$$

The equations (6.7)-(6.8) represent the relation between the amplitudes of the high frequency currents and the magnetic parameters, they are used to estimate the saturation parameters and to validate the proposed saturation model.

Indeed, in (6.7)-(6.8) the voltages $\widetilde{v}_d$ and $\widetilde{v}_q$ and the pulsation Ω are known variables; in addition the values of $\widetilde{i}_d$, $\widetilde{i}_q$, $\bar{i}_d$ and $\bar{i}_q$ are extracted from the measured currents i_d and i_q as explained in 5.3.5. Thus, the only unknown variables in (6.7)-(6.8) are the seven magnetic parameters (L_d, L_q, $\alpha_{3,0}$, $\alpha_{1,2}$, $\alpha_{4,0}$, $\alpha_{2,2}$, $\alpha_{0,4}$). The inductances L_d and L_q are estimated at zero current $\bar{i}_d = \bar{i}_q = 0$ as we will see in the sequel. The five magnetic saturation parameters ($\alpha_{3,0}$, $\alpha_{1,2}$, $\alpha_{4,0}$, $\alpha_{2,2}$, $\alpha_{0,4}$) are estimated from (6.7)-(6.8) by simple linear least squares.

6.1.2 Estimation of the parameters

The estimation of the saturation parameters is based on (6.6)–(6.8). We begin by estimating the motor inductances. This is done by adding a high frequency voltage at zero low frequency currents $\bar{i}_d = \bar{i}_q = 0$. Thus (6.7)-(6.8) lead to

$$L_d = \frac{1}{\Omega}\frac{\widetilde{v}_d}{\widetilde{i}_d} \tag{6.9}$$

$$L_q = \frac{1}{\Omega}\frac{\widetilde{v}_q}{\widetilde{i}_q}. \tag{6.10}$$

The expressions of L_d and L_q are proportional to the ratio of the high frequency voltage amplitude to the high frequency current amplitude. According to (6.6) the low frequency currents $\bar{i}_d$ and $\bar{i}_d$ are set to zero using $\bar{v}_d = \bar{v}_q = 0$. In the sequel we consider that the inductances L_d and L_q are known variables.

Since combinations of the magnetic parameters always enter linearly (6.7)-(6.8), they can be estimated by simple linear least squares. Moreover by suitably choosing $\overline{\mathbf{v}}_{dq}$ and $\widetilde{\mathbf{v}}_{dq}$, the whole least squares problem for the five saturation parameters ($\alpha_{3,0}$, $\alpha_{1,2}$, $\alpha_{4,0}$, $\alpha_{2,2}$, $\alpha_{0,4}$) can be split into several subproblems involving fewer parameters:

Table 6.1: Rated parameters of test motors

Motor	IPM	SPM
Rated power	750 W	1500 W
Rated current I_n (peak)	4.51 A	5.19 A
Rated voltage (peak per phase)	110 V	245 V
Rated speed	1800 rpm	3000 rpm
Rated torque	3.98 Nm	6.06 Nm
n	3	5
R	1.52 Ω	2.1 Ω
λ (peak)	196 mWb	155 mWb
Inertia moment J	5.5 gm^2	5.3 gm^2

- with the total low frequency current along the d- axis and the high frequency voltage along the d- axis also: $\overline{v}_q = 0$, hence $\bar{i}_q := 0$, and $\widetilde{v}_q = 0$ (6.7) reads

$$\widetilde{i}_d = \frac{\widetilde{v}_d}{\Omega}\left(\frac{1}{L_d} + 6\alpha_{3,0}L_d\bar{i}_d + 12\alpha_{4,0}L_d^2\bar{i}_d^2\right) \tag{6.11}$$

- with the total low frequency current along the q- axis and the high frequency voltage along the d- axis: $\overline{v}_d = 0$, hence $\bar{i}_d := 0$, and $\widetilde{v}_q = 0$ (6.7)-(6.8) lead to

$$\widetilde{i}_d = \frac{\widetilde{v}_d}{\Omega}\left(\frac{1}{L_d} + 2\alpha_{2,2}L_q^2\bar{i}_q^2\right) \tag{6.12}$$

$$\widetilde{i}_q = \frac{2\widetilde{v}_d}{\Omega}\alpha_{1,2}L_q\bar{i}_q \tag{6.13}$$

- with the total low frequency current along the q- axis and the high frequency voltage along the q- axis: $\overline{v}_d = 0$, hence $\bar{i}_d := 0$, and $\widetilde{v}_d = 0$ (6.8) lead to

$$\widetilde{i}_q = \frac{\widetilde{v}_q}{\Omega}\left(\frac{1}{L_q} + 12\alpha_{0,4}L_q^2\bar{i}_q^2\right). \tag{6.14}$$

To estimate the saturation parameters, several runs are performed with various $\overline{v}_d$ (resp. $\overline{v}_q$) such that $\bar{i}_d$ (resp. $\bar{i}_q$) ranges from -200% to $+200\%$ of the rated current according to (6.6). The parameters $\alpha_{3,0}$ and $\alpha_{4,0}$ are jointly estimated by linear least squares from (6.11) where $\widetilde{i}_d$ is a linear function of $\alpha_{3,0}$ and $\alpha_{4,0}$. The parameters $\alpha_{2,2}$, $\alpha_{1,2}$ and $\alpha_{0,4}$ are separately estimated by linear least squares from respectively (6.12), (6.13) and (6.14).

6.1.3 Experimental results and discussions

The parameter estimation procedure developed in this chapter was tested on two types of motors, an Interior Magnet PMSM (IPM) and a Surface-Mounted PMSM (SPM), with rated parameters listed in table 6.1.

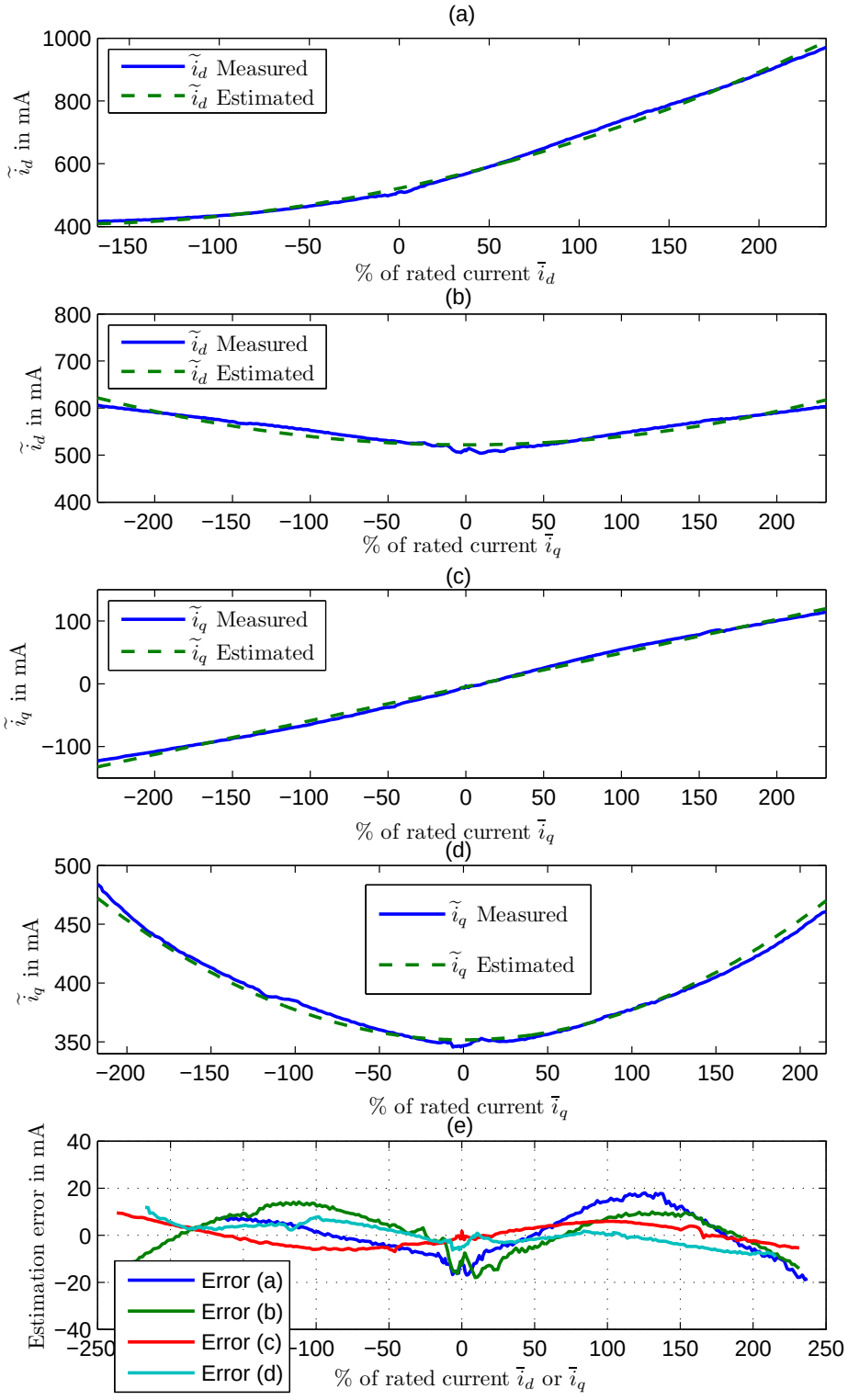

Figure 6.2: IPM motor: fitted values vs measurements for (6.11) in (a); (6.12) in (b); (6.13) in (c); (6.14) in (d); in (e) estimation error corresponding to (a)-(b)-(c)-(d).

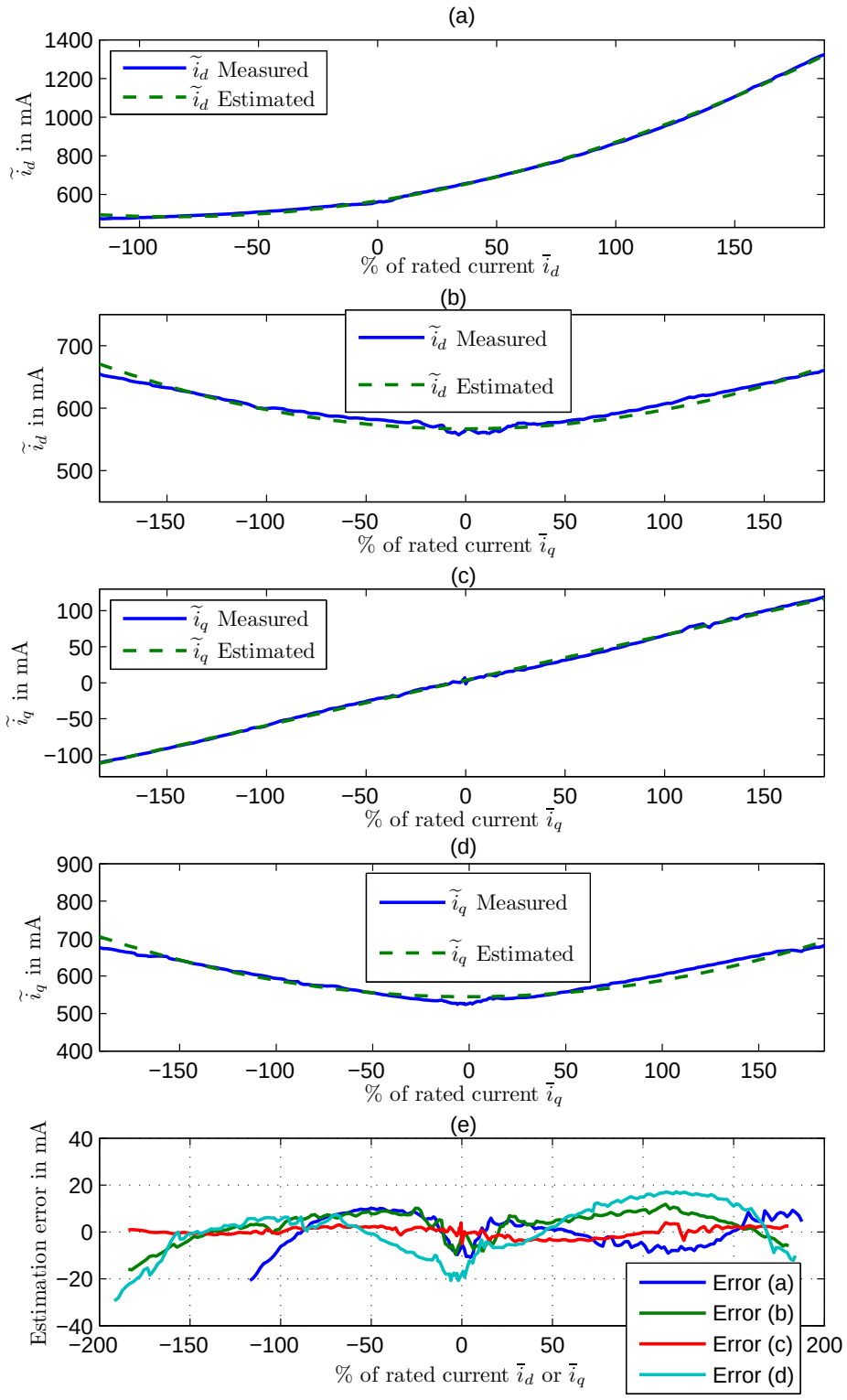

Figure 6.3: SPM motor: fitted values vs measurements for (6.11) in (a); (6.12) in (b); (6.13) in (c); (6.14) in (d); in (e) estimation error corresponding to (a)-(b)-(c)-(d).

Table 6.2: Estimated magnetic parameters of test motors

Motor	IPM	SPM
L_d	9.15 ± 0.26 mH	7.86 ± 0.21 mH
L_q	13.58 ± 0.58 mH	8.18 ± 0.23 mH
$\alpha_{3,0}\ (A.Wb^{-2})$	102.3 ± 0.9	176 ± 1.6
$\alpha_{1,2}\ (A.Wb^{-2})$	93.3 ± 1.2	165.6 ± 2.6
$\alpha_{4,0}\ (A.Wb^{-3})$	329.1 ± 8.1	1254 ± 18
$\alpha_{2,2}\ (A.Wb^{-3})$	497.3 ± 10.4	1907.5 ± 43.4
$\alpha_{0,4}\ (A.Wb^{-3})$	118.6 ± 3	453.5 ± 9.9

Table 6.3: RMSE between measured and fitted data

Motor	IPM	SPM
RMSE for (6.11)	1.5%	0.87%
RMSE for (6.12)	1.58%	1.07%
RMSE for (6.13)	5.8%	3.1%
RMSE for (6.14)	1.1%	1.8%

Table 6.4: Dimensionless saturation parameters of test motors

Motor	IPM	SPM
$\alpha_{3,0}L_d^2 I_n$	0.039	0.056
$\alpha_{1,2}L_d L_q I_n$	0.053	0.055
$\alpha_{4,0}L_d^3 I_n^2$	0.0051	0.0164
$\alpha_{2,2}L_d L_q^2 I_n^2$	0.0171	0.027
$\alpha_{0,4}L_q^3 I_n^2$	0.0060	0.0067

With the rotor locked in the position $\theta := 0$, a square wave voltage with pulsation $\Omega := 2\pi \times 500\,\text{rad/s}$ and constant amplitude $\widetilde{v}_d$ or $\widetilde{v}_q$ (15 V for the IPM, 14 V for the SPM) is applied to the motor. Several runs are performed with various $\overline{v}_d$ (resp. $\overline{v}_q$) such that $\overline{i}_d$ (resp. $\overline{i}_q$) ranges inside the interval -200% to $+200\%$ of the rated current. The current is slowly incremented in order to scan the whole possible working area (the length of the current interval varies according to test conditions). The magnetic parameters are then estimated as explained in the section 6.1.2, yielding the values in the table 6.2. The uncertainty in the estimation stems from a $\pm 15\ mA$ uncertainty in the current measurements.

Fig. 6.2 (IPM motor) and fig 6.3 (SPM motor) show the fitted values of $\widetilde{i}_d$ and $\widetilde{i}_q$ in terms of $\overline{i}_d$ and $\overline{i}_q$ obtained according to (6.11)–(6.14) and using the estimated saturation parameters listed in the table 6.2; these fitted values are compared to the experimental measured values of $\widetilde{i}_d$ and $\widetilde{i}_q$. Fig. 6.2-(a) and fig. 6.3-(a) compare the measured and the fitted values of $\widetilde{i}_d$ which corresponds to (6.11); it is clear in this figure that the model fits well the measurements. This result is similar for fig. 6.2-(b) and 6.3-(b) which correspond to (6.12) and fig. 6.2-(c) and 6.3-(c) which correspond to (6.13) and fig. 6.2-(d) and 6.3-(d) which correspond to (6.14); they demonstrate the good agreement between the fitted curves and the measurements. Notice (6.11) corresponds to saturation on a single axis while (6.13) corresponds to cross-saturation.

The figures 6.2-(b)-(c)-(d) and 6.3-(b)-(c)-(d) show also that the high frequency current amplitudes are always symmetric with respect to $\overline{i}_q$ (they are even functions with respect to $\overline{i}_q$). This results validates the symmetry condition used in (4.122).

Fig. 6.2(e)-6.3(e) show the estimation error between the measured and the fitted values of $\widetilde{i}_d$ and $\widetilde{i}_q$ corresponding to figures 6.2(a)-(b)-(c)-(d) and figures 6.3(a)-(b)-(c)-(d) respectively. These figures show clearly that the estimation errors are less than 15 mA in a large majority of cases, hence these estimation errors are in order of the current measurement uncertainty. To test the quality of interpolation, we calculate the root mean square error $RMSE$ for each cases of (6.11)–(6.14). Table 6.3 shows the RMSE between measured and fitted data; it is always less than 5.8% and it is in most of the cases less than 2%.

We verify the robustness of the model by evaluating the parameter errors caused by measurement uncertainty. Using linear least squares and supposing that we have a measurement uncertainty of 15 mA, we get the parameter uncertainties listed in table 6.2. It is clear that these uncertainties are very small comparing to the parameter values; they are less than 4.3%. This result shows that the magnetic parameters are not sensitive to measurement errors; hence they represent the magnetic behavior of the PMSM.

In (4.134) and (4.135) we assumed that the saturation parameters are small. To verify this assumption, we must use dimensionless parameters. Table 6.4 shows the dimensionless saturation parameters where the rated current I_n and the inductances L_d and L_q are used for parameters normalization. This table shows that the dimensionless parameters are very small comparing to one, which validates the small parameters assumption in (4.134) and (4.135).

Finally, the figures 6.2–6.3 provide an important experimental interpretation of the choice of a quartic function (polynomial of degree four) to express the magnetic energy $\mathcal{H}$ proposed in (4.131). Indeed, these figures show that the measured high frequency current amplitudes $\widetilde{\mathbf{i}}_{dq}$ are quadratic functions of

$$\overline{\mathbf{i}}_{dq} \approx \left[\mathbf{L}^{dq}\right]^{-1} \overline{\mathbf{\Phi}}_{dq},$$

hence

$$\widetilde{\mathbf{i}}_{dq} \approx \mathbf{Q}\left(\overline{\mathbf{\Phi}}_{dq}\right)$$

where $\mathbf{Q}$ is a quadratic function of $\overline{\mathbf{\Phi}}_{dq}$. In addition, using (6.5) we get

$$\widetilde{\mathbf{i}}_{dq} = D\mathcal{I}_{dq}\left(\overline{\mathbf{\Phi}}_{dq}\right)\frac{\widetilde{\mathbf{v}}_{dq}}{\Omega}$$

Thus, the two previous expressions of $\widetilde{\mathbf{i}}_{dq}$ yield

$$D\mathcal{I}_{dq}\left(\overline{\mathbf{\Phi}}_{dq}\right)\frac{\widetilde{\mathbf{v}}_{dq}}{\Omega} = \mathbf{Q}\left(\overline{\mathbf{\Phi}}_{dq}\right).$$

Replacing $D\mathcal{I}_{dq}$ by its expression in (4.144) leads to

$$\begin{pmatrix} \frac{\partial^2\mathcal{H}}{\partial\phi_d{}^2}\left(\overline{\mathbf{\Phi}}_{dq}\right) & \frac{\partial^2\mathcal{H}}{\partial\phi_d\partial\phi_q}\left(\overline{\mathbf{\Phi}}_{dq}\right) \\ \frac{\partial^2\mathcal{H}}{\partial\phi_q\partial\phi_d}\left(\overline{\mathbf{\Phi}}_{dq}\right) & \frac{\partial^2\mathcal{H}}{\partial\phi_q{}^2}\left(\overline{\mathbf{\Phi}}_{dq}\right) \end{pmatrix}\frac{\widetilde{\mathbf{v}}_{dq}}{\Omega} = \mathbf{Q}\left(\overline{\mathbf{\Phi}}_{dq}\right).$$

Hence, all the second order partial derivatives of $\mathcal{H}(\overline{\mathbf{\Phi}}_{dq})$ are quadratic functions of $\overline{\mathbf{\Phi}}_{dq}$ and therefore the energy $\mathcal{H}$ is a quartic (polynomial of degree four) function of the fluxes. Hence, it is not necessary to use terms with degree higher than four in the energy expression, the terms of degree less or equal to four are sufficient to explain the current response when a high frequency voltage is injected to the motor. This result is an experimental validation of the choice of the total magnetic energy expression proposed in (4.131).

The experimental results of parameters estimation discussed in this section validate the proposed saturation model using the interpolation of the experimental data by linear least square. Indeed, they show that the measured high frequency current amplitudes are well explained by the proposed model and the estimation errors are small. To check the validity of the model with non interpolated data, we use in the sequel other combinations of $\bar{i}_d$, $\bar{i}_q$, $\widetilde{v}_d$ and $\widetilde{v}_q$ in (6.7)-(6.8). In addition, we use a step voltage to test the model with another type of input voltage signal.

6.2 Model validation and verification

In the previous section, we proposed a method for estimating the magnetic parameters of the proposed saturation model (4.132)-(4.133). This estimation procedure relies on (6.11)–(6.14), using three special combinations of $\bar{i}_d$, $\bar{i}_q$, $\widetilde{v}_d$ and $\widetilde{v}_q$ as described in section 6.1.2. This method was applied to an IPM motor and a SPM motor where the parameters were estimated from the measured high frequency currents by fitting the values predicted by the model. In this section we verify that the model gives good prediction for the data not used to estimate the saturation parameters, i.e. using other combinations of $\bar{i}_d$, $\bar{i}_q$, $\widetilde{v}_d$ and $\widetilde{v}_q$ than those used to estimate the saturation parameters.

For example, fig. 6.4 shows the experimental and estimated values of $\widetilde{i}_d$ in terms of $\bar{i}_q$ when the total low frequency current is along the q- axis and the high frequency voltage is along the q- axis ($\bar{i}_d := 0$, $\widetilde{v}_d = 0$). This case is similar to (6.14), but the measured high frequency current is $\widetilde{i}_d$ (instead of $\widetilde{i}_q$) which were not used to estimate the saturation parameters. The estimated values of $\widetilde{i}_d$ are obtained using (4.132) where $\bar{i}_d := 0$ and $\widetilde{v}_d = 0$:

$$\widetilde{i}_d = \frac{2\widetilde{v}_q}{\Omega}\alpha_{1,2}L_q\bar{i}_q. \tag{6.15}$$

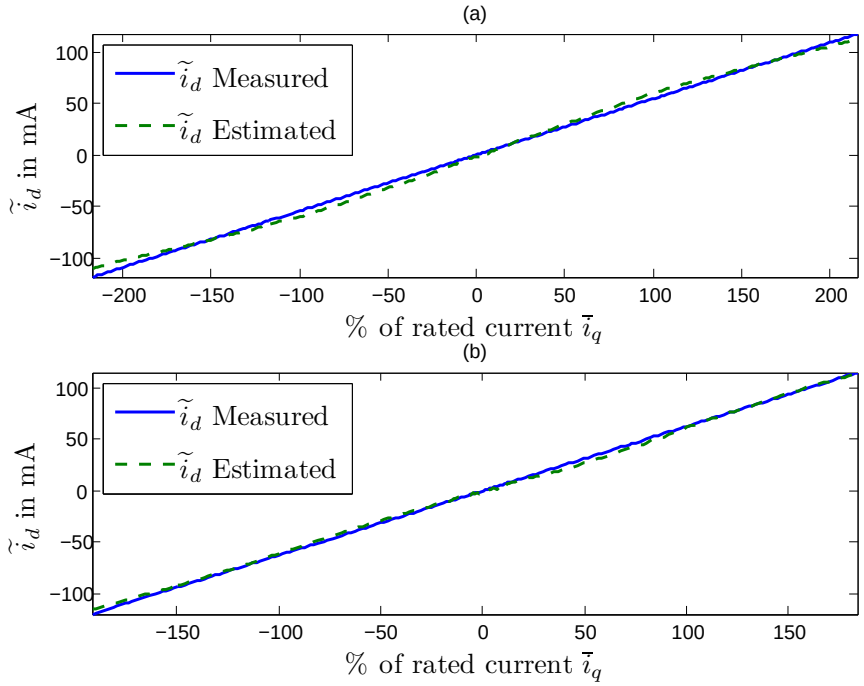

Figure 6.4: Estimated values vs measurements values of $\widetilde{i}_d$ corresponding to (6.15): (a) IPM motor; (b) SPM motor.

This figure shows good accordance between the measured and predicted values of $\widetilde{i}_d$. Thus, the saturation model can predict the values of $\widetilde{i}_d$ in this case. We note that the expression (obtained using the saturation model) of $\widetilde{i}_q$ in (6.13) is the same as the expression (also obtained using the saturation model) of $\widetilde{i}_d$ in (6.15). This result is confirmed experimentally by comparing fig (6.2)-(c) to fig. (6.4)-(a) and fig. (6.3)-(c) to fig. (6.4)-(a).

In addition, to check the validity of the model, tests were conducted with multiple combinations of $\bar{i}_d$ and $\bar{i}_q$ using current vectors with various angles and magnitudes on the whole operating ranges. The current amplitude $|\bar{i}|$ is ranging from 0 to 200% of the rated current with a small increment and the current angle $\arg(i)$ varies from -90 deg to 90 deg (90 deg is sufficient because the motor is symmetric according to q- axis) where $|\bar{i}|$ and $\arg(i)$ are given by

$$|\bar{i}| = \sqrt{\bar{i}_d^2 + \bar{i}_q^2}, \quad \arg(\bar{i}) = \arctan\left(\frac{\bar{i}_q}{\bar{i}_d}\right).$$

Fig. 6.5 shows for instance the estimated and measured values of high frequency current amplitudes $\widetilde{i}_d$ and $\widetilde{i}_q$ in terms of the total low frequency current $|\bar{i}| \times sign(\arg(\bar{i}))$ for the current angles $\arg(\bar{i}) = \pm 30\,\text{deg}, \pm 45\,\text{deg}, \pm 60\,\text{deg}, \pm 75\,\text{deg}$ for the SPM motor (the results of the IPM motor are similar but they are not shown here) with the injection of high frequency voltage along the d- axis i.e. $\widetilde{v}_d = 15\ V$ and $\widetilde{v}_q = 0$. This figure shows a good agreement between the measured values of high frequency currents and those predicted by the model over a wide operation range. This result validates the saturation model at a large number of possible working points.

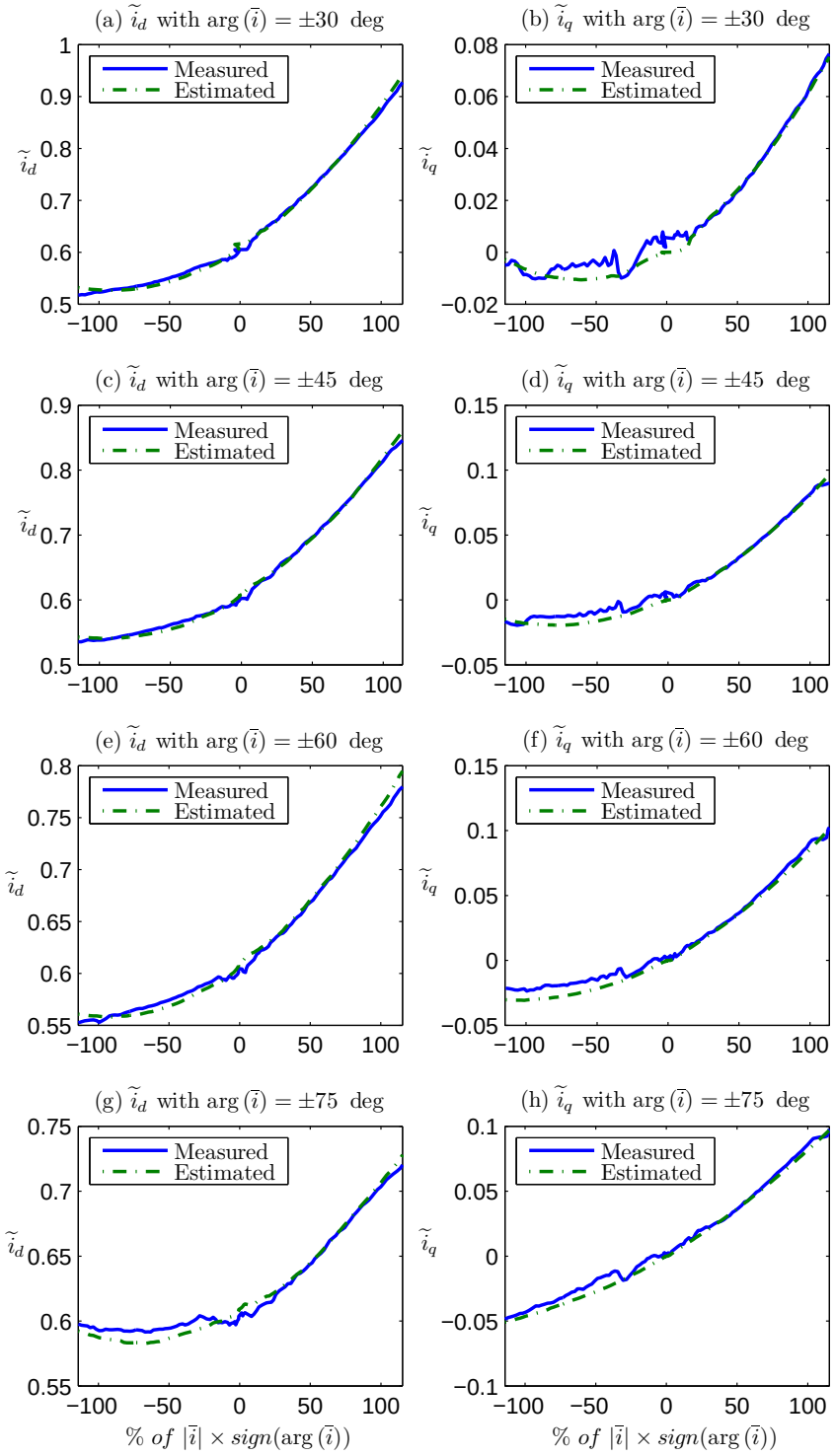

Figure 6.5: Measured values compared to model-predicted (estimated) values of $\widetilde{i}_d$ and $\widetilde{i}_q$ for multiple current angles $\arg(\bar{i})$ with the SPM motor.

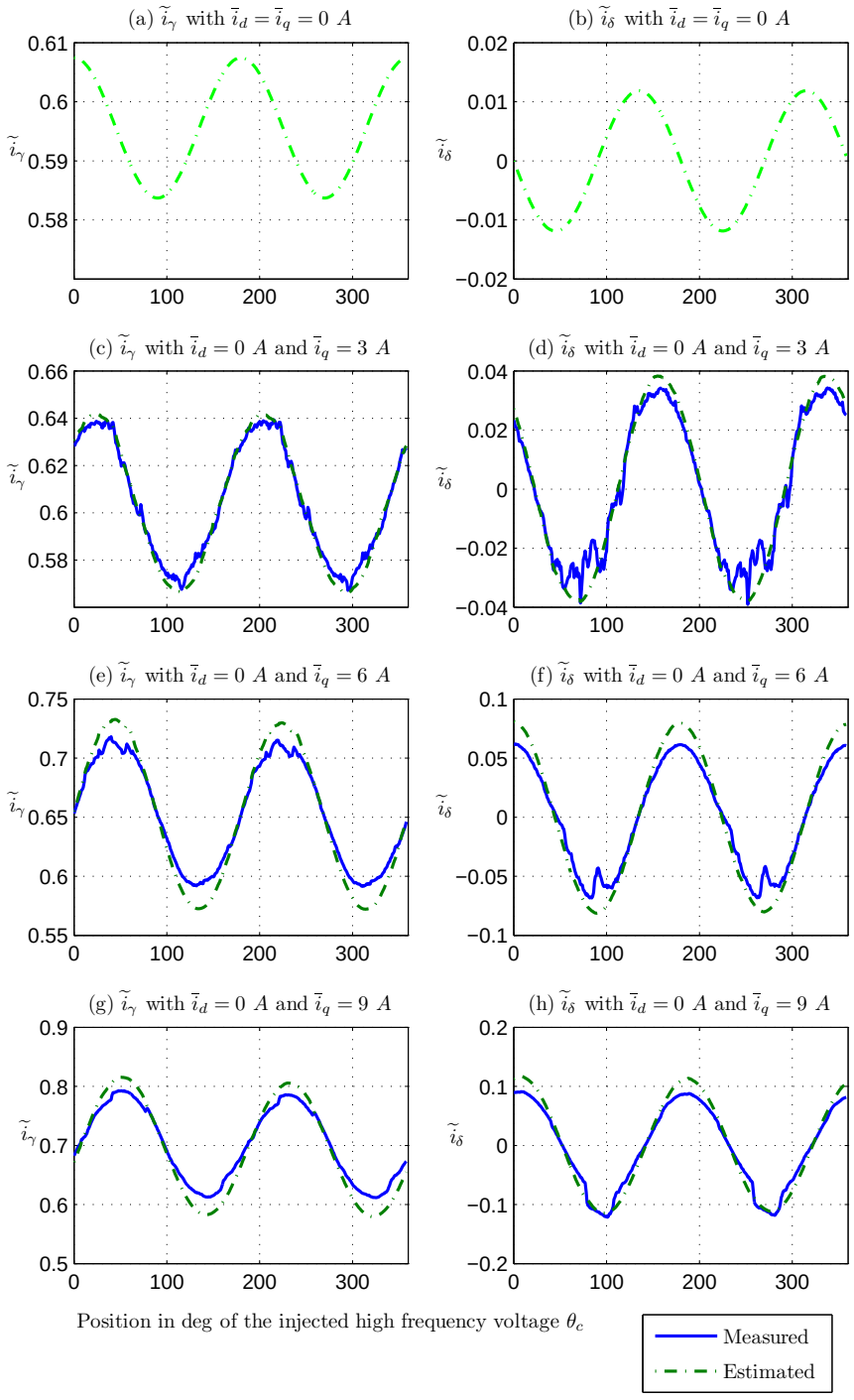

Figure 6.6: Measured values compared to model-predicted (estimated) values of $\widetilde{i}_\gamma$ and $\widetilde{i}_\delta$ for the SPM motor: (a) and (b) $\overline{i}_q = 0$; (c) and (d) $\overline{i}_q = 3$ A; (e) and (f) $\overline{i}_q = 6$ A; (g) and (h) $\overline{i}_q = 9$ A.

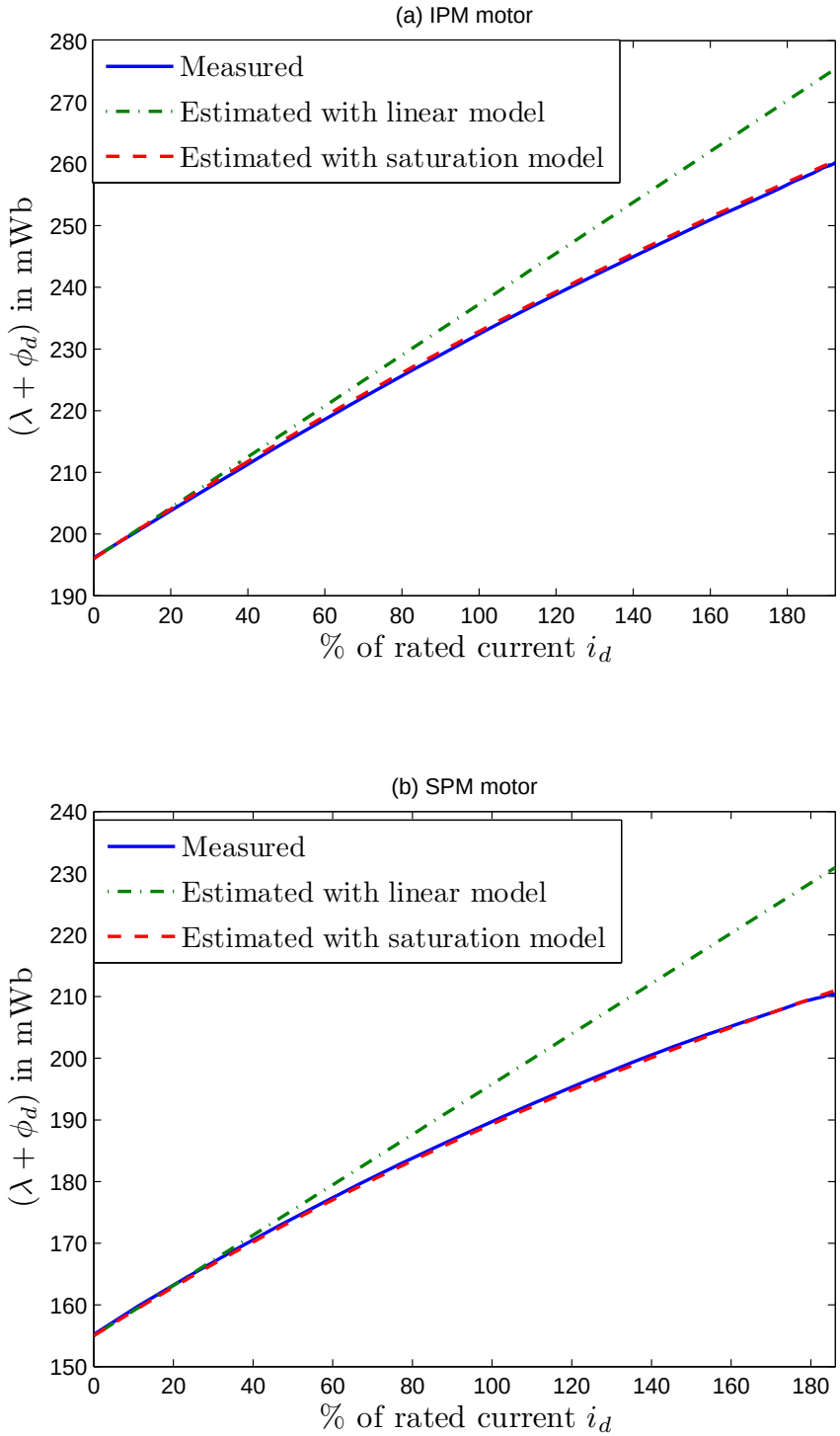

Figure 6.7: Saturation curve $\phi_d - i_d$; measured ϕ_d (dashed line), estimated ϕ_d with saturation model (solid line), estimated ϕ_d without saturation (dash-dot line): (a) IPM motor; (b) SPM motor.

We verify now if the model predicts the dependence of the high frequency current amplitude on the rotor position and if it explains the impact of cross coupling saturation on the motor saliency. To do that, a high frequency voltage is injected on the $\gamma\delta$ reference frame where the angle θ_c is varied from 0 to 360 electrical degree. The rotation of the high frequency voltage permits to scan the saliency of the motor for each possible electrical position. At the same time, constant low frequency currents $\bar{i}_d$ (magnetizing current) and $\bar{i}_q$ (torque current) are applied to the motor in dq frame for setting the saturation level of the motor.

Fig. 6.6 shows the the estimated and measured values of high frequency current amplitudes in $\gamma\delta$ frame $\widetilde{i}_\gamma$ and $\widetilde{i}_\delta$ in terms of θ_c when a high frequency voltage is added along the γ axis ($\widetilde{v}_\gamma = 15$ and $\widetilde{v}_\delta = 0$. The results correspond to the SPM motor (the results of the IPM motor are similar but they are not shown here) where $\bar{i}_q = 0, 3, 6, 9\ A$ (torque current) and $\bar{i}_d = 0$. Firstly, this figure shows a good accordance between model predicted and estimated values of $\widetilde{i}_\gamma$ and $\widetilde{i}_\delta$ for various values of $\bar{i}_q$ which means that the model predicts well the variation of $\widetilde{i}_\gamma$ and $\widetilde{i}_\delta$ with the rotor position.

Secondly, fig. 6.6 illustrates clearly the effect of cross saturation. Indeed, $\widetilde{i}_\gamma$ and $\widetilde{i}_\delta$ are sinusoidal functions of θ_c with period $180\ \text{deg}$; the amplitudes and phases of these sinusoidal functions vary with the intensity of the current $\bar{i}_q$ (which is nearly proportional to the motor load torque). The figures 6.6-(a)-(c)-(e)-(g) show the variation of $\widetilde{i}_\gamma$ with $\bar{i}_q$; we see in these figures that the maximum and minimum of $\widetilde{i}_\gamma$ (which define the saliency position) are shifted with $\bar{i}_q$. Furthermore, the figures 6.6-(b)-(d)-(f)-(h) show the variation of $\widetilde{i}_\delta$ with $\bar{i}_q$; we see in these figures that the zeros of $\widetilde{i}_\delta$ (which define also the saliency position) are shifted with $\bar{i}_q$. Thus, the saliency position is shifted due to cross saturation; and therefore the saturation effects must be compensated to get a good estimation of the rotor position.

As a kind of cross-validation we also examined the current time responses to a large voltage step. At locked rotor, a large voltage step is applied to the motor d- axis voltage as follows

$$v_d(t) = \begin{cases} v_{step} & \text{if} \quad t \geq 0 \\ 0 & \text{if} \quad t < 0 \end{cases}$$

where v_{step} is a constant voltage. In this case, the flux expression can be written as

$$\phi_d(t) = \int_0^t \big(v_{step} - R i_d(\tau)\big) d\tau.$$

Fig. 6.7 shows the good agreement also between the "measured" values of ϕ_d and values obtained by simulation of ϕ_d for the IPM motor and SPM motor. This is an interesting cross validation result because the step voltage contain low and high frequency components. Thus, the saturation model can explain the motor behavior also using general signals.

In this first part, the saturation model was validated via various type of voltage signal and using different scenarios. The impact of the saturation on the relation between the high frequency signals and the rotor position is pointed out where it is clear that saturation effects must be considered to estimate the rotor position. In the sequel we propose a validation procedure of the position estimation method proposed in the previous chapter. Firstly, we focus on the position estimation method without using a speed controller i.e. by using only a V/f law. Secondly, we test and validate the sensorless control low speed law proposed in the previous chapter.

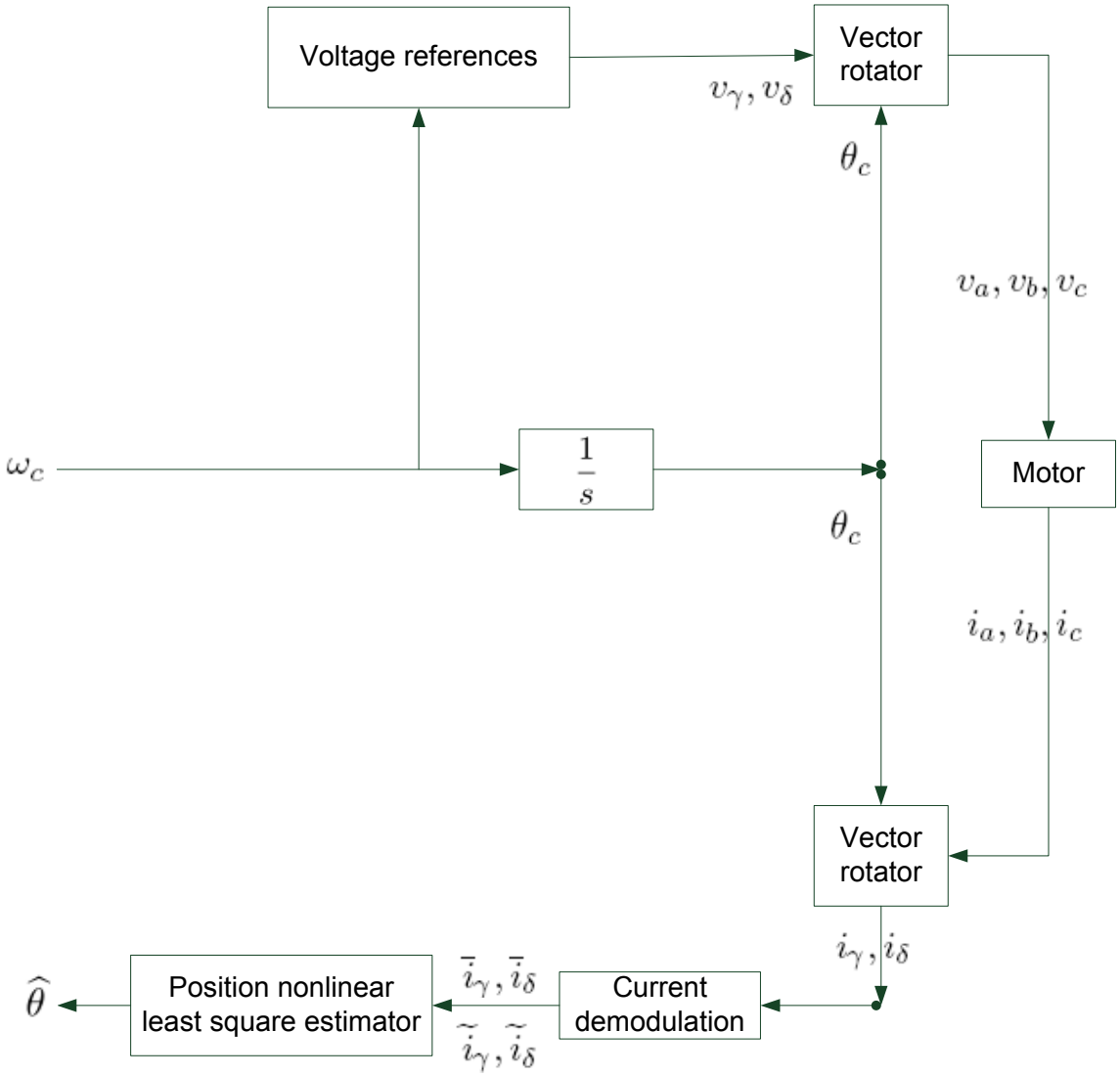

Figure 6.8: Bloc diagram of the proposed V/f control scheme.

6.3 Experimental validation of position estimation procedure

After the experimental validation of the saturation model, we present in this section experimental test and validation of the position estimation procedure proposed in the section 5.3.2 of the chapter 5.

The relevance of the position estimation methodology developed in the section 5.3.2 was tested on two types of motors, an Interior Magnet PMSM (IPM) and a Surface-Mounted PMSM (SPM), with rated parameters and saturation parameters listed in the tables 6.1 and 6.2 . Since the goal in this section is only to test the validity of the angle estimation procedure, a very simple V/f fully open-loop is used; the test with complete sensorless speed control law is presented in the next section. The control law proposed in (5.37)–(5.42) is used where Ω_c and $\mathcal{U}_{\gamma\delta}$ do not depend on $\mathbf{i}_{\gamma\delta}$; a fast-varying square voltage with pulsation $\Omega := 2\pi \times 500$ rad/s and with constant amplitude is added in accordance

with (5.43), resulting in

$$\begin{aligned}\frac{d\theta_c}{dt} &= \omega_c(t)\\ \mathbf{v}_{\gamma\delta} &= \mathbf{u}^{rd}_{\gamma\delta}(t) + \omega_c(t)\mathbf{\Phi}_m + \widetilde{\mathbf{v}}_{\gamma\delta} f(\Omega t).\end{aligned}$$

where

- $\omega_c(t)$ is the motor speed reference
- $\mathbf{u}^{rd}_{\gamma\delta}(t)$ is a filtered piece-wise constant vector compensating the resistive voltage drop in order to maintain the torque level and the motor stability
- the high frequency voltage is added only to the γ- axis voltage such that $\widetilde{\mathbf{v}}_{\gamma\delta} := (\widetilde{v}, 0)^T$ with $\widetilde{v} := 15\,\text{V}$.

Fig. 6.8 shows the bloc diagram of he proposed V/f control scheme.

6.3.1 Test benchmark

During the experimental tests, the speed and the load torque of the motor are changed over a period of 210 seconds; the speed remains between $\pm 5\%$ of the rated speed and the torque varies from 0% to 180% of the rated torque. More precisely, the sequence of speed reference and torque load used in the experimental tests are described as follows

- *Initialization phase*: at first, the rotor position is initialized at $\theta = 0$ where the torque and speed are set to zero during this phase.
- *Speed step at zero torque*: after few seconds of initialization, the speed is increased suddenly from 0 to a low speed value at zero load torque; then the motor is running at this constant low speed. This phase is used to test the dynamic behavior of the position estimator with respect to a fast speed variation.
- *Torque step at low speed*: the load torque is increased rapidly from 0 to a high level (greater than rated torque), this is done at the constant low speed settled in the previous phase. This phase is used to test the dynamic behavior of the position estimator with respect to a fast torque variation.
- *Slow speed reversal at high load torque*: the motor speed is slowly reversed at high load torque; the motor speed remains close to zero a large period of time (about 10 sec or 20 sec). After this phase, the motor speed is negative and motor torque has a high positive value, hence the machine switches from the motor mode to the generator mode at low speed and a high torque. The static behavior of the estimator is tested in this case; the motor states remain close to the region defined by $\omega = 0$ where the position is difficult to estimate.
- *Speed variation from negative low value to zero at high load torque*: the speed is changed from its previous negative low value to zero at the previous high load torque. This is a dynamic test where the speed is changed at a high load torque.

- *Torque step from a high value to zero at zero speed*: this is a dynamic test where the torque is decreased rapidly from its previous high level to zero at zero speed.

- *Torque step from zero to a high value at zero speed*: this is also a dynamic test where the torque is increased rapidly from zero to a high level at zero speed.

- *Speed variation from zero to a low value at high load torque*: the speed is changed from zero to a low value at the previous high load torque. This is also a dynamic test where the speed is changed at a high load torque.

- *Sequential torque steps*: In this phase, the speed is maintained constant at its previous low value and the load torque is changed using multiple sequential steps.

The phases described previously represent a benchmark which is used is the sequel to test the position estimator and the sensorless speed control law. This benchmark represents typical operation conditions at low speed and at high load torque. Fig. 6.9 shows an example of speed and torque profiles used to realize this benchmark.

6.3.2 Results

The rotor position $\widehat{\theta}$ is estimated according to (5.84) where the value of

$$\arg \min_{\mu \in]-\pi,\pi]} \left[\mathcal{M}(\mu, \bar{\mathbf{i}}_{\gamma\delta}, \widetilde{\mathbf{i}}_{\gamma\delta}) \right]$$

is calculated using a nonlinear recursive estimation algorithm as described in (5.85)–(5.87). As explained in the section 5.3.3, the position $\widehat{\theta}_n = \widehat{\theta}(nT_s)$ is estimated at each discrete time $t = nT_s$ as follows

$$\widehat{\theta}_n = \theta_c(nT_s) + \widehat{\mu}_n. \tag{6.16}$$

To solve (5.87), $\widehat{\mu}_n$ is initialized at $n = 0$ by $\widehat{\mu}_0 = \widehat{\mu}(0) = 0$ and the rotor position θ is initialized by $\theta = 0$ also. In addition we take the sampling time equal to $T_s = T = \frac{2\pi}{\Omega} = 2\ ms$ (one period of the high frequency voltage), $\rho = 450\ Hz$ and $\epsilon = 10^{-6}\ A^4.rad^{-4}$.

Fig. 6.10 and 6.11 show experimental results when the load and speed sequences of the benchmark described previously are applied to the IPM and SPM motors respectively. Fig. 6.10-(a) and 6.11-(a) compare the measured position $\mu = \theta - \theta_c$ (blue line) to the estimated position $\widehat{\mu} = \widehat{\theta} - \theta_c$ obtained using (5.87) with saturation model (green line) and without saturation model (red line). It is clear from these two figures that when the saturation model is used the agreement between the estimated position and the measured position is very good, with an error always smaller than a few (electrical) degrees. By contrast, the estimation error without using the saturation model (i.e. with all the magnetic saturation parameters α_{ij} taken to zero) can reach up to $40°$ for the IPM and $70°$ the SPM in particular at high load torque level. This demonstrates the importance of considering an adequate saturation model including in particular cross-saturation. Thanks to the saturation model, we note that the position $\theta - \theta_c$ is estimated even at large angle values (up to hundred degrees) which is not possible using a linear saturation model.

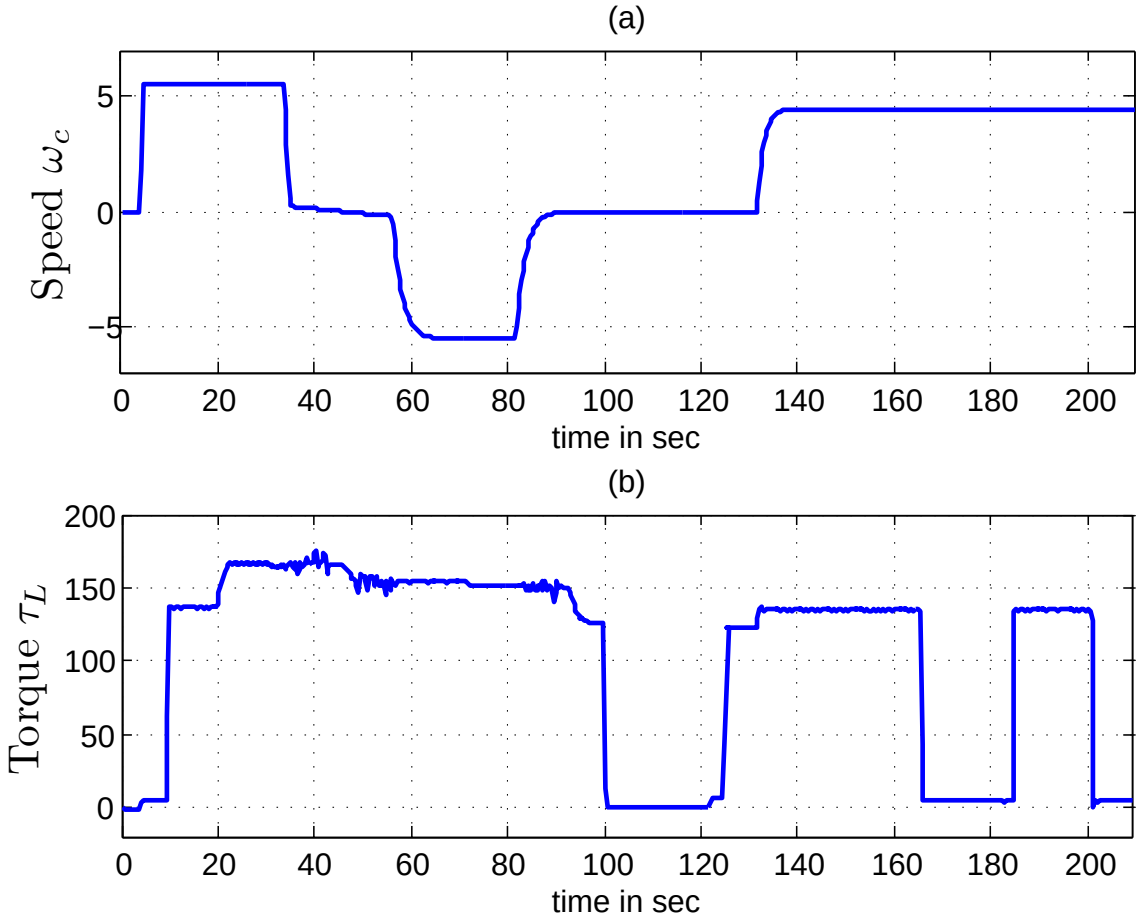

Figure 6.9: Experimental tests: (a) reference speed ω_c; (b) applied load torque τ_L.

Slow speed reversal: to test the proposed position estimation method near zero speed, the motor speed is slowly inverted between 35 s and 55 s (of the benchmark test) at approximatively 150% of the rated torque. This is a very demanding test since the motor always remains in the poor observability region, moreover under high load. Once again the estimated angle closely agrees with the measured angle.

Load steps: the load is suddenly changed from 0% to approximatively 100% of the rated torque (in the benchmark test) while the motor is at rest (around $t = 125\ s$) or is running at low speed (around $t = 185\ s$). Fig. 6.14–6.17 illustrate the quality of the estimation under the high dynamic torque conditions. They show that the estimated rotor position follow the measured position when a high dynamic torque variation occurs at a very short time (between $40\ ms$ and $80\ ms$ only).

In this section we presented experimental results which validates the estimation of the rotor position at low speed by recursive nonlinear least squares. The magnetic saturation model proposed in (4.132)–(4.133) was used to compensate nonlinear magnetic and cross coupling effects. This validation was done using a V/f fully open loop control law where the focus was on the position esti-

mation and not on the speed control. In the next section, we propose a complete low speed sensorless control law of PMSM where this procedure is used at real time in a speed and position estimator inside a global sensorless control law. The values of the controller parameters for each motor are listed in the table 6.5. These parameters are adjusted by simulations and experimentally where the essential condition of time scale separation (5.111) is respected. The values of the remaining parameters of the controller are obtained from 5.2.

6.4 Validation of the sensorless law

In the previous section we validated the rotor position estimation procedure even when the difference is large between the position θ_c of $\gamma\delta$ frame and the position θ of dq frame. In this section, we present an experimental validation of the sensorless control law proposed in section 5.4 of chapter 5. The tests are carried out on the IPM and SPM motors used in previous section having parameters listed in the tables 6.1 and 6.2. The current measurements are sampled at the frequency $f_s = \frac{1}{Ts} = 4\ kHz$. The controller sampling frequency is also $4\ kHz$. The pulsation of the injected high frequency voltage is $\Omega = 2\pi \times 500\ rad.s^{-1}$. The gradient descent gain Λ is chosen equal to the controller sampling frequency f_s divided by the mean value of $\frac{\partial^2 \mathcal{M}}{\partial \mu^2}$ which is equal to $\frac{1}{5}$ for IPM motor and $\frac{1}{8}$ for SPM motor.

Table 6.5: Parameter values of the sensorless low speed controller for the IPM and SPM motors

Description	IPM motor	SPM motor
Bandwidth (Hz) of the current controller	$f_i = 100$	$f_i = 80$
Damping factor of the current controller	$\xi_i = 0.75$	$\xi_i = 0.8$
Bandwidth (Hz) of the position estimator	$f_\theta = 20$	$f_\theta = 11$
Damping factor of the position estimator	$\xi_\theta = 0.75$	$\xi_\theta = 0.8$
Bandwidth (Hz) of the speed controller	$f_\omega = 4$	$f_\omega = 3$
Damping factor of the speed controller	$\xi_\omega = 0.75$	$\xi_\omega = 0.8$
Cutoff frequency (Hz) of the current filter	$f_i^f = 180$	$f_i^f = 140$
Cutoff frequency (Hz) of the high frequency current filter	$f_{\widetilde{i}} = 300$	$f_{\widetilde{i}} = 300$
Cutoff frequency (Hz) of the speed filter	$f_\omega^f = 50$	$f_\omega^f = 50$
Cutoff frequency (Hz) of the reference current filter	$f_i^r = 50$	$f_i^r = 50$
Amplitude (V) of the injected high frequency voltage	$\widetilde{v} = 15$	$\widetilde{v} = 15$
Gradient descent gain ($rad^2.A^{-2}.s^{-1}$)	$\Lambda = 5f_s$	$\Lambda = 8f_s$

6.4.1 IPM motor case

The IPM motor has a high level of geometric saliency where the difference between the inductances L_d and L_q is relatively high; according to the table 6.2, for IPM motor we have

$$L_d = 9.15\ mH, \quad L_q = 13.58\ mH, \quad |L_d - L_q| = 4.43\ mH = 48.41\% \text{ of } L_d.$$

The high saliency level of this motor facilitates the low speed control by high frequency voltage injection. Indeed, in this case current measurement noises and power stage voltage losses have small effects on the estimated rotor position. However, at high load torque, the saturation and cross coupling effects must be compensated to get acceptable performances of speed control.

Fig. 6.18 shows the experimental results when the speed and torque reference of the test benchmark defined previously are applied to the IPM motor. The blue curve in fig. 6.18-(a) illustrates the position error obtained when the saturation model is used to estimate the rotor position as explained in (5.112); and the green curve in fig. 6.18-(a) illustrates the position error obtained when the standard method is used to estimate the rotor position as explained in (5.26). It is clear in this figure that the compensation of the saturation effects reduce significatively the rotor position estimation error mainly at high load torque where the error is reduced from nearly 35 electrical degree (without saturation compensation) to less than 5 electrical degree with saturation compensation. This result validates the proposed sensorless control law for IPM with the proposed position estimation procedure.

6.4.2 SPM motor case

The SPM motor has a low level of geometric saliency where the difference between the inductances L_d and L_q is relatively low; according to the table 6.2, for SPM motor we have

$$L_d = 7.86\ mH, \quad L_q = 8.18\ mH, \quad |L_d - L_q| = 0.32\ mH = 4\% \text{ of } L_d.$$

The low saliency level of this motor complicates the low speed control by high frequency voltage injection. Indeed, at high load torque or at high magnetizing current the saturation and cross coupling effects introduce large errors on the estimated rotor position when the linear model is used. Furthermore; these effects reduce the saliency level and can even destroy it. In addition, in this case, current measurement noises and power stage voltage losses introduce large noises on the estimated high frequency currents which highly disturb the estimated position. Therefore, the saturation effects must inevitably be compensated to control the SPM motor at low speed using high frequency voltage injection.

Fig. 6.19 shows experimental results of the SPM motor when the saturation effects are not compensated i.e. the equation (5.26) instead of (5.112) is used to estimate the rotor position. The speed and torque reference used in this test are the first three phases of the benchmark proposed in 6.3: initialization phase; speed step at zero torque; torque step at low speed. It is clear in this figure that the controller and motor loose the stability when the load is increased (at $t = 10.17\ s$). Even when the load is slowly increased, the controller does not stabilize the motor. The reason is that at $t = 10.17$ the position estimation error increases up to -37 deg and the rotor saliency becomes very small. Thus, for this SPM motor, the standard sensorless controller can not be used when is load torque is greater than 54% of the rated torque. The solution is to use the sensorless control law with compensation of the saturation effects using (5.112).

Fig. 6.20 shows the experimental results when the speed and torque reference of the test benchmark defined previously are applied to the SPM motor. It is clear in this figure that the compensation of the saturation effects reduce significatively the rotor position estimation error mainly at high load torque to less than 10 electrical degree. This is an important result: the compensation of the saturation makes it possible to control the SPM motor and reduce the position estimation error to less than 10 electrical degree; which was not possible with standard method of sensorless control as shown in fig. 6.19.

The results presented in this section validate the proposed low speed sensorless control law for the SPM and IPM motors. The position estimation error is reduced to 5 electrical degree in the case of the IPM motor and to 10 electrical degree in the case of the SPM motor.

Conclusion

A simple identification procedure based on high frequency voltage injection of the magnetic saturation model (4.132)-(4.133) parameters has been proposed in this chapter. Experimental tests on two kinds of PMSM (IPM and SPM) demonstrate the relevance of this method. In addition, the position estimation procedure was validated and the sensorless control law based on it was successfully applied to the IPM motor and the SPM motor having little geometric saliency.

The experimental results show that by using the proposed saturation model, the position estimation errors drop to less than 5 electrical degree for the IPM motor and to less than 10 electrical degree for the SPM motor. We show that the last motor cannot be controlled at low speed and high torque without compensating the saturation effects. In this chapter, we presented important experimental results which validate the energy based modeling of PMSM proposed in the chapter 4 and the PMSM position estimation procedure based on second order averaging proposed in chapter 5.

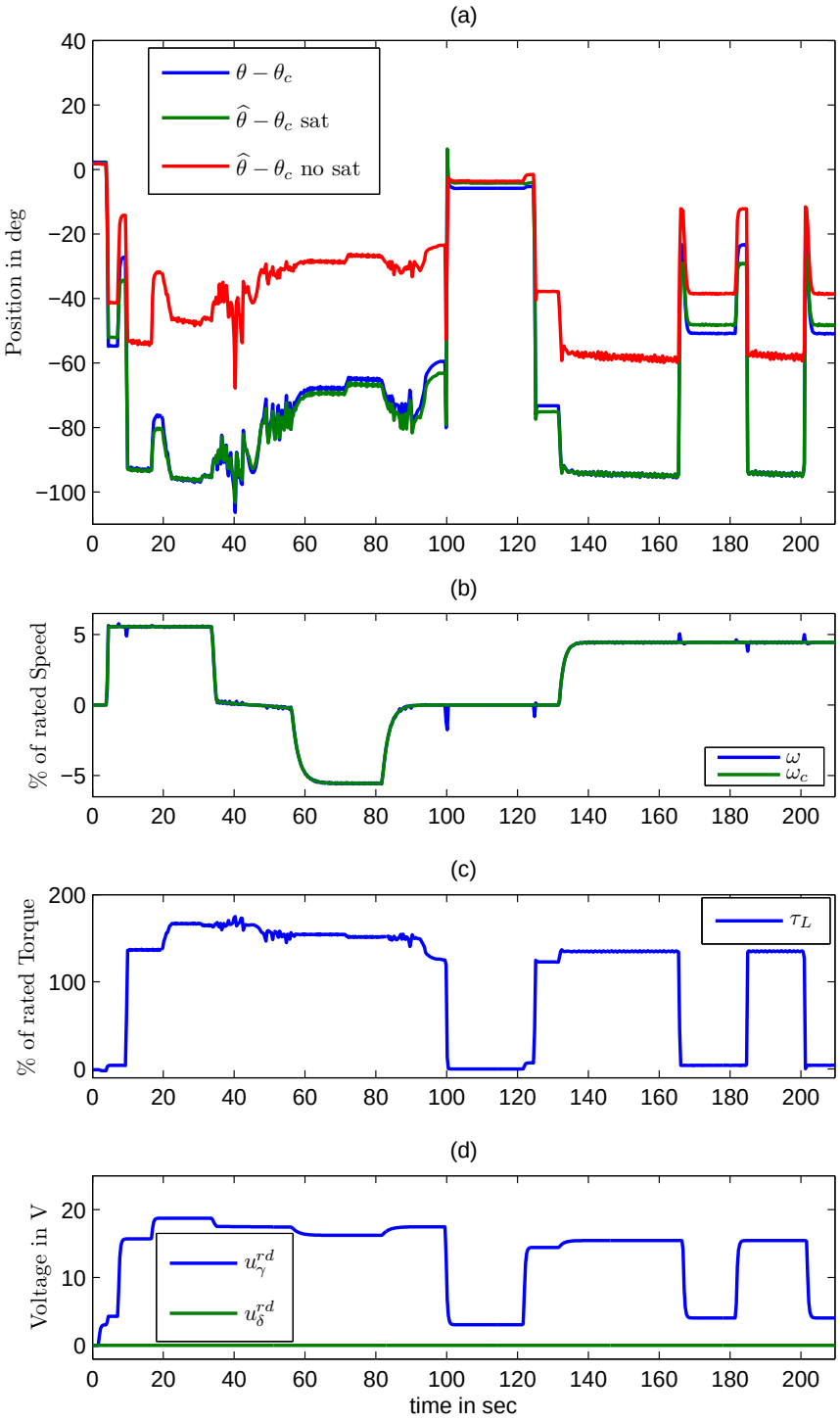

Figure 6.10: Benchmark test for IPM: (a) measured $\theta - \theta_c$ (blue line), estimated $\widehat{\theta} - \theta_c$ with saturation compensation (green line) and without saturation compensation using linear model (red line); (b) measured speed ω (blue line), reference speed ω_c (green line) (c) load torque τ_L; (d) voltages $u_{\gamma\delta}^{rd}$

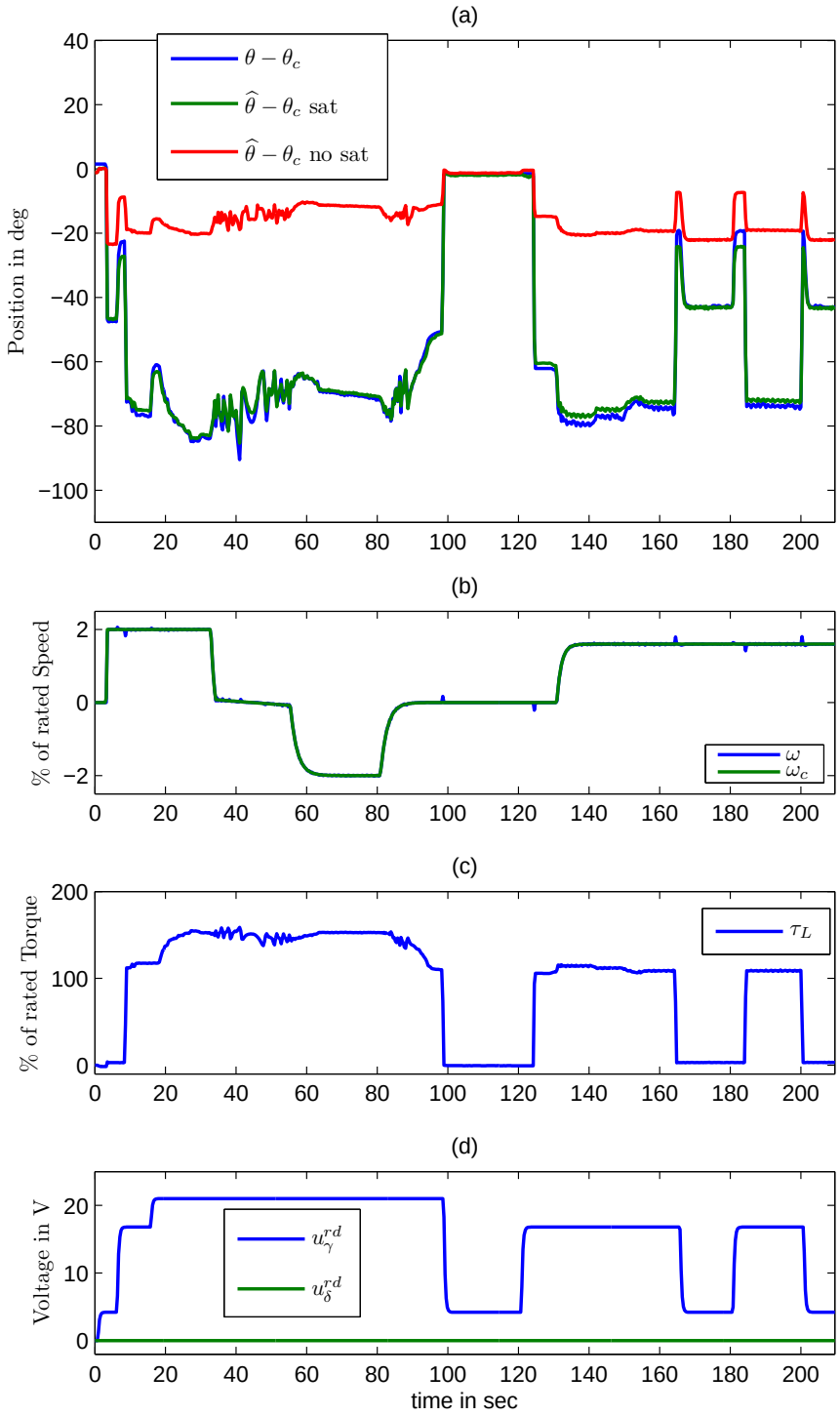

Figure 6.11: Benchmark test for SPM: (a) measured $\theta - \theta_c$ (blue line), estimated $\widehat{\theta} - \theta_c$ with saturation compensation (green line) and without saturation compensation using linear model (red line); (b) measured speed ω (blue line), reference speed ω_c (green line) (c) load torque τ_L; (d) voltages $u_{\gamma\delta}^{rd}$

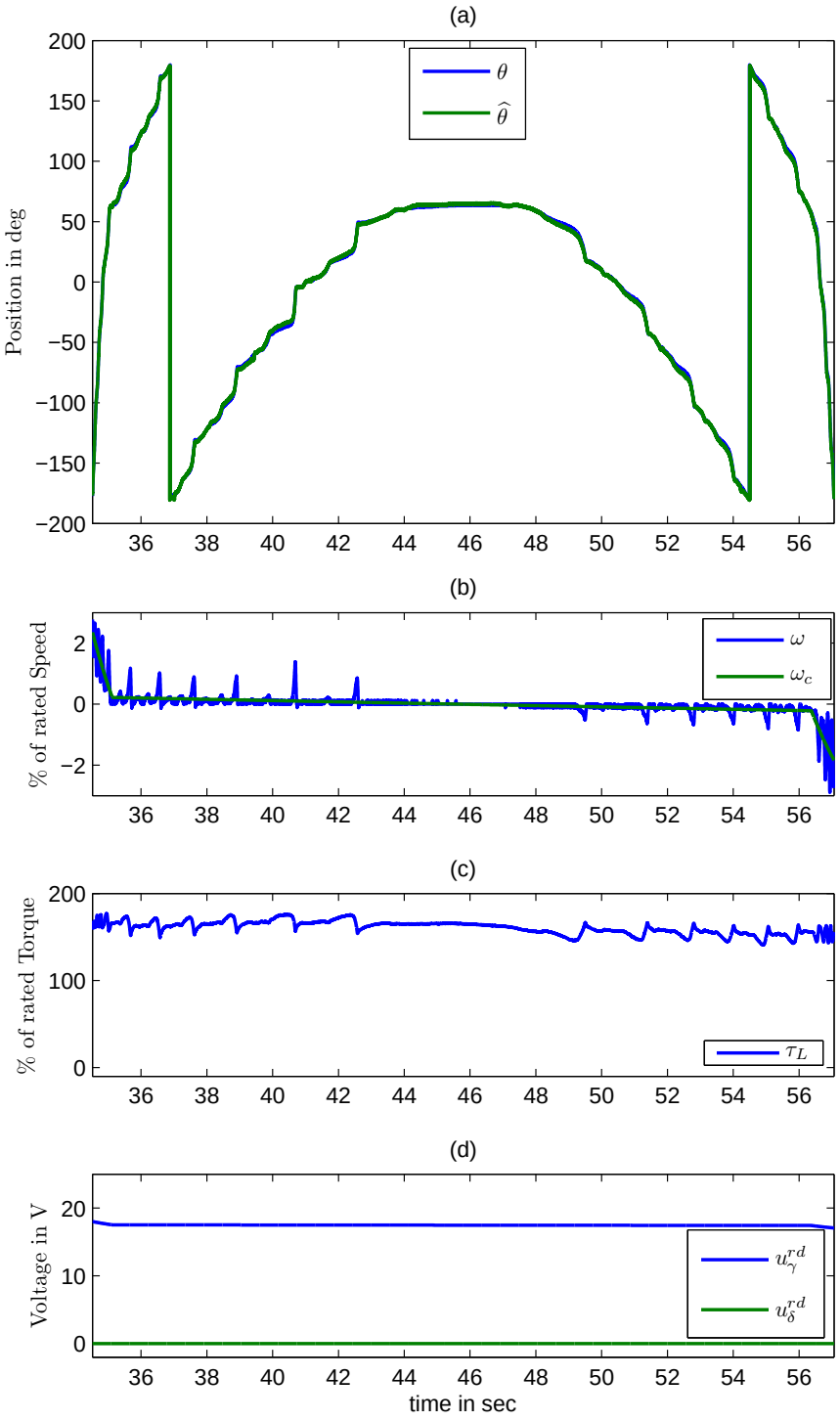

Figure 6.12: Slow speed reversal for IPM: (a) measured θ (blue line), estimated $\widehat{\theta}$ (green line); (b) measured speed ω (blue line), reference speed ω_c (green line); (c) load torque τ_L; (d) voltages $u_{\gamma\delta}^{rd}$

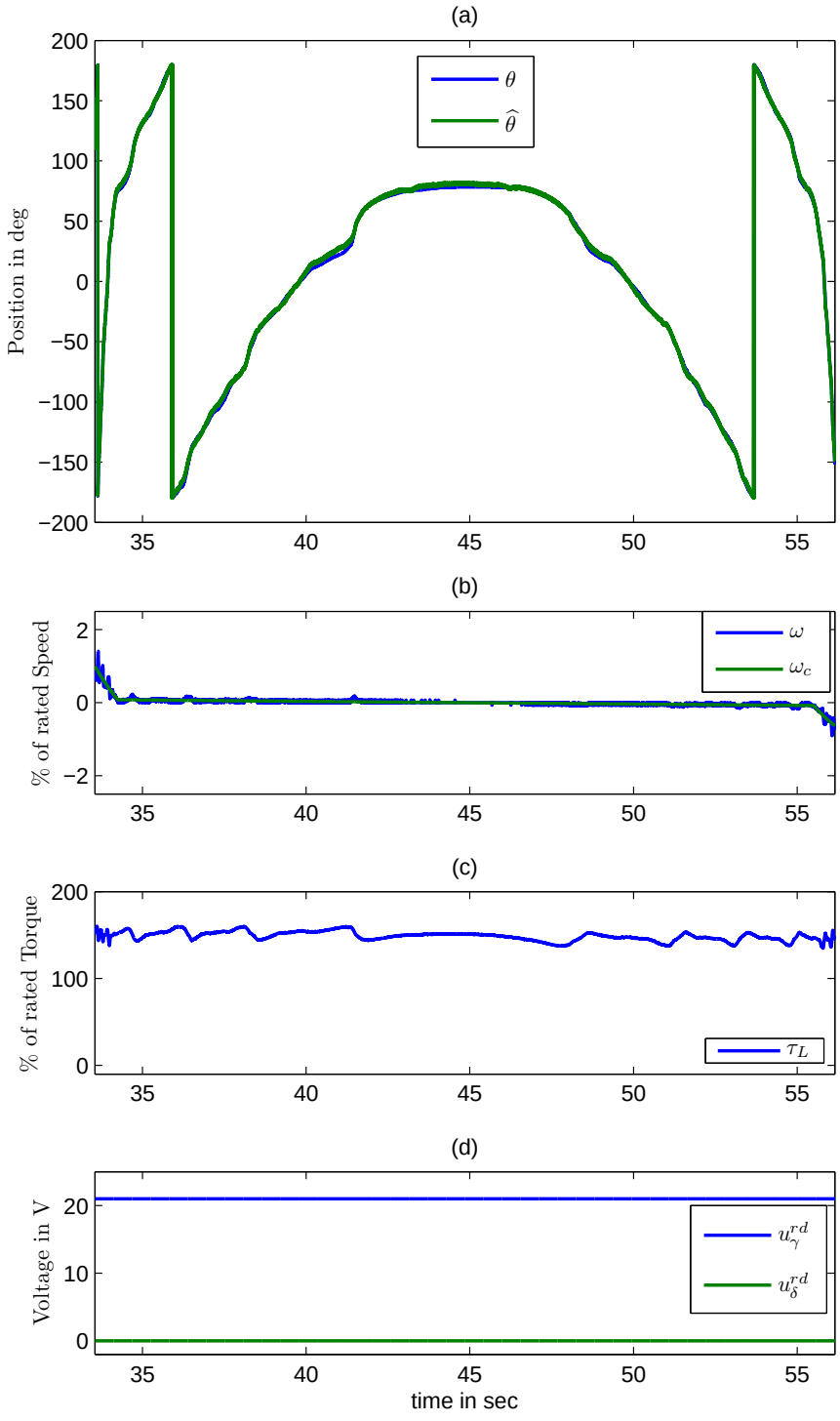

Figure 6.13: Slow speed reversal for SPM: (a) measured θ (blue line), estimated $\widehat{\theta}$ (green line); (b) measured speed ω (blue line), reference speed ω_c (green line); (c) load torque τ_L; (d) voltages $u_{\gamma\delta}^{rd}$

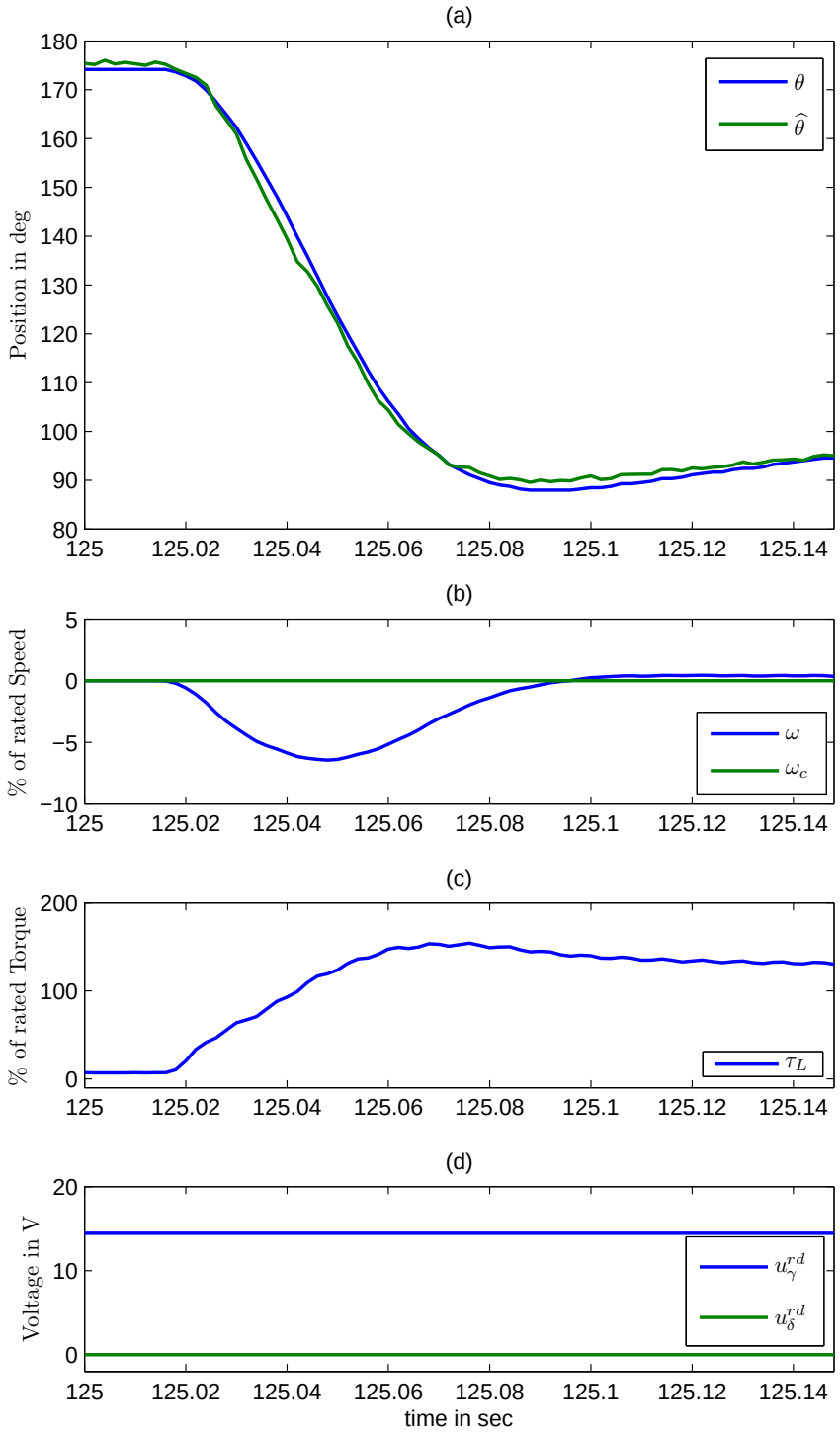

Figure 6.14: Load step at zero speed for IPM: (a) measured θ (blue line), estimated $\widehat{\theta}$ (green line); (b) measured speed ω (blue line), reference speed ω_c (green line); (c) load torque τ_L; (d) voltages $u_{\gamma\delta}^{rd}$

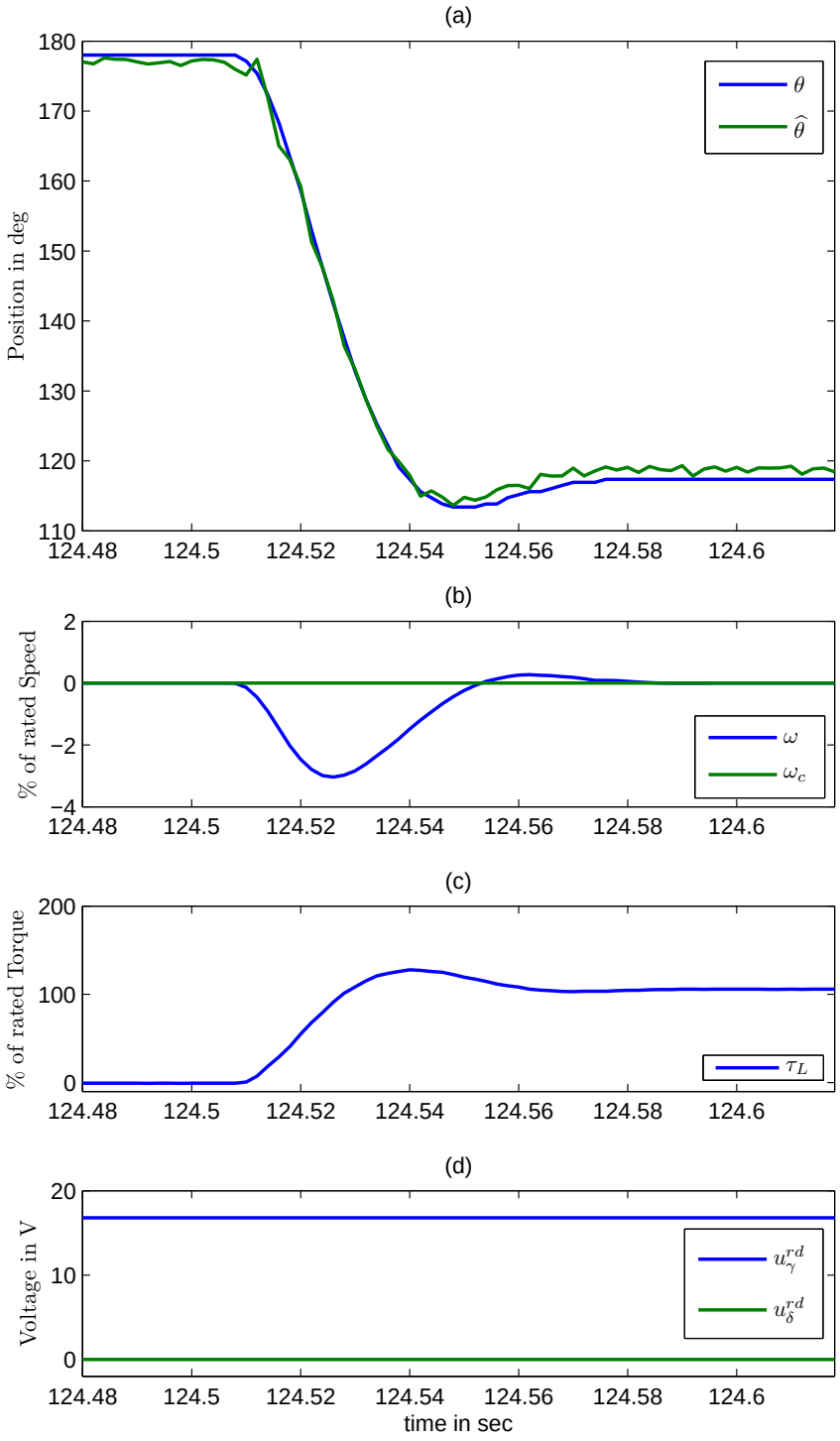

Figure 6.15: Load step at zero speed for SPM: (a) measured θ (blue line), estimated $\widehat{\theta}$ (green line); (b) measured speed ω (blue line), reference speed ω_c (green line); (c) load torque τ_L; (d) voltages $u_{\gamma\delta}^{rd}$

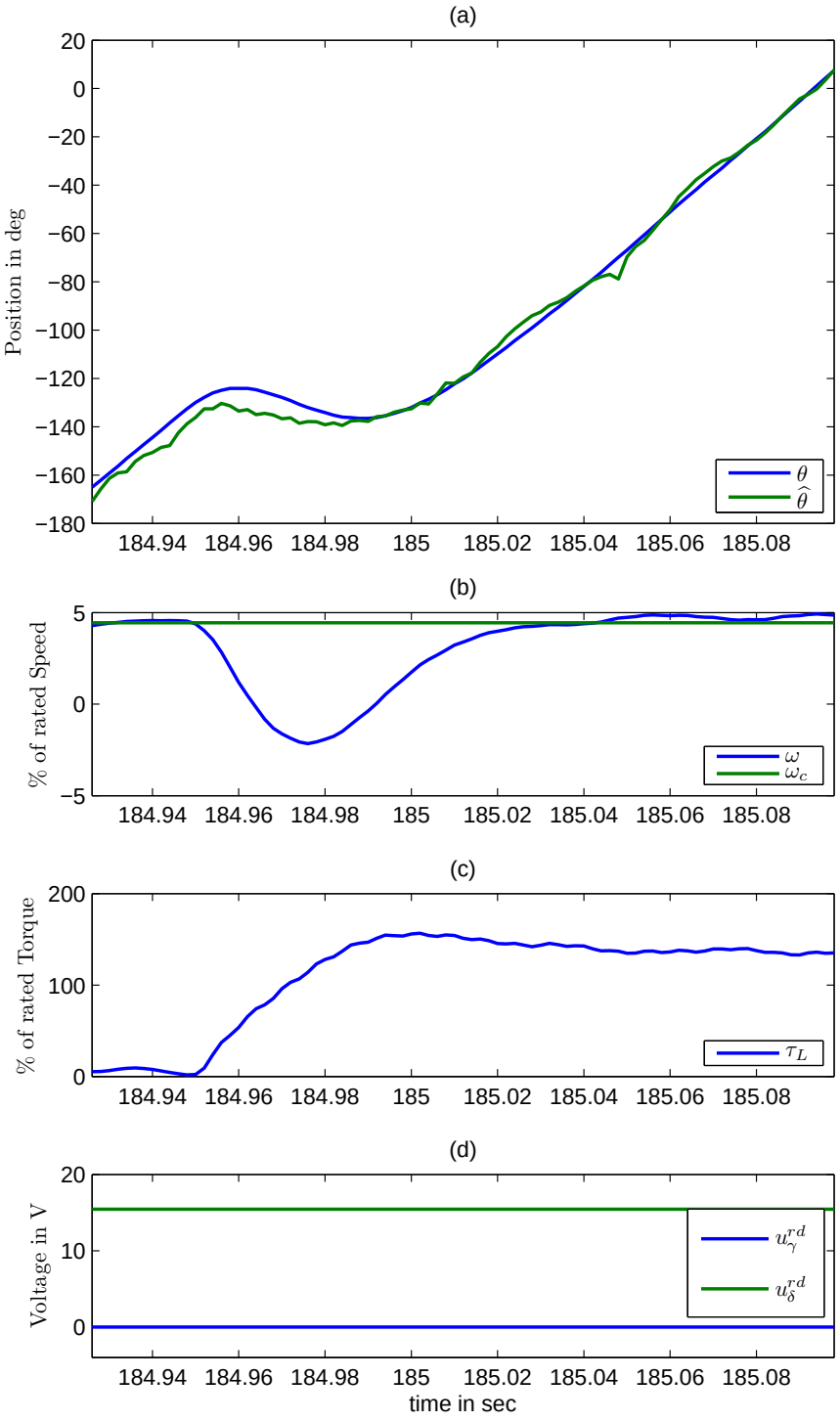

Figure 6.16: Load step at low speed for IPM: (a) measured θ (blue line), estimated $\widehat{\theta}$ (green line); (b) measured speed ω (blue line), reference speed ω_c (green line); (c) load torque τ_L; (d) voltages $u_{\gamma\delta}^{rd}$

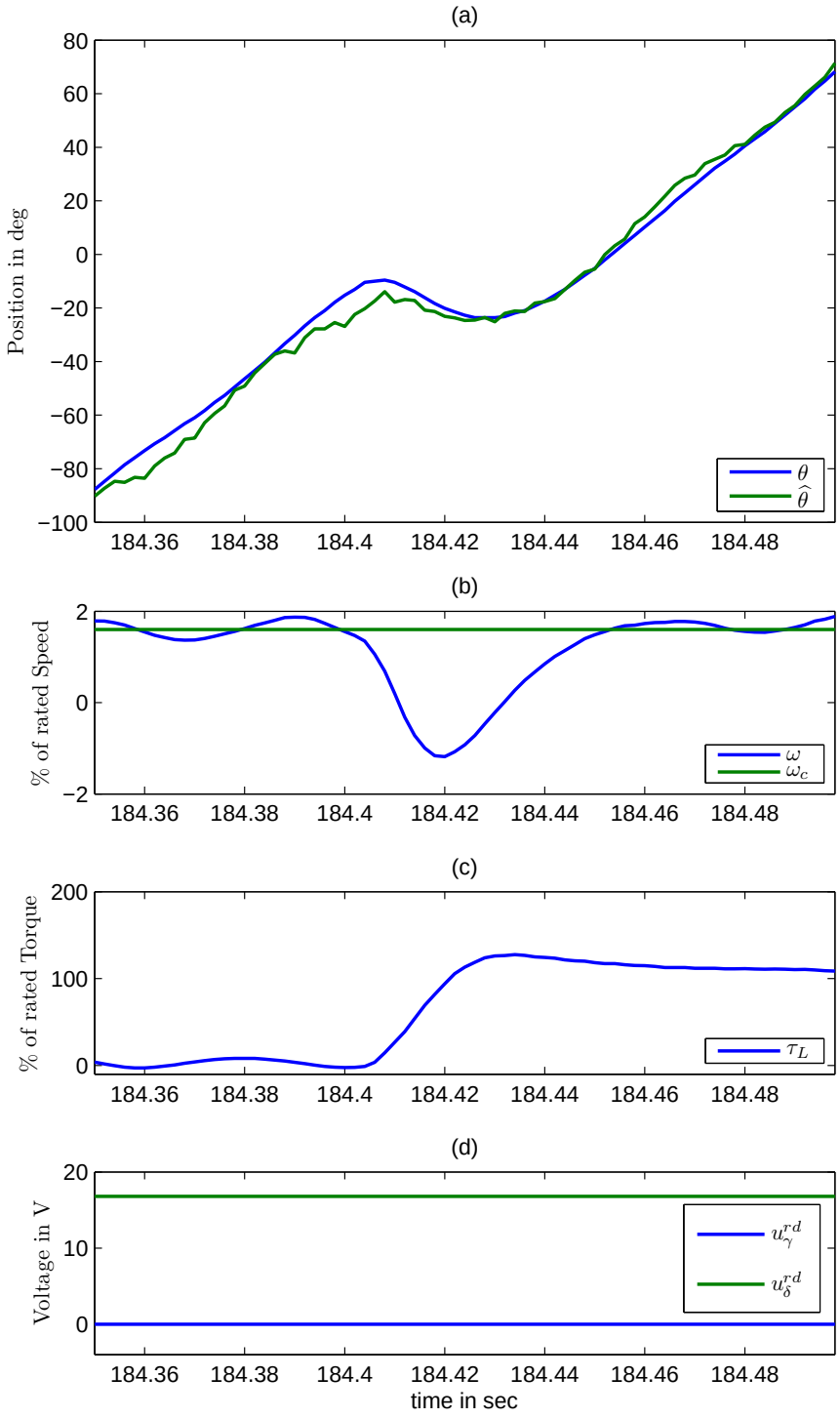

Figure 6.17: Load step at low speed for SPM: (a) measured θ (blue line), estimated $\widehat{\theta}$ (green line); (b) measured speed ω (blue line), reference speed ω_c (green line); (c) load torque τ_L; (d) voltages $u_{\gamma\delta}^{rd}$

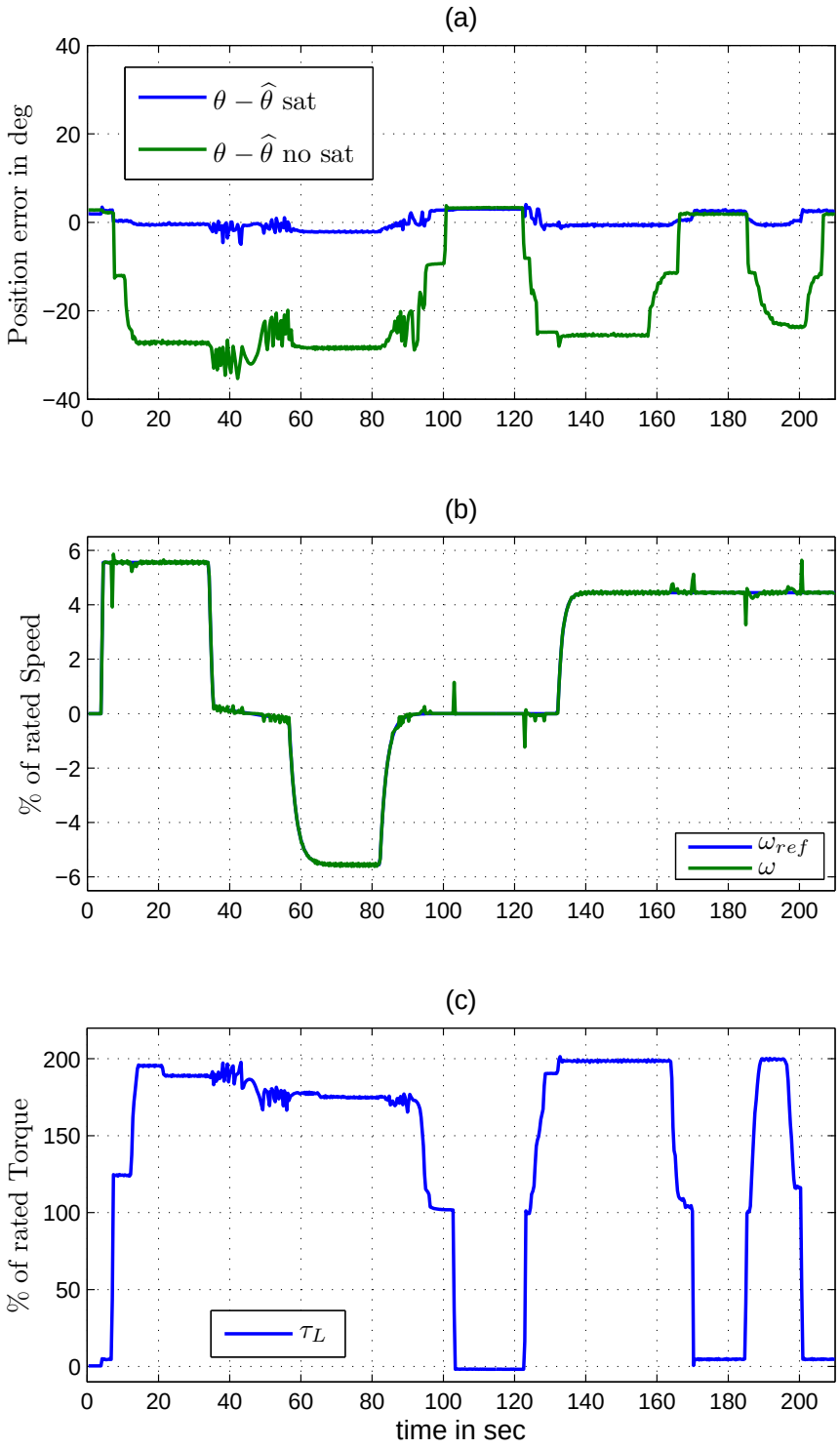

Figure 6.18: Benchmark test for IPM with sensorless control law: (a) position error $\theta - \widehat{\theta}$ with saturation compensation (blue line), position error $\theta - \widehat{\theta}$ without saturation compensation (green line); (b) measured speed ω (blue line), reference speed ω^{ref} (green line); (c) load torque τ_L.

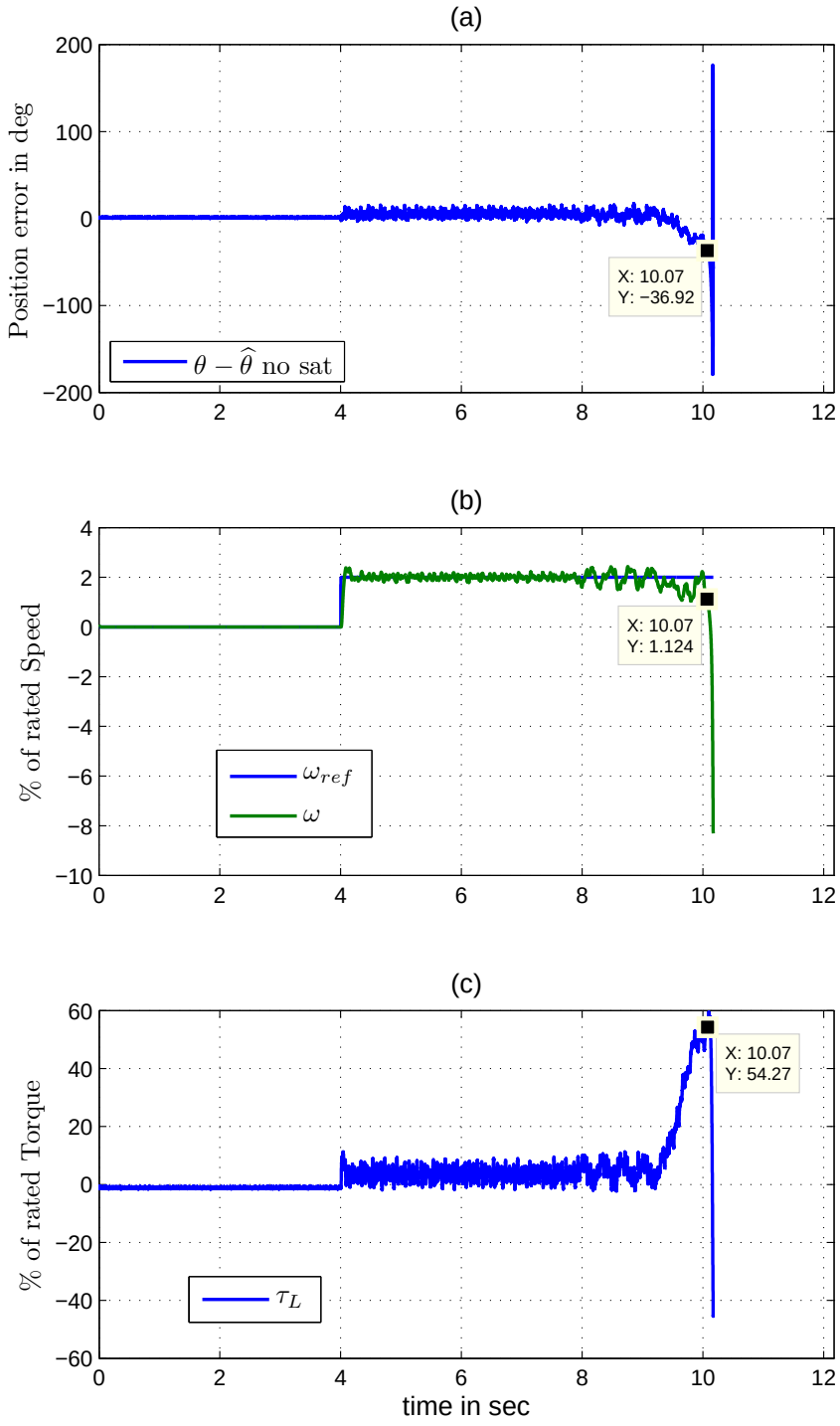

Figure 6.19: Experimental result for SPM with sensorless control law and without saturation compensation: (a) position error $\theta - \widehat{\theta}$ without saturation compensation; (b) measured speed ω (blue line), reference speed ω^{ref} (green line); (c) load torque τ_L.

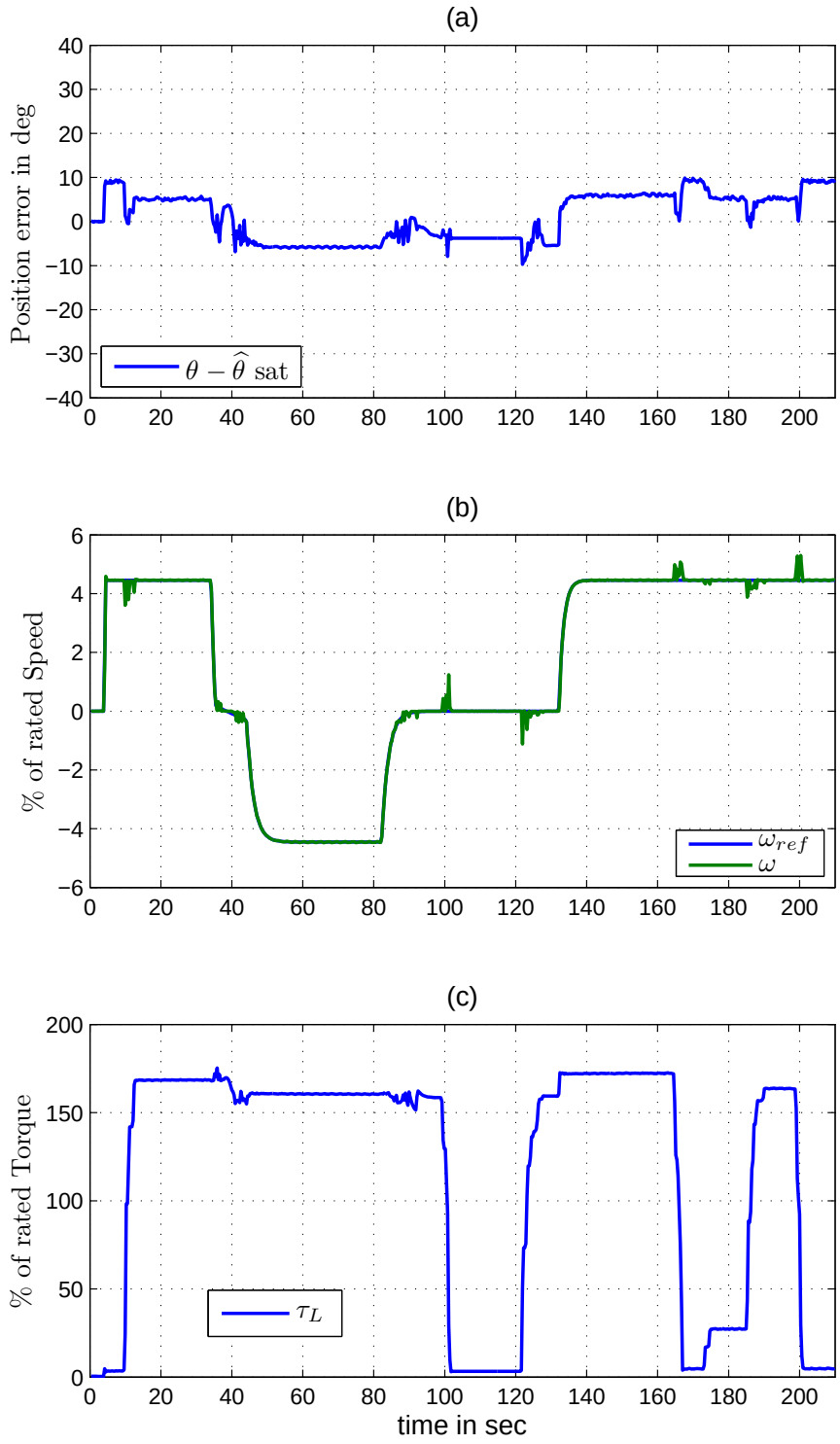

Figure 6.20: Benchmark test for SPM with sensorless control law and with saturation compensation: (a) position error $\theta - \widehat{\theta}$ with saturation compensation; (b) measured speed ω (blue line), reference speed ω^{ref} (green line); (c) load torque τ_L.

Chapter 7

Conclusion

Dans ce travail, nous avons proposé un modèle de saturation magnétique du moteur MSAP ainsi qu'un observateur de position à basse vitesse et sans capteur par l'injection de signaux en utilisant ce modèle. Cet observateur est basé sur l'injection de tension à haute fréquence. Les effets de la saturation sont compensés pour obtenir des estimations précises de position en temps réel pour contrôler la vitesse du moteur. Le concept de modélisation par l'énergie a été utilisé pour la modélisation du MSAP saturé. Les dynamiques du système, y compris les effets non linéaires de la saturation magnétique, ont été représentées simplement par une énergie polynomiale de degré quatre qui ne dépend que de cinq paramètres de saturation (grâce aux symétries géométriques du moteur). Ensuite, les équations de moteur sont obtenues à partir de cette fonction d'énergie en utilisant la formulation Hamiltonienne. Les paramètres de saturation sont estimés par moindres carrés linéaires.

Ensuite, une méthode d'estimation de position est proposée et validée en utilisant ce modèle de saturation et l'injection de signaux. Nous avons proposé une analyse originale basée sur la moyennisation de second ordre du système du moteur avec injection de signaux hautes fréquences (HF). Nous avons présenté une interprétation mathématique claire, basée sur la moyennisation, de la séparation entre le système basse fréquence et le système haute fréquence du moteur. En utilisant la moyennisation, nous avons donné une relation explicite entre la position du rotor et le courant HF. Cette relation n'est pas linéaire et elle dépend des paramètres de saturation. Enfin, la position est estimée par moindres carrés non linéaires récursives à partir du courant HF.

Le modèle proposé du MSAP ainsi que l'estimateur de position ont été testés et validés sur deux moteurs (MSAI et MSAS). Les tests expérimentaux montrent une bonne performance de cet estimateur. Les erreurs d'estimation sont petites (quelques degrés électriques). Cette méthode peut être utilisée avec n'importe quel type du MSAP même avec des moteurs ayant une très faible saillance comme le moteur MSAS utilisé dans ce travail.

Pour la suite de ces travaux, certaines améliorations seront possibles:

- *le but de ce travail était seulement de montrer la validité de la procédure proposée d'estimation de position. Mais, pour une utilisation simple et une mise en œuvre pratique, l'estimateur de position par moindres carrés non-linéaires récursifs peut être amélioré et remplacé par un simple observateur (basé sur la relation entre le courant HF et la position) avec moins de calculs. Par exemple, il existe dans la literature d'autres types d'observateurs [110, 111]*
- *le rotor a été bloqué (par un frein) pour estimer les paramètres de saturation du moteur.*

Mais, pour un usage industriel pratique, il est important de trouver une autre méthode pour l'estimation des paramètres sans l'utilisation d'un tel frein mécanique.

Enfin, cette modélisation énergétique du moteur électrique et la moyennisation du second ordre peuvent être également utilisées pour les moteurs asynchrones où la saillance géométrique est très faible et quasi inexistante. Pour ce type de moteur, la prise en compte de la saturation magnétique est inévitable pour élaborer un contrôleur sans capteur à basse vitesse où la saillance magnétique est incontournable pour estimer la position et l'amplitude du flux magnétique du rotor.

In this work, we proposed a magnetic saturation model of PMSM and a low speed sensorless position observer based on this model. This observer is based on high frequency voltage injection. The saturation effects are compensated to get accurate position estimations in real time that can be used for speed control.

The energy modeling concept was used for saturated PMSM modeling. The system dynamics including nonlinear saturation effects were represented by a simple polynomial energy function of fourth degree depending on five saturation parameters thanks to construction symmetries. Then, the motor equations are obtained from this energy using Hamiltonian formulation. The saturation parameters are estimated by simple linear least square.

Then, a position estimation method is proposed and validated using this saturation model and signal injection. We proposed an original analysis of the motor system with HF signal injection based on second order averaging. A mathematical interpretation based on averaging of the separation between low frequency motor system and HF system was given. And, an explicit relation between the motor position and HF currents is obtained by averaging also. This relation is nonlinear and it depends on the saturation parameters. Finally, the position is estimated by recursive nonlinear least squares using this relation.

The PMSM model and position observer were tested and validated on two types of PMSM (IPM and SPM). Experimental tests show good performance. The estimation errors are small (few electrical degrees). This method can be used with any type of PMSM even with motors having extremely low geometric saliency as the SPM motor considered here.

In the future, some improvements are possible:

- the goal here was to show the effectiveness of the proposed estimation procedure only. But, for easier use and implementation, the nonlinear least square position observer used here can be improved and substituted by a simpler observer with less computations. For example, other types of observers exist in the literature [110, 111]

- the rotor was locked to estimate the motor saturation parameters. But, for industrial use, it is important to find a method for saturation parameter estimations without using a brake.

Finally, such energy based modeling of electric motor and the second order averaging may be used also for asynchronous motors where the geometric saliency is very small and almost nonexistent. For this type of motor, the consideration of magnetic saturation is crucial to design a sensorless low speed controller where the magnetic saliency is essential to track the rotor flux position and amplitude.

Bibliography

[1] T. Sebastian, G. Slemon, and M. Rahman, "Modelling of permanent magnet synchronous motors," *IEEE Transactions on Magnetics*, vol. 22, no. 5, pp. 1069–1071, September 1986.

[2] P. Pillay and R. Krishnan, "Modeling of permanent magnet motor drives," *IEEE Transactions on Industrial Electronics*, vol. 35, no. 4, pp. 537–541, 1988.

[3] P. C. Krause, O. Wasynczuk, and S. D. Sudhoff, *Analysis of Electric Machinery and Drive Systems*, 2nd ed. Wiley-IEEE Press, March 2002.

[4] A. Proca, A. Keyhani, A. El-Antably, W. Lu, and M. Dai, "Analytical model for permanent magnet motors with surface mounted magnets," *IEEE Transactions on Energy Conversion*, vol. 18, no. 3, pp. 386–391, 2003.

[5] T. M. Jahns, G. B. Kliman, and T. W. Neumann, "Interior permanent-magnet synchronous motors for adjustable-speed drives," *IEEE Transactions on Industry Applications*, vol. IA-22, no. 4, pp. 738–747, 1986.

[6] S.-K. Sul, *Control of Electric Machine Drive Systems*. Wiley-IEEE Press, February 2011.

[7] P. Chandana Perera, F. Blaabjerg, J. Pedersen, and P. Thøgersen, "A sensorless, stable v/f control method for permanent-magnet synchronous motor drives," *IEEE Transactions on Industry Applications*, vol. 39, no. 3, pp. 783–791, 2003.

[8] P. Jansen and R. Lorenz, "Transducerless position and velocity estimation in induction and salient AC machines," *IEEE Trans. Industry Applications*, vol. 31, pp. 240–247, 1995.

[9] L. Idkhajine, E. Monmasson, M. Naouar, A. Prata, and K. Bouallaga, "Fully integrated fpga-based controller for synchronous motor drive," *IEEE Transactions on Industrial Electronics*, vol. 56, no. 10, pp. 4006–4017, 2009.

[10] R. Wu and G. R. Slemon, "A permanent magnet motor drive without a shaft sensor," *IEEE Transactions on Industry Applications*, vol. 27, no. 5, pp. 1005–1011, 1991.

[11] A. Consoli, F. Russo, G. Scarcella, and A. Testa, "Low- and zero-speed sensorless control of synchronous reluctance motors," *IEEE Transactions on Industry Applications*, vol. 35, no. 5, pp. 1050–1057, 1999.

[12] B.-H. Bae, S.-K. Sul, J.-H. Kwon, and J.-S. Byeon, "Implementation of sensorless vector control for super-high-speed PMSM of turbo-compressor," *IEEE Transactions on Industry Applications*, vol. 39, no. 3, pp. 811–818, 2003.

[13] L. Zhong, M. Rahman, W. Hu, and K. Lim, "Analysis of direct torque control in permanent magnet synchronous motor drives," *IEEE Transactions on Power Electronics*, vol. 12, no. 3, pp. 528–536, 1997.

[14] I.-C. Baik, K.-H. Kim, and M.-J. Youn, "Robust nonlinear speed control of PM synchronous motor using boundary layer integral sliding mode control technique," *IEEE Transactions on Control Systems Technology*, vol. 8, no. 1, pp. 47–54, 2000.

[15] M. Ezzat, J. De Leon, N. Gonzalez, and A. Glumineau, "Observer-controller scheme using high order sliding mode techniques for sensorless speed control of permanent magnet synchronous motor," in *Proceedings of the IEEE Conference on Decision and Control*, 2010, pp. 4012–4017.

[16] Z. Chen, M. Tomita, S. Doki, and S. Okuma, "An extended electromotive force model for sensorless control of interior permanent-magnet synchronous motors," *IEEE Transactions on Industrial Electronics*, vol. 50, no. 2, pp. 288–295, 2003.

[17] J.-K. Seok, J.-K. Lee, and D.-C. Lee, "Sensorless speed control of nonsalient permanent-magnet synchronous motor using rotor-position-tracking pi controller," *IEEE Transactions on Industrial Electronics*, vol. 53, no. 2, pp. 399–405, 2006.

[18] S. Bolognani, R. Oboe, and M. Zigliotto, "Sensorless full-digital PMSM drive with ekf estimation of speed and rotor position," *IEEE Transactions on Industrial Electronics*, vol. 46, no. 1, pp. 184–191, 1999.

[19] P. Vaclavek and P. Blaha, "Synchronous machine drive observability analysis for sensorless control design," in *Proceedings of the IEEE International Conference on Control Applications*, 2007, pp. 1113–1117.

[20] D. Zaltni, M. Abdelkrim, M. Ghanes, and J. Barbot, "Observability analysis of PMSM," in *3rd International Conference on Signals, Circuits and Systems, SCS 2009*, 2009, pp. –.

[21] D. Basic, F. Malrait, and P. Rouchon, "Euler-Lagrange models with complex currents of three-phase electrical machines and observability issues," *IEEE Trans. Automatic Control*, vol. 55, pp. 212–217, 2010.

[22] C. Ortega, A. Arias, C. Caruana, C. Staines, J. Balcells, and J. Cilia, "Sensorless direct torque control of a surface mounted PMSM using high frequency injection," in *IEEE International Symposium on Industrial Electronics*, vol. 3, 2006, pp. 2332–2337.

[23] G. Foo and M. Rahman, "Sensorless sliding-mode MTPA control of an IPM synchronous motor drive using a sliding-mode observer and HF signal injection," *IEEE Trans. Industrial Electronics*, vol. 57, no. 4, pp. 1270–1278, 2010.

[24] M. Corley and R. Lorenz, "Rotor position and velocity estimation for a salient-pole permanent magnet synchronous machine at standstill and high speeds," *IEEE Trans. Industry Applications*, vol. 34, pp. 784–789, 1998.

[25] L. Wang and R. D. Lorenz, "Rotor position estimation for permanent magnet synchronous motor using saliency-tracking self-sensing method," in *Conference Record - IAS Annual Meeting (IEEE Industry Applications Society)*, vol. 1, 2000, pp. 445–450.

[26] H. Kim and R. Lorenz, "Carrier signal injection based sensorless control methods for IPM synchronous machine drives," in *Conference Record - IAS Annual Meeting (IEEE Industry Applications Society)*, vol. 2, 2004, pp. 977–984.

[27] D. Raca, P. García, D. Reigosa, F. Briz, and R. Lorenz, "A comparative analysis of pulsating vs. rotating vector carrier signal injection-based sensorless control," in *Conference Proceedings - IEEE Applied Power Electronics Conference and Exposition - APEC*, 2008, pp. 879–885.

[28] N. Bianchi, E. Fornasiero, and S. Bolognani, "Effect of stator and rotor saturation on sensorless rotor position detection," in *IEEE Energy Conversion Congress and Exposition*, 2011, pp. 1528–1535.

[29] S. Shinnaka, "New "mirror-phase vector control" for sensorless drive of permanent-magnet synchronous motor with pole saliency," *IEEE Transactions on Industry Applications*, vol. 40, no. 2, pp. 599–606, 2004.

[30] S. Bolognani, S. Calligaro, R. Petrella, and M. Tursini, "Sensorless control of IPM motors in the low-speed range and at standstill by hf injection and dft processing," *IEEE Transactions on Industry Applications*, vol. 47, no. 1, pp. 96–104, 2011.

[31] J.-I. Ha and S.-K. Sul, "Sensorless field-orientation control of an induction machine by high-frequency signal injection," *IEEE Transactions on Industry Applications*, vol. 35, no. 1, pp. 45–51, 1999.

[32] J.-H. Jang, S.-K. Sul, J.-I. Ha, K. Ide, and M. Sawamura, "Sensorless drive of surface-mounted permanent-magnet motor by high-frequency signal injection based on magnetic saliency," *IEEE Trans. Industry Applications*, vol. 39, pp. 1031–1039, 2003.

[33] M. Linke, R. Kennel, and J. Holtz, "Sensorless speed and position control of synchronous machines using alternating carrier injection," in *IEEE International Electric Machines and Drives Conference*, vol. 2, june 2003, pp. 1211 – 1217.

[34] J. Holtz, "Acquisition of position error and magnet polarity for sensorless control of PM synchronous machines," *IEEE Transactions on Industry Applications*, vol. 44, no. 4, pp. 1172–1180, 2008.

[35] G.-D. Andreescu and C. Schlezinger, "Enhancement sensorless control system for PMSM drives using square-wave signal injection," in *SPEEDAM 2010 - International Symposium on Power Electronics, Electrical Drives, Automation and Motion*, 2010, pp. 1508–1511.

[36] Y.-D. Yoon, S.-K. Sul, S. Morimoto, and K. Ide, "High-bandwidth sensorless algorithm for AC machines based on square-wave-type voltage injection," *IEEE Trans. Industry Applications*, vol. 47, no. 3, pp. 1361–1370, 2011.

[37] C. Wang and L. Xu, "A novel approach for sensorless control of PM machines down to zero speed without signal injection or special pwm technique," *IEEE Transactions on Power Electronics*, vol. 19, no. 6, pp. 1601–1607, 2004.

[38] L. Harnefors and H.-P. Nee, "A general algorithm for speed and position estimation of AC motors," *IEEE Trans. Industrial Electronics*, vol. 47, no. 1, pp. 77–83, 2000.

[39] C. Silva, G. Asher, and M. Sumner, "Hybrid rotor position observer for wide speed-range sensorless PM motor drives including zero speed," *IEEE Transactions on Industrial Electronics*, vol. 53, no. 2, pp. 373–378, 2006.

[40] A. Piippo, M. Hinkkanen, and J. Luomi, "Analysis of an adaptive observer for sensorless control of interior permanent magnet synchronous motors," *IEEE Trans. Industrial Electronics*, vol. 55, no. 2, pp. 570–576, 2008.

[41] T. Aihara, A. Toba, T. Yanase, A. Mashimo, and K. Endo, "Sensorless torque control of salient-pole synchronous motor at zero-speed operation," *IEEE Trans. Power Electronics*, vol. 14, pp. 202–208, 1999.

[42] S. Morimoto, A. Shimmei, M. Sanada, and Y. Takeda, "Position and speed sensorless control system of permanent magnet synchronous motor with parameter identification," *IEEJ Transactions on Industry Applications*, vol. 126, no. 6, pp. 748–755+9, 2006.

[43] A. Vagati, M. Pastorelli, and F. Scapino, "Impact of cross saturation in synchronous reluctance motors of the transverse-laminated type," *IEEE Transactions on Industry Applications*, vol. 36, no. 4, pp. 1039–1046, 2000.

[44] E. Capecchi, P. Guglielmi, M. Pastorelli, and A. Vagati, "Position-sensorless control of the transverse-laminated synchronous reluctance motor," *IEEE Transactions on Industry Applications*, vol. 37, no. 6, pp. 1768–1776, 2001.

[45] F. Briz, M. Degner, A. Diez, and R. Lorenz, "Measuring, modeling, and decoupling of saturation-induced saliencies in carrier-signal injection-based sensorless AC drives," *IEEE Transactions on Industry Applications*, vol. 37, no. 5, pp. 1356–1364, 2001.

[46] ——, "Static and dynamic behavior of saturation-induced saliencies and their effect on carrier-signal-based sensorless AC drives," *IEEE Transactions on Industry Applications*, vol. 38, no. 3, pp. 670–678, 2002.

[47] P. Guglielmi, M. Pastorelli, G. Pellegrino, and A. Vagati, "Position-sensorless control of permanent-magnet-assisted synchronous reluctance motor," *IEEE Transactions on Industry Applications*, vol. 40, no. 2, pp. 615–622, 2004.

[48] F. De Belie, J. Melkebeek, L. Vandevelde, R. Boel, K. Geldhof, and T. Vyncke, "A nonlinear model for synchronous machines to describe high-frequency signal based position estimators," in *2005 IEEE International Conference on Electric Machines and Drives*, 2005, pp. 696–703.

[49] P. Guglielmi, M. Pastorelli, and A. Vagati, "Cross-saturation effects in IPM motors and related impact on sensorless control," *IEEE Trans. Industry Applications*, vol. 42, pp. 1516–1522, 2006.

[50] ——, "Impact of cross-saturation in sensorless control of transverse-laminated synchronous reluctance motors," *IEEE Transactions on Industrial Electronics*, vol. 53, no. 2, pp. 429–439, 2006.

[51] N. Bianchi and S. Bolognani, "Influence of rotor geometry of an IPM motor on sensorless control feasibility," *IEEE Transactions on Industry Applications*, vol. 43, no. 1, pp. 87–96, 2007.

[52] N. Bianchi, S. Bolognani, J.-H. Jang, and S.-K. Sul, "Comparison of PM motor structures and sensorless control techniques for zero-speed rotor position detection," *IEEE Trans. Power Electronics*, vol. 22, no. 6, pp. 2466–2475, 2007.

[53] Y. Li, Z. Zhu, D. Howe, and C. Bingham, "Modeling of cross-coupling magnetic saturation in signal-injection-based sensorless control of permanent-magnet brushless AC motors," *IEEE Transactions on Magnetics*, vol. 43, no. 6, pp. 2552–2554, 2007.

[54] S.-Y. Kim and I.-J. Ha, "A new observer design method for hf signal injection sensorless control of ipmsms," *IEEE Transactions on Industrial Electronics*, vol. 55, no. 6, pp. 2525–2529, 2008.

[55] D. Reigosa, P. García, D. Raca, F. Briz, and R. Lorenz, "Measurement and adaptive decoupling of cross-saturation effects and secondary saliencies in sensorless controlled IPM synchronous machines," *IEEE Trans. Industry Applications*, vol. 44, no. 6, pp. 1758–1767, 2008.

[56] Y. Li, Z. Zhu, D. Howe, C. Bingham, and D. Stone, "Improved rotor-position estimation by signal injection in brushless AC motors, accounting for cross-coupling magnetic saturation," *IEEE Trans. Industry Applications*, vol. 45, pp. 1843–1850, 2009.

[57] E. Armando, P. Guglielmi, G. Pellegrino, M. Pastorelli, and A. Vagati, "Accurate modeling and performance analysis of IPM-PMASR motors," *IEEE Trans. Industry Applications*, vol. 45, no. 1, pp. 123–130, 2009.

[58] P. Sergeant, F. De Belie, and J. Melkebeek, "Effect of rotor geometry and magnetic saturation in sensorless control of PM synchronous machines," *IEEE Trans. Magnetics*, vol. 45, no. 3, pp. 1756–1759, 2009.

[59] H. De Kock, M. Kamper, and R. Kennel, "Anisotropy comparison of reluctance and PM synchronous machines for position sensorless control using HF carrier injection," *IEEE Trans. Power Electronics*, vol. 24, no. 8, pp. 1905–1913, 2009.

[60] N. Bianchi, S. Bolognani, and A. Faggion, "Predicted and measured errors in estimating rotor position by signal injection for salient-pole PM synchronous motors," in *IEEE International Electric Machines and Drives Conference*, 2009, pp. 1565–1572.

[61] D. Raca, P. García, D. Reigosa, F. Briz, and R. Lorenz, "Carrier-signal selection for sensorless control of PM synchronous machines at zero and very low speeds," *IEEE Trans. Industry Applications*, vol. 46, no. 1, pp. 167–178, 2010.

[62] Z. Zhu and L. Gong, "Investigation of effectiveness of sensorless operation in carrier-signal-injection-based sensorless-control methods," *IEEE Transactions on Industrial Electronics*, vol. 58, no. 8, pp. 3431–3439, 2011.

[63] P. Sergeant, F. De Belie, and J. Melkebeek, "Rotor geometry design of interior pmsms with and without flux barriers for more accurate sensorless control," *IEEE Transactions on Industrial Electronics*, vol. 59, no. 6, pp. 2457–2465, 2012.

[64] A. Jebai, F. Malrait, P. Martin, and P. Rouchon, "Estimation of saturation of permanent-magnet synchronous motors through an energy-based model," in *IEEE International Electric Machines Drives Conference*, 2011, pp. 1316 –1321.

[65] ——, "Sensorless position estimation of permanent-magnet synchronous motors using a non-linear magnetic saturation model," in *Proceedings - 2012 20th International Conference on Electrical Machines, ICEM 2012*, 2012, pp. 2245–2251.

[66] ——, "Signal injection and averaging for position estimation of permanent-magnet synchronous motors." in *IEEE Conference on Decision and Control (CDC)*, 2012.

[67] D. Basic, A. Jebai, F. Malrait, P. Martin, and P. Rouchon, "Using hamiltonians to model saturation in space vector representations of AC electrical machines," *Lecture Notes in Control and Information Sciences*, vol. 407, pp. 41–48, 2010.

[68] C. Silva, G. Asher, and M. Sumner, "Influence of dead-time compensation on rotor position estimation in surface mounted PM machines using hf voltage injection," in *Proceedings of the Power Conversion Conference, 2002. PCC Osaka.*, vol. 3, 2002, pp. 1279–1284.

[69] K. Wiedmann, F. Wallrapp, and A. Mertens, "Analysis of inverter nonlinearity effects on sensorless control for permanent magnet machine drives based on high-frequency signal injection," in *2009 13th European Conference on Power Electronics and Applications, EPE '09*, 2009.

[70] F. Gabriel, F. De Belie, P. Druyts, X. Neyt, J. Melkebeek, and M. Acheroy, "Compensating the influence of the stator resistor and inverter nonlinearities in signal-injection based sensorless strategies," in *5th IEEE Vehicle Power and Propulsion Conference, VPPC '09*, 2009, pp. 283–290.

[71] R. Raute, C. Caruana, C. Staines, J. Cilia, M. Sumner, and G. Asher, "Analysis and compensation of inverter nonlinearity effect on a sensorless PMSM drive at very low and zero speed operation," *IEEE Transactions on Industrial Electronics*, vol. 57, no. 12, pp. 4065–4074, 2010.

[72] Y. Yourgrau and S. Mandelstam, *Variational Principles in Dynamics and Quantum Theory*, 3rd ed. Dover, New-York, 1979.

[73] L. Landau and E. Lifshitz, *Mechanics*, 4th ed. Mir, Moscow, 1982.

[74] R. Ortega, J. Loria Perez, P. Nicklasson, and H. Sira-Ramirez, *Passivity-based Control of Euler-Lagrange Systems*, 1st ed. Springer, 1998.

[75] J. Chiasson, *Modeling and High Performance Control of Electric Machines*. Wiley-IEEE Press, May 2005.

[76] E. Favre, L. Cardoletti, and M. Jufer, "Permanent-magnet synchronous motors: a comprehensive approach to cogging torque suppression," *IEEE Transactions on Industry Applications*, vol. 29, no. 6, pp. 1141–1149, 1993.

[77] N. Bianchi and S. Bolognani, "Design techniques for reducing the cogging torque in surface-mounted PM motors," *IEEE Transactions on Industry Applications*, vol. 38, no. 5, pp. 1259–1265, 2002.

[78] R. Islam, I. Husain, A. Fardoun, and K. McLaughlin, "Permanent-magnet synchronous motor magnet designs with skewing for torque ripple and cogging torque reduction," *IEEE Transactions on Industry Applications*, vol. 45, no. 1, pp. 152–160, 2009.

[79] K. Corzine, B. Kuhn, S. Sudhoff, and H. Hegner, "An improved method for incorporating magnetic saturation in the q-d synchronous machine model," *IEEE Transactions on Energy Conversion*, vol. 13, no. 3, pp. 270–275, 1998.

[80] E. Levi, "Saturation modelling in d-q axis models of salient pole synchronous machines," *IEEE Transactions on Energy Conversion*, vol. 14, no. 1, pp. 44–50, 1999.

[81] E. Levi and V. Levi, "Impact of dynamic cross-saturation on accuracy of saturated synchronous machine models," *IEEE Transactions on Energy Conversion*, vol. 15, no. 2, pp. 224–230, 2000.

[82] C. Hwang, S. Chang, C. Pan, and T. Chang, "Estimation of parameters of interior permanent magnet synchronous motors," *Journal of Magnetism and Magnetic Materials*, vol. 239, no. 1-3, pp. 600–603, 2002.

[83] C. Mademlis, "Compensation of magnetic saturation in maximum torque to current vector controlled synchronous reluctance motor drives," *IEEE Transactions on Energy Conversion*, vol. 18, no. 3, pp. 379–385, 2003.

[84] B. Štumberger, G. Štumberger, D. Dolinar, A. Hamler, and M. Trlep, "Evaluation of saturation and cross-magnetization effects in interior permanent-magnet synchronous motor," *IEEE Trans. Industry Applications*, vol. 39, no. 5, pp. 1264–1271, 2003.

[85] G. Štumberger, B. Štumberger, M. Toman, and D. Dolinar, "Evaluation of experimental methods for determining the magnetically nonlinear characteristics of electromagnetic devices," *IEEE Trans. Magnetics*, vol. 41, no. 10, pp. 4030–4032, 2005.

[86] Y. Kano, T. Kosaka, and N. Matsui, "Simple nonlinear magnetic analysis for permanent-magnet motors," *IEEE Transactions on Industry Applications*, vol. 41, no. 5, pp. 1205–1214, 2005.

[87] J.-Y. Lee, S.-H. Lee, G.-H. Lee, J.-P. Hong, and J. Hur, "Determination of parameters considering magnetic nonlinearity in an interior permanent magnet synchronous motor," *IEEE Transactions on Magnetics*, vol. 42, no. 4, pp. 1303–1306, 2006.

[88] S. Yamamoto, T. Ara, and K. Matsuse, "A method to calculate transient characteristics of synchronous reluctance motors considering iron loss and cross-magnetic saturation," *IEEE Transactions on Industry Applications*, vol. 43, no. 1, pp. 47–56, 2007.

[89] M. Hadžiselimović, G. Štumberger, B. Štumberger, and I. Zagradišnik, "Magnetically nonlinear dynamic model of synchronous motor with permanent magnets," *Journal of Magnetism and Magnetic Materials*, vol. 316, no. 2 SPEC. ISS., pp. e257–e260, 2007.

[90] G. Štumberger, T. Marcic, B. Štumberger, and D. Dolinar, "Experimental method for determining magnetically nonlinear characteristics of electric machines with magnetically nonlinear and anisotropic iron core, damping windings, and permanent magnets," *IEEE Transactions on Magnetics*, vol. 44, no. 11 PART 2, pp. 4341–4344, 2008.

[91] Y. Wang, J. Zhu, S. Wang, Y. Guo, and W. Xu, "Nonlinear magnetic model of surface mounted PM machines incorporating saturation saliency," *IEEE Transactions on Magnetics*, vol. 45, no. 10, pp. 4684–4687, 2009.

[92] Z. Qu, T. Tuovinen, and M. Hinkkanen, "Inclusion of magnetic saturation in dynamic models of synchronous reluctance motors," in *Proceedings - 2012 20th International Conference on Electrical Machines, ICEM 2012*, 2012, pp. 994–1000.

[93] J.-H. Jang, J.-I. Ha, M. Ohto, K. Ide, and S.-K. Sul, "Analysis of permanent-magnet machine for sensorless control based on high-frequency signal injection," *IEEE Trans. Industry Applications*, vol. 40, no. 6, pp. 1595–1604, 2004.

[94] J.-I. Ha, K. Ide, T. Sawa, and S.-K. Sul, "Sensorless rotor position estimation of an interior permanent-magnet motor from initial states," *IEEE Trans. Industry Applications*, vol. 39, no. 3, pp. 761–767, 2003.

[95] R. Hermann and A. J. Krener, "Nonlinear controllability and observability," *IEEE Transactions on Automatic Control*, vol. AC-22, no. 5, pp. 728–740, 1977.

[96] S. Ogasawara and H. Akagi, "Implementation and position control performance of a position-sensorless IPM motor drive system based on magnetic saliency," *IEEE Transactions on Industry Applications*, vol. 34, no. 4, pp. 806–812, 1998.

[97] A. Consoli, G. Scarcella, and A. Testa, "Industry application of zero-speed sensorless control techniques for PM synchronous motors," *IEEE Trans. Industry Applications*, vol. 37, no. 2, pp. 513–521, 2001.

[98] F. Briz, "Dynamic operation of carrier-signal-injection-based sensorless direct field-oriented AC drives," *IEEE Transactions on Industry Applications*, vol. 36, no. 5, pp. 1360–1368, 2000.

[99] R. Masaki, S. Kaneko, M. Hombu, T. Sawada, and S. Yoshihara, "Development of a position sensorless control system on an electric vehicle driven by a permanent magnet synchronous motor," in *Proceedings of the Power Conversion Conference, 2002. PCC Osaka 2002.*, vol. 2, 2002, pp. 571 –576.

[100] F. Briz, M. Degner, P. García, and R. Lorenz, "Comparison of saliency-based sensorless control techniques for AC machines," *IEEE Transactions on Industry Applications*, vol. 40, no. 4, pp. 1107–1115, 2004.

[101] O. Wallmark, L. Harnefors, and O. Carlson, "An improved speed and position estimator for salient permanent-magnet synchronous motors," *IEEE Trans. Industrial Electronics*, vol. 52, no. 1, pp. 255–262, 2005.

[102] O. Wallmark and L. Harnefors, "Sensorless control of salient PMSM drives in the transition region," *IEEE Transactions on Industrial Electronics*, vol. 53, no. 4, pp. 1179–1187, 2006.

[103] C.-H. Choi and J.-K. Seok, "Pulsating signal injection-based axis switching sensorless control of surface-mounted permanent-magnet motors for minimal zero-current clamping effects," *IEEE Transactions on Industry Applications*, vol. 44, no. 6, pp. 1741–1748, 2008.

[104] S. Shinnaka, "A new speed-varying ellipse voltage injection method for sensorless drive of permanent-magnet synchronous motors with pole saliency - New PLL method using high-frequency current component multiplied signal," *IEEE Trans. Industry Applications*, vol. 44, no. 3, pp. 777–788, 2008.

[105] F. Cupertino, G. Pellegrino, P. Giangrande, and L. Salvatore, "Sensorless position control of permanent-magnet motors with pulsating current injection and compensation of motor end effects," *IEEE Transactions on Industry Applications*, vol. 47, no. 3, pp. 1371–1379, 2011.

[106] M. Degner and R. Lorenz, "Using multiple saliencies for the estimation of flux, position, and velocity in AC machines," *IEEE Transactions on Industry Applications*, vol. 34, no. 5, pp. 1097–1104, 1998.

[107] O. Mansouri-Toudert, H. Zeroug, F. Auger, and A. Chibah, "Improved rotor position estimation of salient-pole PMSM using high frequency carrier signal injection." in *20th International Conference on Electrical Machines, ICEM*, 2012.

[108] Y.-D. Yoon, S.-K. Sul, S. Morimoto, and K. Ide, "High bandwidth sensorless algorithm for AC machines based on square-wave type voltage injection," in *2009 IEEE Energy Conversion Congress and Exposition, ECCE 2009*, 2009, pp. 2123–2130.

[109] J. A. Sanders, F. Verhulst, and J. Murdock, *Averaging methods in nonlinear dynamical systems*, 2nd ed., ser. Applied Mathematical Sciences. Springer, 2007, no. 59.

[110] M. Hamida, A. Glumineau, and J. De Leon, "Robust integral backstepping control for sensorless IPM synchronous motor controller," *Journal of the Franklin Institute*, vol. 349, no. 5, pp. 1734–1757, 2012.

[111] M. Hamida, J. De Leon, A. Glumineau, and R. Boisliveau, "An adaptive interconnected observer for sensorless control of PM synchronous motors with online parameter identification," *IEEE Transactions on Industrial Electronics*, vol. 60, no. 2, pp. 739–748, 2013.

Titre: Commande sans capteur des moteurs synchrones à aimants permanents par injection de signaux

Résumé: Cette thèse étudie la problématique du fonctionnement sans capteur et à basse vitesse des moteurs synchrones à aimants permanents (MSAP) par l'injection de signaux (nous nous focalisons sur les effets de la saturation magnétique car leur compensation est primordiale pour résoudre cette problématique). Nous proposons une méthode originale pour modéliser la saturation magnétique en utilisant une approche énergétique (les formulations Lagrangienne et Hamiltonienne), où les symétries physiques sont exploitées pour simplifier l'expression de l'énergie magnétique. Les données expérimentales montrent qu'un polynôme de degré 4 est suffisant pour décrire avec précision les effets de la saturation. Ensuite, nous proposons une analyse claire et originale basée sur la moyennisation de second ordre et qui explique comment obtenir l'information de position à partir de l'injection des signaux (en utilisant le modèle proposé). Nous donnons une relation explicite entre les oscillations des courants statoriques et la position du rotor; cette relation est utilisée en temps réel. Ce modèle de saturation magnétique ainsi que la procédure d'estimation de position ont été testés et validés sur deux types de moteurs à aimants permanents: à l'intérieur ou en surface du rotor. Les résultats expérimentaux obtenus sur un banc de test montrent que l'erreur d'estimation de la position du rotor n'excède pas quelques degrés électriques dans la zone d'opération à basse vitesse.

Mots clés: Saturation, Contrôle sans capteur, Moteurs électriques, Moteur synchrone à aimants permanents, Tension haute fréquence, Moyennisation, Modèle Hamiltonien.

Title: Sensorless control of synchronous permanent magnet motors by signal injection

Abstract: This thesis addresses the problematic of sensorless low speed operation of permanent magnet synchronous motors (PMSM) by signal injection. We focus on the effects of magnetic and cross saturations because their compensation is paramount to solve this problematic. We propose an original way of modeling magnetic saturation using an energy approach (Lagrangian and Hamiltonian formulations), where the physical symmetries are exploited to simplify the expression of the magnetic energy. Experimental data show that a simple polynomial of degree 4 is sufficient to describe accurately magnetic saturation effects. Then we propose a clear and original analysis based on second-order averaging of how to recover the position information from signal injection (using the proposed model). We give an explicit relation between stator current ripples and rotor position; this relation is used in real time operation. Such magnetic saturation model and the resulting position estimates were tested and validated on two types of motors: with interior and surface permanent magnets (IPM and SPM). Experimental results obtained on a test bench show that estimation errors of the rotor position do not exceed few electrical degrees in the low speed operating domain.

Keywords: Saturation, Sensorless control, Electric motors, Permanent magnet synchronous motor PMSM, High frequency voltage, Averaging, Hamiltonian model.

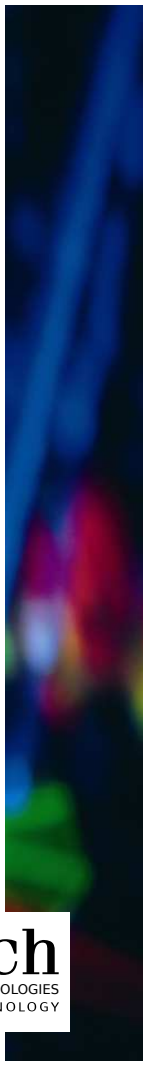

MINES ParisTech

ParisTech
INSTITUT DES SCIENCES ET TECHNOLOGIES
PARIS INSTITUTE OF TECHNOLOGY